Electromagnetic field coupling to thin wires above a ground

Dissertation

zur Erlangung des akademischen Grades

Doktoringenieur

(Dr.-Ing.)

von **M. Sc. Felix Middelstädt**

geb. am 13.01.1991 in Stralsund

genehmigt durch die Fakultät für Elektrotechnik und Informationstechnik

der Otto-von-Guericke-Universität Magdeburg

Gutachter:

Prof. Dr.-Ing. Ralf Vick

Prof. Dr. Farhad Rachidi-Haeri

Promotionskolloquium am 28. Februar 2024

Res Electricae Magdeburgenses
Magdeburger Forum zur Elektrotechnik, Jg. 22, Band 99, 2024
http://www.mafo.ovgu.de/

IMPRESSUM

1. Auflage, Magdeburg, Otto-von-Guericke-Universität, 2024
Zugl.: Magdeburg, Univ., Diss., 2024

Auflage: 50

Redaktionsschluss: April 2024

ISSN: 1612-2526
ISBN: 978-3-948749-45-3
DOI: 10.24352/UB.OVGU-2024-082

Bezug über die Herausgeber

Druck: docupoint GmbH
Otto-von-Guericke-Allee 14, 39179 Barleben

Abstract

Transmission lines play an important role in many electronic and electrical systems. They guide signals and power between different components. However, they can also act unintentionally as an antenna that receives surrounding electromagnetic fields that might destroy sensitive components. Furthermore, the transmission line might emit electromagnetic fields that could interfere with other devices in the same environment. Hence, the analysis of the transmission line is important, especially in the context of electromagnetic compatibility analysis.

There are different kinds of transmission lines, e.g. microstrip lines on printed circuit boards or thin wires above a large ground plane. The goal of this thesis is the analytic and semi-analytic analysis of the current along thin wires above a large ground plane in frequency domain. The general understanding of the wave propagation along and the field coupling to this important class of transmission lines shall be improved by this work.

The considered thin wires are excited by a plane wave. They are assumed to be long compared to the wave length and must have a uniform section somewhere along the trajectory. Apart from the uniform section the trajectory of the wire can be arbitrary and lumped impedances can be present at the ports. Multiple wires above a ground plane are considered as well.

For these transmission lines the so called asymptotic approach is applicable. It provides an analytic expression for the current in the uniform section of the wire and plays a key role in the analytic and semi-analytic analysis of the current. It is assumed that the current in the uniform section is a superposition of transverse electromagnetic modes and a forced response. The amplitudes of these modes depend on the scattering and reflection coefficients of the wire ports. These coefficients are in general complex, frequency dependent and consider the trajectory of the wire at the ports. They might include high frequency effects like radiation at discontinuities. This is a notable difference to the classical transmission line theory. Hence, the asymptotic approach is applicable to much higher frequencies than the classical theory.

The scattering and reflection coefficients can be approximated by numerical and analytic methods. The main focus of this thesis lays on the analytic approximation. An iterative method is used that is derived from the general mixed potential integral equations for thin wires. The iteration is initialized by the classical transmission line solution. Each following solution depends on the previous iteration step. The analytic approximation is compared to a numerical one (method of moments) and a very good agreement is observed. Furthermore, the examples show the significantly improved accuracy compared to the classical transmission line theory.

Moreover, the analytic and numerical approximations are compared to measurement results. The complex radar cross section of thin wires above a ground plane is measured and the complex resonant frequencies, the so called natural frequencies, are extracted. The analytic natural frequencies are obtained by using the asymptotic approach and the iterative method. Very good agreement between measurement, analytic and numerical solution is observed for multiple examples.

Kurzfassung

Leitungen spielen in vielen elektrischen und elektronischen Geräten eine große Rolle. Sie werden zur Übertragung von Informationen oder Leistung zwischen unterschiedlichen Komponenten verwendet. Sie können jedoch auch ungewollt als Antenne wirken und somit ein Einfallstor für elektromagnetische Störungen durch externe elektromagnetische Felder sein. Außerdem können über die Leitungen elektromagnetische Felder abgestrahlt werden, die wiederum andere benachbarte Geräte stören. Daher ist es speziell im Bereich der elektromagnetischen Verträglichkeit wichtig die physikalischen Mechanismen der Feldeinkopplung in und Datenübertragung auf Leitungen zu untersuchen.

Es gibt verschiedene Leitungstypen, z.B. Mikrostreifenleitungen auf Leiterplatten oder dünnen Drähte über einer Masseebene. Das Ziel dieser Dissertation ist die analytische und semi-analytische Untersuchung der Ströme auf dünnen Drähten über einer großen Masseebene im Frequenzbereich. Das allgemeine Verständnis der Ausbreitung von Wellen auf Leitungen soll hiermit verbessert werden.

Die untersuchten dünnen Drähte werden durch ebene Wellen angeregt. Verglichen mit der Wellenlänge sind die Leitungen lang und besitzen einen gleichförmigen Abschnitt entlang der Trajektorie. Bis auf den gleichförmigen Abschnitt ist die Trajektorie der Leitung beliebig und Abschlussimpedanzen werden berücksichtigt. Mehrere parallele Drähte werden ebenfalls untersucht.

Für diese Leitungen ist der sogenannte asymptotischen Ansatz anwendbar. Der Ansatz liefert einen analytischen Ausdruck für den Strom im gleichförmigen Abschnitt des Drahtes. Er spielt eine zentrale Rolle bei der analytischen und semi-analytischen Untersuchung des Stromes. Es wird angenommen, dass der Strom eine Superposition aus mehrere transversal elektromagnetischen Moden und einer erzwungenen Antwort ist. Die Amplituden der Moden hängen von sogenannten Streu- und Reflexionskoeffizienten an den Leitungstoren ab. Diese Koeffizienten sind im Allgemeinen komplex, frequenzabhängig und von der Trajektorie am Leitungsende abhängig. Daher beinhalten die Koeffizienten Hochfrequenzeffekte, wie z.B. Feldabstrahlung an Ungleichförmigkeiten entlang der Leitung. Dies ist ein entscheidender Unterschied zur klassischen Leitungstheorie. Daher ist der asymptotische Ansatz für deutlich höhere Frequenzen anwendbar als die klassischen Theorie.

Die Streu- und Reflexionskoeffizienten können durch numerische und analytische Methoden approximiert werden. Das Hauptaugenmerk liegt in dieser Arbeit auf der analytischen Näherung. Eine iterative Methode wird verwendet, um die Koeffizienten ausgehend von den "Mixed Potential Integral Equations" für dünne Drähte analytisch zu approximieren. Die Iteration wird mit der Lösung der klassischen Leitungstheorie initialisiert. Jeder weitere Iterationsschritt nutzt die vorheriege Lösung als Quelle, um eine bessere Approximation zu finden. Die analytische Lösung wird mit einer numerischen (Momentenmethode) verglichen. Es ist eine sehr gute Übereinstimmung zu beobachten. Außerdem zeigen die Beispiele, dass die iterative Lösung signifikant genauer ist als die klassische Lösung aus der Leitungstheorie.

Darüber hinaus werden die analytischen und numerischen Approximationen mit Messergebnissen verglichen. Der komplexe Radarrückstreuquerschnitt von dünnen Drähten wird dazu gemessen und die komplexen Resonanzfrequenzen, die sogenannten natürlichen Frequenzen, werden extrahiert. Die analytischen natürlichen Frequenzen werden mithilfe des asymptotischen Ansatzes und der iterativen Methode bestimmt. Eine sehr gute Übereinstimmung zwischen den Messergebnissen, der analytischen Näherung und der numerischen Lösung ist für alle gewählte Beispiele zu beobachten.

Contents

Chapter 1

Introduction

High-tech cars, computers, smartwatches and many more electronic devices are an indispensable part of today's life. They all need to function while not disturbing other devices and while not being disturbed by other devices in the same environment. These two problems are the core of the electromagnetic compatibility (EMC) analysis.

One important component that is often considered in EMC analysis is the transmission line. There are different kinds of transmission lines, e.g. thin wires, microstrip lines on printed circuit boards, big cable harnesses. On one hand, transmission lines guide power and signals between different components and systems. On the other hand, they can pick up surrounding electromagnetic (EM) fields that can create disturbances in the system. This might lead to the malfunction of the electronic device or the destruction of components. Furthermore, transmission lines can unintentionally radiate EM fields that could interfere with other surrounding electronic systems. Hence, the analysis of transmission lines plays an important role. Transmission lines can be analyzed by numerical methods, analytic methods or a combination of both, so called semi-analytic methods.

There are different numerical solvers available to analyze all different kinds of transmission lines, e.g. the method of moments (MoM) [1], the finite elements method [2], [3], the finite differences method [4], and the finite integration technique [5]. However, they only give numeric solutions to specific problems. Further physical insight to understand the propagation of the EM waves along transmission lines can only be gained with analytic or semi-analytic methods.

The classical transmission line theory gives an analytic description of the transmission line problem (see e.g. [6], [7]). A summary of its development is presented in [8]. The theory can be seen as a simplified form of the complete Maxwell theory. It is widely used and a quite accurate approximation for low frequencies, i.e. for wavelengths that are much larger than the transverse dimensions of the transmission line. The theory only considers transverse electromagnetic (TEM) or quasi-TEM modes and only uniform transmission lines are regarded. Hence, high frequency effects, e.g. radiation effects, that usually appear at discontinuities and ports, are neglected. Numerous extensions to the classical theory to incorporate specific effects or to push the frequency limit are sought. Some of them are given in [8]–[11].

Thin wires above a ground form an important class of transmission lines. In [12]–[14] an asymptotic approach is introduced to describe the current in the middle of a partially uniform wire above a ground. The asymptotic approach assumes only TEM modes and a forced response in the middle section of the wire. These modes are reflected at the ports or other discontinuities. The amplitudes of the TEM modes depend on reflection

and scattering coefficients in a certain way. These coefficients characterize each port or discontinuity along the transmission line. The coefficients can be determined using the classical transmission line theory, which results in the well known classical transmission line approximation. However, the asymptotic approach allows for a more complex definition of the scattering and reflection coefficient as well. It is possible to include high frequency effects that appear at the port for the coefficients. Hence, the general asymptotic approach is more versatile than the classical transmission line theory for thin wires.

Apart from a numerical method to determine the complex and frequency dependent scattering and reflection coefficient an iterative method is introduced in [13], [15] for the simplest possible configuration, i.e. a straight open circuited wire above an infinite ground plane. The iterative method yields an analytic approximation for the coefficients. The iteration is initialized with the classical transmission line result. Each following iteration uses the previous one to improve the overall approximation. Excellent results are shown in [13], [15] for the example of the open circuited straight wire above a ground, with only one iteration step. The solution is valid for much higher frequencies than the classical one when compared to a numerical reference.

The goal of this thesis is to continue the work on the asymptotic approach and the iterative method. The objectives can be summarized as follows:

1. Generalize the iterative method to ports with an arbitrary wire trajectory and lumped loads.

2. Generalize the iterative method to multiple wires above a ground.

3. Compare the analytic approximations to numerical ones and experimental results to validate the asymptotic approach and iterative method.

Furthermore, it is interesting to analyze the iterative solution. One question that arises is: Can the solution be obtained by another way and are there similarities to other known methods? Hence, it is compared to the induced electromotive force (EMF) method. The induced EMF method is usually used to determine the input impedance on wire antennas. However, it can also be used to approximate the reflection coefficient of a wire port.

Structure of the thesis

After the introduction Ch. 2 presents mostly known results and methods that are needed throughout the thesis, e.g. the mixed potential integral equations, the method of moments and the singularity expansion method. Some novel derivations are presented. Chapter 3 describes and derives the asymptotic approach in a new way (compared to [13]). All details are given for the single wire case. The asymptotic approach for multiple wires is presented as well. The iterative method to analytically approximate the scattering and reflection coefficient is derived in detail in Ch. 4. The first order iteration is presented and compared to a numerical solution. Moreover, the convergence and uniqueness of the iterative method is discussed. An extension to multiple wires above a ground is presented as well. The numerical and analytic approximations are compared in Ch. 5 to experimental results. The measurement setup is described in detail and multiple examples are shown. The general findings and an outlook is presented in Ch. 6.

Chapter 2

Fundamentals

Theoretical results that are important for the rest of this thesis are summarized in this chapter. The mixed potential integral equations and the electric field integral equation are derived for thin wires above a ground plane. Furthermore, the current on an infinitely long, straight, thin wire above a ground is analytically analyzed. A short summary of the classical transmission line theory is presented. Finally, an introduction for the method of moments for thin wires and the singularity expansion method are given.

2.1 The general mixed potential integral equations and the electric field integral equation

In this section the mixed potential integral equations and the electric field integral equation are derived for perfect electric conductors that are surrounded by vacuum.

Let there be a three dimensional scatterer above an infinite ground plane as shown in Fig. 2.1. The scatterer is assumed to be a three dimensional object that is a perfect electric conductor. It is illuminated by an electromagnetic field $(\boldsymbol{E}_{\text{ex}}, \boldsymbol{H}_{\text{ex}})$. The goal of this section is to derive known equations that connect the electric field strength $\boldsymbol{E}_{\text{ex}}$ and the current density on the scatterer.

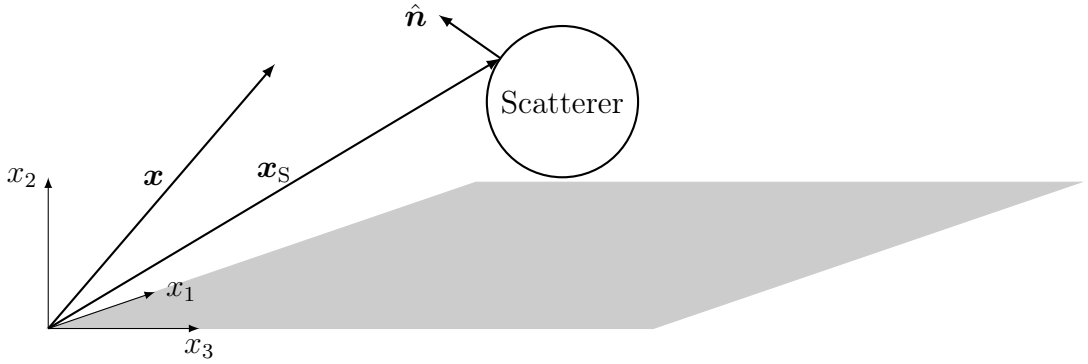

Figure 2.1: Arbitrary three dimensional scatterer above an infinite perfect electric ground.

Maxwell's equations fully describe the electromagnetic field strengths $(\boldsymbol{E}, \boldsymbol{H})$ that arise from a current density $\boldsymbol{J}$ and a corresponding charge density ϱ. They are given in

frequency domain for the vacuum (see [16]) as

$$\operatorname{div} \boldsymbol{E} = \frac{\varrho}{\varepsilon_0} \tag{2.1}$$

$$\operatorname{div} \boldsymbol{H} = 0 \tag{2.2}$$

$$\operatorname{curl} \boldsymbol{E} = -\mathrm{j}\omega\mu_0 \boldsymbol{H} \tag{2.3}$$

$$\operatorname{curl} \boldsymbol{H} = \mathrm{j}\omega\varepsilon_0 \boldsymbol{E} + \boldsymbol{J}\,, \tag{2.4}$$

where ω is the angular frequency and the imaginary unit is denoted by j. The permittivity and permeability of vacuum are denoted by ε_0 and μ_0 respectively. From Eqs. (2.1) and (2.4) follows directly the continuity equation

$$\operatorname{div} \boldsymbol{J} = -\mathrm{j}\omega\varrho\,. \tag{2.5}$$

It is convenient to introduce auxiliary potentials, i.e. the scalar potential Φ and the vector potential $\boldsymbol{A}$. They are defined as

$$\operatorname{div} \boldsymbol{A} + \frac{\mathrm{j}\omega}{c^2}\Phi = 0 \tag{2.6}$$

$$\operatorname{curl} \boldsymbol{A} = \mu_0 \boldsymbol{H} \tag{2.7}$$

$$-\mathrm{j}\omega\boldsymbol{A} - \operatorname{grad}\Phi = \boldsymbol{E}\,. \tag{2.8}$$

Equation (2.6) is the so called Lorenz gauge [17], where c denotes the speed of light in vacuum. The Lorenz gauge is used for the rest of this thesis, due to its practicability.

Combining the potential definitions and Maxwell's equations results in the inhomogeneous Helmholtz equation for the scalar potential and the inhomogeneous vector Helmholtz equation for the vector potential, i.e.

$$(\Delta + k^2)\Phi = -\frac{\varrho}{\varepsilon_0} \tag{2.9}$$

$$(\Delta + k^2)\boldsymbol{A} = -\mu_0 \boldsymbol{J} \tag{2.10}$$

with the wave number

$$k = \frac{\omega}{c}\,. \tag{2.11}$$

The current density vector can be resolved into the product of its complex scalar value J and a unit vector $\hat{\boldsymbol{e}}_\mathrm{J}$ indicating the direction, i.e.

$$\boldsymbol{J}(\boldsymbol{x}) = J(\boldsymbol{x})\hat{\boldsymbol{e}}_J(\boldsymbol{x})\,. \tag{2.12}$$

Equations (2.9) and (2.10) are solved using the integral kernels G_Φ and $\boldsymbol{G}_\mathrm{A}$. It holds

$$\Phi(\boldsymbol{x}) = \frac{1}{4\pi\varepsilon_0}\int_{\mathcal{V}} G_\Phi(\boldsymbol{x},\boldsymbol{x}')\varrho(\boldsymbol{x}')\,\mathrm{d}\boldsymbol{x}' \tag{2.13}$$

$$\boldsymbol{A}(\boldsymbol{x}) = \frac{\mu_0}{4\pi}\int_{\mathcal{V}} \boldsymbol{G}_\mathrm{A}(\boldsymbol{x},\boldsymbol{x}')J(\boldsymbol{x}')\,\mathrm{d}\boldsymbol{x}'\,, \tag{2.14}$$

where the integration variable $\boldsymbol{x}'$ denotes the so called source points. The volume $\mathcal{V}$ contains all physical sources ϱ and $\boldsymbol{J}$. The vector $\boldsymbol{x}$ is an arbitrary vector in space with the Cartesian components (x_1, x_2, x_3).

The kernels depend on the boundary conditions of the problem. Since an infinite perfect electric ground plane is present for the considered problems, the kernels are

$$G_\Phi(\boldsymbol{x},\boldsymbol{x}') = \frac{\exp(-\mathrm{j}k\|\boldsymbol{x}-\boldsymbol{x}'\|)}{\|\boldsymbol{x}-\boldsymbol{x}'\|} - \frac{\exp(-\mathrm{j}k\|\boldsymbol{x}-\underset{\vee}{\boldsymbol{x}}'\|)}{\|\boldsymbol{x}-\underset{\vee}{\boldsymbol{x}}'\|} \tag{2.15}$$

$$\boldsymbol{G}_\mathrm{A}(\boldsymbol{x},\boldsymbol{x}') = \frac{\exp(-\mathrm{j}k\|\boldsymbol{x}-\boldsymbol{x}'\|)}{\|\boldsymbol{x}-\boldsymbol{x}'\|}\hat{\boldsymbol{e}}_J - \frac{\exp(-\mathrm{j}k\|\boldsymbol{x}-\underset{\vee}{\boldsymbol{x}}'\|)}{\|\boldsymbol{x}-\underset{\vee}{\boldsymbol{x}}'\|}\hat{\underset{\vee}{\boldsymbol{e}}}_J \tag{2.16}$$

where $\|\ \|$ denotes the Euclidean norm and the vector $\underset{\vee}{\boldsymbol{x}}'$ is $\boldsymbol{x}'$ mirrored at the ground plane at $x_2 = 0$, i.e.

$$\underset{\vee}{\boldsymbol{x}}' = \boldsymbol{x}' - 2(\boldsymbol{x}'\cdot\hat{\boldsymbol{x}}_2)\hat{\boldsymbol{x}}_2. \tag{2.17}$$

The kernels are obtained from the free space Green's function and using the image theory [18]. They satisfy the Sommerfeld radiation condition [19] and include the reflections at the ground plane.

The tangential component of the total electric field vanishes on the surface of perfect electric conductors [20]. The total electric field is in this context the sum of the exciting electric field $\boldsymbol{E}_\mathrm{ex}$ and the scattered electric field $\boldsymbol{E}$. Hence, it holds

$$\hat{\boldsymbol{n}}(\boldsymbol{x}_\mathrm{S}) \times (\boldsymbol{E}_\mathrm{ex}(\boldsymbol{x}_\mathrm{S}) + \boldsymbol{E}(\boldsymbol{x}_\mathrm{S})) = 0 \tag{2.18}$$

where $\boldsymbol{x}_\mathrm{S}$ is a vector pointing on the surface of the perfectly conducting scatterer and $\hat{\boldsymbol{n}}$ is the normal vector on the scatterer surface as shown in Fig. 2.1.

Inserting Eqs. (2.8) and (2.14) into Eq. (2.18) and rearranging the terms yields

$$\hat{\boldsymbol{n}}(\boldsymbol{x}_\mathrm{S}) \times \left[\operatorname{grad}\Phi(\boldsymbol{x}_\mathrm{S}) + \mathrm{j}\omega\frac{\mu_0}{4\pi}\int_\mathcal{V} \boldsymbol{G}_\mathrm{A}(\boldsymbol{x}_\mathrm{S},\boldsymbol{x}')J(\boldsymbol{x}')\,\mathrm{d}\boldsymbol{x}'\right] = \hat{\boldsymbol{n}}(\boldsymbol{x}_\mathrm{S}) \times \boldsymbol{E}_\mathrm{ex}(\boldsymbol{x}_\mathrm{S})\,. \tag{2.19}$$

The variables ε_0 and μ_0 are substituted by the speed of light c and the free space impedance Z_0 for better readability. It holds

$$\varepsilon_0 = \frac{1}{Z_0\, c} \tag{2.20}$$

$$\mu_0 = \frac{Z_0}{c}\,. \tag{2.21}$$

With these substitutions Eq. (2.19) and (2.13) become

$$\hat{\boldsymbol{n}}(\boldsymbol{x}_\mathrm{S}) \times \left[\operatorname{grad}\Phi(\boldsymbol{x}_\mathrm{S}) + \mathrm{j}k\frac{Z_0}{4\pi}\int_\mathcal{V} \boldsymbol{G}_\mathrm{A}(\boldsymbol{x}_\mathrm{S},\boldsymbol{x}')J(\boldsymbol{x}')\,\mathrm{d}\boldsymbol{x}'\right] = \hat{\boldsymbol{n}}(\boldsymbol{x}_\mathrm{S}) \times \boldsymbol{E}_\mathrm{ex}(\boldsymbol{x}_\mathrm{S}) \tag{2.22}$$

$$\int_\mathcal{V} G_\Phi(\boldsymbol{x}_\mathrm{S},\boldsymbol{x}')\operatorname{div}\boldsymbol{J}(\boldsymbol{x}')\,\mathrm{d}\boldsymbol{x}' + \mathrm{j}k\frac{4\pi}{Z_0}\,\Phi(\boldsymbol{x}_\mathrm{S}) = 0\,. \tag{2.23}$$

Equation (2.23) is obtained by inserting Eq. (2.5) into Eq. (2.13) with Eq. (2.20).

Equations (2.22) and (2.23) are the so called Mixed Potential Integral Equations (MPIE) for general perfectly conducting surfaces. They hold for any point on the surfaces. From a given exciting electric field $\boldsymbol{E}_\mathrm{ex}$ a current density $\boldsymbol{J}$ can be found with Eqs. (2.22) and (2.23).

For some applications it is convenient to insert Eq. (2.23) into Eq. (2.22) to eliminate the scalar potential. The so called Electric Field Integral Equation (EFIE) for general surfaces above a ground is obtained, namely

$$\hat{\boldsymbol{n}}(\boldsymbol{x}_\mathrm{S}) \times \left[\mathrm{grad} \int_\mathcal{V} G_\Phi(\boldsymbol{x}_\mathrm{S}, \boldsymbol{x}') \,\mathrm{div}\, \boldsymbol{J}(\boldsymbol{x}') \,\mathrm{d}\boldsymbol{x}' + k^2 \int_\mathcal{V} \boldsymbol{G}_\mathrm{A}(\boldsymbol{x}_\mathrm{S}, \boldsymbol{x}') J(\boldsymbol{x}') \,\mathrm{d}\boldsymbol{x}' \right] = -\mathrm{j}k \frac{4\pi}{Z_0} \hat{\boldsymbol{n}}(\boldsymbol{x}_\mathrm{S}) \times \boldsymbol{E}_\mathrm{ex}(\boldsymbol{x}_\mathrm{S}) \,. \quad (2.24)$$

The EFIE and the MPIE are equivalent. Both will be used in a simplified form for thin wires throughout the thesis.

2.2 Thin wires above a ground

In this section the MPIE are formulated for thin wires above an infinite ground plane. The thin wire approximation is used to approximate and to simplify Eqs. (2.22) and (2.23). Furthermore, the EFIE for thin wires is formulated.

Let there be a single wire above an infinite ground plane as shown in Fig. 2.2. The wire is characterized by the trajectory $\boldsymbol{x}_\mathrm{c}(l)$, where l is a parameter with $\mathcal{L}_\mathrm{min} < l < \mathcal{L}_\mathrm{max}$. The wire is excited by an external electromagnetic field $(\boldsymbol{E}_\mathrm{ex}, \boldsymbol{H}_\mathrm{ex})$ as in Sec. 2.1.

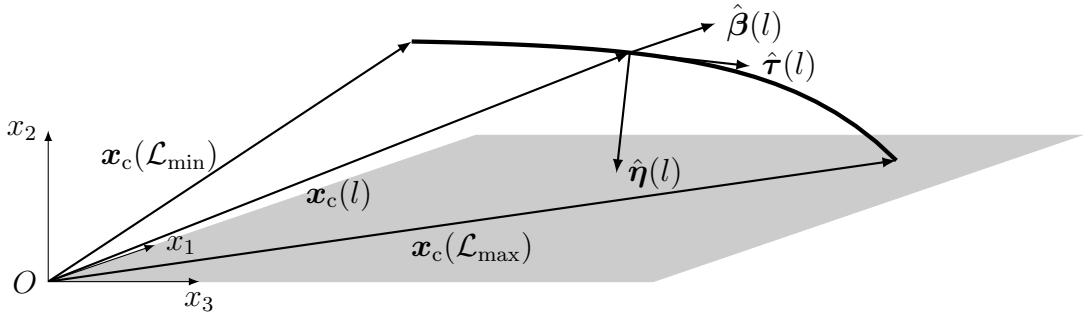

Figure 2.2: Arbitrary thin wire above an infinite perfect electric ground.

A new coordinate description is convenient to describe the vectors pointing on the wire surface. Hence, the so called Frenet-Serret frame is introduced [21]. It is shown in Fig. 2.2 and moves along the wire trajectory with the parameter l. The three orthonormal vectors are defined as

$$\hat{\boldsymbol{\tau}}(l) = \frac{1}{\xi(l)} \frac{\mathrm{d}}{\mathrm{d}l} \boldsymbol{x}_\mathrm{c}(l) \qquad \text{(tangential unit vector)} \quad (2.25)$$

$$\hat{\boldsymbol{\eta}}(l) = \frac{1}{\kappa(l)\xi(l)} \frac{\mathrm{d}}{\mathrm{d}l} \hat{\boldsymbol{\tau}}(l) \qquad \text{(normal unit vector)} \quad (2.26)$$

$$\hat{\boldsymbol{\beta}}(l) = \hat{\boldsymbol{\tau}}(l) \times \hat{\boldsymbol{\eta}}(l) \qquad \text{(binormal unit vector)} \quad (2.27)$$

where $\xi(l)$ ensures the normalization of $\hat{\boldsymbol{\tau}}$. The curvature of the trajectory is denoted by $\kappa(l)$.

All points inside or on the wire can now be easily characterized by the coordinates (l, r, ϕ), i.e.

$$\boldsymbol{x}(l, r, \phi) = \boldsymbol{x}_\mathrm{c}(l) + r\cos(\phi)\hat{\boldsymbol{\eta}}(l) + r\sin(\phi)\hat{\boldsymbol{\beta}}(l) \,. \quad (2.28)$$

The shortest distance between the point $\boldsymbol{x}$ and the wire core is denoted by r with the corresponding polar angle ϕ as depicted in Fig. 2.3. With Eq. (2.28) the integral and differential operators used in Eqs. (2.22) and (2.23) can be expressed for the new coordinates (l, r, ϕ). This is shown in detail in App. A.1.

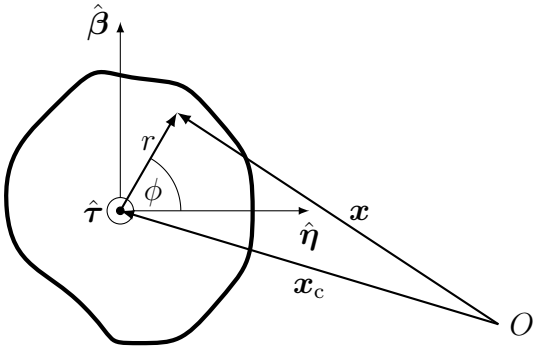

Figure 2.3: Non-circular wire cross section with polar coordinates to characterize each point inside the wire.

In the following, the wire is assumed to be thin with a circular cross section and with the wire radius a. That means a is small compared to the wavelength λ and to the total wire length $\mathcal{L}$, i.e.

$$a \ll \lambda, \mathcal{L}\,. \tag{2.29}$$

This leads to further assumptions for the physical quantities on the wire surface:

- $\boldsymbol{J}$, Φ and $\boldsymbol{E}_\mathrm{ex}$ are independent of ϕ on the wire surface,
- $\boldsymbol{J}$ points only in the direction tangential to the wire core $\hat{\boldsymbol{\tau}}$.

The current density exists only on the wire surface since the wire is assumed to be a perfect electric conductor. These assumptions lead to the following model of the current density

$$\boldsymbol{J}(\boldsymbol{x}) = J_\mathrm{S}(l)\delta(r-a)\hat{\boldsymbol{\tau}}(l) \tag{2.30}$$

with the surface current density J_S. The Dirac delta function is denoted by δ.

Furthermore, the integral kernels in Eq. (2.24) depend on $\|\boldsymbol{x}_\mathrm{S} - \boldsymbol{x}'_\mathrm{S}\|$. For the thin wire kernel approximation the distance between two surface points is approximated with

$$\|\boldsymbol{x}_\mathrm{S} - \boldsymbol{x}'_\mathrm{S}\| \approx \sqrt{\|\boldsymbol{x}_\mathrm{c}(l) - \boldsymbol{x}_\mathrm{c}(l')\|^2 + a^2}\,, \tag{2.31}$$

where l and l' are two parameters that characterize the position along the wire core. This means the ϕ and ϕ' dependence is ignored for the distance of two surface points. In a physical context this means that the source terms $\boldsymbol{x}'$ are on the wire core and the observation point is chosen for one specific ϕ so that Eq. (2.31) holds. This approximation strictly holds if the two surface points $\boldsymbol{x}_\mathrm{S}$ and $\boldsymbol{x}'_\mathrm{S}$ are in a great distance from each other. Nevertheless, good results are obtained if Eq. (2.31) is used for the entire domain as long as the radius a is small [22]. Moreover, an integration over a singular point is omitted with the approximation in Eq. (2.31). This simplifies the following treatments while maintaining a good accuracy.

With this model of the current density, Eq. (2.31) and the results derived in App. A.1 the general MPIE are modified in the following.

2.2.1 First mixed potential integral equation for thin wires

First, Eq. (2.22) is analyzed. The cross product $(\hat{\boldsymbol{n}}(\boldsymbol{x}_\mathrm{S}) \times \dots)$ extracts the tangential components. Since every physical quantity on the wire surface is assumed to be independent of ϕ and the surface current density points only in the direction of $\hat{\boldsymbol{\tau}}$, the cross product can be replaced by the dot product $(\hat{\boldsymbol{\tau}}(l) \cdot \dots)$. Inserting the current density (2.30) into (2.22) results in

$$\hat{\boldsymbol{\tau}}(l) \cdot \operatorname{grad} \Phi(l,a) + \mathrm{j}k\frac{Z_0}{4\pi} \int_{\mathcal{V}} \hat{\boldsymbol{\tau}}(l) \cdot \boldsymbol{G}_\mathrm{A}(\boldsymbol{x}_\mathrm{S}, \boldsymbol{x}') J_\mathrm{S}(l') \delta(r'-a) \,\mathrm{d}\boldsymbol{x}' = \hat{\boldsymbol{\tau}}(l) \cdot \boldsymbol{E}_\mathrm{ex}(l,a)\,. \quad (2.32)$$

Next, the gradient in direction of $\hat{\boldsymbol{\tau}}$ is inserted from Eq. (A.21) and the differential volume element $\mathrm{d}\boldsymbol{x}'$ is expanded as in Eq. (A.19). It follows

$$\begin{aligned} &\frac{1}{\xi(l)[1-a\kappa(l)\cos(\phi)]} \frac{\partial}{\partial l} \Phi(l,a) \\ &+ \mathrm{j}k\frac{Z_0}{4\pi} \int_{\mathcal{L}_\mathrm{min}}^{\mathcal{L}_\mathrm{max}} \int_0^{2\pi} \int_0^{a} \hat{\boldsymbol{\tau}}(l) \cdot \boldsymbol{G}_\mathrm{A}(\boldsymbol{x}_\mathrm{S}, \boldsymbol{x}') J_\mathrm{S}(l') \delta(r'-a) \xi(l') r' [1 - r'\kappa(l')\cos(\phi')] \,\mathrm{d}r' \,\mathrm{d}\phi' \,\mathrm{d}l' \\ &\qquad = \hat{\boldsymbol{\tau}}(l) \cdot \boldsymbol{E}_\mathrm{ex}(l,a)\,, \end{aligned} \quad (2.33)$$

where l', r' and ϕ' characterize the points containing the sources. Solving the integral in the r' coordinate yields

$$\begin{aligned} &\frac{1}{\xi(l)[1-a\kappa(l)\cos(\phi)]} \frac{\partial}{\partial l} \Phi(l,a) \\ &+ \mathrm{j}k\frac{Z_0}{4\pi} \int_{\mathcal{L}_\mathrm{min}}^{\mathcal{L}_\mathrm{max}} \int_0^{2\pi} \hat{\boldsymbol{\tau}}(l) \cdot \boldsymbol{G}_\mathrm{A}(\boldsymbol{x}_\mathrm{S}, \boldsymbol{x}'_\mathrm{S}) J_\mathrm{S}(l') \xi(l') a [1 - a\kappa(l')\cos(\phi')] \,\mathrm{d}\phi' \,\mathrm{d}l' \\ &\qquad = \hat{\boldsymbol{\tau}}(l) \cdot \boldsymbol{E}_\mathrm{ex}(l,a)\,. \end{aligned} \quad (2.34)$$

Due to the approximate ϕ-independence of all physical quantities on the wire surface, ϕ is chosen such that $\cos(\phi) = 0$ is fulfilled. Furthermore, instead of evaluating the exciting electric field $\boldsymbol{E}_\mathrm{ex}(l,a)$ at the radius a it is evaluated at the location of the wire core. This is justified because of $a \ll \lambda$. Hence, it follows

$$\begin{aligned} &\frac{1}{\xi(l)} \frac{\partial}{\partial l} \Phi(l,a) + \mathrm{j}k\frac{Z_0}{4\pi} \int_{\mathcal{L}_\mathrm{min}}^{\mathcal{L}_\mathrm{max}} \int_0^{2\pi} \hat{\boldsymbol{\tau}}(l) \cdot \boldsymbol{G}_\mathrm{A}(\boldsymbol{x}_\mathrm{S}, \boldsymbol{x}'_\mathrm{S}) J_\mathrm{S}(l') \xi(l') a [1 - a\kappa(l')\cos(\phi')] \,\mathrm{d}\phi' \,\mathrm{d}l' \\ &\qquad = \hat{\boldsymbol{\tau}}(l) \cdot \boldsymbol{E}_\mathrm{ex}(l,0)\,. \end{aligned} \quad (2.35)$$

Furthermore, the integral kernel is approximated by using Eq. (2.31) to allow a straight forward integration in the ϕ' coordinate.

Finally, the substitutions

$$\begin{aligned} g_\mathrm{A}(l,l') = &\frac{\exp(-\mathrm{j}k\sqrt{\|\boldsymbol{x}_\mathrm{c}(l) - \boldsymbol{x}_\mathrm{c}(l')\|^2 + a^2})}{\sqrt{\|\boldsymbol{x}_\mathrm{c}(l) - \boldsymbol{x}_\mathrm{c}(l')\|^2 + a^2}} \hat{\boldsymbol{\tau}}(l) \cdot \hat{\boldsymbol{\tau}}(l') \\ &- \frac{\exp(-\mathrm{j}k\sqrt{\|\boldsymbol{x}_\mathrm{c}(l) - \underset{\sim}{\boldsymbol{x}}_\mathrm{c}(l')\|^2 + a^2})}{\sqrt{\|\boldsymbol{x}_\mathrm{c}(l) - \underset{\sim}{\boldsymbol{x}}_\mathrm{c}(l')\|^2 + a^2}} \hat{\boldsymbol{\tau}}(l) \cdot \hat{\underset{\sim}{\boldsymbol{\tau}}}(l') \end{aligned} \quad (2.36)$$

and

$$I(l) = J_\mathrm{S}(l) 2\pi a \tag{2.37}$$

$$E_\mathrm{tan}(l) = \hat{\boldsymbol{\tau}}(l) \cdot \boldsymbol{E}_\mathrm{ex}(l, 0) \tag{2.38}$$

are made and the integration in the ϕ' coordinate is evaluated to result in the approximation of Eq. (2.22) for thin, perfect electrically conducting wires. It holds

$$\frac{1}{\xi(l)} \frac{\partial}{\partial l} \Phi(l, a) + \mathrm{j}k \frac{Z_0}{4\pi} \int\limits_{\mathcal{L}_\mathrm{min}}^{\mathcal{L}_\mathrm{max}} g_\mathrm{A}(l, l') I(l') \xi(l') \,\mathrm{d}l' = E_\mathrm{tan}(l) \,. \tag{2.39}$$

2.2.2 Second mixed potential integral equation for thin wires

Similar approximations are applied to Eq. (2.23). The divergence operator from Eq. (A.23) and the differential volume element from Eq. (A.19) are inserted into Eq. (2.23) with Eq. (2.30). It holds

$$\int\limits_{\mathcal{L}_\mathrm{min}}^{\mathcal{L}_\mathrm{max}} \int\limits_{0}^{2\pi} \int\limits_{0}^{a} G_\Phi(\boldsymbol{x}_\mathrm{S}, \boldsymbol{x}') \frac{\partial}{\partial l'} J_\mathrm{S}(l') \delta(r' - a) r' \,\mathrm{d}l' \,\mathrm{d}\phi' \,\mathrm{d}r' + \mathrm{j}k \frac{4\pi}{Z_0} \Phi(l, a) = 0 \,. \tag{2.40}$$

The integral kernel G_Φ is approximated with Eq. (2.31) as well. With the substitution

$$g_\Phi(l, l') = \frac{\exp(-\mathrm{j}k\sqrt{\|\boldsymbol{x}_\mathrm{c}(l) - \boldsymbol{x}_\mathrm{c}(l')\|^2 + a^2})}{\sqrt{\|\boldsymbol{x}_\mathrm{c}(l) - \boldsymbol{x}_\mathrm{c}(l')\|^2 + a^2}} - \frac{\exp(-\mathrm{j}k\sqrt{\|\boldsymbol{x}_\mathrm{c}(l) - \mathring{\boldsymbol{x}}_\mathrm{c}(l')\|^2 + a^2})}{\sqrt{\|\boldsymbol{x}_\mathrm{c}(l) - \mathring{\boldsymbol{x}}_\mathrm{c}(l')\|^2 + a^2}} \tag{2.41}$$

the integration in the r' and ϕ' coordinate can be carried out to yield

$$\int\limits_{\mathcal{L}_\mathrm{min}}^{\mathcal{L}_\mathrm{max}} g_\Phi(l, l') \frac{\partial}{\partial l'} J_\mathrm{S}(l') 2\pi a \,\mathrm{d}l' + \mathrm{j}k \frac{4\pi}{Z_0} \Phi(l, a) = 0 \,. \tag{2.42}$$

Furthermore, the current I can be substituted via Eq. (2.37) to finally result in the second MPIE for thin wires

$$\int\limits_{\mathcal{L}_\mathrm{min}}^{\mathcal{L}_\mathrm{max}} g_\Phi(l, l') \frac{\partial}{\partial l'} I(l') \,\mathrm{d}l' + \mathrm{j}k \frac{4\pi}{Z_0} \Phi(l, a) = 0 \,. \tag{2.43}$$

2.2.3 Summary for the mixed potential integral equations for thin wires

For a shorter notation the scalar potential $\Phi(l, a)$ is written as $\Phi(l)$. Furthermore, it is assumed that the wire trajectory is parametrized with its arc length. This means

$$\xi(l) = 1 = \text{const.} \tag{2.44}$$

In theory this parametrization is always possible [21]. However, not for all cases a closed form natural parametrization can be obtained, e.g. for elliptic curves. Nevertheless, in this thesis rather simple trajectories are analyzed and the parameter ξ is omitted from now on.

The MPIE for thin wires are summarized as

$$\frac{\partial}{\partial l}\Phi(l) + \mathrm{j}k\frac{Z_0}{4\pi}\int\limits_{\mathcal{L}_{\min}}^{\mathcal{L}_{\max}} g_{\mathrm{A}}(l,l')I(l')\,\mathrm{d}l' = E_{\tan}(l) \tag{2.45}$$

$$\int\limits_{\mathcal{L}_{\min}}^{\mathcal{L}_{\max}} g_{\Phi}(l,l')\frac{\partial}{\partial l'}I(l')\,\mathrm{d}l' + \mathrm{j}k\frac{4\pi}{Z_0}\,\Phi(l) = 0\,. \tag{2.46}$$

With the thin wire MPIE the current I and the scalar potential Φ on a thin wire can be determined from a given tangential electric field $E_{\tan}$.

2.2.4 Electric field integral equation for thin wires

The EFIE for thin wires is obtained by inserting Eq. (2.46) into Eq. (2.45) to eliminate the scalar potential. It holds

$$\frac{\partial}{\partial l}\int\limits_{\mathcal{L}_{\min}}^{\mathcal{L}_{\max}} g_{\Phi}(l,l')\frac{\partial}{\partial l'}I(l')\,\mathrm{d}l' + k^2\int\limits_{\mathcal{L}_{\min}}^{\mathcal{L}_{\max}} g_{\mathrm{A}}(l,l')I(l')\,\mathrm{d}l' = -\mathrm{j}k\frac{4\pi}{Z_0}\,E_{\tan}(l)\,. \tag{2.47}$$

Equation (2.47) is the thin wire version of Eq. (2.24). It is equivalent to the thin wire MPIE. Both, the MPIE and the EFIE for thin wires, are used throughout this thesis.

2.3 The straight, infinite wire above an infinite ground plane

The problem setup of the straight, infinite wire above a ground is shown in Fig. 2.4. The small wire radius is again denoted by a and the wire height above the ground is h. It is assumed that $a \ll h$. With no loss of generality, it is assumed that the wire is located at $x_1 = 0$. An exact analytic solution of the thin wire EFIE for the infinite wire can be obtained [23]–[26]. The exact solution is briefly derived and discussed in this section.

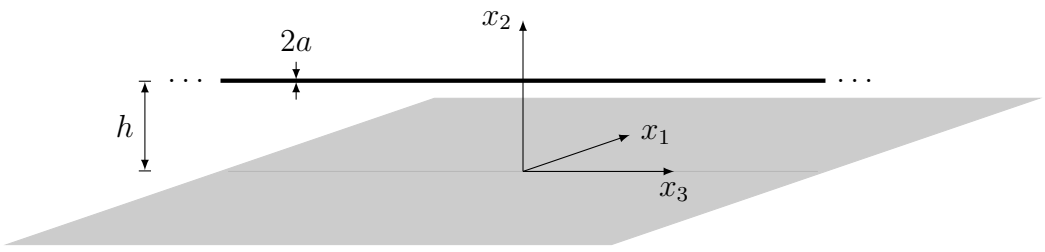

Figure 2.4: Straight, infinite wire above an infinite perfect electric ground.

First, the thin wire EFIE (see Eq. (2.47)) is derived to suit the specific problem. The wire is parameterized with

$$\boldsymbol{x}_{\mathrm{c}}(l) = h\,\hat{\boldsymbol{x}}_2 + l\,\hat{\boldsymbol{x}}_3\,, \tag{2.48}$$

where

$$-\infty < l < \infty\,. \tag{2.49}$$

According to Eq. (2.25) the tangential unit vector is

$$\hat{\boldsymbol{\tau}}(l) = \hat{\boldsymbol{x}}_3 = \text{const.} \tag{2.50}$$

Furthermore, it holds with Eq. (2.17)

$$\underset{\sim}{\boldsymbol{x}}_{\mathrm{c}}(l) = -h\,\hat{\boldsymbol{x}}_2 + l\,\hat{\boldsymbol{x}}_3 \tag{2.51}$$

$$\underset{\sim}{\hat{\boldsymbol{\tau}}}(l) = \hat{\boldsymbol{x}}_3\,. \tag{2.52}$$

Inserting the trajectory and tangential unit vector into Eqs. (2.36) and (2.41) results in

$$g_{\mathrm{A}}(l,l') = g_{\Phi}(l,l') = g_0(l-l') \tag{2.53}$$

with

$$g_0(l-l') = \frac{\exp(-\mathrm{j}k\sqrt{(l-l')^2+a^2})}{\sqrt{(l-l')^2+a^2}} - \frac{\exp(-\mathrm{j}k\sqrt{(l-l')^2+4h^2})}{\sqrt{(l-l')^2+4h^2}}\,. \tag{2.54}$$

For the second term in the latter equation $4h^2 + a^2 \approx 4h^2$ is used.

Therefore, the EFIE for the infinite wire is

$$\frac{\partial}{\partial l}\int\limits_{-\infty}^{\infty} g_0(l-l')\frac{\partial}{\partial l'}I(l')\,\mathrm{d}l' + k^2\int\limits_{-\infty}^{\infty} g_0(l-l')I(l')\,\mathrm{d}l' = -\mathrm{j}k\frac{4\pi}{Z_0}\,E_{\tan}(l)\,. \tag{2.55}$$

There is now only one single integral kernel g_0. It depends on the difference $l - l'$. Hence, the integrals can be interpreted as convolutions of g_0 with the current $I(l')$ or its derivative, i.e. $\frac{\partial}{\partial l'}I(l')$.

The spacial Fourier transform can be used to solve Eq. (2.55). It is defined as

$$\tilde{I}(k_l) = \int\limits_{-\infty}^{\infty} I(l)\exp(-\mathrm{j}k_l l)\,\mathrm{d}l \tag{2.56}$$

with the corresponding inverse Fourier transform

$$I(l) = \frac{1}{2\pi}\int\limits_{-\infty}^{\infty} \tilde{I}(k_l)\exp(\mathrm{j}k_l l)\,\mathrm{d}k_l\,, \tag{2.57}$$

where k_l is an auxiliary wave number and the tilde marks the transform respectively. The convolution becomes a multiplication of the transforms and the differentiation becomes a multiplication with $\mathrm{j}k_l$. It follows an algebraic equation for the transform of the current $\tilde{I}$, i.e.

$$(k^2 - k_l^2)\tilde{g}_0(k_l)\tilde{I}(k_l) = -\mathrm{j}k\frac{4\pi}{Z_0}\,\tilde{E}_{\tan}(k_l)\,. \tag{2.58}$$

Here, the tilde marks the Fourier transform. The Fourier transform of the kernel is

$$\tilde{g}_0(k_l) = \begin{cases} 2\left[K_0\left(a\sqrt{k_l^2 - k^2}\right) - K_0\left(2h\sqrt{k_l^2 - k^2}\right)\right] & \text{for } k_l^2 \neq k^2 \\ 2\ln\left(\frac{2h}{a}\right) & \text{for } k_l^2 = k^2\,. \end{cases} \tag{2.59}$$

where K_n is the modified Bessel function of the second kind and order n.

Rearranging Eq. (2.58) and applying the inverse (spatial) Fourier transform (ref. Eq. (2.57)) results in

$$I(l) = \mathrm{j}k\frac{2}{Z_0}\int_{-\infty}^{\infty} \frac{\tilde{E}_{\tan}(k_l)\exp(\mathrm{j}k_l l)}{(k_l^2 - k^2)\tilde{g}_0(k_l)}\,\mathrm{d}k_l\,. \tag{2.60}$$

This is the exact solution of the current for any excitation $E_{\tan}$. In the following Eq. (2.60) is solved for two important kinds of excitation:

1. the lumped excitation and
2. the plane wave excitation.

The solution for the lumped excitation can be seen as a Green's function for the problem with a general excitation. A plane wave excitation is a good model for many practical problems.

2.3.1 Lumped excitation

The goal is to solve the integral in Eq. (2.60) for a lumped excitation. That means there is a lumped voltage source along the wire at the point $l = 0$. The tangential electric field along the wire and its Fourier transform is modeled as in [27, p. 131], namely

$$E_{\tan}(l) = V_0\,\delta(l) \tag{2.61}$$

$$\tilde{E}_{\tan}(k_l) = V_0 \tag{2.62}$$

with the complex voltage amplitude V_0. Inserting the tangential electric field into Eq. (2.60) results in

$$I(l) = \mathrm{j}k\frac{2V_0}{Z_0}\int_{-\infty}^{\infty} \frac{\exp(\mathrm{j}k_l l)}{(k_l^2 - k^2)\tilde{g}_0(k_l)}\,\mathrm{d}k_l\,. \tag{2.63}$$

The integral in Eq. (2.63) can be solved using the residue theorem as in [24]–[26]. The integrand is extended for complex k_l. The residue theorem states that the integration along the closed path in the complex plane is equal to the sum of the residues of all enclosed poles of the integrand if the integrand is analytic along the path.

The integrand in Eq. (2.63) has infinitely many complex poles k_n as indicated in Fig. 2.5. Furthermore, there are two branch cuts with branch points at $k_l = \pm k$. The original integration path along the real axis is extended to a closed path in the complex plane as shown in Fig. 2.5. From Cauchy's residue theorem follows

$$\int_{-\infty}^{\infty} + \int_{\mathcal{C}_1} + \int_{\mathcal{C}_2} + \int_{\mathcal{C}_3} + \int_{\mathcal{C}_4} + \int_{\mathcal{C}_5} = 4\pi\mathrm{j}\sum_n \mathrm{Res}(k_n)\,. \tag{2.64}$$

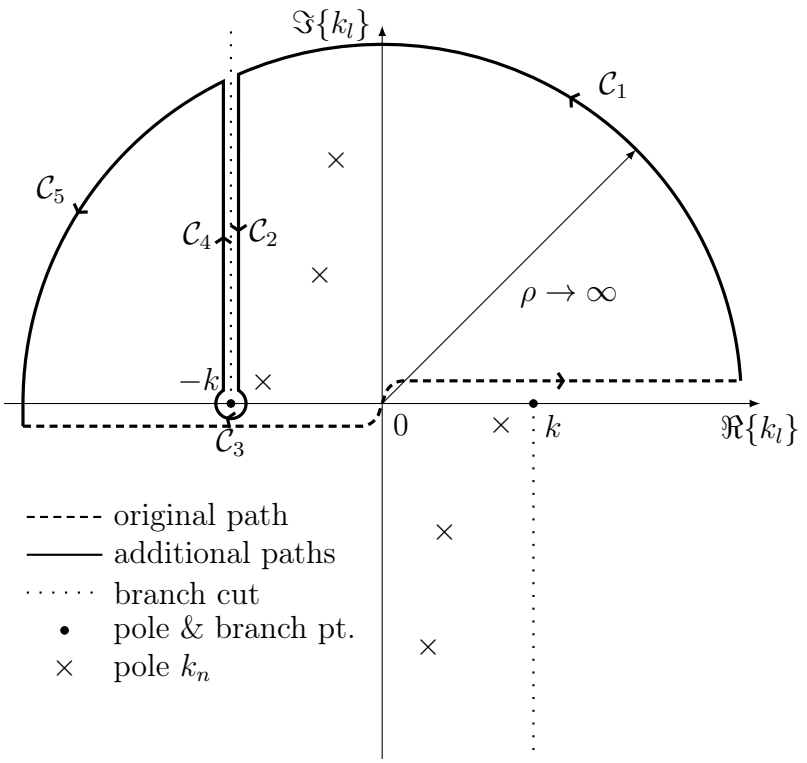

Figure 2.5: Closed integration contour in the complex k_l plane.

The radius ρ tends to ∞. Due to the exponential function in the integrand, the integration along $\mathcal{C}_1$ and $\mathcal{C}_5$ is zero for $l > 0$. If $l < 0$, the contour is mirrored at the origin $k_l = 0$. Rearranging Eq. (2.64) leads to

$$\int_{-\infty}^{\infty} = -\int_{\mathcal{C}_3} + 4\pi\mathrm{j}\sum_n \mathrm{Res}(k_n) - \int_{\mathcal{C}_2} - \int_{\mathcal{C}_4} . \tag{2.65}$$

The current I is composed of three kinds of modes as shown in [26], i.e. a TEM mode I_{TEM}, leaky modes $I_{n,\mathrm{Leaky}}$ and a radiation mode I_{Rad}. It holds

$$I(l) = I_{\mathrm{TEM}}(l) + \sum_n I_{n,\mathrm{Leaky}}(l) + I_{\mathrm{Rad}}(l) . \tag{2.66}$$

The TEM mode arises from the integration around the branch point at $k_l = \pm k$. The residues in Eq. (2.65) are connected to the leaky modes and the integration along the branch cut gives rise to the radiation mode. As shown in [25], [26] in more detail, it holds

$$I_{\mathrm{TEM}}(l) = \frac{V_0}{2Z_{\mathrm{C}}}\,\mathrm{e}^{-\mathrm{j}k|l|} \tag{2.67}$$

$$I_{n,\mathrm{Leaky}}(l) = -\frac{V_0}{2Z_{n,\mathrm{Leaky}}}\,\mathrm{e}^{\mathrm{j}k_n|l|} \tag{2.68}$$

with

$$Z_{\mathrm{C}} = \frac{Z_0}{2\pi}\ln\left(\frac{2h}{a}\right) \tag{2.69}$$

$$Z_{n,\mathrm{Leaky}} = \frac{Z_0}{2\pi}\frac{k_n\sqrt{k_n^2-k^2}}{2k}\left[aK_1\left(-a\sqrt{k_n^2-k^2}\right) - 2hK_1\left(-2h\sqrt{k_n^2-k^2}\right)\right] \tag{2.70}$$

For the radiation mode holds (see [26] for details)

$$I_{\mathrm{Rad}}(l) = k\frac{V_0}{Z_0}\,\mathrm{e}^{-\mathrm{j}k|l|}\int_0^\infty \frac{\exp(-\zeta|l|)}{\zeta(\zeta+2\mathrm{j}k)}\left[\frac{1}{K_0(-a\sqrt{\zeta(\zeta+2\mathrm{j}k)})-K_0(-2h\sqrt{\zeta(\zeta+2\mathrm{j}k)})}\right.$$
$$\left.-\frac{1}{K_0(a\sqrt{\zeta(\zeta+2\mathrm{j}k)})-K_0(2h\sqrt{\zeta(\zeta+2\mathrm{j}k)})}\right]\mathrm{d}\zeta\,, \quad (2.71)$$

where ζ is an auxiliary variable.

The TEM mode experiences no damping along the wire. It is excited at the voltage source and travels outward towards $\pm\infty$ with a constant amplitude and with the frequency k. The EM field associated with I_{TEM} is a wave traveling in positive and negative x_3-direction away from the source. The field components are only present in the transverse plane of the transmission line, i.e. the x_1-x_2-plane.

The leaky modes are exponentially damped with increasing distance from the source. The damping coefficient is $|\Im\{k_n\}|$ and the oscillation frequency is $|\Re\{k_n\}|$. Hence, they only contribute to the total current in a small region around the lumped source.

The integral of the radiation mode has to be evaluated numerically. However, for large $|l|$ the asymptotic behavior can be analyzed [26], i.e.

$$I_{\mathrm{Rad}}(l) \sim \frac{V_0}{2Z_{\mathrm{C}}}\frac{\mathrm{j}kh^2}{\ln\left(\frac{2h}{a}\right)}\frac{\exp(-\mathrm{j}k|l|)}{|l|} = \frac{\mathrm{j}kh^2}{\ln\left(\frac{2h}{a}\right)}\frac{I_{\mathrm{TEM}}(l)}{|l|} \qquad \text{for } |l| \gg 0 \quad (2.72)$$

Hence, the radiation mode oscillates with frequency k and is damped with $|l|^{-1}$ far away from the source.

Another representation for the exact current is given in [23]. The amplitude of all modes is proportional to V_0. Hence, it holds

$$I(l) = V_0\,\left[Y_{\mathrm{TEM}}(l) + Y_{\mathrm{Leaky}}(l) + Y_{\mathrm{Rad}}(l)\right] \quad (2.73)$$

with the admittance functions

$$Y_{\mathrm{TEM}}(l) = \frac{1}{2Z_{\mathrm{C}}}\,\mathrm{e}^{-\mathrm{j}k|l|} \quad (2.74)$$

$$Y_{\mathrm{Leaky}}(l) = -\sum_n \frac{1}{2Z_{n,\mathrm{Leaky}}}\,\mathrm{e}^{-\mathrm{j}k_n|l|} \quad (2.75)$$

$$Y_{\mathrm{Rad}}(l) = k\frac{1}{Z_0}\,\mathrm{e}^{-\mathrm{j}k|l|}\int_0^\infty \frac{\exp(-\zeta|l|)}{\zeta(\zeta+2\mathrm{j}k)}\left[\frac{1}{K_0(-a\sqrt{\zeta(\zeta+2\mathrm{j}k)})-K_0(-2h\sqrt{\zeta(\zeta+2\mathrm{j}k)})}\right.$$
$$\left.-\frac{1}{K_0(a\sqrt{\zeta(\zeta+2\mathrm{j}k)})-K_0(2h\sqrt{\zeta(\zeta+2\mathrm{j}k)})}\right]. \quad (2.76)$$

If the voltage source is located at $l = l_0$ the current is obtained by shifting the solution for $l = 0$ by l_0, i.e.

$$I_{l_0}(l) = V_0\,\left[Y_{\mathrm{TEM}}(l-l_0) + Y_{\mathrm{Leaky}}(l-l_0) + Y_{\mathrm{Rad}}(l-l_0)\right] \quad (2.77)$$

To conclude, at a far distance from the source only the TEM mode has a significant influence on the total current. The leaky modes and radiation mode decay with increasing distance.

2.3.2 Plane wave excitation

In this subsection Eq. (2.60) is analytically solved for the plane wave excitation of the infinite wire. The plane wave is characterized by the angle of incidence θ as shown in Fig 2.6. The vectors of the plane wave are defined as

$$\boldsymbol{k} = k[-\sin(\theta)\,\hat{\boldsymbol{x}}_2 + \cos(\theta)\,\hat{\boldsymbol{x}}_3] \tag{2.78}$$

$$\boldsymbol{E}_{\text{inc}}(\boldsymbol{x}) = E_0[\cos(\theta)\,\hat{\boldsymbol{x}}_2 + \sin(\theta)\,\hat{\boldsymbol{x}}_3]\,\mathrm{e}^{-\mathrm{j}\boldsymbol{k}\cdot\boldsymbol{x}} \tag{2.79}$$

$$\boldsymbol{H}_{\text{inc}}(\boldsymbol{x}) = -\frac{E_0}{Z_0}\,\hat{\boldsymbol{x}}_1\,\mathrm{e}^{-\mathrm{j}\boldsymbol{k}\cdot\boldsymbol{x}} \tag{2.80}$$

where E_0 is an arbitrary complex amplitude of the electric field. A more general definition of the plane wave is possible, e.g. a general polarization or a second angle in the x_3-x_1-plane could be included. However, this specific example is enough to show the desired effects while keeping the equations simple.

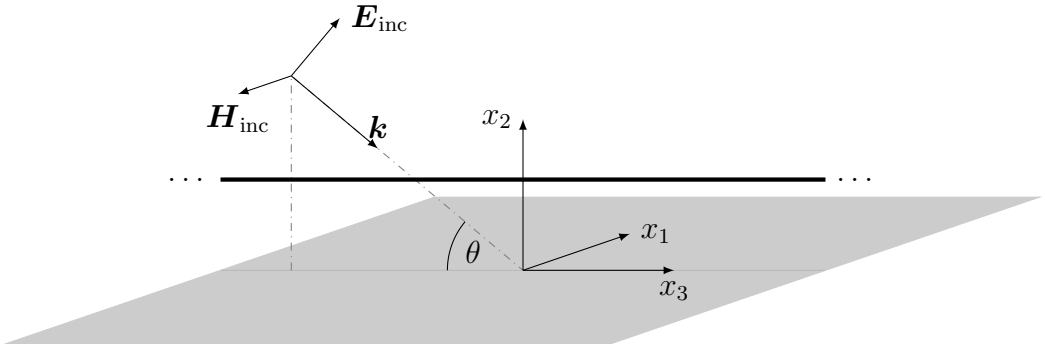

Figure 2.6: Straight, infinite wire above an infinite perfect electric ground with a plane wave excitation.

The external electric field that excites the current in Eq. (2.55) is obtained from the superposition of the plane wave and its reflection. Therefore, it holds

$$E_{\tan}(l) = 2\mathrm{j}E_0\sin(\theta)\sin(kh\sin(\theta))\,\mathrm{e}^{-\mathrm{j}k_\theta l} \tag{2.81}$$

with

$$k_\theta = k\cos(\theta)\,. \tag{2.82}$$

The Fourier transform of the the tangential electric field is

$$\tilde{E}_{\tan}(k_l) = 4\pi\mathrm{j}E_0\sin(\theta)\sin(kh\sin(\theta))\,\delta(k_l + k_\theta)\,. \tag{2.83}$$

Inserting Eq. (2.83) into Eq. (2.60) and using the integral property of the delta function yields

$$I(l) = k\frac{8\pi}{Z_0}\frac{E_0\sin(\theta)\sin(kh\sin(\theta))}{(k^2 - k_\theta^2)\tilde{g}_0(k_\theta)}\,\mathrm{e}^{-\mathrm{j}k_\theta l}\,. \tag{2.84}$$

Rearranging the terms finally results in

$$I(l) = \frac{4\pi}{Z_0\tilde{g}_0(k_\theta)}\frac{2E_0\sin(kh\sin(\theta))}{k\sin(\theta)}\,\mathrm{e}^{-\mathrm{j}k_\theta l}\,. \tag{2.85}$$

Equation (2.85) is the exact solution of the thin wire EFIE for the infinite wire above a ground with a plane wave excitation.

As for the TEM mode for the lumped excitation (see Eq. (2.67)) the amplitude of the current is constant along the wire. However, it depends on the angle of incidence θ. Furthermore, the effective wave number k_θ is smaller or equal to k and depends on the angle of incidence as well (see Eq. (2.82)).

If θ tends to zero, the plane wave travels along the wire axis as a TEM mode. Taking the limit $\theta \to 0$ for Eq. (2.85) yields

$$\lim_{\theta \to 0} I(l) = \frac{2hE_0}{Z_\mathrm{C}} \, \mathrm{e}^{-\mathrm{j}kl} \, . \tag{2.86}$$

The current has a similar form as I_TEM in Eq. (2.67) with an equivalent voltage $4hE_0$. This behavior is also noted in [26], [28].

2.4 Classical transmission line theory

It is possible to find exact solutions for the current along infinite wires. For practical, finite problems no exact general solution is known. However, if the wave length is much greater than the transverse dimensions of a long uniform wire, the classical transmission line theory (CTLT) can be applied.

To simplify the treatment of the problem, it is assumed that the TEM mode is the dominant mode and that other modes can be neglected. Under this condition Maxwell's equations simplify and are reduced to the so called telegraphers equations [6], [7], [13], [27]. For the scalar potential Φ and the current I along lossless uniform wires holds

$$\frac{\partial}{\partial l}\Phi(l) + \mathrm{j}kZ_\mathrm{C} I(l) = 0 \tag{2.87}$$

$$\frac{\partial}{\partial l} I(l) + \mathrm{j}k \frac{1}{Z_\mathrm{C}} \Phi(l) = 0 \tag{2.88}$$

with the characteristic impedance Z_C from Eq. (2.69).

The solution of the telegraphers equations has a form similar to the TEM mode for the infinite wire. However, on the finite wire two TEM modes that travel in opposite directions coexist. The amplitudes of the two TEM modes depend on the boundary conditions, i.e. the lumped loads and sources at the wire ends.

Field coupling is included in the homogeneous telegraphers equations by inserting source terms in Eqs. (2.87) and (2.88), i.e.

$$\frac{\partial}{\partial l}\Phi(l) + \mathrm{j}kZ_\mathrm{C} I(l) = V'_\mathrm{ex}(l) \tag{2.89}$$

$$\frac{\partial}{\partial l} I(l) + \mathrm{j}k \frac{1}{Z_\mathrm{C}} \Phi(l) = I'_\mathrm{ex}(l) \, . \tag{2.90}$$

There are three well known models that define the two source terms V'_ex and I'_ex, namely the Taylor model [29], the Agrawal model [30], and the Rachidi model [31]. The three models are all equivalent.

The Agrawal model is closely related to the MPIE for thin wires (see Eqs. (2.45) and (2.46)). In this model the source terms are

$$V'_\mathrm{ex}(l) = E_{x_2}(l, h) \tag{2.91}$$

$$I'_\mathrm{ex}(l) = 0 \, , \tag{2.92}$$

where E_{x_2} is the electric field component that is orthogonal to the ground plane. This way the total current and a scattered potential Φ are determined with Eqs. (2.89) and (2.90). The total scalar potential is obtained with

$$\Phi_{\text{tot}}(l) = \Phi(l) - \int_0^h E_{x_2}(l, x_2)\,\mathrm{d}x_2\,. \tag{2.93}$$

The boundary conditions are

$$\Phi(0) = -Z_1 I(0) + \int_0^h E_{x_2}(0, x_2)\,\mathrm{d}x_2 \tag{2.94}$$

$$\Phi(\mathcal{L}) = -Z_2 I(\mathcal{L}) + \int_0^h E_{x_2}(\mathcal{L}, x_2)\,\mathrm{d}x_2\,, \tag{2.95}$$

where Z_1 and Z_2 are the loads at the ports, $\mathcal{L}$ is the wire length and h is the wire height above the ground. Risers at the wire ends are usually neglected in the Agrawal model [30], due to the small transverse dimensions of the wire. Only the horizontal part of the wire and the loads are considered.

The advantage of the CTLT is its simplicity. The telegraphers equations are solvable using standard methods as is shown in Ch. 4. Furthermore, the theory can be used to generate stable networks for frequency and time domain simulations [32], [33].

However, the CTLT simplifies the general Maxwell theory significantly. The method does not include radiation effects at the wire terminals. Furthermore, it is difficult to include the non-uniformity of the wire terminals, e.g. risers, which play a significant role for smaller wavelengths. Hence, it is restricted to large wavelengths compared to the wire height above the ground.

2.5 The method of moments for thin wires

The method of moments (MoM) is a widely used numerical method to solve linear boundary value problems. It is often used to approximate the current on wires induced by external electromagnetic fields in frequency domain. In the following the general idea of the MoM is described. Furthermore, it is applied to the thin wire EFIE.

2.5.1 General aspects

The MoM can be used to discretize linear operators. The solution can then be approximated by solving a linear system of equations. The method is described in full detail in [1], [34].

A general linear problem is described by

$$(\hat{\boldsymbol{\mathcal{T}}} I)(l) = F(l)\,, \tag{2.96}$$

where $\hat{\boldsymbol{\mathcal{T}}}$ is an arbitrary linear operator acting on an unknown function I (in this case the current) and F is the excitation or forcing function. To solve this problem numerically, the

sought function I is described as a weighted sum of N linearly independent basis functions β_n, i.e.

$$I(l) = \sum_{n=1}^{N} i_n \beta_n(l) \tag{2.97}$$

where i_n are unknown coefficients, sometimes called the degrees of freedom. Since the operator is linear, it acts on the basis functions independently. It holds

$$\sum_{n=1}^{N} i_n (\hat{\boldsymbol{\mathcal{T}}} \beta_n)(l) = F(l)\,. \tag{2.98}$$

The latter equation is weighted with N test functions w_m, i.e.

$$\sum_{n=1}^{N} i_n \langle w_m, \hat{\boldsymbol{\mathcal{T}}} \beta_n \rangle = \langle w_m, F \rangle \qquad \text{for } m = 1, 2, ..., N\,, \tag{2.99}$$

where $\langle \cdot, \cdot \rangle$ denotes the inner product depending on the domain of $\hat{\boldsymbol{\mathcal{T}}}$. Equation (2.99) can be rewritten in matrix form as

$$\begin{bmatrix} \langle w_1, \hat{\boldsymbol{\mathcal{T}}} \beta_1 \rangle & \langle w_1, \hat{\boldsymbol{\mathcal{T}}} \beta_2 \rangle & \cdots & \langle w_1, \hat{\boldsymbol{\mathcal{T}}} \beta_N \rangle \\ \langle w_2, \hat{\boldsymbol{\mathcal{T}}} \beta_1 \rangle & \langle w_2, \hat{\boldsymbol{\mathcal{T}}} \beta_2 \rangle & \cdots & \langle w_2, \hat{\boldsymbol{\mathcal{T}}} \beta_N \rangle \\ \vdots & \vdots & \ddots & \vdots \\ \langle w_N, \hat{\boldsymbol{\mathcal{T}}} \beta_1 \rangle & \langle w_N, \hat{\boldsymbol{\mathcal{T}}} \beta_2 \rangle & \cdots & \langle w_N, \hat{\boldsymbol{\mathcal{T}}} \beta_N \rangle \end{bmatrix} \begin{bmatrix} i_1 \\ i_2 \\ \vdots \\ i_N \end{bmatrix} = \begin{bmatrix} \langle w_1, F \rangle \\ \langle w_2, F \rangle \\ \vdots \\ \langle w_N, F \rangle \end{bmatrix}. \tag{2.100}$$

Many numerical methods (finite element method, finite integration technique, ...) result in a system of equations with a form similar to (2.100). Therefore, the MoM can be seen as some kind of generalization of the numerical methods for linear operators. But usually the MoM refers to the numerical solution of integro-differential equations.

The performance of the algorithm, e.g. the accuracy and speed, depends on the choice of test and basis functions. Global basis functions, that span the whole domain of interest, are possible choices. Their specific form depends on the properties of $\hat{\boldsymbol{\mathcal{T}}}$ [35], [36].

However, local basis and test functions, that have a compact support, are more convenient for general numerical applications [22], [35], [36].

2.5.2 Thin wires above a ground plane

In this section the same thin wires are considered as in Sec. 2.2. For thin wires the EFIE, i.e. Eq. (2.47), has to be solved for the current. The MoM shall be applicable for complex frequencies s for later application. This is established by substituting $\mathrm{j}\omega$ with s.

Therefore, the linear operator is

$$(\hat{\boldsymbol{\mathcal{T}}} I)(l) = \frac{\partial}{\partial l} \int_{\mathcal{L}_{\min}}^{\mathcal{L}_{\max}} g_\Phi(l, l') \frac{\partial}{\partial l'} I(l')\,\mathrm{d}l' - \frac{s^2}{c^2} \int_{\mathcal{L}_{\min}}^{\mathcal{L}_{\max}} g_\mathrm{A}(l, l') I(l')\,\mathrm{d}l' \tag{2.101}$$

and the forcing function is

$$F(l) = -\frac{s}{c} \frac{4\pi}{Z_0} E_{\tan}(l)\,. \tag{2.102}$$

The inner product for this problem is defined to be

$$\langle w_m, F\rangle = \int_{\mathcal{L}_{\min}}^{\mathcal{L}_{\max}} w_m(l)F(l)\,\mathrm{d}l\,. \tag{2.103}$$

The wire is divided into straight segments to approximate the wire trajectory as described in [1], [34].

The physical current is continuously differentiable. Hence, the so called Numerical Electromagnetics Code (NEC) basis functions are chosen [34]. They are defined as

$$\beta_n(l) = \begin{cases} A_{\mathrm{L},n} + B_{\mathrm{L},n}\mathfrak{e}_{n-1}^{+}(l) + C_{\mathrm{L},n}\mathfrak{e}_{n-1}^{-}(l) & \text{for } l_{n-1} < l < l_n \\ -1 + B_{\mathrm{M},n}\mathfrak{e}_{n}^{+}(l) + C_{\mathrm{M},n}\mathfrak{e}_{n}^{-}(l) & \text{for } l_n \le l \le l_{n+1} \\ A_{\mathrm{R},n} + B_{\mathrm{R},n}\mathfrak{e}_{n+1}^{+}(l) + C_{\mathrm{R},n}\mathfrak{e}_{n+1}^{-}(l) & \text{for } l_{n+1} < l < l_{n+2} \\ 0 & \text{otherwise} \end{cases} \tag{2.104}$$

with

$$\mathfrak{e}_n^{\pm}(l) = \exp\Big(\pm\frac{s}{c}\,(l - c_n)\Big)\,. \tag{2.105}$$

The bounds of segment n are denoted by l_n and l_{n+1} respectively. The center of segment n is at $l = c_n$. The NEC basis functions span three complete wire segments and are zero elsewhere.

The eight coefficients $A_{\mathrm{L},n}, B_{\mathrm{L},n}, C_{\mathrm{L},n}, B_{\mathrm{M},n}, C_{\mathrm{M},n}, A_{\mathrm{R},n}, B_{\mathrm{R},n}$, and $C_{\mathrm{R},n}$ are determined by enforcing that β_n has a continuous first derivative for all $l = l_n$ or that all β_n fulfill the current boundary conditions at the wire ends, i.e.

$$I(l_{\mathrm{end}}) = 0 \qquad \text{open-circuit boundary condition} \tag{2.106}$$

$$\frac{\partial}{\partial l} I(l_{\mathrm{end}}) = 0 \qquad \text{short-circuit boundary condition} \tag{2.107}$$

Four example basis functions are shown in Fig. 2.7 with an open circuit at $l = l_1$ and a short circuit at $l = l_5$ (connection to ground). With the NEC basis functions the integrals in $(\hat{\boldsymbol{\mathcal{T}}}\beta_n)(l)$ can be solved almost completely analytically leaving only a well behaved integrand that can be evaluated by straight forward numerical integration [34].

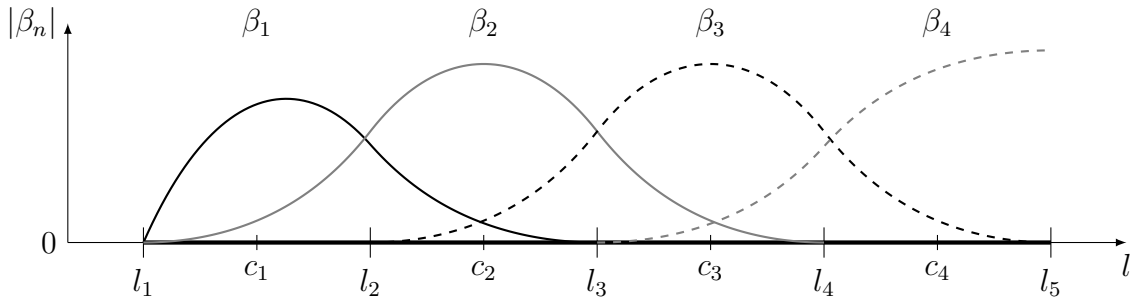

Figure 2.7: Absolute value of NEC basis functions for a wire consisting of four segments with an open circuit on the left side and a short circuit on the right side.

Since all basis functions β_n are continuously differentiable the resulting current approximation is continuously differentiable for all l. Hence, the charge per unit length q' can be determined directly from the current for all l. The continuity equation for the current is

$$\frac{\partial}{\partial l} I(l) = -sq'(l)\,. \tag{2.108}$$

Therefore, it holds

$$q'(l) = -\frac{1}{s}\sum_{n=1}^{N} i_n \frac{\partial}{\partial l}\beta_n(l) \tag{2.109}$$

with

$$\frac{\partial}{\partial l}\beta_n(l) = \frac{s}{c}\begin{cases} B_{\mathrm{L},n}\mathfrak{e}^{+}_{n-1}(l) - C_{\mathrm{L},n}\mathfrak{e}^{-}_{n-1}(l) & \text{for } l_{n-1} < l < l_n \\ B_{\mathrm{M},n}\mathfrak{e}^{+}_{n}(l) - C_{\mathrm{M},n}\mathfrak{e}^{-}_{n}(l) & \text{for } l_n \leq l \leq l_{n+1} \\ B_{\mathrm{R},n}\mathfrak{e}^{+}_{n+1}(l) - C_{\mathrm{R},n}\mathfrak{e}^{-}_{n+1}(l) & \text{for } l_{n+1} < l < l_{n+2} \\ 0 & \text{otherwise.} \end{cases} \tag{2.110}$$

Next the test functions need to be chosen. Point matching is used for thin wires [1], [34]. That means

$$w_m(l) = \delta(l - c_m)\,. \tag{2.111}$$

The main advantage is that the integration from the inner product can be solved analytically. As a drawback the test functions enforce the electric field boundary condition only on the segment center c_m. Nevertheless, accurate results are achieved with point matching.

2.6 The singularity expansion method and natural frequencies

The singularity expansion method (SEM) is introduced in this section. After a general description of the main idea, two possibilities to obtain the important complex natural frequencies are presented.

2.6.1 General aspects

The SEM was developed in the 1970s for the analysis of electromagnetic field interaction with general passive objects [27], [37]–[40]. Figure 2.8 shows the absolute value of an example response of the current I at one point on a thin dipole in free space as a function of a normalized frequency. The length of the dipole is denoted by $\mathcal{L}$. The specific dimensions of the dipole are not important at this moment. Many peaks with different relative widths can be seen. This observation is characteristic for the responses of all passive objects.

The main idea of the SEM is the decomposition of the response of any passive object into a series of infinitely many resonators. In the context of the SEM physical quantities, e.g. the current I, are modeled as

$$I(s) = \sum_{n} \frac{r_n}{s - s_n} + I_{\mathrm{forced}}(s) + I_{\mathrm{analytic}}(s) \tag{2.112}$$

in frequency domain, where s is the complex frequency that arises from the two sided Laplace transform, s_n are the so called natural frequencies, and r_n are the corresponding residues. The current I_{forced} is a current that depends on the excitation and may include singularities as well. The current I_{analytic} is an analytic function, i.e. a function without any singularities that is differentiable for all s, that exists in theory. However, I_{analytic} vanishes for most practical problems [27], [37].

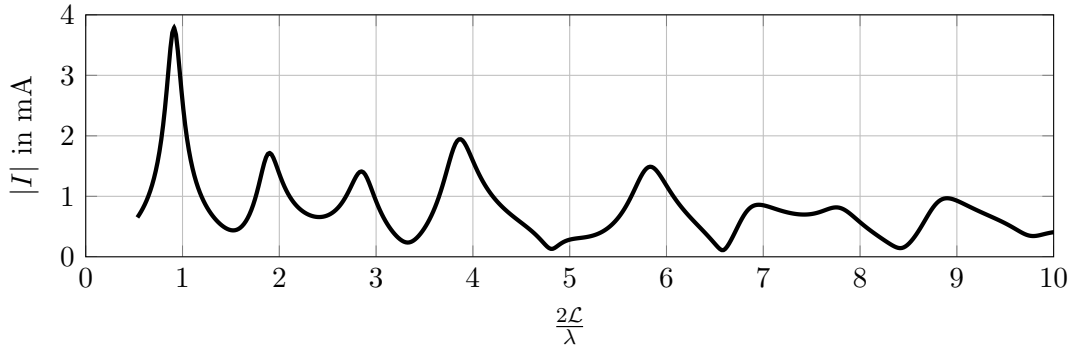

Figure 2.8: Absolute value of the complex current on a thin dipole in free space that is illuminated by a plane wave as a function of a normalized frequency with many visible resonances.

Equation (2.112) fully describes any passive system that is excited by a specific source. There are different approaches to find the unknowns in Eq. (2.112), e.g. fitting algorithms for measurement or numerical data. Analytic expressions can usually be developed into a series that looks similar to Eq. (2.112).

An advantage of the model in Eq.(2.112) is the possibility to easily find the transform in time domain. It holds

$$\hat{I}(t) = \sum_n r_n \exp(s_n t) + \hat{I}_{\text{forced}}(t) + \hat{I}_{\text{analytic}}(t)\,, \tag{2.113}$$

where the hat denotes the transforms in time domain. The significance of the parameters r_n and s_n becomes clearer in Eq. (2.113).

The imaginary part of each natural frequency s_n is the oscillation frequency of each resonator. The real part describes the damping of the corresponding oscillation in time domain. In frequency domain the imaginary part of the natural frequencies is the frequency where a maximum of the amplitude response is located. The real part corresponds to the relative width of each resonant peak. The complex natural frequencies s_n of each resonator are independent of the excitation. Their location in the complex plane just depends on the properties of the object, e.g. its geometry, material properties, lumped elements [27], [37].

The complex residues r_n describe the coupling of the excitation to each natural mode. Hence, they depend on the system and the specific excitation. For practical problems the specific excitation, e.g. direction of the source, number of sources, etc., is not always known. Therefore, the analysis of the r_n is usually omitted. The analysis of the natural frequencies is often sufficient to gain relevant information about the system behavior. It can be used to detect vulnerabilities of the system or to identify unknown objects.

The complex natural frequencies of the current on a conducting sphere with radius R can be determined analytically [37], [41]. Figure 2.9 shows the normalized natural frequencies in the complex s-plane. The natural frequencies can be grouped into different layers as indicated in Fig. 2.9. The first layer is the closest to the imaginary axis. Therefore, these natural frequencies would have the biggest influence on an observed frequency response. The higher order layers are further away from the imaginary axis and contribute less to the physical response. Hence, it is difficult or impossible to detect them from measurement data. This is further illustrated by the example at the end of this section.

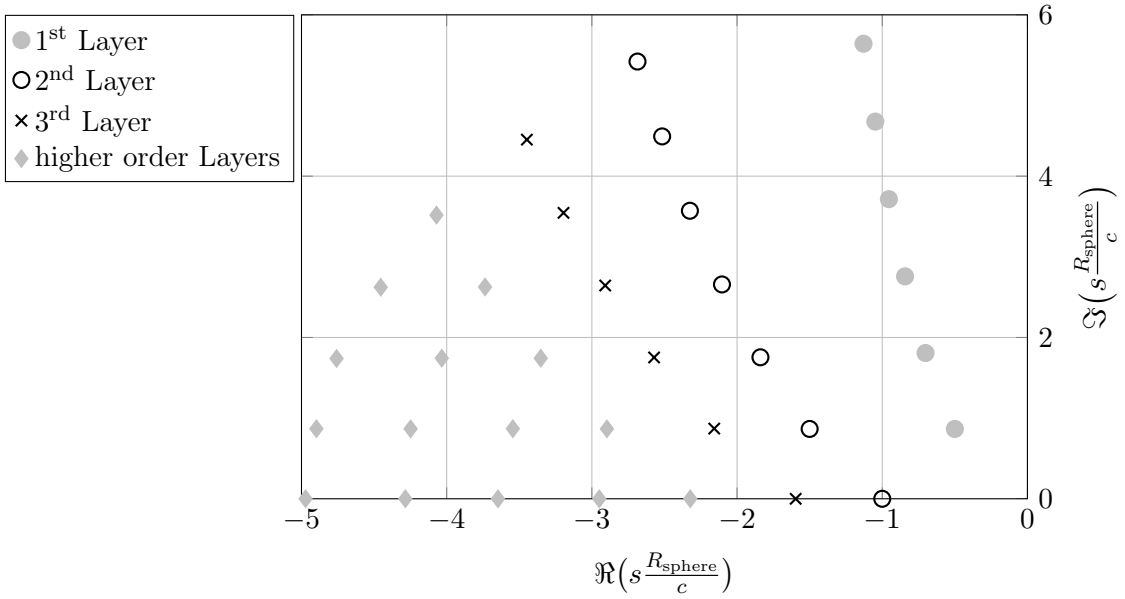

Figure 2.9: Normalized natural frequencies of a perfectly conducting sphere with radius R_{sphere} in free space.

2.6.2 Determining the natural frequencies

It is usually straight forward to determine the natural frequencies from analytic expressions, e.g. for the perfectly conducting sphere [37], [41]. If numerical methods are used or measurement data is available, there are different time domain and frequency domain methods to extract the natural frequencies. In the following, two frequency domain methods that are used later in the thesis are shortly described, i.e.

1. Contour integration for MoM and
2. Vector fitting for frequency domain data.

There are methods that work on time domain data, e.g. the matrix pencil method [42]. However, it is not further used in this thesis and is, therefore, not described in the following.

Contour integration for the method of moments

The contour integration method can be applied if the current can be evaluated for complex frequencies, e.g. using the MoM. To apply the method, the system of equations in Eq. (2.100) is written in a shorter notation as

$$\underline{\underline{\boldsymbol{Z}}}_{\text{MoM}}(s)\underline{\boldsymbol{I}}_{\text{MoM}}(s) = \underline{\boldsymbol{V}}_{\text{MoM}}(s) \tag{2.114}$$

with the matrix

$$\underline{\underline{\boldsymbol{Z}}}_{\text{MoM}}(s) = \begin{bmatrix} \langle w_1, \hat{\boldsymbol{T}}\beta_1\rangle(s) & \langle w_1, \hat{\boldsymbol{T}}\beta_2\rangle(s) & \cdots & \langle w_1, \hat{\boldsymbol{T}}\beta_N\rangle(s) \\ \langle w_2, \hat{\boldsymbol{T}}\beta_1\rangle(s) & \langle w_2, \hat{\boldsymbol{T}}\beta_2\rangle(s) & \cdots & \langle w_2, \hat{\boldsymbol{T}}\beta_N\rangle(s) \\ \vdots & \vdots & \ddots & \vdots \\ \langle w_N, \hat{\boldsymbol{T}}\beta_1\rangle(s) & \langle w_N, \hat{\boldsymbol{T}}\beta_2\rangle(s) & \cdots & \langle w_N, \hat{\boldsymbol{T}}\beta_N\rangle(s) \end{bmatrix} \tag{2.115}$$

and the column vectors

$$\underline{\boldsymbol{I}}_{\mathrm{MoM}}(s) = \begin{bmatrix} i_1(s) & i_2(s) & \dots & i_N(s) \end{bmatrix}^T \tag{2.116}$$

$$\underline{\boldsymbol{V}}_{\mathrm{MoM}}(s) = \begin{bmatrix} \langle w_1, F \rangle(s) & \langle w_1, F \rangle(s) & \cdots & \langle w_1, F \rangle(s) \end{bmatrix}^T . \tag{2.117}$$

Hence, it follows for the coefficient vector

$$\underline{\boldsymbol{I}}_{\mathrm{MoM}}(s) = \underline{\underline{\boldsymbol{Z}}}^{-1}_{\mathrm{MoM}}(s) \underline{\boldsymbol{V}}_{\mathrm{MoM}}(s) . \tag{2.118}$$

If $s = s_n$, there exists a nontrivial current vector $\underline{\boldsymbol{I}}_{\mathrm{MoM}}$ even if there is no excitation [43]. This holds if and only if the determinant of $\underline{\underline{\boldsymbol{Z}}}_{\mathrm{MoM}}$ is zero. Hence, the task of finding the natural frequencies is reduced to finding the zeros of $\det \underline{\underline{\boldsymbol{Z}}}_{\mathrm{MoM}}(s)$, i.e. for all singularities s_n holds

$$\det \underline{\underline{\boldsymbol{Z}}}_{\mathrm{MoM}}(s_n) = 0 . \tag{2.119}$$

The algorithm in [44] uses contour integration in the complex s-plane to find the complex roots of an analytic function. The main idea is to use Cauchy's argument principle [45].

A closed contour in the complex s-plane is chosen. A numerical integration of $\det \underline{\underline{\boldsymbol{Z}}}_{\mathrm{MoM}}$ along the contour is performed. After straight forward data processing an accurate approximation of all zeros inside the contour is obtained. Details can be found in [44].

The advantage of the algorithm is the accuracy. It finds all zeros (i.e. natural frequencies) in the given area in the complex frequency plane (see [46] for comparison). Furthermore, no excitation is need. The algorithm only uses the properties of the passive system that are completely contained in $\underline{\underline{\boldsymbol{Z}}}_{\mathrm{MoM}}$.

However, the algorithm uses a lot of computing time since the determinant of $\underline{\underline{\boldsymbol{Z}}}_{\mathrm{MoM}}$ needs to be evaluated for a lot of different frequency points in the complex plane to obtain accurate integrals.

Vector fitting for frequency domain data

The vector fitting algorithm [47]–[49] can be applied to any kind of data in frequency domain, i.e. measurement data or numerical results. The main idea is to fit for example the current response $I(\mathrm{j}\omega)$ with

$$I_{\mathrm{fit}}(\mathrm{j}\omega) = \sum_{n=1}^{N} \frac{r_{n,\mathrm{fit}}}{\mathrm{j}\omega - s_{n,\mathrm{fit}}} + \mathrm{j}\omega\, r_{N+1,\mathrm{fit}} + r_{N+2,\mathrm{fit}} . \tag{2.120}$$

The unknowns $r_{n,\mathrm{fit}}$ and $s_{n,\mathrm{fit}}$ are determined iteratively with data points from the MoM algorithm. If a satisfying fit is found, the algorithm terminates and N singularities $s_{n,\mathrm{fit}}$ are found.

The advantage of the vector fitting algorithm is its fast computing time compared to the contour integration method. Only $2N + 2$ data point are needed to find N singularities. Furthermore, it can be applied to noisy measurement data [47].

However, the accuracy of the found singularities strongly depends on the number of starting poles N . Moreover, only the first layer of natural frequencies is accurately found with the vector fitting algorithm. This is shown in the following example.

Example and comparison

To illustrate the performance of the two mentioned algorithms the natural frequencies of a thin dipole (with length $\mathcal{L} = 1\,\mathrm{m}$ and radius $a = 5\,\mathrm{mm}$) are approximated. The dipole is excited by a plane wave and the current on one wire segment is determined using the MoM algorithm. The number of segments to discretize the dipole is always 40 to get an accurate numerical result. The number of poles for the vector fitting algorithm are 12 and 16. The fitting curves are shown in Fig. 2.10 alongside the original simulation data. Both fits look similar and are accurate compared to the original data.

Figure 2.11 shows the extracted natural frequencies from both algorithms with different numbers of poles for the vector fitting algorithm. The natural frequencies in the first layer (close to the imaginary axis) are found by both methods. However, the second and third layer are only found by the contour integration algorithm.

Furthermore, it can be seen that the vector fitting solution is sensitive to the number of starting poles N. If N is chosen too large (e.g. $N \geq 16$), more poles are found close to the imaginary axis. The algorithm then finds an incorrect sharp pole with small residue to take numerical noise into account. Hence, the number N needs to be chosen carefully.

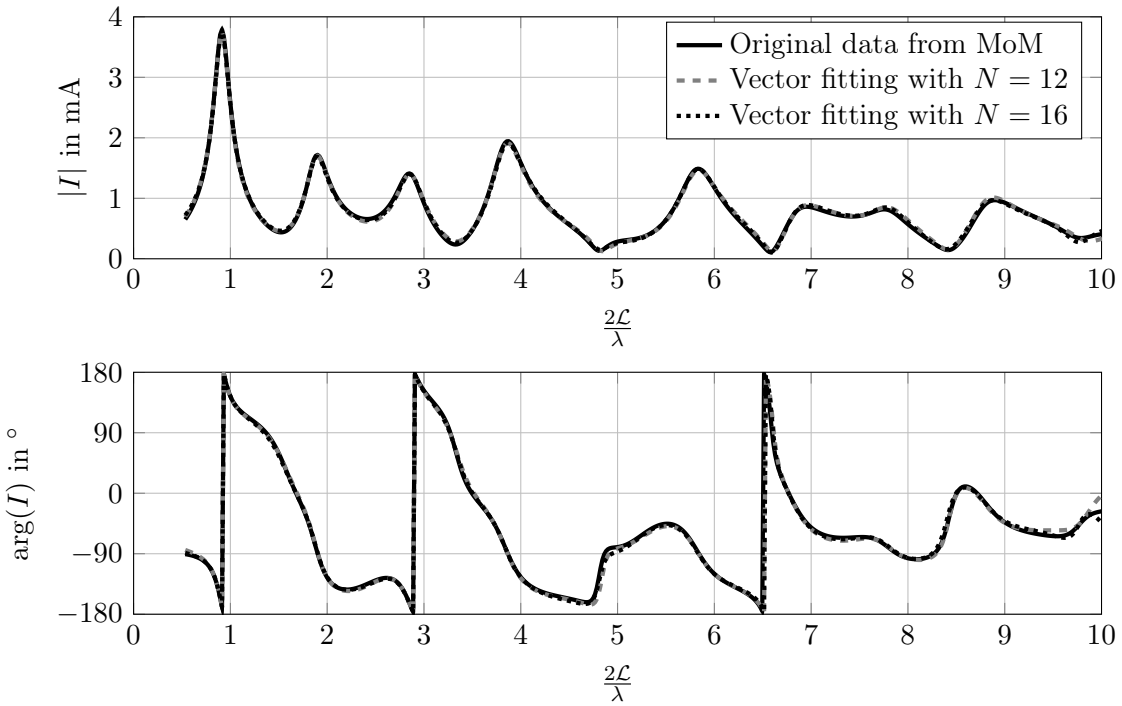

Figure 2.10: Complex current from a simulation compared to the fits from the vector fitting algorithm with a different number of starting poles N.

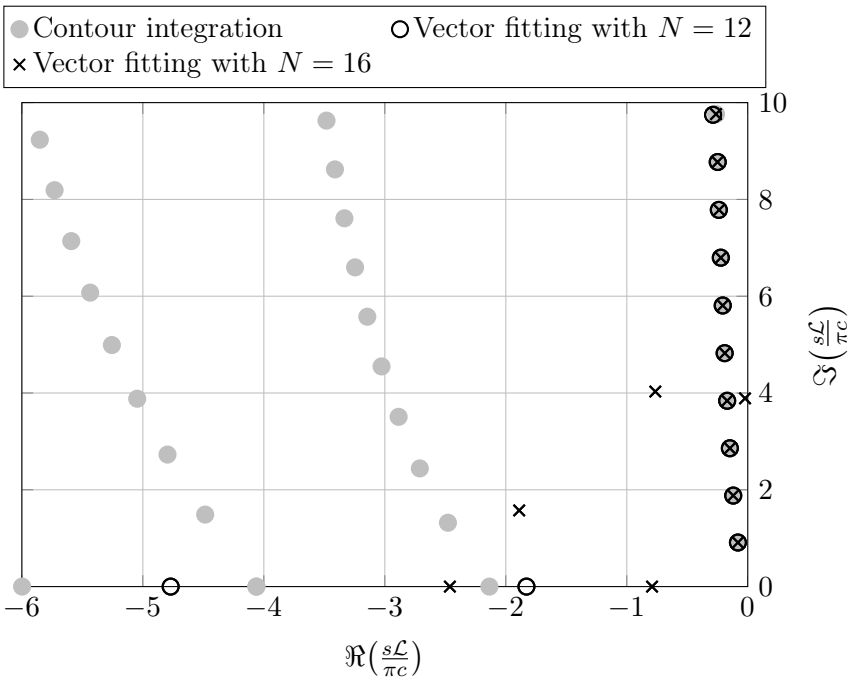

Figure 2.11: Natural frequencies of a thin dipole in free space extracted from numerical data with different methods.

Chapter 3

Asymptotic approach for the current on a finite wire above a ground

In this chapter the asymptotic approach is described. The asymptotic approach yields a general, analytic description of the current along a uniform part of a thin wire above a ground plane. Besides analyzing the plane wave coupling to a finite wire, it can be used to find a fixed point equation for the natural frequencies of the current on the wire. The asymptotic approach is introduced in [12], [13]. However, a different derivation is presented in the following.

Starting from the infinite wire with lumped loads and lumped sources above a ground plane an equation for the current on a long finite wire above a ground with arbitrary ports is derived. The solution is restricted to the uniform part of the wire. It depends on the reflection and scattering coefficients. Furthermore, it is shown how the coefficients can be extracted from numerical data. A fixed point equation for the natural frequencies is derived. Extensions of the asymptotic approach to piecewise uniform wires and multiconductor transmission lines are described as well.

3.1 Infinite wire with a lumped impedance and a plane wave excitation – the scattering coefficient

Let there be an infinite wire with a lumped impedance Z and a plane wave excitation as shown in Fig. 3.1. The lumped impedance is located at $l = l_Z$ and the parameterization (2.48) is used. The current on the wire generates a voltage across the impedance. This additional voltage has to be taken into account for the electric field boundary condition. The tangential field along the infinite wire (see also Eq. (2.81)) becomes

$$E_{\tan}(l) = 2\mathrm{j}E_0 \sin(\theta) \sin(kh \sin(\theta)) \, \mathrm{e}^{-\mathrm{j}k_\theta l} - V_Z(I) \, \delta(l - l_Z) \tag{3.1}$$

with

$$V_Z(I) = ZI(l_Z) \,, \tag{3.2}$$

where k_θ is defined in Eq. (2.82). The additional voltage V_Z across the impedance is subtracted since it arises due to the current. It is no external voltage source and, hence, has a different sign than the lumped source in Sec. 2.3.

The resulting current along the infinite wire is the superposition of the current imposed by the plane wave and the current scattered from the lumped impedance. With the results

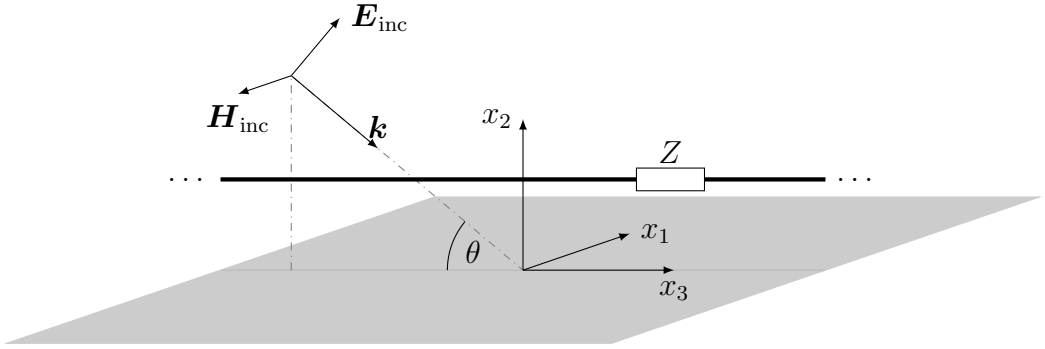

Figure 3.1: Infinite wire above an infinite perfect electric ground with a lumped impedance.

from Sec. 2.3 it holds

$$I(l) = I_\infty \mathrm{e}^{-\mathrm{j}k_\theta l} - V_Z(I) Y_\infty(l - l_Z) \tag{3.3}$$

$$= I_\infty \mathrm{e}^{-\mathrm{j}k_\theta l} - Z I(l_Z) Y_\infty(l - l_Z)\,. \tag{3.4}$$

The current I_∞ is the amplitude of the current that is enforced by the plane wave on the infinite wire (see Eq. (2.85)), i.e.

$$I_\infty = \frac{4\pi}{Z_0 \tilde{g}_0(k_\theta)} \frac{2E_0 \sin(kh\sin(\theta))}{k\sin(\theta)}\,. \tag{3.5}$$

The admittance function $Y_\infty(l)$ combines the admittance functions of all modes that arise at the lumped impedance on the uniform, infinite wire (see Eqs. (2.74), (2.75), (2.76)), i.e.

$$Y_\infty(l) = Y_{\text{TEM}}(l) + Y_{\text{Leaky}}(l) + Y_{\text{Rad}}(l)\,. \tag{3.6}$$

Setting $l = l_Z$ in (3.4) results in

$$I(l_Z) = I_\infty \mathrm{e}^{-\mathrm{j}k_\theta l_Z} \frac{1}{1 + ZY_\infty(0)} \tag{3.7}$$

and

$$I(l) = I_\infty \mathrm{e}^{-\mathrm{j}k_\theta l} - I_\infty \mathrm{e}^{-\mathrm{j}k_\theta l_Z} \frac{Z}{1 + ZY_\infty(0)} Y_\infty(l - l_Z)\,. \tag{3.8}$$

The admittance $Y_\infty(0)$ is the total input admittance of the infinite wire that is seen by a lumped voltage source. The latter equation is the exact current for the infinite wire above a ground with a lumped impedance and a plane wave excitation. The solution consists of the forced response from the plane wave and the lumped voltage source solution. At the location of the lumped impedance all modes are excited by the plane wave current $I_\infty \mathrm{e}^{-\mathrm{j}k_\theta l_Z}$ and travel away from the lumped element. The amplitude of the voltage V_Z depends on the impedance Z and I_∞.

In a far distance from the impedance, i.e. if $|l - l_Z|$ becomes large, only a scattered TEM mode and the forced response I_∞ are dominant. It holds asymptotically

$$I(l) \sim I_\infty \mathrm{e}^{-\mathrm{j}k_\theta l} - I_\infty \mathrm{e}^{-\mathrm{j}k_\theta l_Z} \frac{Z}{1 + ZY_\infty(0)} Y_{\text{TEM}}(l - l_Z) \tag{3.9}$$

$$= I_\infty \mathrm{e}^{-\mathrm{j}k_\theta l} - I_\infty \mathrm{e}^{-\mathrm{j}k_\theta l_Z} \frac{Z}{2Z_{\text{C}}(1 + ZY_\infty(0))} \mathrm{e}^{-\mathrm{j}k|l - l_Z|}\,, \tag{3.10}$$

where Y_{TEM} is given in Eq. (2.74). The amplitude of the scattered TEM mode is the product of the forced current I_∞ and a constant factor that depends on the impedance Z. The constant factor is the so called scattering coefficient Υ. With

$$\Upsilon = -\frac{Z}{2Z_{\mathrm{C}}(1 + ZY_\infty(0))} \tag{3.11}$$

it follows

$$I(l) \sim I_\infty \mathrm{e}^{-\mathrm{j}k_\theta l} + I_\infty \mathrm{e}^{-\mathrm{j}k_\theta l_Z} \Upsilon \, \mathrm{e}^{-\mathrm{j}k|l-l_Z|} \,. \tag{3.12}$$

Comparing this asymptotic approximation to Eq. (3.3) results in

$$-V_Z(I)Y_\infty(l - l_Z) \sim I_\infty \mathrm{e}^{-\mathrm{j}k_\theta l_Z} \Upsilon \, \mathrm{e}^{-\mathrm{j}k|l-l_Z|} \,. \tag{3.13}$$

3.2 Infinite wire with a lumped impedance and a lumped voltage source – the reflection coefficient

Now, let there be an infinite wire with a lumped impedance as before but with a lumped voltage source instead of a plane wave excitation. The lumped impedance Z is again located at $l = l_Z$ and the lumped voltage source V_0 is located at $l = l_V$.

The tangential electric filed is then

$$E_{\tan} = V_0 \, \delta(l - l_V) - V_Z(I) \, \delta(l - l_Z) \,. \tag{3.14}$$

with the voltage V_Z as in Eq. (3.2). The resulting total current is then

$$I(l) = V_0 Y_\infty(l - l_V) - ZI(l_Z)Y_\infty(l - l_Z) \,. \tag{3.15}$$

Setting $l = l_Z$ in Eq. (3.15) results in

$$I(l_Z) = V_0 Y_\infty(l_Z - l_V) \frac{1}{1 + ZY_\infty(0)} \tag{3.16}$$

and

$$I(l) = V_0 Y_\infty(l - l_V) - V_0 Y_\infty(l_Z - l_V) \frac{Z}{1 + ZY_\infty(0)} Y_\infty(l - l_Z) \,. \tag{3.17}$$

If the voltage source and the lumped impedance are far apart, i.e. $|l_Z - l_V|$ is large, it holds

$$I(l) \sim V_0 Y_\infty(l - l_V) - \frac{V_0}{2Z_{\mathrm{C}}} \, \mathrm{e}^{-\mathrm{j}k|l_Z - l_V|} \frac{Z}{1 + ZY_\infty(0)} Y_\infty(l - l_Z) \,. \tag{3.18}$$

If, furthermore, the observation point l is at a large distance to the two lumped elements, it holds asymptotically

$$I(l) \sim V_0 Y_{\mathrm{TEM}}(l - l_V) - \frac{V_0}{2Z_{\mathrm{C}}} \, \mathrm{e}^{-\mathrm{j}k|l_Z - l_V|} \frac{Z}{1 + ZY_\infty(0)} Y_{\mathrm{TEM}}(l - l_Z) \tag{3.19}$$

$$= \frac{V_0}{2Z_{\mathrm{C}}} \, \mathrm{e}^{-\mathrm{j}k|l - l_V|} - \frac{V_0}{2Z_{\mathrm{C}}} \, \mathrm{e}^{-\mathrm{j}k|l_Z - l_V|} \frac{Z}{2Z_{\mathrm{C}}(1 + ZY_\infty(0))} \, \mathrm{e}^{-\mathrm{j}k|l - l_Z|} \,. \tag{3.20}$$

The latter equation describes a TEM mode that travels from the lumped source towards the lumped impedance and one that is reflected at the load. Hence, a TEM reflection coefficient Γ is defined as

$$\Gamma = -\frac{Z}{2Z_{\mathrm{C}}(1 + ZY_{\infty}(0))}\,. \tag{3.21}$$

The asymptotic approximation for the current is then

$$I(l) \sim \frac{V_0}{2Z_{\mathrm{C}}}\,\mathrm{e}^{-\mathrm{j}k|l-l_V|} + \frac{V_0}{2Z_{\mathrm{C}}}\,\mathrm{e}^{-\mathrm{j}k|l_Z-l_V|}\Gamma\,\mathrm{e}^{-\mathrm{j}k|l-l_Z|}\,. \tag{3.22}$$

The amplitude of the reflected TEM mode depends on the reflection coefficient Γ and the amplitude of the incoming current wave $\frac{V_0}{2Z_{\mathrm{C}}}$. Strictly speaking another TEM mode with the same amplitude as the reflected TEM mode is transmitted by the lumped impedance and travels away from the source and the impedance. In this case a transmission coefficient T could be introduced. However, this differentiation by cases is omitted here for simplicity.

The TEM scattering and reflection coefficient for the lumped impedance on the infinite wire have the same value. The difference is the way the scattered wave is excited compared to the reflected one. This concept is soon generalized and the difference between the two parameters will be more obvious for the next case.

3.3 Infinite wire with two lumped impedances and a plane wave excitation

Next, an infinite wire with two lumped impedances above a ground is excited by a plane wave (see Fig. 3.2). The impedances Z_1 and Z_2 are located at $l = l_1$ and $l = l_2$ respectively. An asymptotic approximation for the current in-between the impedances is sought. It is assumed that the impedances are far apart and that the observation point is not near the impedances. Then only the forced response from the plane wave and two TEM modes are dominant at the observation point. The two TEM modes travel in opposite directions and include all re-reflections.

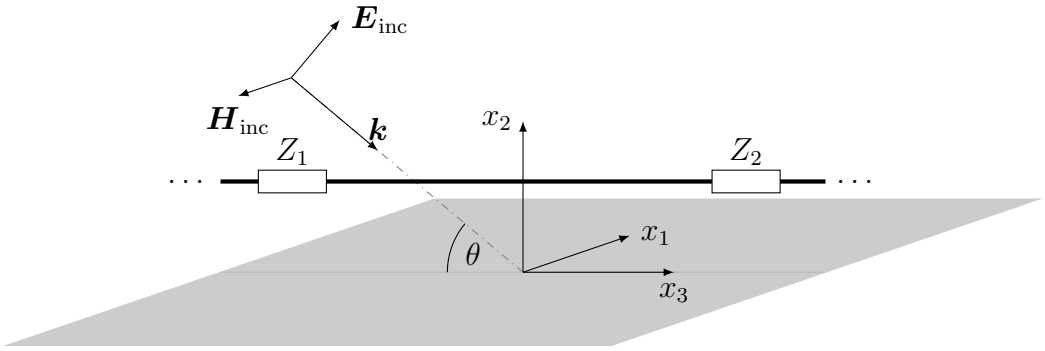

Figure 3.2: Infinite wire above an infinite perfect electric ground with two lumped impedances.

The plane wave excites a current with amplitude I_{∞} as for the undisturbed infinite wire. This current is scattered at the impedances as described above for the single impedance case. The scattered TEM modes reach the opposite impedance and are then reflected.

The reflected TEM modes travel back and forth due to infinitely many re-reflections at the loads.

The total current in the asymptotic region between the loads is

$$I(l) \sim I_\infty \mathrm{e}^{-\mathrm{j}k_\theta l} + I_{Z_1}(l) + I_{Z_2}(l)\,, \tag{3.23}$$

where I_{Z_1} and I_{Z_1} are the currents that arise due to the scattering at the impedance Z_1 or Z_2 respectively. It holds

$$\begin{aligned} I_{Z_1}(l) = \underbrace{I_\infty \mathrm{e}^{-\mathrm{j}k_\theta l_1} \Upsilon_1 \, \mathrm{e}^{-\mathrm{j}k|l-l_1|}}_{\text{scattered TEM mode at } Z_1} + \underbrace{I_\infty \mathrm{e}^{-\mathrm{j}k_\theta l_1} \Upsilon_1 \, \mathrm{e}^{-\mathrm{j}k|l_2-l_1|} \Gamma_2 \, \mathrm{e}^{-\mathrm{j}k|l-l_2|}}_{\text{reflection at } Z_2} \\ + \underbrace{I_\infty \mathrm{e}^{-\mathrm{j}k_\theta l_1} \Upsilon_1 \, \mathrm{e}^{-2\mathrm{j}k|l_2-l_1|} \Gamma_2 \Gamma_1 \, \mathrm{e}^{-\mathrm{j}k|l-l_1|}}_{\text{re-reflection at } Z_1} \\ + \underbrace{I_\infty \mathrm{e}^{-\mathrm{j}k_\theta l_1} \Upsilon_1 \, \mathrm{e}^{-3\mathrm{j}k|l_2-l_1|} \Gamma_2^2 \Gamma_1 \, \mathrm{e}^{-\mathrm{j}k|l-l_2|}}_{\text{re-reflection at } Z_2} + \dots \end{aligned} \tag{3.24}$$

There are infinitely many re-reflections of the TEM modes. Compiling similar terms results in

$$I_{Z_1}(l) = I_\infty \mathrm{e}^{-\mathrm{j}k_\theta l_1} \Upsilon_1 \Big(\mathrm{e}^{-\mathrm{j}k|l-l_1|} + \Gamma_2 \, \mathrm{e}^{-\mathrm{j}k|l_1-l_2|} \mathrm{e}^{-\mathrm{j}k|l-l_2|} \Big) \sum_{n=0}^{\infty} \Big(\Gamma_1 \Gamma_2 \, \mathrm{e}^{-2\mathrm{j}k|l_1-l_2|} \Big)^n . \tag{3.25}$$

Due to the passivity of the loads, no reflection coefficient is larger than 1. The geometric sum converges if and only if the absolute value of at least one reflection coefficient is smaller than one, i.e. if and only if $|\Gamma_1 \Gamma_2| < 1$. Then it holds

$$I_{Z_1}(l) = I_\infty \mathrm{e}^{-\mathrm{j}k_\theta l_1} \Upsilon_1 \Big(\mathrm{e}^{-\mathrm{j}k|l-l_1|} + \Gamma_2 \, \mathrm{e}^{-\mathrm{j}k|l_1-l_2|} \, \mathrm{e}^{-\mathrm{j}k|l-l_2|} \Big) \frac{1}{1 - \Gamma_1 \Gamma_2 \, \mathrm{e}^{-2\mathrm{j}k|l_1-l_2|}} . \tag{3.26}$$

Similarly, for the current that arises due to the scattering at the second load Z_2 holds

$$I_{Z_2}(l) = I_\infty \mathrm{e}^{-\mathrm{j}k_\theta l_2} \Upsilon_2 \Big(\mathrm{e}^{-\mathrm{j}k|l-l_2|} + \Gamma_1 \, \mathrm{e}^{-\mathrm{j}k|l_1-l_2|} \, \mathrm{e}^{-\mathrm{j}k|l-l_1|} \Big) \frac{1}{1 - \Gamma_1 \Gamma_2 \, \mathrm{e}^{-2\mathrm{j}k|l_1-l_2|}} . \tag{3.27}$$

Inserting Eqs. (3.26) and (3.27) into Eq. (3.23) and rearranging the terms finally results in

$$\begin{aligned} I(l) = I_\infty \mathrm{e}^{-\mathrm{j}k_\theta l} + I_\infty \frac{\Upsilon_1 \, \mathrm{e}^{-\mathrm{j}k_\theta l_1} + \Upsilon_2 \, \mathrm{e}^{-\mathrm{j}k_\theta l_2} \Gamma_1 \, \mathrm{e}^{-\mathrm{j}k\mathcal{L}}}{1 - \Gamma_1 \Gamma_2 \, \mathrm{e}^{-2\mathrm{j}k\mathcal{L}}} \, \mathrm{e}^{-\mathrm{j}k|l-l_1|} \\ + I_\infty \frac{\Upsilon_2 \, \mathrm{e}^{-\mathrm{j}k_\theta l_2} + \Upsilon_1 \, \mathrm{e}^{-\mathrm{j}k_\theta l_1} \Gamma_2 \, \mathrm{e}^{-\mathrm{j}k\mathcal{L}}}{1 - \Gamma_1 \Gamma_2 \, \mathrm{e}^{-2\mathrm{j}k\mathcal{L}}} \, \mathrm{e}^{-\mathrm{j}k|l-l_2|} \end{aligned} \tag{3.28}$$

with the distance $\mathcal{L}$ between the two lumped loads, i.e.

$$\mathcal{L} = |l_1 - l_2| \,. \tag{3.29}$$

Equation (3.28) is the asymptotic approximation for the current between the two lumped impedances. It is composed of the forced response and two TEM modes that travel in opposite directions. The amplitudes of the TEM modes depend on the forced current I_∞ and the scattering and reflection coefficients at both loads. The asymptotic

approximation is valid if leaky and radiation modes can be neglected compared to the TEM mode at the location l. As shown in Eq. (2.72) this is the case when

$$\frac{kh^2}{\ln\left(\frac{2h}{a}\right)} \ll |l - l_1| \tag{3.30}$$

and

$$\frac{kh^2}{\ln\left(\frac{2h}{a}\right)} \ll |l - l_2| \,. \tag{3.31}$$

Next, the reflection and scattering coefficients are generalized for long *finite* wires to find an asymptotic description for the current.

3.4 Finite wire with arbitrary ports and a plane wave excitation

Let there be a thin wire above a ground with arbitrary ports, i.e. with an arbitrary wire trajectory and arbitrary lumped impedances, at both ends. The wire is excited by a plane wave as depicted in Fig. 3.3. The goal is to find an analytic expression for the current on the straight part in the middle of the wire. This is possible if the wire is long compared to the wire height. Similar results as shown here are published in [12], [13], [50], [51]. But a different approach is used.

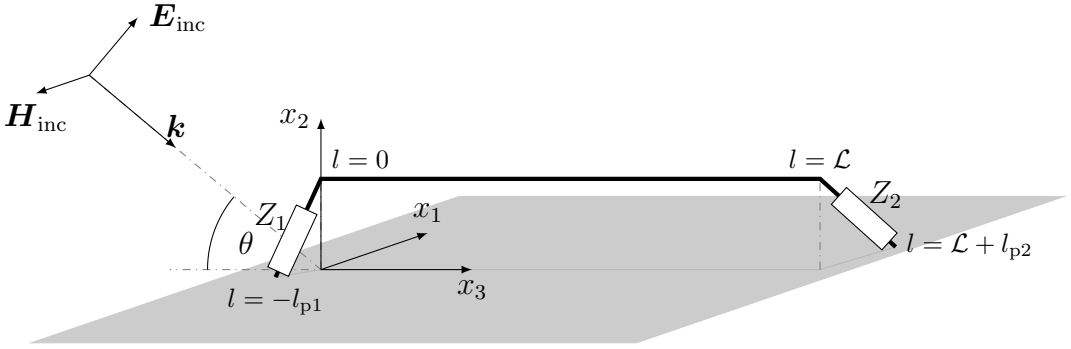

Figure 3.3: Finite wire above a ground with an arbitrary wire trajectory at the ports and a uniform middle section.

The wire parameterization is

$$\boldsymbol{x}_{\text{c}}(l) = \begin{cases} \boldsymbol{x}_{\text{c1}}(l) & \text{for } -l_{\text{p1}} \leq l < 0 \\ h\,\hat{\boldsymbol{x}}_2 + l\,\hat{\boldsymbol{x}}_3 & \text{for } 0 \leq l \leq \mathcal{L} \\ \boldsymbol{x}_{\text{c2}}(l) & \text{for } \mathcal{L} < l \leq \mathcal{L} + l_{\text{p2}} \,. \end{cases} \tag{3.32}$$

The length of the straight horizontal wire part is denoted with $\mathcal{L}$. The arbitrary trajectory and the port length of port n are denoted with $\boldsymbol{x}_{cn}$ and $l_{\text{p}n}$ respectively. The ports are terminated by an impedance Z_1 or Z_2 respectively.

The wire is uniform in the middle section. The trajectory of the wire ports, i.e. for $l < 0$ and $l > \mathcal{L}$, is in general nonuniform. To fulfill the electric field boundary conditions on the wire surface different kinds of modes apart from the TEM modes, e.g. transerve

electric and magnetic modes, are excited at the ports. As for the infinite wire with lumped elements it can be assumed that only the TEM modes are dominant in a far distance from the ports. The other modes radiate away from the wire and are damped along the wire.

This is the same idea as for the infinite wire with two lumped loads. Therefore, for the current in the asymptotic region the ansatz

$$I(l) = I_\infty \mathrm{e}^{-\mathrm{j}k_\theta l} + I_\infty \frac{\Upsilon_1 + \Upsilon_2 \,\mathrm{e}^{-\mathrm{j}k_\theta \mathcal{L}} \Gamma_1 \,\mathrm{e}^{-\mathrm{j}k\mathcal{L}}}{1 - \Gamma_1 \Gamma_2 \,\mathrm{e}^{-2\mathrm{j}k\mathcal{L}}} \,\mathrm{e}^{-\mathrm{j}kl} + I_\infty \frac{\Upsilon_2 \,\mathrm{e}^{-\mathrm{j}k_\theta \mathcal{L}} + \Upsilon_1 \Gamma_2 \,\mathrm{e}^{-\mathrm{j}k\mathcal{L}}}{1 - \Gamma_1 \Gamma_2 \,\mathrm{e}^{-2\mathrm{j}k\mathcal{L}}} \,\mathrm{e}^{-\mathrm{j}k\mathcal{L}} \,\mathrm{e}^{\mathrm{j}kl} \quad (3.33)$$

is made (see Eq. (3.28)). However, the reflection and scattering coefficients are different as for the infinite wire. The coefficients depend on the wire trajectories at the ports $\boldsymbol{x}_{cn}$ and the loads Z_n. They can include the influence of all modes at the port depending on the chosen method to determine the coefficients. Hence, the task of finding an accurate approximation of the current in the asymptotic region on a long wire is reduced to finding the scattering and reflection coefficients for each isolated port.

After finding a general expression for the current on the finite wire in the asymptotic region, it can be used to find the natural frequencies of the wire as well. The natural frequencies s_n can be determined by finding the roots of the denominator in Eq. (3.33), i.e.

$$1 - \Gamma_1(s_n)\Gamma_2(s_n) \,\mathrm{e}^{-2s_n\mathcal{L}/c} = 0\,. \quad (3.34)$$

For the latter equation the physical frequency ω is expanded to the complex frequency s by the substitution $\mathrm{j}\omega \to s$. In general the reflection coefficients are frequency dependent. Therefore, the reflection coefficients of the ports determine the location of the natural frequencies s_n in the complex plane.

Equation (3.34) can be rearranged to yield

$$2\frac{s_n}{c}\mathcal{L} - 2\pi\mathrm{j}n = \ln\big(\Gamma_1(s_n)\Gamma_2(s_n)\big)\,. \quad (3.35)$$

The reflection coefficients are in general complex, i.e. they have an amplitude and a phase denoted with $\arg(\Gamma)$. Applying the logarithm on the complex reflection coefficient results in the fixed point equation

$$s_n = \frac{\ln\big(\big|\Gamma_1(s_n)\Gamma_2(s_n)\big|\big)}{2\mathcal{L}}c + \mathrm{j}\,\frac{\arg\big(\Gamma_1(s_n)\Gamma_2(s_n)\big)}{2\mathcal{L}}c + \mathrm{j}\,\frac{\pi n c}{\mathcal{L}}\,. \quad (3.36)$$

The fixed point equation is solved in detail in Ch. 5.

3.5 Numerical evaluation of the scattering and reflection coefficients

There are different methods to determine the scattering and reflection coefficients. In the following, one possible way to extract the coefficients from numerical simulation data is described.

The coefficients are independent of the wire length $\mathcal{L}$. Hence, a much shorter wire can be used to find the coefficients as long as there is an asymptotic region.

The current in the asymptotic region is given by Eq. (3.33). It has the form

$$I(l) = I_\infty \mathrm{e}^{-\mathrm{j}k_\theta l} + I_1\,\mathrm{e}^{-\mathrm{j}kl} + I_2\,\mathrm{e}^{-\mathrm{j}k\mathcal{L}}\,\mathrm{e}^{\mathrm{j}kl} \tag{3.37}$$

with

$$I_1 = I_\infty \frac{\Upsilon_1 + \Upsilon_2\,\mathrm{e}^{-\mathrm{j}k_\theta\mathcal{L}}\Gamma_1\,\mathrm{e}^{-\mathrm{j}k\mathcal{L}}}{1 - \Gamma_1\Gamma_2\,\mathrm{e}^{-2\mathrm{j}k\mathcal{L}}} \tag{3.38}$$

$$I_2 = I_\infty \frac{\Upsilon_2\,\mathrm{e}^{-\mathrm{j}k_\theta\mathcal{L}} + \Upsilon_1\Gamma_2\,\mathrm{e}^{-\mathrm{j}k\mathcal{L}}}{1 - \Gamma_1\Gamma_2\,\mathrm{e}^{-2\mathrm{j}k\mathcal{L}}}\,. \tag{3.39}$$

The scattering coefficients can be expressed as a function of I_1 and I_2 by rearranging Eqs. (3.38) and (3.39), i.e.

$$\Upsilon_1 = \frac{I_1 - I_2\Gamma_1\,\mathrm{e}^{-\mathrm{j}k\mathcal{L}}}{I_\infty} \tag{3.40}$$

$$\Upsilon_2 = \frac{I_2 - I_1\Gamma_2\,\mathrm{e}^{-\mathrm{j}k\mathcal{L}}}{I_\infty}\,\mathrm{e}^{\mathrm{j}k_\theta\mathcal{L}}\,. \tag{3.41}$$

Therefore, if the amplitudes I_1 and I_2 and the reflection coefficients are known, the scattering coefficients can be determined.

Next, the amplitudes are extracted from numerical data. Usually, the charge per unit length q' (ref. Eq. (2.108)) is determined by standard MoM algorithms as well. It holds with Eq. (3.23)

$$cq'(l) = I_\infty \frac{k_\theta}{k}\,\mathrm{e}^{-\mathrm{j}k_\theta l} + I_1\,\mathrm{e}^{-\mathrm{j}kl} - I_2\,\mathrm{e}^{-\mathrm{j}k\mathcal{L}}\,\mathrm{e}^{\mathrm{j}kl}\,. \tag{3.42}$$

Combining Eqs. (3.37) and (3.42) and solving for I_1 and I_2 results in

$$I_1 = \frac{1}{2}\left(I(l) + cq'(l) - I_\infty\left(1 + \frac{k_\theta}{k}\right)\mathrm{e}^{-\mathrm{j}k_\theta l}\right)\mathrm{e}^{\mathrm{j}kl} \tag{3.43}$$

$$I_2 = \frac{1}{2}\left(I(l) - cq'(l) - I_\infty\left(1 - \frac{k_\theta}{k}\right)\mathrm{e}^{-\mathrm{j}k_\theta l}\right)\mathrm{e}^{\mathrm{j}k\mathcal{L}}\,\mathrm{e}^{-\mathrm{j}kl}\,. \tag{3.44}$$

Finally, the reflection coefficients are sought. A different excitation is needed to extract the reflection coefficients of each port separately. To determine Γ_1, i.e. the reflection coefficient of the left port in Fig. 3.3, the wire in Fig. 3.4 is used. The second port is left open and a lumped voltage source is placed at the open end.

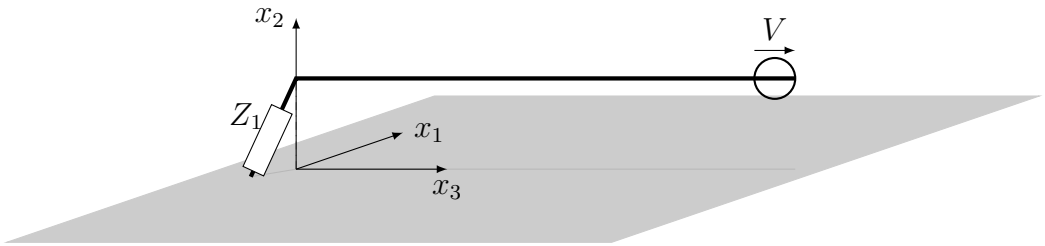

Figure 3.4: Finite wire above ground for the simulation to extract the reflection coefficient of the left port.

Since no plane wave excitation is present the current in the asymptotic region has to be adapted. There is no forced response I_∞. The lumped voltage source excites a TEM

mode that travels to the left port and is reflected. Infinitely many re-reflections occur. To get an expression for the current in the asymptotic region, the scattering coefficients in Eq. (3.33) are adapted. It holds

$$I_\infty \Upsilon_{V1} = 0 \tag{3.45}$$

$$I_\infty \mathrm{e}^{-\mathrm{j}k_\theta \mathcal{L}} \Upsilon_{V2} = I_{V2}\,, \tag{3.46}$$

where I_{V2} is an unknown current that is excited by the lumped voltage source. Hence, the current in the asymptotic region excited by the lumped voltage source is

$$I_V(l) = \frac{I_{V2}\Gamma_1\,\mathrm{e}^{-\mathrm{j}k\mathcal{L}}}{1-\Gamma_1\Gamma_{V2}\,\mathrm{e}^{-2\mathrm{j}k\mathcal{L}}}\,\mathrm{e}^{-\mathrm{j}kl} + \frac{I_{V2}}{1-\Gamma_1\Gamma_{V2}\,\mathrm{e}^{-2\mathrm{j}k\mathcal{L}}}\,\mathrm{e}^{-\mathrm{j}k\mathcal{L}}\,\mathrm{e}^{\mathrm{j}kl}\,. \tag{3.47}$$

The reflection coefficient of the right port is denoted with Γ_{V2} and differs in general from Γ_2. For the charge per unit length holds

$$cq'_V(l) = \frac{I_{V2}\Gamma_1\,\mathrm{e}^{-\mathrm{j}k\mathcal{L}}}{1-\Gamma_1\Gamma_{V2}\,\mathrm{e}^{-2\mathrm{j}k\mathcal{L}}}\,\mathrm{e}^{-\mathrm{j}kl} - \frac{I_{V2}}{1-\Gamma_1\Gamma_{V2}\,\mathrm{e}^{-2\mathrm{j}k\mathcal{L}}}\,\mathrm{e}^{-\mathrm{j}k\mathcal{L}}\,\mathrm{e}^{\mathrm{j}kl}\,. \tag{3.48}$$

Solving Eqs. (3.47) and (3.48) for Γ_1 yields

$$\Gamma_1 = \frac{I_V(l) + cq'_V(l)}{I_V(l) - cq'_V(l)}\,\mathrm{e}^{2\mathrm{j}kl}\,. \tag{3.49}$$

Similarly, Γ_2 can be obtained from simulation.

To conclude, the steps to obtain the scattering and reflection coefficients from numerical simulation data are:

1. Simulation of isolated ports (see Fig. 3.4 for port 1) with lumped voltage source to find Γ_1 (with Eq. (3.49)) and Γ_2 respectively.

2. Simulation of the original wire with plane wave excitation to find $\hat{I}_1$ and $\hat{I}_2$ with Eqs. (3.43) and (3.44) and Υ_1 and Υ_2 with Eqs. (3.40) and (3.41).

The procedure makes clear that the reflection coefficients are in general independent of the plane wave excitation. The plane wave is excluded in the simulation for Γ. However, the scattering coefficients depend on the plane wave excitation, i.e. the angle of incidence.

In [13] an alternative method is shown. There the finite wire is simulated with two different lengths $\mathcal{L}$ and the plane wave excitation. The results are comparable.

Example

The current on an example wire is approximated using the asymptotic approach to illustrate its accuracy. The example wire is shown in Fig. 3.5. It consists of a horizontal part and a riser with a connection to the ground at port 1. The wire is left open at port 2. The wire parameterization is

$$\boldsymbol{x}_\mathrm{c}(l) = \begin{cases} (h+l)\,\hat{\boldsymbol{x}}_2 & \text{for } -h \le l < 0 \\ h\,\hat{\boldsymbol{x}}_2 + l\,\hat{\boldsymbol{x}}_3 & \text{for } 0 \le l \le \mathcal{L}\,. \end{cases} \tag{3.50}$$

with the dimensions

Wire radius	a	0.5 mm
Height above ground	h	10 mm
Horizontal length	$\mathcal{L}$	200 mm.

The excitation is a plane wave as described before with the following parameters

Angle of incidence	θ	40°
Amplitude of plane wave	E_0	$1\,\mathrm{V\,m^{-1}}$
Wave number	k	$\pi \cdot 10^2\,\mathrm{m^{-1}}$

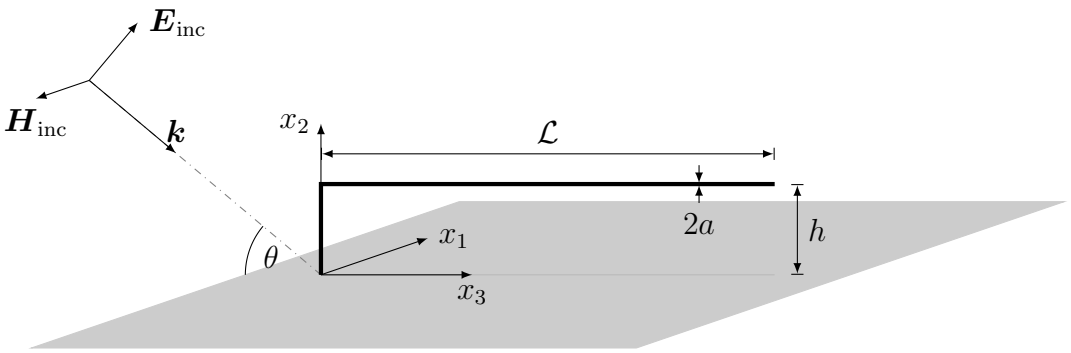

Figure 3.5: Example wire above a ground with a short-circuit at port 1 and an open-circuit at port 2.

The current along the wire is obtained using the MoM algorithm with 107 segments. Figure 3.6 shows the current obtained with the asymptotic approach compared to the numeric reference form the MoM algorithm. The scattering and reflection coefficients are extracted from the current at $l = 100\,\mathrm{mm}$. As expected the asymptotic approach yields inaccurate results at the wire ends (i.e. if $l \approx -h$ and $l \approx \mathcal{L}$). However,the asymptotic approximation and the full wave solution are indistinguishable in a large distance from the ports.

The coefficients can be extracted from any point l_{loc} on the horizontal wire part. Figures 3.7 and 3.8 show the dependence of the scattering and reflection coefficients as a function of l_{loc} . They are approximately constant in a large middle region of the wire. The behavior of the coefficients is unpredictably at the ports. The region with almost constant coefficients is the asymptotic region.

The wave length is about twice as large as the wire height above the ground. Hence, the CTLT is not applicable. Therefore, the reflection coefficients for the short-circuit at the left port and the open-circuit at the right port are not as expected from CTLT. In Ch. 4 more details on the behavior of the reflection and scattering coefficients are shown.

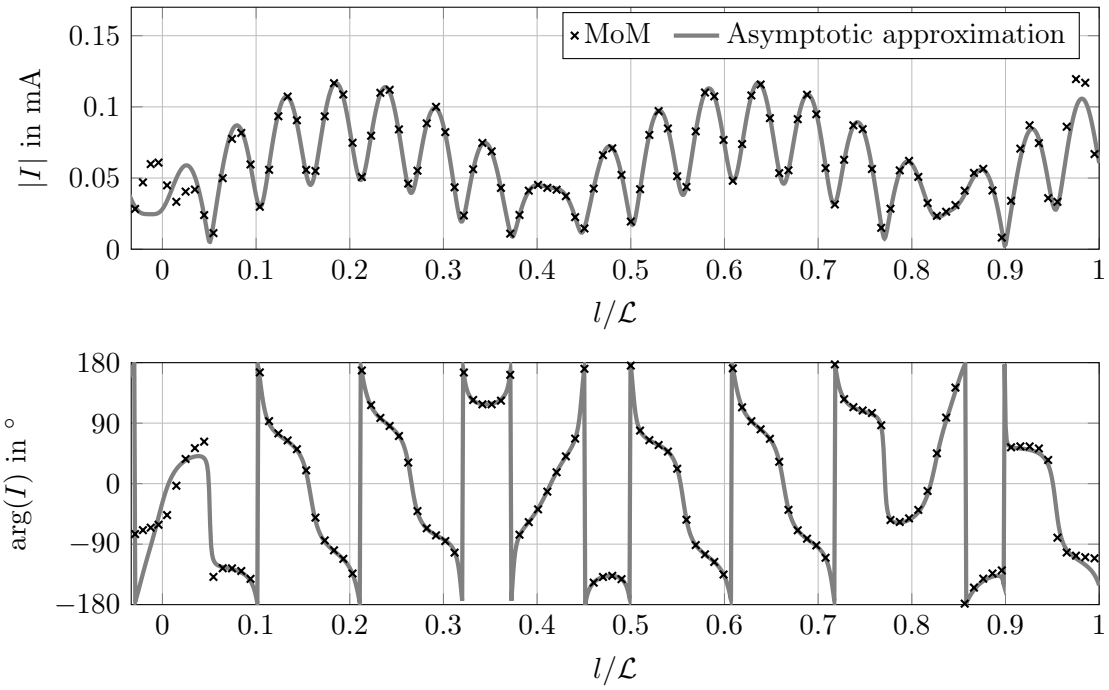

Figure 3.6: Complex current along the example wire to illustrate the accuracy of the asymptotic approach.

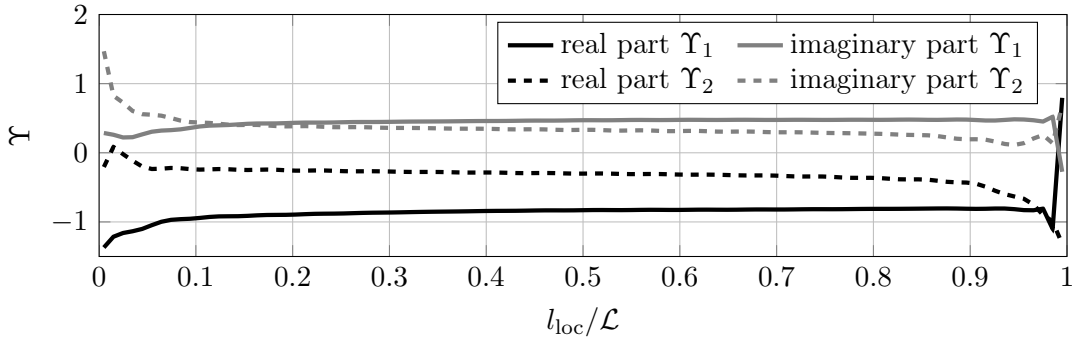

Figure 3.7: Complex scattering coefficients extracted from the current at different locations along the wire.

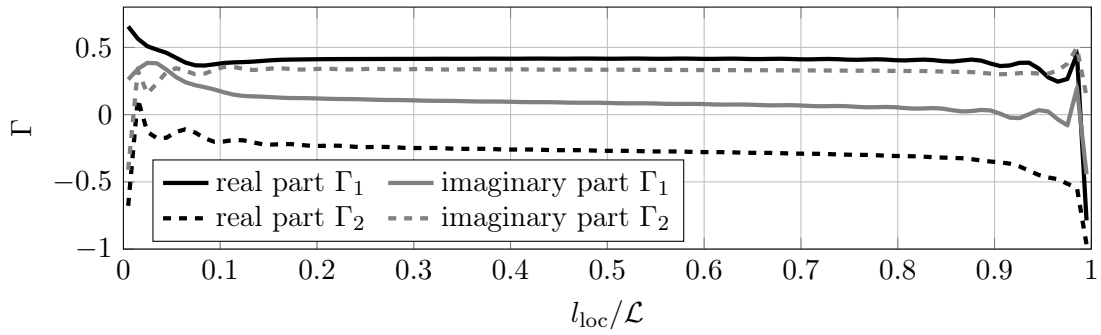

Figure 3.8: Complex reflection coefficients extracted from the current at different locations along the wire.

3.6 Analytic method to determine the scattering and reflection coefficients

The scattering and reflection coefficients characterize each port in a far distance from the port. Each port has to be viewed separately to determine the coefficients. An equivalent problem is depicted in Fig. 3.9. The second port of the finite wire is replaced by an infinite wire. This way, no re-reflections at the second port exist and only the scattering or reflection of a TEM mode at port 1 can be observed. Since the wire is infinitely long in only one direction it is a so called semi-infinite wire (ref. [13]).

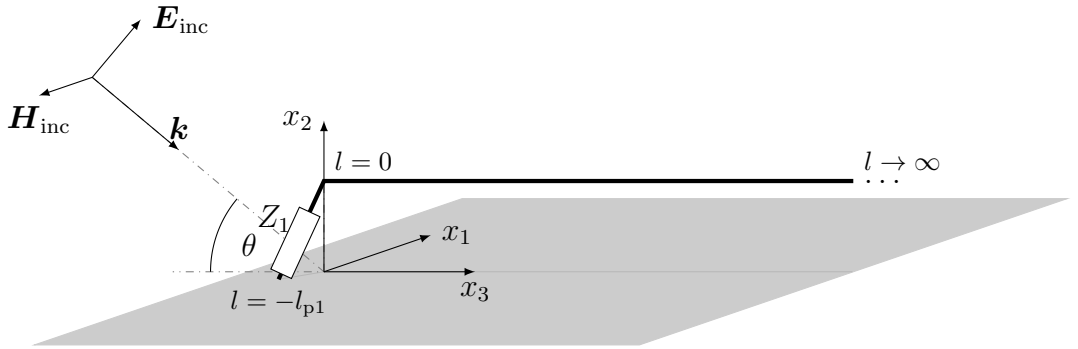

Figure 3.9: Semi-infinite wire with a plane wave excitation to determine the scattering and reflection coefficient of port 1.

3.6.1 Scattering coefficient

The scattering coefficient Υ characterizes the amplitude of the TEM mode that is scattered by the plane wave at the port. The TEM mode travels from the port to infinity along the wire. The wire is parametrized as

$$\boldsymbol{x}_{\text{c}}(l) = \begin{cases} \boldsymbol{x}_{\text{c1}}(l) & \text{for } -l_{\text{p1}} \leq l < 0 \\ h\,\hat{\boldsymbol{x}}_2 + l\,\hat{\boldsymbol{x}}_3 & \text{for } 0 \leq l < \infty\,. \end{cases} \tag{3.51}$$

In a far distance from the port, i.e. if $l \to \infty$, the asymptotic behavior of the current is

$$I(l) \sim I_\infty \mathrm{e}^{-\mathrm{j}k_\theta l} + I_\infty \Upsilon_1\, \mathrm{e}^{-\mathrm{j}kl}\,. \tag{3.52}$$

If an analytic expression for the current on the semi-infinite wire is known, it can be asymptotically approximated. The scattering coefficient can then be picked up from the asymptotic approximation.

The current on the semi-infinite wire satisfies the thin wire MPIE with the plane wave excitation, i.e.

$$\frac{\partial}{\partial l}\Phi(l) + \mathrm{j}k\frac{Z_0}{4\pi}\int\limits_{-l_{\text{p1}}}^{\infty} g_{\text{A}}(l,l')I(l')\,\mathrm{d}l' = E_{\tan}(l) \tag{3.53}$$

$$\int\limits_{-l_{\text{p1}}}^{\infty} g_\Phi(l,l')\frac{\partial}{\partial l'}I(l')\,\mathrm{d}l' + \mathrm{j}k\frac{4\pi}{Z_0}\,\Phi(l) = 0 \tag{3.54}$$

with

$$E_{\tan} = \begin{cases} E_{\mathrm{p1}}(l) & \text{for } -l_{\mathrm{p1}} < l < 0 \\ E_{\tan}(l) = 2\mathrm{j}E_0 \sin(\theta) \sin(kh\sin(\theta))\, \mathrm{e}^{-\mathrm{j}k_\theta l} & \text{for } 0 \leq l < \infty\,. \end{cases} \tag{3.55}$$

The electric field E_{p1} depends on the trajectory of port 1. In Ch. 4 the thin wire MPIE is approximately solved for the semi-infinite wire. The scattering coefficient is extracted from the asymptotic approximation. Equation (3.53) does not include the influence of the lumped impedance at $l = -l_{\mathrm{p1}}$. Hence, it is only valid for $l > -l_{\mathrm{p1}}$. The lumped impedance at the wire port is included in the boundary condition for the current as shown in detail in Ch. 4.

3.6.2 Reflection coefficient

The semi-infinite wire shown in Fig. 3.9 is used to find the reflection coefficient. However, the plane wave excitation is replaced by a lumped voltage source at $l \to \infty$. The source excites a TEM mode that travels towards the port. A TEM mode is reflected with an amplitude proportional to Γ_1. For the asymptotic approximation of the current on the semi-infinite wire holds

$$I(l) \sim I_V\, \mathrm{e}^{\mathrm{j}kl} + I_V \Gamma_1\, \mathrm{e}^{-\mathrm{j}kl}\,, \tag{3.56}$$

where I_V is an unknown amplitude.

To obtain the current for $l > -l_{\mathrm{p1}}$, the homogeneous thin wire MPIE, i.e.

$$\frac{\partial}{\partial l}\Phi(l) + \mathrm{j}k\frac{Z_0}{4\pi} \int_{-l_{\mathrm{p1}}}^{\infty} g_{\mathrm{A}}(l,l') I(l')\, \mathrm{d}l' = 0 \tag{3.57}$$

$$\int_{-l_{\mathrm{p1}}}^{\infty} g_{\Phi}(l,l') \frac{\partial}{\partial l'} I(l')\, \mathrm{d}l' + \mathrm{j}k\frac{4\pi}{Z_0}\, \Phi(l) = 0 \tag{3.58}$$

have to be solved. An approximation for the reflection coefficient is shown in detail in Ch. 4. The influence of the lumped impedance at the wire end is included in the boundary condition of the current as shown in Ch. 4.

3.7 Scattering and reflection coefficients for piecewise uniform wires

Let there be a wire with two long uniform parts that are separated by a lumped impedance Z as depicted in Fig. 3.10. The lengths of the horizontal parts are $\mathcal{L}_1$ and $\mathcal{L}_2$ respectively. Suppose there is an asymptotic region on each uniform part.

Each asymptotic region is bounded by one port and the lumped impedance in the middle. The reflection coefficients at the ports Γ_1 and Γ_2 are unaltered by the lumped impedance, due to the large lengths $\mathcal{L}_1$ and $\mathcal{L}_2$.

However, the effective TEM reflection coefficient at the lumped impedance is a combination of the reflection coefficient Γ_0 of the isolated impedance, the transmission coefficient T_0 of the isolated impedance and the reflection coefficient of the following port respectively.

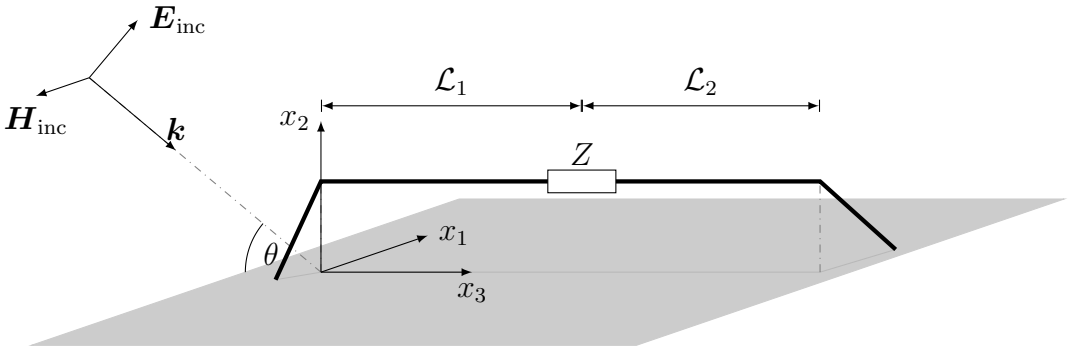

Figure 3.10: Finite wire with a lumped impedance as an addition discontinuity in the middle.

The idea of inifitely many re-reflections at each discontinuity is used again. For the reflection coefficient at the lumped impedance seen from port 1 holds

$$\Gamma_{01} = \Gamma_0 + T_0^2\,\mathrm{e}^{-2\mathrm{j}k\mathcal{L}_2}\Gamma_2 + T_0^2\,\mathrm{e}^{-4\mathrm{j}k\mathcal{L}_2}\Gamma_2^2\Gamma_0 + T_0^2\,\mathrm{e}^{-6\mathrm{j}k\mathcal{L}_2}\Gamma_2^3\Gamma_0^2 + \ldots \tag{3.59}$$

$$= \Gamma_0 + \frac{T_0^2}{\Gamma_0}\sum_{n=1}^{\infty}\left(\Gamma_2\Gamma_0\,\mathrm{e}^{-2\mathrm{j}k\mathcal{L}_2}\right)^n \tag{3.60}$$

$$= \Gamma_0 + \frac{T_0^2\Gamma_2\,\mathrm{e}^{-2\mathrm{j}k\mathcal{L}_2}}{1-\Gamma_2\Gamma_0\,\mathrm{e}^{-2\mathrm{j}k\mathcal{L}_2}} \tag{3.61}$$

Similarly, it holds for the reflection coefficient on the other side

$$\Gamma_{02} = \Gamma_0 + \frac{T_0^2\Gamma_1\,\mathrm{e}^{-2\mathrm{j}k\mathcal{L}_1}}{1-\Gamma_1\Gamma_0\,\mathrm{e}^{-2\mathrm{j}k\mathcal{L}_1}} \tag{3.62}$$

The effective scattering coefficient at the lumped impedance can be determined in a similar way. From the view of port one a TEM mode is scattered at the lumped impedance in the middle with the scattering coefficient Υ_0. Moreover, a second TEM mode is scattered at the second port with Υ_2. The scattered TEM modes are reflected, transmitted and re-reflected in the second asymptotic region. The superposition of all TEM modes gives the amplitude of the effective scattering coefficient. More specifically it holds

$$\begin{aligned}\Upsilon_{01} = &\underbrace{\Upsilon_0 + \Upsilon_0 T_0\Gamma_2\,\mathrm{e}^{-2\mathrm{j}k\mathcal{L}_2} + \Upsilon_0 T_0\Gamma_2^2\Gamma_0\,\mathrm{e}^{-4\mathrm{j}k\mathcal{L}_2} + \Upsilon_0 T_0\Gamma_2^3\Gamma_0^2\,\mathrm{e}^{-6\mathrm{j}k\mathcal{L}_2} + \ldots}_{\text{Scattering at } Z \text{ and reflections in second asymptotic region}} \\ &+ \underbrace{\Upsilon_2\,\mathrm{e}^{-\mathrm{j}k_\theta\mathcal{L}_2}T_0\,\mathrm{e}^{-\mathrm{j}k\mathcal{L}_2} + \Upsilon_2\,\mathrm{e}^{-\mathrm{j}k_\theta\mathcal{L}_2}T_0\Gamma_0\Gamma_2\,\mathrm{e}^{-3\mathrm{j}k\mathcal{L}_2} + \Upsilon_2\,\mathrm{e}^{-\mathrm{j}k_\theta\mathcal{L}_2}T_0\Gamma_0^2\Gamma_2^2\,\mathrm{e}^{-5\mathrm{j}k\mathcal{L}_2} + \ldots}_{\text{Scattering at port 2 and reflections in second asymptotic region}}\end{aligned} \tag{3.63}$$

It follows

$$\begin{aligned}\Upsilon_{01} = \Upsilon_0 + \frac{\Upsilon_0 T_0}{\Gamma_0}\sum_{n=1}^{\infty}\left(\Gamma_0\Gamma_2\,\mathrm{e}^{-2\mathrm{j}k\mathcal{L}_2}\right)^n \\ + \Upsilon_2\,\mathrm{e}^{-\mathrm{j}k_\theta\mathcal{L}_2}T_0\,\mathrm{e}^{-\mathrm{j}k\mathcal{L}_2}\sum_{n=0}^{\infty}\left(\Gamma_0\Gamma_2\,\mathrm{e}^{-2\mathrm{j}k\mathcal{L}_2}\right)^n\end{aligned} \tag{3.64}$$

and

$$\Upsilon_{01} = \Upsilon_0 + T_0 \frac{\Upsilon_0 \Gamma_2 \, \mathrm{e}^{-2\mathrm{j}k\mathcal{L}_2} + \Upsilon_2 \, \mathrm{e}^{-\mathrm{j}k_\theta \mathcal{L}_2} \, \mathrm{e}^{-\mathrm{j}k\mathcal{L}_2}}{1 - \Gamma_0 \Gamma_2 \, \mathrm{e}^{-2\mathrm{j}k\mathcal{L}_2}} \,. \tag{3.65}$$

Similarly, the scattering coefficient seen from port 2 is

$$\Upsilon_{02} = \Upsilon_0 + T_0 \frac{\Upsilon_0 \Gamma_1 \, \mathrm{e}^{-2\mathrm{j}k\mathcal{L}_1} + \Upsilon_1 \, \mathrm{e}^{\mathrm{j}k_\theta \mathcal{L}_1} \, \mathrm{e}^{-\mathrm{j}k\mathcal{L}_1}}{1 - \Gamma_0 \Gamma_1 \, \mathrm{e}^{-2\mathrm{j}k\mathcal{L}}} \tag{3.66}$$

For the current in the first asymptotic region (for $0 \ll l \ll \mathcal{L}_1$) holds

$$\begin{aligned} I(l) = I_\infty \mathrm{e}^{-\mathrm{j}k_\theta l} + I_\infty \frac{\Upsilon_1 + \Upsilon_{01} \, \mathrm{e}^{-\mathrm{j}k_\theta \mathcal{L}_1} \Gamma_1 \, \mathrm{e}^{-\mathrm{j}k\mathcal{L}_1}}{1 - \Gamma_1 \Gamma_{01} \, \mathrm{e}^{-2\mathrm{j}k\mathcal{L}_1}} \, \mathrm{e}^{-\mathrm{j}kl} \\ + I_\infty \frac{\Upsilon_{01} \, \mathrm{e}^{-\mathrm{j}k_\theta \mathcal{L}_1} + \Upsilon_1 \Gamma_{01} \, \mathrm{e}^{-\mathrm{j}k\mathcal{L}_1}}{1 - \Gamma_1 \Gamma_{01} \, \mathrm{e}^{-2\mathrm{j}k\mathcal{L}_1}} \, \mathrm{e}^{-\mathrm{j}k\mathcal{L}_1} \, \mathrm{e}^{\mathrm{j}kl} \end{aligned} \tag{3.67}$$

and in the second asymptotic region (for $\mathcal{L}_1 \ll l \ll \mathcal{L}_1 + \mathcal{L}_2$) holds

$$\begin{aligned} I(l) = I_\infty \mathrm{e}^{-\mathrm{j}k_\theta l} + I_\infty \frac{\Upsilon_{02} + \Upsilon_2 \, \mathrm{e}^{-\mathrm{j}k_\theta \mathcal{L}_2} \Gamma_{02} \, \mathrm{e}^{-\mathrm{j}k\mathcal{L}_2}}{1 - \Gamma_{02} \Gamma_2 \, \mathrm{e}^{-2\mathrm{j}k\mathcal{L}_2}} \, \mathrm{e}^{-\mathrm{j}k_\theta \mathcal{L}_1} \, \mathrm{e}^{\mathrm{j}k\mathcal{L}_1} \, \mathrm{e}^{-\mathrm{j}kl} \\ + I_\infty \frac{\Upsilon_2 \, \mathrm{e}^{-\mathrm{j}k_\theta \mathcal{L}_2} + \Upsilon_{02} \Gamma_2 \, \mathrm{e}^{-\mathrm{j}k\mathcal{L}_2}}{1 - \Gamma_{02} \Gamma_2 \, \mathrm{e}^{-2\mathrm{j}k\mathcal{L}_2}} \, \mathrm{e}^{-\mathrm{j}k_\theta \mathcal{L}_1} \, \mathrm{e}^{-\mathrm{j}k(\mathcal{L}_1 + \mathcal{L}_2)} \, \mathrm{e}^{\mathrm{j}kl} \,. \end{aligned} \tag{3.68}$$

In this example the discontinuity in the middle of the wire is symbolized by a lumped impedance. However, other modifications are possible. In [52] a bend in the wire is investigated using the asymptotic approach to yield good results. The difference is the specific value of Γ_0, T_0 and Υ_0. These parameters characterize the discontinuity in a far distance where only the TEM mode is dominant.

3.8 Extension to multiconductor transmission lines

Up to this point only a single conductor above a ground is analyzed. In [53] a similar derivation as in [13] is used to generalize the asymptotic approach to multiconductor transmission lines above a ground. For the asymptotic approach to be applicable there needs to be an asymptotic region, i.e. a region where all wires are uniform and in parallel.

The idea is that the reflection and scattering coefficients are matrices that include the coupling between the wires. The derivation from above can be applied here as well. The intermediate steps are omitted. The current in the asymptotic region is

$$\begin{aligned} \underline{\boldsymbol{I}}(l) = \underline{\boldsymbol{I}}_\infty \mathrm{e}^{-\mathrm{j}k_\theta l} + \left(\underline{\underline{\mathbf{1}}} - \underline{\underline{\boldsymbol{\Gamma}}}_1 \underline{\underline{\boldsymbol{\Gamma}}}_2 \, \mathrm{e}^{-2\mathrm{j}k\mathcal{L}} \right)^{-1} \left(\underline{\underline{\boldsymbol{\Upsilon}}}_1 + \underline{\underline{\boldsymbol{\Gamma}}}_1 \underline{\underline{\boldsymbol{\Upsilon}}}_2 \, \mathrm{e}^{-\mathrm{j}k_\theta \mathcal{L}} \, \mathrm{e}^{-\mathrm{j}k\mathcal{L}} \right) \underline{\boldsymbol{I}}_\infty \mathrm{e}^{-\mathrm{j}kl} \\ + \left(\underline{\underline{\mathbf{1}}} - \underline{\underline{\boldsymbol{\Gamma}}}_2 \underline{\underline{\boldsymbol{\Gamma}}}_1 \, \mathrm{e}^{-2\mathrm{j}k\mathcal{L}} \right)^{-1} \left(\underline{\underline{\boldsymbol{\Upsilon}}}_2 \, \mathrm{e}^{-\mathrm{j}k_\theta \mathcal{L}} + \underline{\underline{\boldsymbol{\Gamma}}}_2 \underline{\underline{\boldsymbol{\Upsilon}}}_1 \, \mathrm{e}^{-\mathrm{j}k\mathcal{L}} \right) \underline{\boldsymbol{I}}_\infty \mathrm{e}^{-\mathrm{j}k\mathcal{L}} \, \mathrm{e}^{\mathrm{j}kl} \,, \end{aligned} \tag{3.69}$$

where $\underline{\underline{\mathbf{1}}}$ is the unit matrix. The components of the vector $\underline{\boldsymbol{I}}$ are the currents on each wire. Similarly, $\underline{\boldsymbol{I}}_\infty$ contains the forced response on each wire.

The natural frequencies of multiconductor transmission lines are obtained by solving

$$\det\left(\underline{\underline{\mathbf{1}}} - \underline{\underline{\boldsymbol{\Gamma}}}_1(s_n) \underline{\underline{\boldsymbol{\Gamma}}}_2(s_n) \, \mathrm{e}^{-2s_n\mathcal{L}} \right) = 0 \tag{3.70}$$

and

$$\det\left(\underline{\underline{\mathbf{1}}} - \underline{\underline{\boldsymbol{\Gamma}}}_2(s_n) \underline{\underline{\boldsymbol{\Gamma}}}_1(s_n) \, \mathrm{e}^{-2s_n\mathcal{L}} \right) = 0 \,. \tag{3.71}$$

Sylvester's determinant theorem [54] states that the two problems are equivalent. Hence, the natural frequencies are the same for both TEM modes. More details are given in Ch. 5.

3.9 Summary

The asymptotic approach is derived in this chapter. A different derivation than in [12], [13] is presented. The asymptotic approach yields an analytic description of the current in an asymptotic region, i.e. a uniform part, of a thin wire above a ground that is excited by a plane wave. The current is characterized by TEM scattering and reflection coefficients (see Eq. (3.33)). These coefficients depend on the wire trajectory and loads at the port. In general these coefficients are frequency dependent and may include radiation and other effects at the ports. The asymptotic approach is also applicable to piecewise uniform wires and multiple wires with at least one long uniform section above a ground.

Moreover, an algorithm to determine the scattering and reflection coefficients from numerical data is derived. The method is different than the one described in [13]. The basic idea to analytically approximate the scattering and reflection coefficients is presented in this chapter as well.

Chapter 4

Iterative method

The iterative method is an analytic method to approximate the scattering and reflection coefficients. The method is described in detail in this chapter. The MPIE for thin wires are modified and perturbation theory is applied to find a current approximation for the semi-infinite wire introduced in Sec. 3.6. An analytic solution for the scattering and reflection coefficients is extracted from the current. The analytic approximation is compared to numerical results for three example ports. Lastly, it is shown that the first order iterative solution coincides with an approximation that is obtained with the induced EMF method.

4.1 Reflection coefficient

First, the reflection coefficient is approximated using the iterative method. The same problem is solved in [55], [56] using the same method. A special case is solved in [13], [15]. The idea is to solve the homogeneous MPIE for the semi-infinite wire (see Eqs. (3.57) and (3.58)) for the current and to extract the reflection coefficient from the current approximation with Eq. (3.56).

For the formulation of the iterative method it is convenient to introduce operators. The first derivative of a function is expressed with the operator $\hat{\boldsymbol{\mathcal{D}}}$, i.e.

$$\hat{\boldsymbol{\mathcal{D}}} I(l) = \frac{\partial}{\partial l} I(l)\,. \tag{4.1}$$

Furthermore, two integral operators are introduced

$$\hat{\boldsymbol{\mathcal{G}}}_\Phi I(l) = \int_{-l_\mathrm{p}}^{\infty} g_\Phi(l,l') I(l')\,\mathrm{d}l' \tag{4.2}$$

$$\hat{\boldsymbol{\mathcal{G}}}_\mathrm{A} I(l) = \int_{-l_\mathrm{p}}^{\infty} g_\mathrm{A}(l,l') I(l')\,\mathrm{d}l'\,, \tag{4.3}$$

where l_p denotes the length of the port trajectory (see Fig 3.9). The kernels g_A and g_Φ are defined in Eqs. (2.36) and (2.41).

With these operators the MPIE for the semi-infinite wire become

$$\hat{\boldsymbol{\mathcal{D}}}\Phi(l) + \mathrm{j}k\frac{Z_0}{4\pi}\hat{\boldsymbol{\mathcal{G}}}_\mathrm{A} I(l) = 0 \tag{4.4}$$

$$\hat{\boldsymbol{\mathcal{G}}}_\Phi \hat{\boldsymbol{\mathcal{D}}} I(l) + \mathrm{j}k\frac{4\pi}{Z_0}\Phi(l) = 0\,, \tag{4.5}$$

for $l > -l_\mathrm{p}$.

The operators $\hat{\boldsymbol{\mathcal{G}}}_\mathrm{A}$ and $\hat{\boldsymbol{\mathcal{G}}}_\Phi$ contain the information about the trajectory of the wire. Hence, they depend on the specific problem at hand. In general the integral kernels are quite complicated. They have a singular behavior for $l = l'$. Therefore, it is useful to regularize these operators. For the regularization the operator $\hat{\boldsymbol{\mathcal{G}}}_0$ with

$$\hat{\boldsymbol{\mathcal{G}}}_0 I(l) = \int_{-l_\mathrm{p}}^{\infty} g_0(l-l') I(l') \,\mathrm{d}l' \,, \tag{4.6}$$

where g_0 is defined in Eq. (2.54), is used. The MPIE are extended to

$$\hat{\boldsymbol{\mathcal{D}}}\Phi(l) + \mathrm{j}k\frac{Z_0}{4\pi}\hat{\boldsymbol{\mathcal{G}}}_0 I(l) = -\mathrm{j}k\frac{Z_0}{4\pi}[\hat{\boldsymbol{\mathcal{G}}}_\mathrm{A} - \hat{\boldsymbol{\mathcal{G}}}_0] I(l) \tag{4.7}$$

$$\hat{\boldsymbol{\mathcal{G}}}_0\hat{\boldsymbol{\mathcal{D}}} I(l) + \mathrm{j}k\frac{4\pi}{Z_0}\Phi(l) = -[\hat{\boldsymbol{\mathcal{G}}}_\Phi - \hat{\boldsymbol{\mathcal{G}}}_0]\hat{\boldsymbol{\mathcal{D}}} I(l) \,. \tag{4.8}$$

Now the operators $\hat{\boldsymbol{\mathcal{G}}}_\mathrm{A}$ and $\hat{\boldsymbol{\mathcal{G}}}_\Phi$ are regularized since $\hat{\boldsymbol{\mathcal{G}}}_0$ has the same singular behavior for $l = l'$. But $\hat{\boldsymbol{\mathcal{G}}}_0$ is easier to handle and independent of the specific port trajectory.

The MPIE for the semi-infinite wire are difficult to solve. The simplest example is a straight horizontal wire above a ground. Then

$$\hat{\boldsymbol{\mathcal{G}}}_\mathrm{A} = \hat{\boldsymbol{\mathcal{G}}}_\Phi = \hat{\boldsymbol{\mathcal{G}}}_0 \tag{4.9}$$

holds, due to the specific trajectory as is shown later in the first example on page 59. However, even for this simple semi-infinite problem there is only a very complicated exact solution available [57] that is difficult to extend to the general case. Hence, perturbation theory is used to find an approximate solution. The idea is that the very difficult original problem is split into infinitely many easier problems [58]. The easier problems are often solved iteratively.

For low frequencies, i.e. large wavelengths compared to the transverse dimensions of the wire, the classical transmission line theory (see Sec. 2.4) is an accurate approximation. It should be the initialization of the iteration. Each following iteration should then include more and more high frequency effects that were ignored before.

Hence, the regularized MPIE are extended even further in such a way that the telegraphers equations can be found, i.e.

$$\hat{\boldsymbol{\mathcal{D}}}\Phi(l) + \mathrm{j}kZ_\mathrm{C} I(l) = \mathrm{j}kZ_\mathrm{C}\left[\hat{\mathbf{Id}} - \frac{1}{2\ln\left(\frac{2h}{a}\right)}\hat{\boldsymbol{\mathcal{G}}}_0\right] I(l) - \mathrm{j}k\frac{Z_0}{4\pi}[\hat{\boldsymbol{\mathcal{G}}}_\mathrm{A} - \hat{\boldsymbol{\mathcal{G}}}_0] I(l) \tag{4.10}$$

$$\hat{\boldsymbol{\mathcal{D}}} I(l) + \mathrm{j}k\frac{1}{Z_\mathrm{C}}\Phi(l) = \left[\hat{\mathbf{Id}} - \frac{1}{2\ln\left(\frac{2h}{a}\right)}\hat{\boldsymbol{\mathcal{G}}}_0\right]\hat{\boldsymbol{\mathcal{D}}} I(l) - \frac{1}{2\ln\left(\frac{2h}{a}\right)}[\hat{\boldsymbol{\mathcal{G}}}_\Phi - \hat{\boldsymbol{\mathcal{G}}}_0]\hat{\boldsymbol{\mathcal{D}}} I(l) \,, \tag{4.11}$$

where the characteristic impedance Z_C is defined in Eq. (2.69) and $\hat{\mathbf{Id}}$ denotes the identity operator.

Equations (4.10) and (4.11) have the same form as the telegraphers equations (compare with Eqs. (2.89) and (2.90)) but with sources on the right hand side. However, the additional sources depend on the unknown current I.

The additional sources are negligible if the wire is uniform, the frequency is small, and l is large. For uniform wires Eq. (4.9) is true. Then the last term on the right hand side

of Eqs. (4.10) and (4.11) becomes zero. For small frequencies, i.e. if $k \approx 0$, and for large l holds

$$\left[\hat{\mathbf{Id}} - \frac{1}{2\ln\left(\frac{2h}{a}\right)}\hat{\boldsymbol{\mathcal{G}}}_0\right] I(l) = I(l) - \frac{1}{2\ln\left(\frac{2h}{a}\right)} \int_{-l_{\mathrm{p1}}}^{\infty} g_0(l-l')I(l')\,\mathrm{d}l' \tag{4.12}$$

$$\approx I(l) - \frac{I(l)}{2\ln\left(\frac{2h}{a}\right)} \int_{-l_{\mathrm{p1}}}^{\infty} g_0(l-l')\,\mathrm{d}l' \tag{4.13}$$

$$\approx I(l) - \frac{I(l)}{2\ln\left(\frac{2h}{a}\right)} \int_{-\infty}^{\infty} g_0(l-l')\,\mathrm{d}l' \tag{4.14}$$

$$= I(l) - \frac{I(l)}{2\ln\left(\frac{2h}{a}\right)} \tilde{g}_0(0) \tag{4.15}$$

$$\approx 0\,. \tag{4.16}$$

The kernel g_0 behaves approximately like a delta function if the wire radius a is small. The kernel becomes very large for $l = l'$ compared to the values at $l \neq l'$. This property is used in Eq. (4.13) to move I in front of the integral. In Eq. (4.14) the lower limit of the integral is extended. Again the idea is that the intervals where $|l - l'|$ is much larger than 0 can be neglected and have no influence on the integral. The integral is then the Fourier transform of g_0 with $k_l = 0$ (see Eq. (2.59)). Finally, $k \approx 0$ is used to obtain Eq. (4.16).

Hence, it is shown, that the right hand side in Eqs. (4.10) and (4.11) are small for uniform wires and small frequencies. Furthermore, this only holds if the distance to the port is large, i.e. if $l \gg 0$. This can be seen as an alternative derivation of the telegraphers equations.

In the following the current dependent source terms are treated as small perturbations. Formally, an auxiliary parameter χ is introduced. This parameter is equal to one but is treated as a variable first

$$\hat{\boldsymbol{\mathcal{D}}}\Phi(l) + \mathrm{j}kZ_{\mathrm{C}}I(l) = \chi\left(\mathrm{j}kZ_{\mathrm{C}}\left[\hat{\mathbf{Id}} - \frac{1}{2\ln\left(\frac{2h}{a}\right)}\hat{\boldsymbol{\mathcal{G}}}_0\right] I(l) - \mathrm{j}k\frac{Z_0}{4\pi}[\hat{\boldsymbol{\mathcal{G}}}_{\mathrm{A}} - \hat{\boldsymbol{\mathcal{G}}}_0]I(l)\right) \tag{4.17}$$

$$\hat{\boldsymbol{\mathcal{D}}}I(l) + \mathrm{j}k\frac{1}{Z_{\mathrm{C}}}\Phi(l) = \chi\left(\left[\hat{\mathbf{Id}} - \frac{1}{2\ln\left(\frac{2h}{a}\right)}\hat{\boldsymbol{\mathcal{G}}}_0\right]\hat{\boldsymbol{\mathcal{D}}}I(l) - \frac{1}{2\ln\left(\frac{2h}{a}\right)}[\hat{\boldsymbol{\mathcal{G}}}_{\Phi} - \hat{\boldsymbol{\mathcal{G}}}_0]\hat{\boldsymbol{\mathcal{D}}}I(l)\right). \tag{4.18}$$

Furthermore, the current I and scalar potential Φ are represented as a power series with the parameter χ, i.e.

$$\Phi(l) = \sum_{n=0}^{\infty} \Phi^{(n)}(l)\chi^n \tag{4.19}$$

$$I(l) = \sum_{n=0}^{\infty} I^{(n)}(l)\chi^n \tag{4.20}$$

Inserting this ansatz into Eqs. (4.17) and (4.18) and comparing the coefficients results

in

$$\hat{\boldsymbol{\mathcal{D}}}\Phi^{(0)}(l) + \mathrm{j}kZ_\mathrm{C} I^{(0)}(l) = 0 \tag{4.21}$$

$$\hat{\boldsymbol{\mathcal{D}}} I^{(0)}(l) + \mathrm{j}k\frac{1}{Z_\mathrm{C}}\Phi^{(0)}(l) = 0 \tag{4.22}$$

and

$$\hat{\boldsymbol{\mathcal{D}}}\Phi^{(n)}(l) + \mathrm{j}kZ_\mathrm{C} I^{(n)}(l) = \mathrm{j}kZ_\mathrm{C}\left[\hat{\mathbf{Id}} - \frac{1}{2\ln\left(\frac{2h}{a}\right)}\hat{\boldsymbol{\mathcal{G}}}_0\right] I^{(n-1)}(l) - \mathrm{j}k\frac{Z_0}{4\pi}[\hat{\boldsymbol{\mathcal{G}}}_\mathrm{A} - \hat{\boldsymbol{\mathcal{G}}}_0] I^{(n-1)}(l) \tag{4.23}$$

$$\hat{\boldsymbol{\mathcal{D}}} I^{(n)}(l) + \mathrm{j}k\frac{1}{Z_\mathrm{C}}\Phi^{(n)}(l) = \left[\hat{\mathbf{Id}} - \frac{1}{2\ln\left(\frac{2h}{a}\right)}\hat{\boldsymbol{\mathcal{G}}}_0\right]\hat{\boldsymbol{\mathcal{D}}} I^{(n-1)}(l) - \frac{1}{2\ln\left(\frac{2h}{a}\right)}[\hat{\boldsymbol{\mathcal{G}}}_\Phi - \hat{\boldsymbol{\mathcal{G}}}_0]\hat{\boldsymbol{\mathcal{D}}} I^{(n-1)}(l) \tag{4.24}$$

for $n > 0$.

Equations (4.21), (4.22), (4.23) and (4.24) form the basis for the iterative method. The initialization $I^{(0)}$ is the classical transmission line result. The other iterations $I^{(n)}$ are the solution of the telegraphers equations with an excitation that depends on the previous iteration.

The coupled telegrapher's equations can be decoupled to get a single equation for each current iteration, i.e.

$$[\hat{\boldsymbol{\mathcal{D}}}^2 + k^2] I^{(0)}(l) = 0 \tag{4.25}$$

and

$$[\hat{\boldsymbol{\mathcal{D}}}^2 + k^2] I^{(n)}(l) = -\frac{1}{2\ln\left(\frac{2h}{a}\right)}\left(\hat{\boldsymbol{\mathcal{D}}}[\hat{\boldsymbol{\mathcal{G}}}_\Phi - \hat{\boldsymbol{\mathcal{G}}}_0]\hat{\boldsymbol{\mathcal{D}}} I^{(n-1)}(l) + k^2[\hat{\boldsymbol{\mathcal{G}}}_\mathrm{A} - \hat{\boldsymbol{\mathcal{G}}}_0] I^{(n-1)}(l)\right) + \hat{\boldsymbol{\mathcal{D}}}\left[\hat{\mathbf{Id}} - \frac{1}{2\ln\left(\frac{2h}{a}\right)}\hat{\boldsymbol{\mathcal{G}}}_0\right]\hat{\boldsymbol{\mathcal{D}}} I^{(n-1)}(l) + k^2\left[\hat{\mathbf{Id}} - \frac{1}{2\ln\left(\frac{2h}{a}\right)}\hat{\boldsymbol{\mathcal{G}}}_0\right] I^{(n-1)}(l) \tag{4.26}$$

for $n > 0$.

Due to the $l - l'$ dependence of g_0, the operator $\hat{\boldsymbol{\mathcal{G}}}_0$ and the differentiation $\hat{\boldsymbol{\mathcal{D}}}$ can be interchanged using integration by parts, i.e.

$$\hat{\boldsymbol{\mathcal{G}}}_0\hat{\boldsymbol{\mathcal{D}}} I(l) = \int_{-l_\mathrm{p}}^{\infty} g_0(l - l')\frac{\partial}{\partial l'} I(l')\,\mathrm{d}l' \tag{4.27}$$

$$= \Big[g_0(l - l') I(l')\Big]_{l'=-l_\mathrm{p}}^{\infty} - \int_{-l_\mathrm{p}}^{\infty}\frac{\partial}{\partial l'} g_0(l - l') I(l')\,\mathrm{d}l' \tag{4.28}$$

$$= -g_0(l + l_\mathrm{p}) I(-l_\mathrm{p}) + \int_{-l_\mathrm{p}}^{\infty}\frac{\partial}{\partial l} g_0(l - l') I(l')\,\mathrm{d}l' \tag{4.29}$$

$$= -g_0(l + l_\mathrm{p}) I(-l_\mathrm{p}) + \hat{\boldsymbol{\mathcal{D}}}\hat{\boldsymbol{\mathcal{G}}}_0 I(l)\,. \tag{4.30}$$

Hence it follows

$$\hat{\boldsymbol{\mathcal{D}}}\hat{\boldsymbol{\mathcal{G}}}_0\hat{\boldsymbol{\mathcal{D}}}I(l) = \hat{\boldsymbol{\mathcal{D}}}^2\hat{\boldsymbol{\mathcal{G}}}_0 I(l) - I(-l_\mathrm{p})\hat{\boldsymbol{\mathcal{D}}}g_0(l+l_\mathrm{p}) \tag{4.31}$$

$$= \hat{\boldsymbol{\mathcal{G}}}_0\hat{\boldsymbol{\mathcal{D}}}^2 I(l) + g_0(l+l_\mathrm{p})\hat{\boldsymbol{\mathcal{D}}}I(l')\Big|_{l'=-l_\mathrm{p}} . \tag{4.32}$$

Using the latter identities for Eq. (4.26) results in

$$\begin{aligned}[\hat{\boldsymbol{\mathcal{D}}}^2 + k^2]I^{(n)}(l) = -\frac{1}{2\ln\left(\frac{2h}{a}\right)}\Big(&\hat{\boldsymbol{\mathcal{D}}}[\hat{\boldsymbol{\mathcal{G}}}_\Phi - \hat{\boldsymbol{\mathcal{G}}}_0]\hat{\boldsymbol{\mathcal{D}}}I^{(n-1)}(l) + k^2[\hat{\boldsymbol{\mathcal{G}}}_\mathrm{A} - \hat{\boldsymbol{\mathcal{G}}}_0]I^{(n-1)}(l)\Big) \\ &+ \left[\hat{\mathbf{Id}} - \frac{1}{2\ln\left(\frac{2h}{a}\right)}\hat{\boldsymbol{\mathcal{G}}}_0\right][\hat{\boldsymbol{\mathcal{D}}}^2 + k^2]I^{(n-1)}(l) \\ &- \frac{1}{2\ln\left(\frac{2h}{a}\right)} g_0(l+l_\mathrm{p})\hat{\boldsymbol{\mathcal{D}}}I^{(n-1)}(l')\Big|_{l'=-l_\mathrm{p}}\end{aligned} \tag{4.33}$$

or

$$\begin{aligned}[\hat{\boldsymbol{\mathcal{D}}}^2 + k^2]I^{(n)}(l) = -\frac{1}{2\ln\left(\frac{2h}{a}\right)}\Big(&\hat{\boldsymbol{\mathcal{D}}}[\hat{\boldsymbol{\mathcal{G}}}_\Phi - \hat{\boldsymbol{\mathcal{G}}}_0]\hat{\boldsymbol{\mathcal{D}}}I^{(n-1)}(l) + k^2[\hat{\boldsymbol{\mathcal{G}}}_\mathrm{A} - \hat{\boldsymbol{\mathcal{G}}}_0]I^{(n-1)}(l)\Big) \\ &+ [\hat{\boldsymbol{\mathcal{D}}}^2 + k^2]\left[\hat{\mathbf{Id}} - \frac{1}{2\ln\left(\frac{2h}{a}\right)}\hat{\boldsymbol{\mathcal{G}}}_0\right] I^{(n-1)}(l) \\ &+ \frac{1}{2\ln\left(\frac{2h}{a}\right)} I^{(n-1)}(-l_\mathrm{p})\hat{\boldsymbol{\mathcal{D}}}g_0(l+l_\mathrm{p})\,.\end{aligned} \tag{4.34}$$

for $n > 0$. Equations (4.26), (4.33) and (4.34) are equivalent.

Boundary conditions

The current on the semi-infinite wire has the asymptotic behavior described in Eq. (3.56). When the reflection coefficient is represented as a power series as well, i.e.

$$\Gamma = \sum_{n=0}^{\infty} \Gamma^{(n)}\chi^n\,, \tag{4.35}$$

it follows

$$\sum_{n=0}^{\infty} I^{(n)}(l)\chi^n = I(l) \tag{4.36}$$

$$\sim I_V\left(\mathrm{e}^{\mathrm{j}kl} + \Gamma\,\mathrm{e}^{-\mathrm{j}kl}\right) \tag{4.37}$$

$$= I_V\left(\mathrm{e}^{\mathrm{j}kl} + \sum_{n=0}^{\infty}\Gamma^{(n)}\chi^n\mathrm{e}^{-\mathrm{j}kl}\right). \tag{4.38}$$

Comparing the coefficients results in the asymptotic behavior of each iteration $I^{(n)}$, i.e.

$$I^{(0)}(l) \sim I_V\left(\mathrm{e}^{\mathrm{j}kl} + \Gamma^{(0)}\mathrm{e}^{-\mathrm{j}kl}\right) \tag{4.39}$$

$$I^{(n)}(l) \sim I_V\Gamma^{(n)}\mathrm{e}^{-\mathrm{j}kl} \qquad \text{for } n > 0\,. \tag{4.40}$$

Equations (4.39) and (4.40) can be seen as boundary conditions for the current iterations on the infinite wire end.

A boundary condition at the wire port has to be found to solve the boundary value problems. The lumped impedance is located at $l = -l_\mathrm{p}$ and the current at $l = -l_\mathrm{p}$ should depend on the lumped terminal impedance Z. For the special cases $Z = 0$ and $Z \to \infty$ Eqs. (2.106) and (2.107) hold.

The impedance can be included as an additional current controlled voltage as in Sec. 3.1. To obtain a boundary condition for the current the impedance is moved by a small $\Delta l > 0$ along the wire. For the zeroth iteration holds

$$\hat{\boldsymbol{\mathcal{D}}}\Phi^{(0)}(l) + \mathrm{j}kZ_\mathrm{C}I^{(0)}(l) = -ZI(\Delta l - l_\mathrm{p})\delta(l - \Delta l + l_\mathrm{p}) \tag{4.41}$$

$$\hat{\boldsymbol{\mathcal{D}}}I^{(0)}(l) + \mathrm{j}k\frac{1}{Z_\mathrm{C}}\Phi^{(0)}(l) = 0 \tag{4.42}$$

Integrating both sides of Eq. (4.41) in a small interval from $-l_\mathrm{p}$ to $2\Delta l - l_\mathrm{p}$ yields

$$\Phi^{(0)}(2\Delta l - l_\mathrm{p}) - \Phi^{(0)}(-l_\mathrm{p}) + \mathrm{j}kZ_\mathrm{C}\int\limits_{-l_\mathrm{p}}^{2\Delta l - l_\mathrm{p}} I^{(0)}(l')\,\mathrm{d}l' = -ZI^{(0)}(\Delta l - l_\mathrm{p})\,. \tag{4.43}$$

The impedance was moved by Δl to ensure that the delta function is not on the boundary of the integration interval. The scalar potential at $l = -l_\mathrm{p}$, i.e. at the ground, is defined to be 0. The remaining scalar potential is replaced by the current with Eq. (4.42). It holds

$$-\frac{Z_\mathrm{C}}{\mathrm{j}k}\hat{\boldsymbol{\mathcal{D}}}I^{(0)}(2\Delta l - l_\mathrm{p}) + \mathrm{j}kZ_\mathrm{C}\int\limits_{-l_\mathrm{p}}^{2\Delta l - l_\mathrm{p}} I^{(0)}(l')\,\mathrm{d}l' = -ZI^{(0)}(\Delta l - l_\mathrm{p})\,. \tag{4.44}$$

Finally, the limit $\Delta l \to 0$ is taken. The integral vanishes since $I^{(0)}$ is continuous. The boundary condition for the current at $l = -l_\mathrm{p}$ is

$$\left(\hat{\boldsymbol{\mathcal{D}}} - \mathrm{j}k\frac{Z}{Z_\mathrm{C}}\hat{\mathbf{Id}}\right)I^{(0)}(-l_\mathrm{p}) = 0\,. \tag{4.45}$$

The derivative $\hat{\boldsymbol{\mathcal{D}}}I^{(0)}(-l_\mathrm{p})$ is interpreted as the one-sided limit where l approaches $-l_\mathrm{p}$ from the right.

The boundary condition Eq. (4.45) is only valid for the zeroth iteration $I^{(0)}$. For the higher order iterations a similar method is applied to Eqs. (4.23) and (4.24) to obtain a boundary condition. It holds

$$\left(\hat{\boldsymbol{\mathcal{D}}} - \mathrm{j}k\frac{Z}{Z_\mathrm{C}}\hat{\mathbf{Id}}\right)I^{(n)}(-l_\mathrm{p}) = \hat{\boldsymbol{\mathcal{D}}}I^{(n-1)}(-l_\mathrm{p})\,. \tag{4.46}$$

Zeroth iteration solution

After finding boundary conditions for each current iteration the second order differential equation is solved. First, the zeroth iteration is sought. Equation (4.25) is solved with Eqs. (4.39) and (4.45). The solution process is straight forward. It holds

$$I^{(0)}(l) = I_V\left(\mathrm{e}^{\mathrm{j}kl} + \Gamma^{(0)}\mathrm{e}^{-\mathrm{j}kl}\right), \tag{4.47}$$

where

$$\Gamma^{(0)} = \frac{Z_\mathrm{C} - Z}{Z_\mathrm{C} + Z}\,\mathrm{e}^{-2\mathrm{j}kl_\mathrm{p}}\,. \tag{4.48}$$

As by design the zeroth iteration current and reflection coefficient coincide with the classical result.

First iteration solution

The first iteration current solution is obtained by solving Eq. (4.33) with the boundary conditions Eqs. (4.40) and (4.46). Since the zeroth iteration satisfies Eq. (4.25) it holds

$$[\hat{\boldsymbol{\mathcal{D}}}^2 + k^2]I^{(1)}(l) = -\frac{1}{2\ln\left(\frac{2h}{a}\right)}\Big(\hat{\boldsymbol{\mathcal{D}}}[\hat{\boldsymbol{\mathcal{G}}}_\Phi - \hat{\boldsymbol{\mathcal{G}}}_0]\hat{\boldsymbol{\mathcal{D}}}I^{(0)}(l) + k^2[\hat{\boldsymbol{\mathcal{G}}}_\mathrm{A} - \hat{\boldsymbol{\mathcal{G}}}_0]I^{(0)}(l)\Big) - \frac{1}{2\ln\left(\frac{2h}{a}\right)} g_0(l + l_\mathrm{p})\hat{\boldsymbol{\mathcal{D}}}I^{(0)}(-l_\mathrm{p}) \quad (4.49)$$

The solution of the inhomogeneous ordinary differential equation is composed of a solution of the homogeneous problem and a particular solution. The particular solution is determined using the Green's function

$$K(l, l') = -\frac{1}{2\mathrm{j}k}\left(\mathrm{e}^{-\mathrm{j}k|l-l'|} + \Gamma^{(0)}\mathrm{e}^{-\mathrm{j}k(l+l')}\right). \quad (4.50)$$

The Green's function K satisfies the homogeneous boundary condition

$$\left(\frac{\partial}{\partial l} - \mathrm{j}k\frac{Z}{Z_\mathrm{C}}\right)K(l, l')\Big|_{l=-l_\mathrm{P}} = 0 \quad (4.51)$$

and it has the asymptotic behavior

$$K(l, l') \sim -\frac{1}{2\mathrm{j}k}\left(\mathrm{e}^{\mathrm{j}kl'} + \Gamma^{(0)}\mathrm{e}^{-\mathrm{j}kl'}\right)\mathrm{e}^{-\mathrm{j}kl} \qquad \text{for } l \gg 0\,. \quad (4.52)$$

The solution of the homogeneous problem is (under consideration of the asymptotic behavior in Eq. (4.40)) $A^{(1)}\mathrm{e}^{-\mathrm{j}kl}$ with a constant $A^{(1)}$. Therefore, it holds for the first iteration current

$$I^{(1)}(l) = A^{(1)}\mathrm{e}^{-\mathrm{j}kl} - \frac{\hat{\boldsymbol{\mathcal{D}}}I^{(0)}(-l_\mathrm{p})}{2\ln\left(\frac{2h}{a}\right)}\int_{-l_\mathrm{p}}^{\infty} K(l, l')g_0(l' + l_\mathrm{p})\,\mathrm{d}l' - \frac{1}{2\ln\left(\frac{2h}{a}\right)}\int_{-l_\mathrm{p}}^{\infty} K(l, l')\Big(\hat{\boldsymbol{\mathcal{D}}}[\hat{\boldsymbol{\mathcal{G}}}_\Phi - \hat{\boldsymbol{\mathcal{G}}}_0]\hat{\boldsymbol{\mathcal{D}}}I^{(0)}(l') + k^2[\hat{\boldsymbol{\mathcal{G}}}_\mathrm{A} - \hat{\boldsymbol{\mathcal{G}}}_0]I^{(0)}(l')\Big)\,\mathrm{d}l'. \quad (4.53)$$

The constant $A^{(1)}$ is determined by enforcing the boundary condition Eq. (4.46). Since K satisfies the homogeneous boundary condition it holds

$$\left(\hat{\boldsymbol{\mathcal{D}}} - \mathrm{j}k\frac{Z}{Z_\mathrm{C}}\hat{\mathbf{Id}}\right)I^{(1)}(l) = \left(\hat{\boldsymbol{\mathcal{D}}} - \mathrm{j}k\frac{Z}{Z_\mathrm{C}}\hat{\mathbf{Id}}\right)A^{(1)}\mathrm{e}^{-\mathrm{j}kl} = \hat{\boldsymbol{\mathcal{D}}}I^{(0)}(-l_\mathrm{p})\,. \quad (4.54)$$

It follows

$$A^{(1)} = -I_V\frac{2ZZ_\mathrm{C}}{(Z_\mathrm{C} + Z)^2}\,\mathrm{e}^{-2\mathrm{j}kl_\mathrm{p}}. \quad (4.55)$$

Hence, the current from the first iteration is

$$I^{(1)}(l) = -I_V\frac{2ZZ_\mathrm{C}}{(Z_\mathrm{C} + Z)^2}\,\mathrm{e}^{-2\mathrm{j}kl_\mathrm{p}}\mathrm{e}^{-\mathrm{j}kl} - \frac{\hat{\boldsymbol{\mathcal{D}}}I^{(0)}(-l_\mathrm{p})}{2\ln\left(\frac{2h}{a}\right)}\int_{-l_\mathrm{p}}^{\infty} K(l, l')g_0(l' + l_\mathrm{p})\,\mathrm{d}l' - \frac{1}{2\ln\left(\frac{2h}{a}\right)}\int_{-l_\mathrm{p}}^{\infty} K(l, l')\Big(\hat{\boldsymbol{\mathcal{D}}}[\hat{\boldsymbol{\mathcal{G}}}_\Phi - \hat{\boldsymbol{\mathcal{G}}}_0]\hat{\boldsymbol{\mathcal{D}}}I^{(0)}(l') + k^2[\hat{\boldsymbol{\mathcal{G}}}_\mathrm{A} - \hat{\boldsymbol{\mathcal{G}}}_0]I^{(0)}(l')\Big)\,\mathrm{d}l'. \quad (4.56)$$

The reflection coefficient $\Gamma^{(1)}$ can be extracted from the current by analyzing $I^{(1)}$ asymptotically for large l and comparing the result with Eq. (4.40). The asymptotic behavior of K is given in (4.52). For a shorter notation the function

$$P^{(0)}(l) = \mathrm{e}^{\mathrm{j}kl} + \Gamma^{(0)}\mathrm{e}^{-\mathrm{j}kl} \tag{4.57}$$

is introduced. With this it holds

$$I^{(0)}(l) = I_V P^{(0)}(l) \tag{4.58}$$

$$K(l,l') \sim -\frac{1}{2\mathrm{j}k} P^{(0)}(l')\,\mathrm{e}^{-\mathrm{j}kl}\,. \tag{4.59}$$

The asymptotic approximation of $I^{(1)}$ is then

$$\begin{aligned} I^{(1)}(l) \sim{}& -I_V \frac{2ZZ_\mathrm{C}}{(Z_\mathrm{C}+Z)^2}\,\mathrm{e}^{-2\mathrm{j}kl_\mathrm{p}}\mathrm{e}^{-\mathrm{j}kl} + I_V \frac{\hat{\boldsymbol{\mathcal{D}}}P^{(0)}(-l_\mathrm{p})}{4\mathrm{j}k\ln\left(\frac{2h}{a}\right)} \int\limits_{-l_\mathrm{p}}^{\infty} P^{(0)}(l')g_0(l'+l_\mathrm{p})\,\mathrm{d}l'\,\mathrm{e}^{-\mathrm{j}kl} \\ &+ \frac{I_V\,\mathrm{e}^{-\mathrm{j}kl}}{4\mathrm{j}k\ln\left(\frac{2h}{a}\right)} \int\limits_{-l_\mathrm{p}}^{\infty} P^{(0)}(l')\Big(\hat{\boldsymbol{\mathcal{D}}}[\hat{\boldsymbol{\mathcal{G}}}_\Phi - \hat{\boldsymbol{\mathcal{G}}}_0]\hat{\boldsymbol{\mathcal{D}}}P^{(0)}(l') + k^2[\hat{\boldsymbol{\mathcal{G}}}_\mathrm{A} - \hat{\boldsymbol{\mathcal{G}}}_0]P^{(0)}(l')\Big)\,\mathrm{d}l'. \end{aligned} \tag{4.60}$$

Comparing this result with Eq. (4.40) results in the first iteration reflection coefficient

$$\begin{aligned} \Gamma^{(1)} ={}& -\frac{2ZZ_\mathrm{C}}{(Z_\mathrm{C}+Z)^2}\,\mathrm{e}^{-2\mathrm{j}kl_\mathrm{p}} + \frac{\hat{\boldsymbol{\mathcal{D}}}P^{(0)}(-l_\mathrm{p})}{4\mathrm{j}k\ln\left(\frac{2h}{a}\right)} \int\limits_{-l_\mathrm{p}}^{\infty} P^{(0)}(l')g_0(l'+l_\mathrm{p})\,\mathrm{d}l' \\ &+ \frac{1}{4\mathrm{j}k\ln\left(\frac{2h}{a}\right)} \int\limits_{-l_\mathrm{p}}^{\infty} P^{(0)}(l')\Big(\hat{\boldsymbol{\mathcal{D}}}[\hat{\boldsymbol{\mathcal{G}}}_\Phi - \hat{\boldsymbol{\mathcal{G}}}_0]\hat{\boldsymbol{\mathcal{D}}}P^{(0)}(l') + k^2[\hat{\boldsymbol{\mathcal{G}}}_\mathrm{A} - \hat{\boldsymbol{\mathcal{G}}}_0]P^{(0)}(l')\Big)\,\mathrm{d}l'. \end{aligned} \tag{4.61}$$

Equation (4.61) can be simplified as described in App. B.2 to yield

$$\begin{aligned} \Gamma^{(1)} ={}& \frac{Z_\mathrm{C}^2+Z^2}{(Z_\mathrm{C}+Z)^2}\,\frac{E_1(2\mathrm{j}kh) - E_1(\mathrm{j}ka) + \ln\left(\frac{2h}{a}\right)}{\ln\left(\frac{2h}{a}\right)}\,\mathrm{e}^{-2\mathrm{j}kl_\mathrm{p}} \\ &- \frac{1}{4\mathrm{j}k\ln\left(\frac{2h}{a}\right)} \int\limits_{-l_\mathrm{p}}^{\infty}\int\limits_{-l_\mathrm{p}}^{\infty} \Big\{ \frac{\partial}{\partial l'}P^{(0)}(l')[g_\Phi(l',l'') - g_0(l'-l'')]\frac{\partial}{\partial l''}P^{(0)}(l'') \\ &\qquad - k^2 P^{(0)}(l')[g_\mathrm{A}(l',l'') - g_0(l'-l'')]P^{(0)}(l'') \Big\}\,\mathrm{d}l''\mathrm{d}l', \end{aligned} \tag{4.62}$$

where E_1 is the exponential integral. It is defined as (see [59])

$$E_1(x) = \int\limits_x^{\infty} \frac{\mathrm{e}^{-t}}{t}\,\mathrm{d}t\,. \tag{4.63}$$

The double integral cannot be solved in general since the kernels depend on the specific trajectory of the wire at the port. For complex problems the double integration needs to be solved numerically. However, due to the regularization with g_0 a large portion of the

integrals is zero. If l' and l'' are larger than 0 the kernels g_Φ, g_A and g_0 agree and the integrals vanish. Hence, it holds

$$\int_{-l_\mathrm{p}}^{\infty}\int_{-l_\mathrm{p}}^{\infty}\ldots\mathrm{d}l''\mathrm{d}l' = \int_{-l_\mathrm{p}}^{0}\int_{-l_\mathrm{p}}^{0}\ldots\mathrm{d}l''\mathrm{d}l' + \int_{-l_\mathrm{p}}^{0}\int_{0}^{\infty}\ldots\mathrm{d}l''\mathrm{d}l' + \int_{0}^{\infty}\int_{-l_\mathrm{p}}^{0}\ldots\mathrm{d}l''\mathrm{d}l'. \tag{4.64}$$

Furthermore, the integrands are symmetric in l' and l''. Hence, the last two double integrations in (4.64) are identical. It follows

$$\begin{aligned}\Gamma^{(1)} = {}& \frac{Z_\mathrm{C}^2+Z^2}{(Z_\mathrm{C}+Z)^2}\frac{E_1(2\mathrm{j}kh)-E_1(\mathrm{j}ka)+\ln\left(\frac{2h}{a}\right)}{\ln\left(\frac{2h}{a}\right)}\,\mathrm{e}^{-2\mathrm{j}kl_\mathrm{p}}\\ &-\frac{1}{4\mathrm{j}k\ln\left(\frac{2h}{a}\right)}\int_{-l_\mathrm{p}}^{0}\int_{-l_\mathrm{p}}^{0}\Big\{\frac{\partial}{\partial l'}P^{(0)}(l')[g_\Phi(l',l'')-g_0(l'-l'')]\frac{\partial}{\partial l''}P^{(0)}(l'')\\ &\qquad -k^2P^{(0)}(l')[g_\mathrm{A}(l',l'')-g_0(l'-l'')]P^{(0)}(l'')\Big\}\,\mathrm{d}l''\mathrm{d}l'\\ &-\frac{1}{2\mathrm{j}k\ln\left(\frac{2h}{a}\right)}\int_{-l_\mathrm{p}}^{0}\int_{0}^{\infty}\Big\{\frac{\partial}{\partial l'}P^{(0)}(l')[g_\Phi(l',l'')-g_0(l'-l'')]\frac{\partial}{\partial l''}P^{(0)}(l'')\\ &\qquad -k^2P^{(0)}(l')[g_\mathrm{A}(l',l'')-g_0(l'-l'')]P^{(0)}(l'')\Big\}\,\mathrm{d}l''\mathrm{d}l'.\end{aligned} \tag{4.65}$$

As shown in App. B.3 the integration in the infinite domain can be evaluated using the exponential integral function E_1. The remaining integrals can be solved quickly using standard numerical methods.

The reflection coefficient is approximated using the zeroth and first iteration by setting $\chi = 1$ in Eq. (4.35), i.e.

$$\Gamma \approx \Gamma^{(0)} + \Gamma^{(1)}\,. \tag{4.66}$$

Higher order approximations are possible. However, as is shown in the following examples the first order approximation already greatly improves the classical solution $\Gamma^{(0)}$.

The classical solution $\Gamma^{(0)}$ includes almost no information about the trajectory of the wire at the port. Only a phase shift is included in $\Gamma^{(0)}$. The first iteration $\Gamma^{(1)}$ includes the non-uniformity of the port. The information of the trajectory is included in the kernels g_Φ and g_A. Furthermore, the first iteration includes a frequency dependency. In the following, three examples illustrate the improved accuracy of the analytic solution.

Examples

The following dimensions are used for the three examples:

Wire radius	a	0.5 mm
Height above the ground	h	100 mm.

First, the wire is just left open. It holds $l_\mathrm{p} = 0$ and $Z = \infty$. The wire trajectory is

$$\boldsymbol{x}_\mathrm{c}(l) = h\,\hat{\boldsymbol{x}}_2 + l\,\hat{\boldsymbol{x}}_3\,. \tag{4.67}$$

The zeroth and first iteration are

$$\Gamma^{(0)} = -1 \tag{4.68}$$

$$\Gamma^{(1)} = \frac{E_1(2\mathrm{j}kh) - E_1(\mathrm{j}ka) + \ln\left(\frac{2h}{a}\right)}{\ln\left(\frac{2h}{a}\right)} \,. \tag{4.69}$$

Hence, it holds

$$\Gamma \approx \frac{E_1(2\mathrm{j}kh) - E_1(\mathrm{j}ka)}{\ln\left(\frac{2h}{a}\right)} \,. \tag{4.70}$$

The analytic approximation is compared to a numerical reference in Fig. 4.1. The numerical reference is obtained as described in Sec. 3.5. Excellent agreement can be observed even if the wavelength λ is close to the wire height. The classical reflection coefficient is real and constant. This approximation only holds if $h/\lambda < 0.05$. After that the absolute value of the real part decreases and the imaginary part differs from 0. This illustrates the limits of the classical transmission line approximation. Furthermore, it can be seen that it is sufficient to determine the first order iteration to get an excellent result.

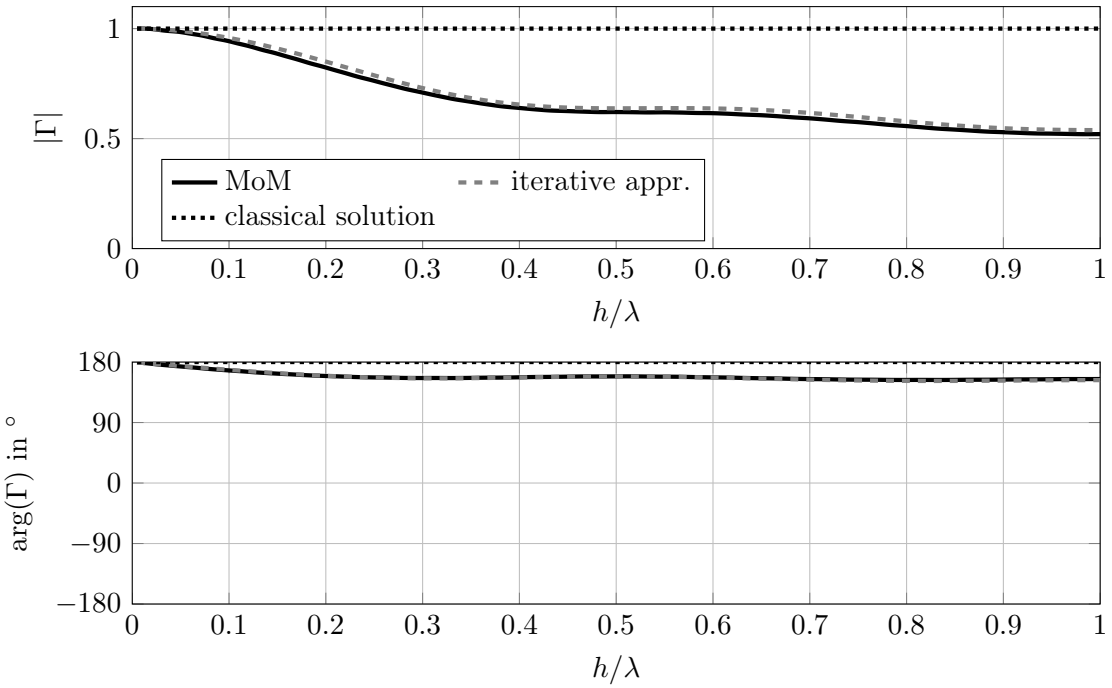

Figure 4.1: Complex reflection coefficient for the open-circuited port.

The **second example** is a transmission line with a ramp at the port that is terminated with a short-circuit, i.e. it is simply connected to the ground plane. Figure 4.2 shows the port. The port is mainly characterized by the angle α. The wire trajectory is parameterized as

$$\boldsymbol{x}_\mathrm{c}(l) = \begin{cases} (l\sin(\alpha) + h)\,\hat{\boldsymbol{x}}_2 + l\cos(\alpha)\,\hat{\boldsymbol{x}}_3 & \text{for } -l_\mathrm{p} < l < 0 \\ h\,\hat{\boldsymbol{x}}_2 + l\,\hat{\boldsymbol{x}}_3 & \text{for } 0 \leq l < \infty \end{cases} \tag{4.71}$$

with the port length

$$l_\mathrm{p} = \frac{h}{\sin(\alpha)} \,. \tag{4.72}$$

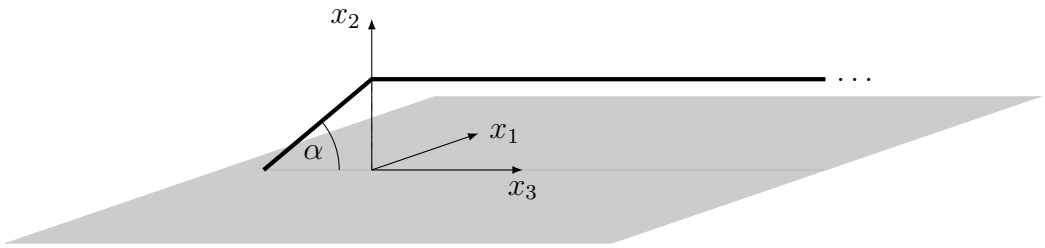

Figure 4.2: Semi-infinite wire with a ramp at the port that is terminated by a short circuit.

The classical solution for this example is

$$\Gamma^{(0)} = \mathrm{e}^{-2\mathrm{j}kl_\mathrm{P}}. \tag{4.73}$$

The integrals in (4.65) need to be solved numerically for this example. However, due to the regularization the computation time is negligible. Figure 4.3 compares the analytic solution with a numerical reference. For this example $\alpha = 40°$ is chosen. Again, the agreement is very good. For larger frequencies the solutions begin to deviate slightly.

The normalized classical solution, i.e. $\Gamma^{(0)}\mathrm{e}^{2\mathrm{j}kl_\mathrm{P}}$, is just 1. The frequency dependence that is seen in Fig. 4.3 strongly depends on the angle α. For a short-circuited port with a different trajectory the reflection coefficient would have a different behavior.

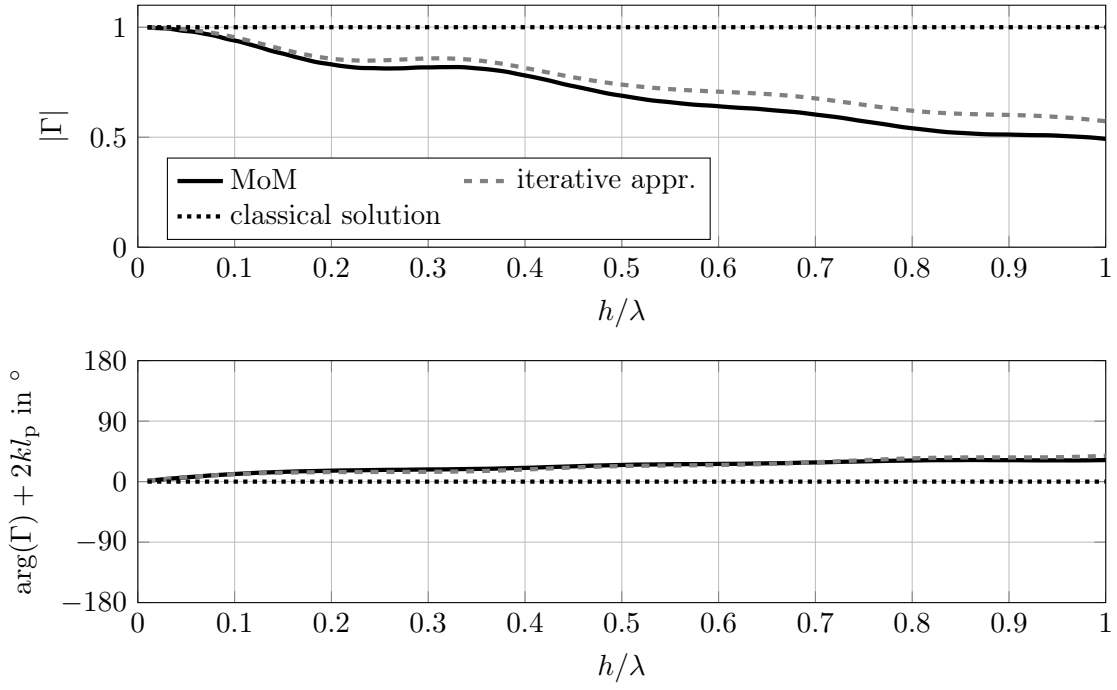

Figure 4.3: Complex reflection coefficient for the port with a ramp and a short-circuit.

The **third example** is a transmission line with a vertical riser. The wire can be seen as a special case from the previous example with $\alpha = 0°$. It is matched, i.e. a terminal impedance $Z = Z_\mathrm{C}$ is chosen. Hence, the classical solution is

$$\Gamma^{(0)} = 0\,. \tag{4.74}$$

The wire trajectory is parameterized as

$$\boldsymbol{x}_\mathrm{c}(l) = \begin{cases} (l+h)\,\hat{\boldsymbol{x}}_2 & \text{for } -h < l < 0 \\ h\,\hat{\boldsymbol{x}}_2 + l\,\hat{\boldsymbol{x}}_3 & \text{for } 0 \leq l < \infty\,. \end{cases} \tag{4.75}$$

The integrals in (4.65) cannot be solved analytically for this example, as well. The results are depicted in Fig. 4.4. The same behavior as for the first two examples can be seen here, too. The classical result is only valid for very large wave lengths compared to the wire height. The first iteration improves the overall approximation significantly. The numerical reference is obtained by using a segment length of 2 mm. This is necessary to model the lumped impedance in a very concentrated point. The lumped load can only be included as a distributed impedance along a single wire segment in the NEC model. An even smaller segment length would return problems since then the ratio of segment length to segment radius becomes too small. Hence, the numerical model and the analytic one do not completely agree and, therefore, slightly larger deviations as seen before are present for this example.

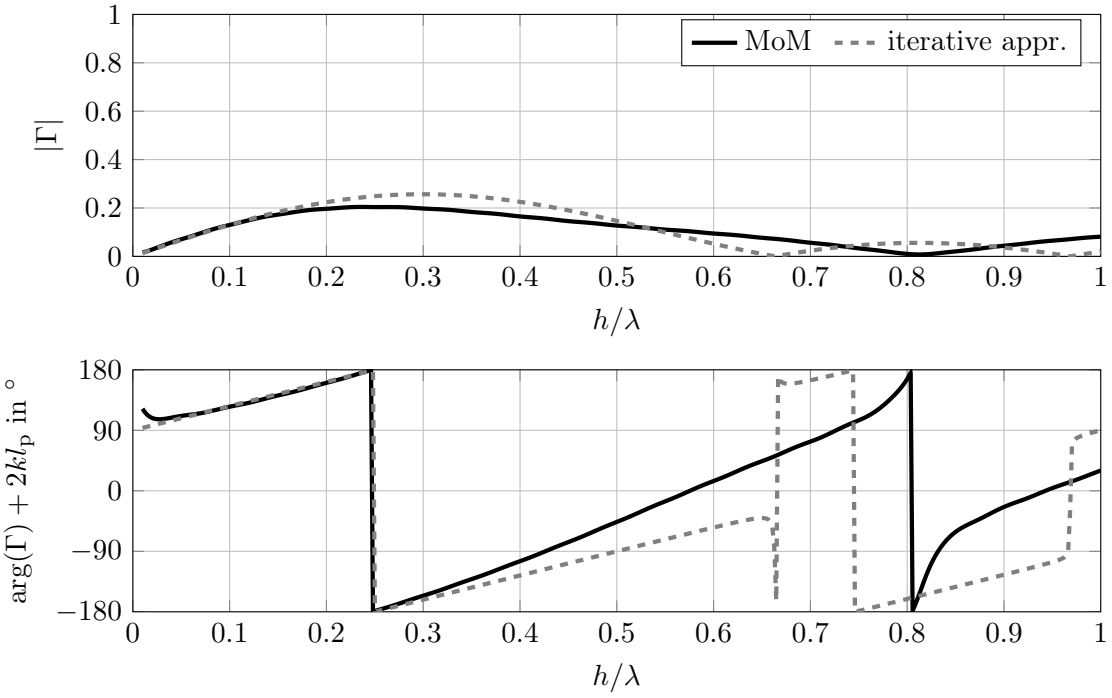

Figure 4.4: Complex reflection coefficient for the port with a riser and a load $Z = Z_\mathrm{C}$.

4.2 Scattering coefficient

Approximating the scattering coefficient can be done in a similar manner as for the reflection coefficient. However, the tangential electric field that arises due to the plane wave excitation has to be taken into account for the scattering coefficient. For the semi-infinite wire Eqs. (3.53) and (3.54) need to be solved for the current. The scattering coefficient can be extracted from the current using the asymptotic behavior in Eq. (3.52).

The inhomogeneous MPIE for the semi-infinite wire in operator form are

$$\hat{\boldsymbol{\mathcal{D}}}\Phi(l) + \mathrm{j}k\frac{Z_0}{4\pi}\hat{\boldsymbol{\mathcal{G}}}_{\mathrm{A}} I(l) = E_{\tan}(l) \tag{4.76}$$

$$\hat{\boldsymbol{\mathcal{G}}}_{\Phi}\hat{\boldsymbol{\mathcal{D}}} I(l) + \mathrm{j}k\frac{4\pi}{Z_0}\Phi(l) = 0\,. \tag{4.77}$$

for $l > -l_{\mathrm{p}}$. The tangential electric field along the wire is

$$E_{\tan}(l) = \begin{cases} E_{\mathrm{p}}(l) & \text{for } -l_{\mathrm{p}} < l < 0 \\ E_{x_3}\,\mathrm{e}^{-\mathrm{j}k_\theta l} & \text{for } 0 \le l < \infty \end{cases} \tag{4.78}$$

with

$$E_{x_3} = 2\mathrm{j}E_0 \sin(\theta)\sin(kh\sin(\theta))\,. \tag{4.79}$$

The function $E_{\mathrm{p}}(l)$ depends on the trajectory of the port.

The inhomogeneous MPIE are extended in a similar form as for the reflection coefficient. Furthermore, perturbation theory is applied as above to result in similar equations for each current iteration. For the zeroth iteration it holds

$$[\hat{\boldsymbol{\mathcal{D}}}^2 + k^2] I^{(0)}(l) = -\mathrm{j}k\frac{1}{Z_{\mathrm{C}}} E_{\tan}(l)\,. \tag{4.80}$$

For the higher iterations Eq. (4.34) is used.

The boundary condition at $l = -l_{\mathrm{p}}$ is the same as for the reflection coefficient, i.e. Eqs. (4.45) and (4.46). The asymptotic behavior for $l \to \infty$, i.e. the second boundary condition, is different. It holds

$$\sum_{n=0}^{\infty} I^{(n)}(l)\chi^n = I(l) \sim \sum_{n=0}^{\infty} I_{\infty}^{(n)}\chi^n\,\mathrm{e}^{-\mathrm{j}k_\theta l} + \sum_{n=0}^{\infty}\Psi^{(n)}\chi^n\,\mathrm{e}^{-\mathrm{j}kl}\,, \tag{4.81}$$

where $I_{\infty}^{(n)}$ and $\Psi^{(n)}$ are unknown coefficients. Hence, the asymptotic behavior for each iteration is

$$I^{(n)}(l) \sim I_{\infty}^{(n)}\chi^n\,\mathrm{e}^{-\mathrm{j}k_\theta l} + \Psi^{(n)}\chi^n\,\mathrm{e}^{-\mathrm{j}kl} \tag{4.82}$$

for $n \ge 0$.

Furthermore, it holds the asymptotic behavior in Eq.(3.52). Equating the two asymptotic approximations (Eqs. (3.52) and (4.81)) results in

$$\Upsilon = \frac{\sum\limits_{n=0}^{\infty}\Psi^{(n)}\chi^n}{\sum\limits_{n=0}^{\infty} I_{\infty}^{(n)}\chi^n}\,. \tag{4.83}$$

The Scattering coefficient Υ shall be developed into a power series as well. Then it holds

$$\Upsilon = \sum_{n=0}^{\infty}\Upsilon^{(n)}\chi^n \tag{4.84}$$

with

$$\Upsilon^{(0)} = \frac{\Psi^{(0)}}{I_\infty^{(0)}} \tag{4.85}$$

$$\Upsilon^{(1)} = \frac{\Psi^{(1)}}{I_\infty^{(0)}} - \frac{\Psi^{(0)} I_\infty^{(1)}}{[I_\infty^{(0)}]^2} \tag{4.86}$$

$$= \frac{\Psi^{(1)}}{I_\infty^{(0)}} - \Upsilon^{(0)} \frac{I_\infty^{(1)}}{I_\infty^{(0)}} \,. \tag{4.87}$$

As for the reflection coefficient only a first order approximation with $\chi = 1$ is sought at this point, i.e.

$$\Upsilon \approx \Upsilon^{(0)} + \Upsilon^{(1)}. \tag{4.88}$$

Next, the zeroth and first order approximation of the coefficient $I_\infty^{(n)}$ and $\Psi^{(n)}$ are sought

Zeroth iteration

The zeroth iteration is obtained by solving Eq. (4.80) with the boundary conditions Eqs. (4.45) and (4.82). Since the tangential electric field has a piecewise definition, the following ansatz is made for the zeroth iteration current

$$I^{(0)}(l) = \begin{cases} I_\mathrm{p}^{(0)}(l) & \text{for } -l_\mathrm{p} < l < 0 \\ I_\infty^{(0)} \, \mathrm{e}^{-\mathrm{j}k_\theta l} + \Psi^{(0)} \, \mathrm{e}^{-\mathrm{j}kl} & \text{for } 0 \leq l < \infty \,. \end{cases} \tag{4.89}$$

Inserting this ansatz into Eq. (4.80) results in

$$I_\infty^{(0)} = -\mathrm{j}k \frac{1}{Z_\mathrm{C}} \frac{E_{x_3}}{k^2 - k_\theta^2} \,. \tag{4.90}$$

The current $I_\mathrm{p}^{(0)}(l)$ is composed of a particular solution $F_1(l)$ and a solution of the corresponding homogeneous problem. The following ansatz is made

$$I_\mathrm{p}^{(0)}(l) = F_1(l) + A_\theta^{(0)} \left(\mathrm{e}^{\mathrm{j}kl} + \Gamma^{(0)} \, \mathrm{e}^{-\mathrm{j}kl} \right) \tag{4.91}$$

with

$$F_1(l) = -\mathrm{j}k \frac{1}{Z_\mathrm{C}} \int_{-l_\mathrm{p}}^{0} K(l, l') E_\mathrm{p}(l') \, \mathrm{d}l' \,, \tag{4.92}$$

where the Green's function K is defined in Eq. (4.50). The Green's function and homogeneous solution are chosen such that the boundary condition Eq. (4.45) is fulfilled.

The current and the charge per unit length, i.e. the first derivative of the current, are continuous along the wire. These two conditions are used at $l = 0$ to determine the two constants $A^{(0)}$ and $\Psi^{(0)}$. Before dealing with these constants the function $F_1(0)$ and its

derivative are analyzed. It holds

$$F_1(0) = -\mathrm{j}k\frac{1}{Z_\mathrm{C}}\int_{-l_\mathrm{p}}^{0} K(0,l')E_\mathrm{p}(l')\,\mathrm{d}l' \tag{4.93}$$

$$= \frac{1}{2Z_\mathrm{C}}\int_{-l_\mathrm{p}}^{0} \left(\mathrm{e}^{\mathrm{j}kl'} + \Gamma^{(0)}\,\mathrm{e}^{-\mathrm{j}kl'}\right)E_\mathrm{p}(l')\,\mathrm{d}l' \tag{4.94}$$

$$= \frac{1}{2Z_\mathrm{C}}\int_{-l_\mathrm{p}}^{0} P^{(0)}(l')E_\mathrm{p}(l')\,\mathrm{d}l' \tag{4.95}$$

and

$$\frac{1}{\mathrm{j}k}\frac{\partial}{\partial l}F_1(l)\Big|_{l=0} = -\frac{1}{Z_\mathrm{C}}\int_{-l_\mathrm{p}}^{0} \frac{\partial}{\partial l}K(l,l')\Big|_{l=0} E_\mathrm{p}(l')\,\mathrm{d}l' \tag{4.96}$$

$$= -\frac{1}{2Z_\mathrm{C}}\int_{-l_\mathrm{p}}^{0} P^{(0)}(l')E_\mathrm{p}(l')\,\mathrm{d}l' \tag{4.97}$$

$$= -F_1(0)\,. \tag{4.98}$$

With these identities it is straight forward to determine the constants $A^{(0)}$ and $\Psi^{(0)}$ from the two continuity conditions. The sought constants are

$$A_\theta^{(0)} = \frac{1}{2}(1-\cos(\theta))I_\infty^{(0)} \tag{4.99}$$

$$\Psi^{(0)} = \left(\frac{1}{2}(1-\cos(\theta))\Gamma^{(0)} - \frac{1}{2}(1+\cos(\theta))\right)I_\infty^{(0)} + \frac{1}{2Z_\mathrm{C}}\int_{-l_\mathrm{p}}^{0} P^{(0)}(l')E_\mathrm{p}(l')\,\mathrm{d}l'\,. \tag{4.100}$$

Inserting the result into Eq. (4.85) yields

$$\Upsilon^{(0)} = \frac{1}{2}(1-\cos(\theta))\Gamma^{(0)} - \frac{1}{2}(1+\cos(\theta)) + \frac{1}{2Z_\mathrm{C}I_\infty^{(0)}}\int_{-l_\mathrm{p}}^{0} P^{(0)}(l')E_\mathrm{p}(l')\,\mathrm{d}l'\,. \tag{4.101}$$

Inserting the current $I_\infty^{(0)}$ from Eq. (4.90) finally results in

$$\Upsilon^{(0)} = \frac{1}{2}(1-\cos(\theta))\Gamma^{(0)} - \frac{1}{2}(1+\cos(\theta)) - \frac{k^2-k_\theta^2}{2\mathrm{j}k}\int_{-l_\mathrm{p}}^{0} P^{(0)}(l')\frac{E_\mathrm{p}(l')}{E_{x_3}}\,\mathrm{d}l'\,. \tag{4.102}$$

This concludes the derivation of the zeroth iteration scattering coefficient. The Green's function K cannot be used for the whole domain $-l_\mathrm{p} < l < \infty$. Due to the oscillatory behavior of the integrand, the integral would not converge. Therefore, the current is split into two domains for the ansatz in Eq. (4.89).

First iteration

Next, Eq. (4.34) is solved with the boundary conditions Eqs. (4.46) and (4.82) to determine the first iteration current. It holds

$$[\hat{\boldsymbol{\mathcal{D}}}^2 + k^2]I^{(1)}(l) = [\hat{\boldsymbol{\mathcal{D}}}^2 + k^2]\left[\hat{\mathbf{Id}} - \frac{1}{2\ln\left(\frac{2h}{a}\right)}\hat{\boldsymbol{\mathcal{G}}}_0\right]I^{(0)}(l) - \frac{1}{2\ln\left(\frac{2h}{a}\right)}\Big(\hat{\boldsymbol{\mathcal{D}}}[\hat{\boldsymbol{\mathcal{G}}}_\Phi - \hat{\boldsymbol{\mathcal{G}}}_0]\hat{\boldsymbol{\mathcal{D}}}I^{(0)}(l) + k^2[\hat{\boldsymbol{\mathcal{G}}}_\mathrm{A} - \hat{\boldsymbol{\mathcal{G}}}_0]I^{(0)}(l)\Big) + \frac{I^{(0)}(-l_\mathrm{p})}{2\ln\left(\frac{2h}{a}\right)}\hat{\boldsymbol{\mathcal{D}}}g_0(l + l_\mathrm{p})\,. \quad (4.103)$$

Again, the Green's function K is used to find a particular solution. The particular solution fulfills the homogeneous boundary condition at $l = -l_\mathrm{p}$. A solution to the homogeneous problem, i.e. $A_\theta^{(1)}\mathrm{e}^{-\mathrm{j}kl}$, is needed to enforce the inhomogeneous boundary condition Eq. (4.46). Hence, the first iteration current has the form

$$I^{(1)}(l) = A_\theta^{(1)}\mathrm{e}^{-\mathrm{j}kl} + \left[\hat{\mathbf{Id}} - \frac{1}{2\ln\left(\frac{2h}{a}\right)}\hat{\boldsymbol{\mathcal{G}}}_0\right]I^{(0)}(l) - \frac{1}{2\ln\left(\frac{2h}{a}\right)}\int_{-l_\mathrm{p}}^{\infty} K(l,l')\Big(\hat{\boldsymbol{\mathcal{D}}}[\hat{\boldsymbol{\mathcal{G}}}_\Phi - \hat{\boldsymbol{\mathcal{G}}}_0]\hat{\boldsymbol{\mathcal{D}}}I^{(0)}(l') + k^2[\hat{\boldsymbol{\mathcal{G}}}_\mathrm{A} - \hat{\boldsymbol{\mathcal{G}}}_0]I^{(0)}(l')\Big)\,\mathrm{d}l' + \frac{I^{(0)}(-l_\mathrm{p})}{2\ln\left(\frac{2h}{a}\right)}\int_{-l_\mathrm{p}}^{\infty} K(l,l')\hat{\boldsymbol{\mathcal{D}}}g_0(l' + l_\mathrm{p})\,\mathrm{d}l'\,. \quad (4.104)$$

The unknown amplitude $A_\theta^{(1)}$ can be determined by enforcing the boundary condition Eq. (4.46). It follows

$$\mathrm{j}k\frac{Z}{Z_\mathrm{C}}I^{(0)}(-l_\mathrm{p}) = \frac{\partial}{\partial l}I^{(0)}(l)\Big|_{l=-l_\mathrm{p}} \quad (4.105)$$

$$= \left(\frac{\partial}{\partial l} - \mathrm{j}k\frac{Z}{Z_\mathrm{C}}\right)I^{(1)}(l)\Big|_{l=-l_\mathrm{p}} \quad (4.106)$$

$$= -\mathrm{j}kA_\theta^{(1)}\left(1 + \frac{Z}{Z_\mathrm{C}}\right)\mathrm{e}^{\mathrm{j}kl_\mathrm{p}} + \frac{\mathrm{j}k}{2\ln\left(\frac{2h}{a}\right)}\frac{Z}{Z_\mathrm{C}}\hat{\boldsymbol{\mathcal{G}}}_0 I^{(0)}(-l_\mathrm{p}) - \frac{\hat{\boldsymbol{\mathcal{D}}}\hat{\boldsymbol{\mathcal{G}}}_0 I^{(0)}(-l_\mathrm{p})}{2\ln\left(\frac{2h}{a}\right)} \quad (4.107)$$

$$= -\mathrm{j}kA_\theta^{(1)}\left(1 + \frac{Z}{Z_\mathrm{C}}\right)\mathrm{e}^{\mathrm{j}kl_\mathrm{p}} + \frac{\mathrm{j}k}{2\ln\left(\frac{2h}{a}\right)}\frac{Z}{Z_\mathrm{C}}\hat{\boldsymbol{\mathcal{G}}}_0 I^{(0)}(-l_\mathrm{p}) - \frac{\hat{\boldsymbol{\mathcal{G}}}_0\hat{\boldsymbol{\mathcal{D}}}I^{(0)}(-l_\mathrm{p})}{2\ln\left(\frac{2h}{a}\right)} - \frac{g_0(0)I^{(0)}(-l_\mathrm{p})}{2\ln\left(\frac{2h}{a}\right)}\,. \quad (4.108)$$

The derivative and the operator $\hat{\boldsymbol{\mathcal{G}}}_0$ are interchanged as in Eq. (4.30). Rearranging the

terms yields

$$A_\theta^{(1)} = \frac{Z}{Z_\mathrm{C}+Z}\,\mathrm{e}^{-\mathrm{j}kl_\mathrm{p}}\left(\frac{1}{2\ln\left(\frac{2h}{a}\right)}\hat{\boldsymbol{\mathcal{G}}}_0 I^{(0)}(-l_\mathrm{p}) - I^{(0)}(-l_\mathrm{p})\right) - \frac{1}{\mathrm{j}k}\frac{Z_\mathrm{C}}{Z_\mathrm{C}+Z}\frac{\mathrm{e}^{-\mathrm{j}kl_\mathrm{p}}}{2\ln\left(\frac{2h}{a}\right)}\left(\hat{\boldsymbol{\mathcal{G}}}_0\hat{\boldsymbol{\mathcal{D}}} I^{(0)}(-l_\mathrm{p}) + g_0(0) I^{(0)}(-l_\mathrm{p})\right). \quad (4.109)$$

To get the coefficients $I_\infty^{(1)}$ and $\Psi^{(1)}$ the current in Eq. (4.104) is evaluated asymptotically for large l. Details are presented in App. B.4. It holds

$$\begin{aligned} I^{(1)}(l) \sim I_\infty^{(0)}&\left(1 - \frac{\tilde{g}_0(k_\theta)}{2\ln\left(\frac{2h}{a}\right)}\right)\mathrm{e}^{-\mathrm{j}k_\theta l} + \frac{Z\,\mathrm{e}^{-\mathrm{j}kl_\mathrm{p}}}{Z_\mathrm{C}+Z}\left(\frac{1}{2\ln\left(\frac{2h}{a}\right)}\hat{\boldsymbol{\mathcal{G}}}_0 I^{(0)}(-l_\mathrm{p}) - I^{(0)}(-l_\mathrm{p})\right)\mathrm{e}^{-\mathrm{j}kl} \\ &+ \frac{I^{(0)}(-l_\mathrm{p})}{4\mathrm{j}k\ln\left(\frac{2h}{a}\right)}\int_{-l_\mathrm{p}}^{\infty}\hat{\boldsymbol{\mathcal{D}}} P^{(0)}(l')g_0(l'+l_\mathrm{p})\,\mathrm{d}l'\Bigg]\mathrm{e}^{-\mathrm{j}kl} \\ &- \frac{1}{4\mathrm{j}k\ln\left(\frac{2h}{a}\right)}\int_{-l_\mathrm{p}}^{\infty}\int_{-l_\mathrm{p}}^{\infty}\Bigg\{\frac{\partial}{\partial l'}P^{(0)}(l')[g_\Phi(l',l'') - g_0(l'-l'')]\frac{\partial}{\partial l''}P^{(0)}(l'') \\ &\qquad - k^2 P^{(0)}(l')[g_\mathrm{A}(l',l'') - g_0(l'-l'')]P^{(0)}(l'')\Bigg\}\,\mathrm{d}l''\mathrm{d}l'\,\mathrm{e}^{-\mathrm{j}kl}. \end{aligned} \quad (4.110)$$

where $\tilde{g}_0$ denotes the Fourier transform of the kernel g_0 as in Eq. (2.59).

Comparing the asymptotic current to Eq. (4.82) yields

$$I_\infty^{(1)} = I_\infty^{(0)}\left(1 - \frac{\tilde{g}_0(k_\theta)}{2\ln\left(\frac{2h}{a}\right)}\right) \quad (4.111)$$

and

$$\begin{aligned} \Psi^{(1)} = \frac{Z\,\mathrm{e}^{-\mathrm{j}kl_\mathrm{p}}}{Z_\mathrm{C}+Z}&\left(\frac{\hat{\boldsymbol{\mathcal{G}}}_0 I^{(0)}(-l_\mathrm{p})}{2\ln\left(\frac{2h}{a}\right)} - I^{(0)}(-l_\mathrm{p})\right) + \frac{I^{(0)}(-l_\mathrm{p})}{4\mathrm{j}k\ln\left(\frac{2h}{a}\right)}\int_{-l_\mathrm{p}}^{\infty}\hat{\boldsymbol{\mathcal{D}}} P^{(0)}(l')g_0(l'+l_\mathrm{p})\,\mathrm{d}l' \\ &- \frac{1}{4\mathrm{j}k\ln\left(\frac{2h}{a}\right)}\int_{-l_\mathrm{p}}^{\infty}\int_{-l_\mathrm{p}}^{\infty}\Bigg\{\frac{\partial}{\partial l'}P^{(0)}(l')[g_\Phi(l',l'') - g_0(l'-l'')]\frac{\partial}{\partial l''}I^{(0)}(l'') \\ &\qquad - k^2 P^{(0)}(l')[g_\mathrm{A}(l',l'') - g_0(l'-l'')]I^{(0)}(l'')\Bigg\}\,\mathrm{d}l''\mathrm{d}l'. \end{aligned} \quad (4.112)$$

The integrals $\hat{\boldsymbol{\mathcal{G}}}_0 I^{(0)}(-l_\mathrm{p})$ and $\int_{-l_\mathrm{p}}^{\infty}\hat{\boldsymbol{\mathcal{D}}} P^{(0)}(l')g_0(l'+l_\mathrm{p})\,\mathrm{d}l'$ can be solved analytically using the identities in App. B.1. It holds

$$\begin{aligned} \frac{I^{(0)}(-l_\mathrm{p})}{4\mathrm{j}k\ln\left(\frac{2h}{a}\right)}\int_{-l_\mathrm{p}}^{\infty}\hat{\boldsymbol{\mathcal{D}}} P^{(0)}(l')g_0(l'+l_\mathrm{p})\,\mathrm{d}l' &= A_\theta^{(0)}\frac{Z_\mathrm{C}Z}{(Z_\mathrm{C}+Z)^2}\,\mathrm{e}^{-2\mathrm{j}kl_\mathrm{p}} \\ &+ A_\theta^{(0)}\frac{Z_\mathrm{C}^2}{(Z_\mathrm{C}+Z)^2}\frac{E_1(2\mathrm{j}kh) - E_1(\mathrm{j}ka) + \ln\left(\frac{2h}{a}\right)}{\ln\left(\frac{2h}{a}\right)}\,\mathrm{e}^{-2\mathrm{j}kl_\mathrm{p}} \\ &+ F_1(-l_\mathrm{p})\frac{1}{2}\left(\frac{Z_\mathrm{C}}{Z_\mathrm{C}+Z}\frac{E_1(2\mathrm{j}kh) - E_1(\mathrm{j}ka)}{\ln\left(\frac{2h}{a}\right)} + 1\right)\mathrm{e}^{-\mathrm{j}kl_\mathrm{p}} \end{aligned} \quad (4.113)$$

and

$$\begin{aligned}
\frac{Z\,\mathrm{e}^{-\mathrm{j}kl_\mathrm{p}}}{Z_\mathrm{C}+Z}\left(\frac{\hat{\boldsymbol{\mathcal{G}}}_0 I^{(0)}(-l_\mathrm{p})}{2\ln\left(\frac{2h}{a}\right)}-I^{(0)}(-l_\mathrm{p})\right) &= -A_\theta^{(0)}\frac{Z_\mathrm{C}Z}{(Z_\mathrm{C}+Z)^2}\,\mathrm{e}^{-2\mathrm{j}kl_\mathrm{p}} \\
&+ A_\theta^{(0)}\frac{Z^2}{(Z_\mathrm{C}+Z)^2}\frac{E_1(2\mathrm{j}kh)-E_1(\mathrm{j}ka)+\ln\left(\frac{2h}{a}\right)}{\ln\left(\frac{2h}{a}\right)}\,\mathrm{e}^{-2\mathrm{j}kl_\mathrm{p}} \\
&+ \left(A_\theta^{(0)}\Gamma^{(0)}-\Psi^{(0)}\right)\frac{Z}{Z_\mathrm{C}+Z}\frac{1}{2\ln\left(\frac{2h}{a}\right)}\Big[E_1(\mathrm{j}k(\sqrt{l_\mathrm{p}^2+4h^2}+l_\mathrm{p})) \\
&\qquad - E_1(\mathrm{j}k(\sqrt{l_\mathrm{p}^2+a^2}+l_\mathrm{p}))\Big] \\
&+ \frac{Z}{Z_\mathrm{C}+Z}\frac{1}{2\ln\left(\frac{2h}{a}\right)}\Bigg\{I_\infty^{(0)}\int_0^\infty g_0(l_\mathrm{p}+l')\,\mathrm{e}^{-\mathrm{j}k_\theta l'}\,\mathrm{d}l'\,\mathrm{e}^{-\mathrm{j}kl_\mathrm{p}} \\
&- A_\theta^{(0)}\left[E_1(\mathrm{j}k(\sqrt{l_\mathrm{p}^2+4h^2}-l_\mathrm{p}))-E_1(\mathrm{j}k(\sqrt{l_\mathrm{p}^2+a^2}-l_\mathrm{p}))+2\ln\left(\frac{2h}{a}\right)\right]\mathrm{e}^{-2\mathrm{j}kl_\mathrm{p}}\Bigg\} \\
&+ \frac{Z}{Z_\mathrm{C}+Z}\frac{1}{2\ln\left(\frac{2h}{a}\right)}\int_{-l_\mathrm{p}}^0 g_0(l_\mathrm{p}+l')F_1(l')\,\mathrm{d}l' - \frac{Z}{Z_\mathrm{C}+Z}F_1(-l_\mathrm{p})\,\mathrm{e}^{-\mathrm{j}kl_\mathrm{p}}\,, \qquad (4.114)
\end{aligned}$$

where the exponential integral E_1 is defined in Eq. (4.63).

Inserting the results into Eq. (4.112) finally yields

$$\begin{aligned}
\Psi^{(1)} &= A_\theta^{(0)}\frac{Z_\mathrm{C}^2+Z^2}{(Z_\mathrm{C}+Z)^2}\frac{E_1(2\mathrm{j}kh)-E_1(\mathrm{j}ka)+\ln\left(\frac{2h}{a}\right)}{\ln\left(\frac{2h}{a}\right)}\,\mathrm{e}^{-2\mathrm{j}kl_\mathrm{p}} \\
&+ \left(A_\theta^{(0)}\Gamma^{(0)}-\Psi^{(0)}\right)\frac{Z}{Z_\mathrm{C}+Z}\frac{1}{2\ln\left(\frac{2h}{a}\right)}\Big[E_1(\mathrm{j}k(\sqrt{l_\mathrm{p}^2+4h^2}+l_\mathrm{p})) \\
&\qquad - E_1(\mathrm{j}k(\sqrt{l_\mathrm{p}^2+a^2}+l_\mathrm{p}))\Big] \\
&+ \frac{Z}{Z_\mathrm{C}+Z}\frac{1}{2\ln\left(\frac{2h}{a}\right)}\Bigg\{I_\infty^{(0)}\int_0^\infty g_0(l_\mathrm{p}+l')\,\mathrm{e}^{-\mathrm{j}k_\theta l'}\,\mathrm{d}l'\,\mathrm{e}^{-\mathrm{j}kl_\mathrm{p}} \\
&- A_\theta^{(0)}\left[E_1(\mathrm{j}k(\sqrt{l_\mathrm{p}^2+4h^2}-l_\mathrm{p}))-E_1(\mathrm{j}k(\sqrt{l_\mathrm{p}^2+a^2}-l_\mathrm{p}))+2\ln\left(\frac{2h}{a}\right)\right]\mathrm{e}^{-2\mathrm{j}kl_\mathrm{p}}\Bigg\} \\
&+ \frac{Z}{Z_\mathrm{C}+Z}\frac{1}{2\ln\left(\frac{2h}{a}\right)}\int_{-l_\mathrm{p}}^0 g_0(l_\mathrm{p}+l')F_1(l')\,\mathrm{d}l' - \frac{Z}{Z_\mathrm{C}+Z}F_1(-l_\mathrm{p})\,\mathrm{e}^{-\mathrm{j}kl_\mathrm{p}} \\
&+ F_1(-l_\mathrm{p})\frac{1}{2}\left(\frac{Z_\mathrm{C}}{Z_\mathrm{C}+Z}\frac{E_1(2\mathrm{j}kh)-E_1(\mathrm{j}ka)}{\ln\left(\frac{2h}{a}\right)}+1\right)\mathrm{e}^{-\mathrm{j}kl_\mathrm{p}} \\
&- \frac{1}{4\mathrm{j}k\ln\left(\frac{2h}{a}\right)}\int_{-l_\mathrm{p}}^\infty\int_{-l_\mathrm{p}}^\infty\Bigg\{\frac{\partial}{\partial l'}P^{(0)}(l')[g_\Phi(l',l'')-g_0(l'-l'')]\frac{\partial}{\partial l''}I^{(0)}(l'') \\
&\qquad - k^2P^{(0)}(l')[g_\mathrm{A}(l',l'')-g_0(l'-l'')]I^{(0)}(l'')\Bigg\}\,\mathrm{d}l''\mathrm{d}l'\,. \qquad (4.115)
\end{aligned}$$

As for the first iteration reflection coefficient, the integrand in the double integral vanishes for a large part of the domain due to the regularization with g_0. Parts of the remaining double integral can be partially solved as in App. B.3 to speed up the numerical integration.

With Eq. (4.111) the approximation for the scattering coefficient (see Eq. (4.88)) simplifies to

$$\Upsilon \approx \frac{\Psi^{(0)}}{I_\infty^{(0)}} \frac{\tilde{g}_0(k_\theta)}{2\ln\left(\frac{2h}{a}\right)} + \frac{\Psi^{(1)}}{I_\infty^{(0)}} \,. \tag{4.116}$$

This analytic approximation is used for the following examples.

Examples

The scattering coefficient and the reflection coefficient are closely related. The difference is that the reflected TEM mode is excited by another TEM mode instead of the general plane wave. Furthermore, there is no field coupling at the port to obtain the reflected wave. Hence, the scattering coefficient should simplify to the reflection coefficient if $\theta = 180°$ and if $E_\mathrm{p}(l) = 0$. From these two assumptions follows

$$k_\theta = -k \tag{4.117}$$
$$F_1(l) = 0 \tag{4.118}$$
$$A^{(0)} = I_\infty^{(0)} \tag{4.119}$$
$$\Psi^{(0)} = \Gamma^{(0)} I_\infty^{(0)} \tag{4.120}$$
$$I^{(0)}(l) = I_\infty^{(0)} P^{(0)}(l) \tag{4.121}$$

for $-l_\mathrm{p} < l < \infty$. From this follows

$$\begin{aligned}\Psi^{(1)} = I_\infty^{(0)} \frac{Z_\mathrm{C}^2 + Z^2}{(Z_\mathrm{C} + Z)^2} \frac{E_1(2\mathrm{j}kh) - E_1(\mathrm{j}ka) + \ln\left(\frac{2h}{a}\right)}{\ln\left(\frac{2h}{a}\right)} \mathrm{e}^{-2\mathrm{j}kl_\mathrm{p}} \\ - \frac{I_\infty^{(0)}}{4\mathrm{j}k\ln\left(\frac{2h}{a}\right)} \int_{-l_\mathrm{p}}^{\infty} \int_{-l_\mathrm{p}}^{\infty} \Big\{ \frac{\partial}{\partial l'} P^{(0)}(l') [g_\Phi(l', l'') - g_0(l' - l'')] \frac{\partial}{\partial l''} P^{(0)}(l'') \\ - k^2 P^{(0)}(l') [g_\mathrm{A}(l', l'') - g_0(l' - l'')] P^{(0)}(l'') \Big\} \,\mathrm{d}l''\mathrm{d}l' \end{aligned} \tag{4.122}$$
$$= \Gamma^{(1)} I_\infty^{(0)} \tag{4.123}$$

and

$$\tilde{g}_0(k_\theta = -k) = 2\ln\left(\frac{2h}{a}\right) . \tag{4.124}$$

Finally, it holds

$$\left[\frac{\Psi^{(0)}}{I_\infty^{(0)}} \frac{\tilde{g}_0(k_\theta)}{2\ln\left(\frac{2h}{a}\right)} + \frac{\Psi^{(1)}}{I_\infty^{(0)}}\right]_{\theta=180°, E_\mathrm{p}=0} = \Gamma^{(0)} + \Gamma^{(1)} \,. \tag{4.125}$$

This confirms the connection between the scattering and reflection coefficient approximation.

Next, three numerical examples that show the accuracy of the analytic approximation of the scattering coefficient are presented. The zeroth and first iteration scattering coefficient are compared to a numerical solution obtained with the algorithm from Sec. 3.5. The

same dimensions as for the reflection coefficient examples are used in the following, i.e. $a = 0.5\,\mathrm{mm}$ and $h = 100\,\mathrm{mm}$.

First, the wire is left open. It holds $l_\mathrm{p} = 0$ and $Z = \infty$. Hence, it follows

$$\Upsilon^{(0)} = -1 \tag{4.126}$$

$$\Upsilon^{(1)} = \frac{E_1(2\mathrm{j}kh) - E_1(\mathrm{j}ka)}{2\ln\left(\frac{2h}{a}\right)} + \frac{1}{2\ln\left(\frac{2h}{a}\right)} \int_0^\infty g_0(l')\,\mathrm{e}^{-\mathrm{j}k_\theta l'}\,\mathrm{d}l' \tag{4.127}$$

and

$$\Upsilon \approx \frac{E_1(2\mathrm{j}kh) - E_1(\mathrm{j}ka)}{2\ln\left(\frac{2h}{a}\right)} + \frac{1}{2\ln\left(\frac{2h}{a}\right)} \int_0^\infty g_0(l')\,\mathrm{e}^{-\mathrm{j}k_\theta l'}\,\mathrm{d}l' - \frac{\tilde{g}_0(k_\theta)}{2\ln\left(\frac{2h}{a}\right)}\,. \tag{4.128}$$

This coincides with the solution in [13]. Figure 4.5 shows the comparison of the analytic approximation with a numerical one. Here $\theta = 80°$ is chosen for the exciting plane wave. The two solutions are practically indistinguishable. Moreover, the zeroth iteration solution is illustrated. It coincides with the other solutions only for small frequencies. However, the zeroth iteration is already quite accurate.

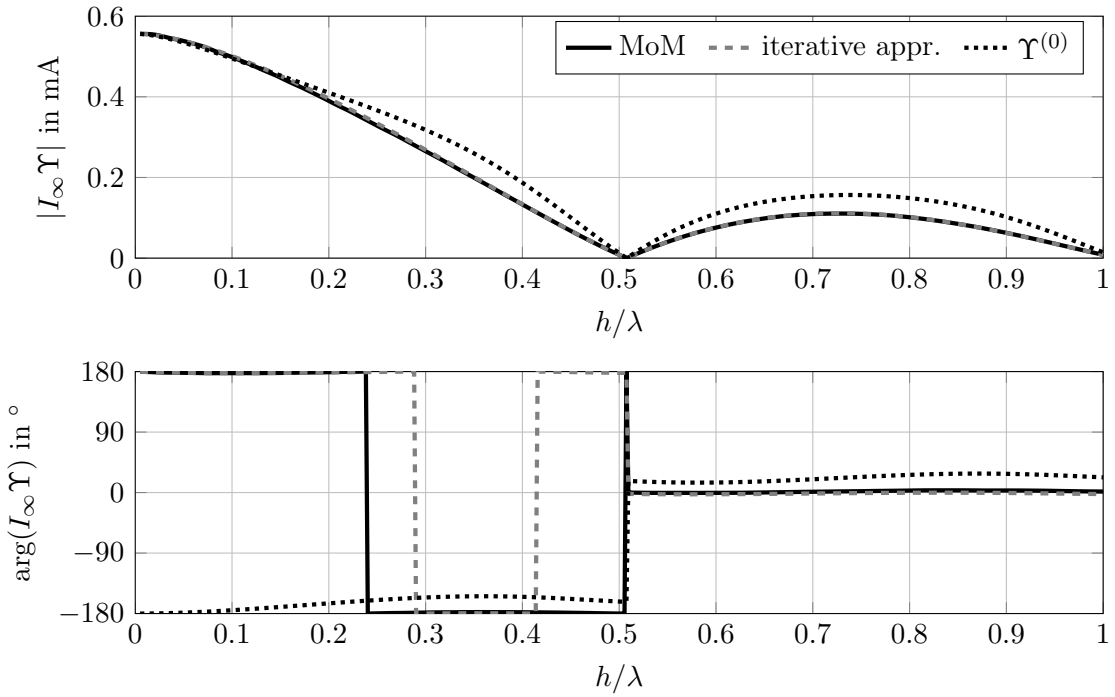

Figure 4.5: Normalized complex scattering coefficient for the open-circuited port with $\theta = 80°$.

For the **second example** a port with a ramp as for the reflection coefficient is considered (see Fig. 4.2). The angle α is 40°. The angle of incidence is $\theta = 50°$. Figure 4.6 shows the results. The accuracy of the first oder approximation is again excellent. The zeroth order approximation is again already quite accurate.

For the **last example** the port with a vertical riser and a lumped load is considered. The load is $Z = 10Z_\mathrm{C}$. The plane wave has an angle of incidence with $\theta = 50°$. The comparison of the analytic and numerical results is shown in Fig. 4.7. Similar findings as for the other examples can be seen here as well.

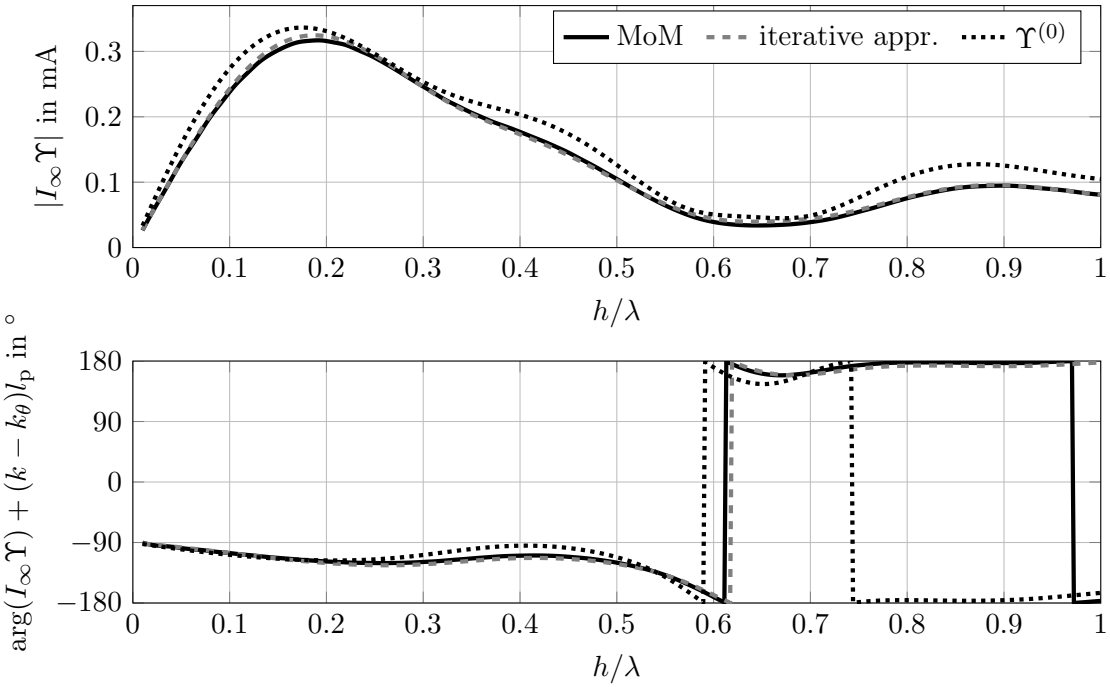

Figure 4.6: Normalized complex scattering coefficient for the port with a ramp and a short-circuit with $\theta = 50°$.

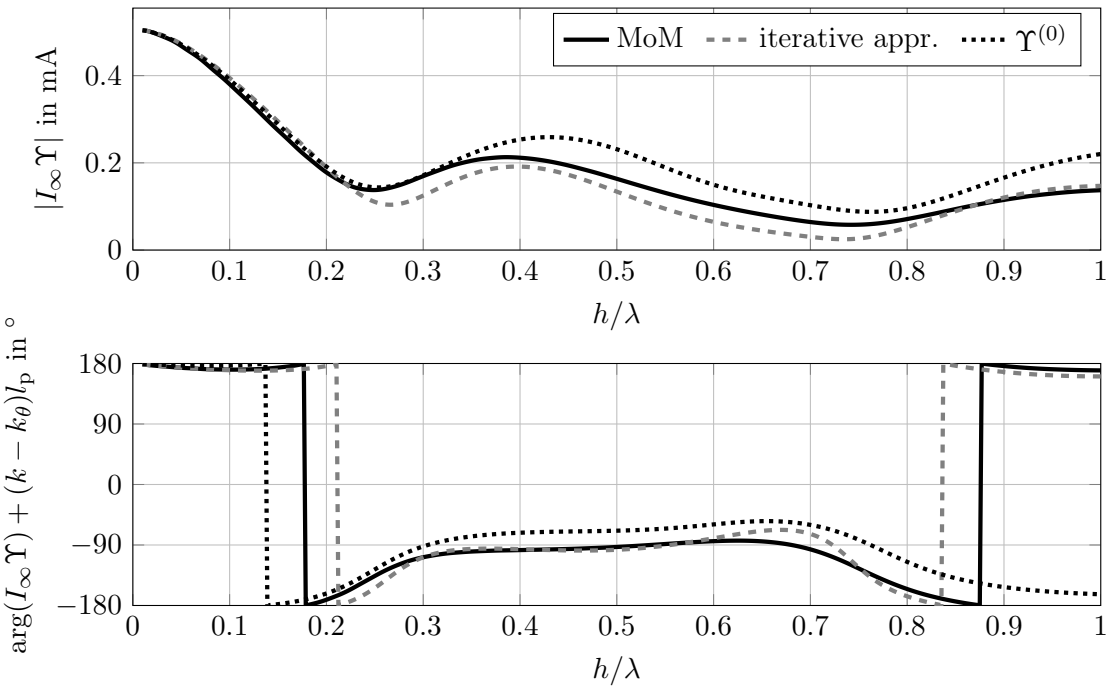

Figure 4.7: Normalized complex scattering coefficient for the port with a riser and $Z = 10Z_\mathrm{C}$ with $\theta = 50°$.

4.3 Validation of the analytic current approximation

After showing examples for the isolated scattering and reflection coefficients the complete current shall be analyzed for an example wire. The wire trajectory is shown in Fig. 4.8. The wire dimensions are

Wire radius	a	0.5 mm
Height above the ground	h	100 mm
Wire length	$\mathcal{L}$	1000 mm
Ramp angle	α	40°.

The loads at the ports are $Z_1 = 0.1Z_\mathrm{C}$ and $Z_2 = 10Z_\mathrm{C}$. The plane wave has an angle of incidence of $\theta = 50°$ and an amplitude of $E_0 = 1\,\mathrm{V\,m^{-1}}$.

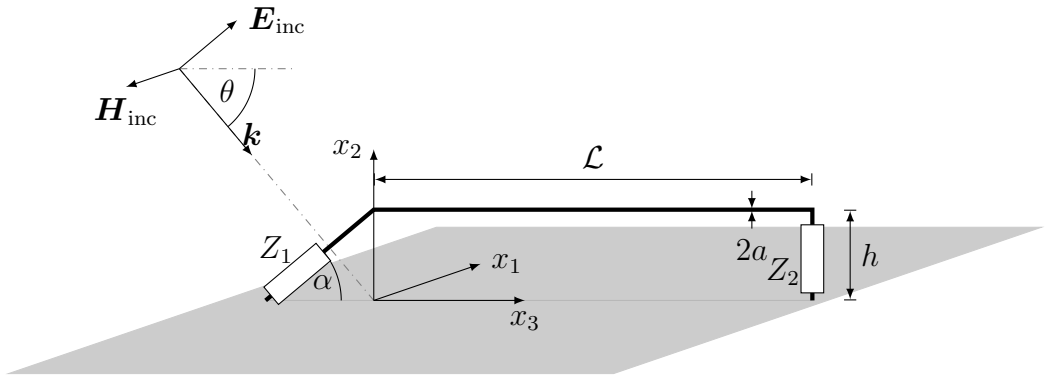

Figure 4.8: Finite wire with a ramp and a riser excited by a plane wave.

The analytic current is compared to a numerical reference in Fig. 4.9. The current is evaluated in the middle of the wire, i.e. at $x_3 = \mathcal{L}/2$. The analytic solution uses the asymptotic approach Eq. (3.33). The coefficients are determined using the first order iterative method as described above.

It can be seen that the analytic approximation coincides with the numerical reference in Fig. 4.9. The resonances of the analytic solution have the correct location and even the correct height and width. Figure 4.10 shows the current approximation with the classical coefficients $\Upsilon^{(0)}$ and $\Gamma^{(0)}$. The resonances are found at the correct location but have an incorrect height. This is due to the absence of radiation effects at the ports in the classical transmission line theory. The first iteration, however, approximates these effects and corrects the current amplitude in the right way.

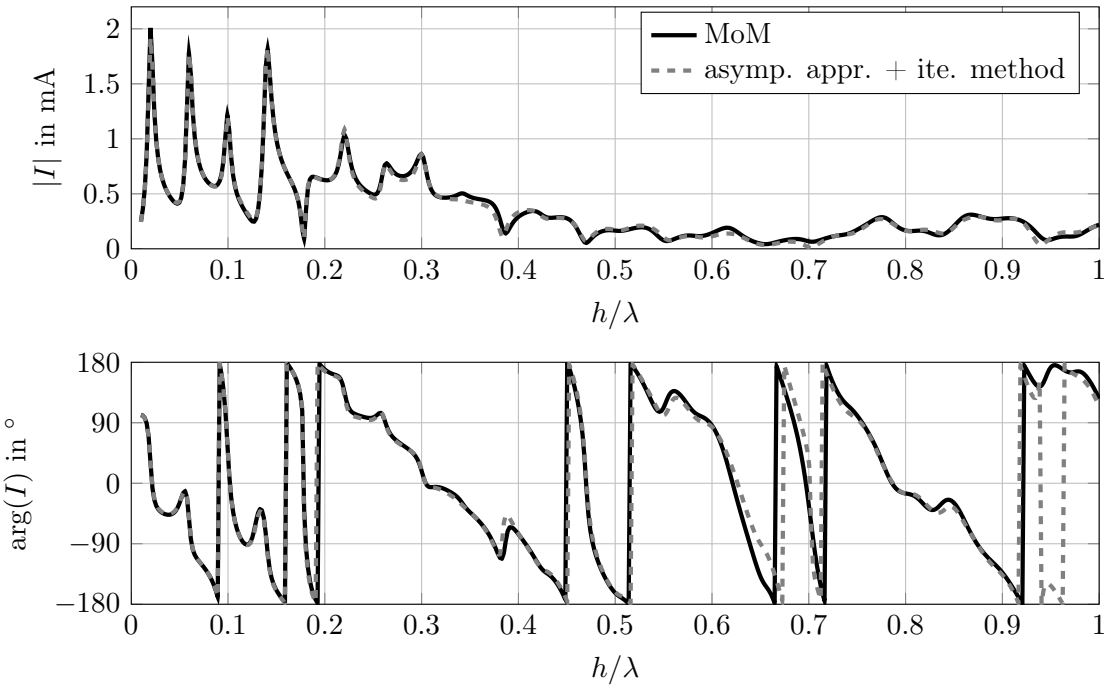

Figure 4.9: Complex current in the center of the wire obtained by using the asymptotic approach and the iterative method.

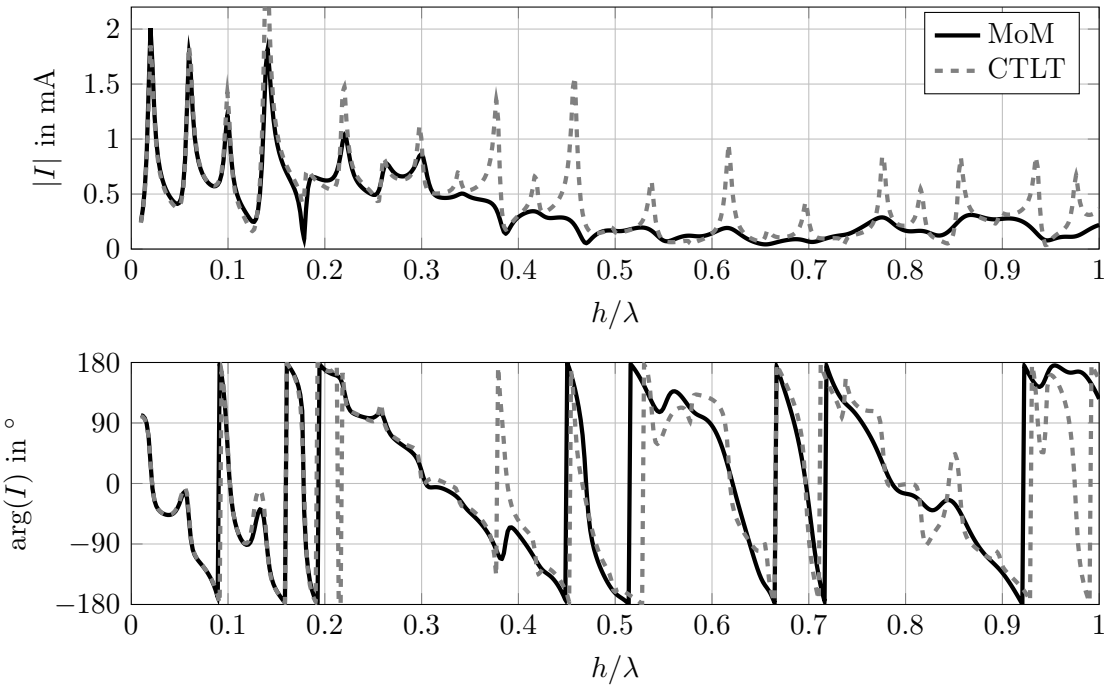

Figure 4.10: Complex current in the center of the wire obtained with the classical transmission line theory.

4.4 Extension to multiconductor transmission lines

The iterative method can be generalized for multiconductor transmission lines as explained in the following. First, a solution for two wires above a ground is presented. After that a general solution for the reflection coefficient matrix for many wires is shown.

4.4.1 Reflection coefficient matrix for two wires

Let there be two parallel semi-infinite wires with a similar trajectory above a ground as shown in Fig. 4.11. The corresponding multicoductor MPIE are

$$\frac{\partial}{\partial l}\underline{\boldsymbol{\Phi}}(l) + \mathrm{j}k\frac{Z_0}{4\pi}\int_{-l_\mathrm{p}}^{\infty} \underline{\underline{\boldsymbol{g}}}_\mathrm{A}(l,l')\underline{\boldsymbol{I}}(l')\,\mathrm{d}l' = 0 \tag{4.129}$$

$$\int_{-l_\mathrm{p}}^{\infty} \underline{\underline{\boldsymbol{g}}}_\Phi(l,l')\frac{\partial}{\partial l'}\underline{\boldsymbol{I}}(l')\,\mathrm{d}l' + \mathrm{j}k\frac{4\pi}{Z_0}\,\underline{\boldsymbol{\Phi}}(l) = 0\,. \tag{4.130}$$

where the vector $\underline{\boldsymbol{I}}$ contains the current on each wire and $\underline{\boldsymbol{\Phi}}$ describes the scalar potential on each wire.

The components of the kernel matrices are

$$g_{\Phi,mn}(l,l') = \frac{\exp(-\mathrm{j}k\sqrt{\|\boldsymbol{x}_{\mathrm{c},m}(l)-\boldsymbol{x}_{\mathrm{c},n}(l')\|^2+a^2})}{\sqrt{\|\boldsymbol{x}_{\mathrm{c},m}(l)-\boldsymbol{x}_{\mathrm{c},n}(l')\|^2+a^2}} - \frac{\exp(-\mathrm{j}k\sqrt{\|\boldsymbol{x}_{\mathrm{c},m}(l)-\breve{\boldsymbol{x}}_{\mathrm{c},n}(l')\|^2+a^2})}{\sqrt{\|\boldsymbol{x}_{\mathrm{c},m}(l)-\breve{\boldsymbol{x}}_{\mathrm{c},n}(l')\|^2+a^2}} \tag{4.131}$$

$$g_{\mathrm{A},mn}(l,l') = \frac{\exp(-\mathrm{j}k\sqrt{\|\boldsymbol{x}_{\mathrm{c},m}(l)-\boldsymbol{x}_{\mathrm{c},n}(l')\|^2+a^2})}{\sqrt{\|\boldsymbol{x}_{\mathrm{c},m}(l)-\boldsymbol{x}_{\mathrm{c},n}(l')\|^2+a^2}}\hat{\boldsymbol{\tau}}_m(l)\cdot\hat{\boldsymbol{\tau}}_n(l') - \frac{\exp(-\mathrm{j}k\sqrt{\|\boldsymbol{x}_{\mathrm{c},m}(l)-\breve{\boldsymbol{x}}_{\mathrm{c},n}(l')\|^2+a^2})}{\sqrt{\|\boldsymbol{x}_{\mathrm{c},m}(l)-\breve{\boldsymbol{x}}_{\mathrm{c},n}(l')\|^2+a^2}}\hat{\boldsymbol{\tau}}_m(l)\cdot\breve{\hat{\boldsymbol{\tau}}}_n(l') \tag{4.132}$$

where $\boldsymbol{x}_{\mathrm{c},n}$ denotes the trajectory of wire n and $\hat{\boldsymbol{\tau}}_n$ is the tangential unitvector respectively. The mirrored vectors are marked with $\breve{}$. A formal derivation can be found in [60].

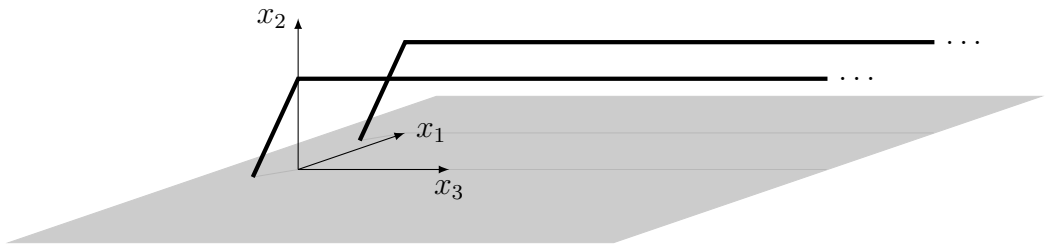

Figure 4.11: Semi-infinite multiconductor transmission line above a ground.

The kernel matrices in Eqs. (4.129) and (4.130) can be diagonalized. Then two decoupled sets of MPIE appear: one for the common mode current and one for the differential mode current. For the common mode current two currents of equal value with

equal direction flow on both wires. For the differential mode the two currents on the wires are equal in value but are different in the sign.

The two current modes can then be treated like the current for the single wire above a ground. However, the kernels for the modes are

$$g_{\mathrm{A},\pm}(l,l') = g_{\mathrm{A},11}(l,l') \pm g_{\mathrm{A},12}(l,l') \tag{4.133}$$

$$g_{\Phi,\pm}(l,l') = g_{\Phi,11}(l,l') \pm g_{\Phi,12}(l,l')\,. \tag{4.134}$$

The plus stands for the common mode and the minus for the differential mode. The iterative solution for arbitrary ports can then be derived as described above for the single wire case. For the special case of two open circuited wires above the ground it follows

$$\Gamma_{\pm}^{(0)} = -1 \tag{4.135}$$

$$\Gamma_{\pm}^{(1)} = \frac{E_1(2\mathrm{j}kh) - E_1(\mathrm{j}ka) \pm \left(E_1(\mathrm{j}k\sqrt{d^2+4h^2}) - E_1(\mathrm{j}kd)\right)}{\ln\left(\frac{2h}{a}\right) \pm \frac{1}{2}\ln\left(1+\frac{4h^2}{d^2}\right)}\,, \tag{4.136}$$

where the horizontal distance between the two wires is denoted with d.

The common mode and differential mode reflection coefficient are the same for the zeroth iteration. But they are different from each other starting with the first iteration. As shown in [61] the iterative solution coincides very well with a numerical reference. Unfortunately, the differential mode reflection coefficient for the open circuit case is slightly larger than 1 for small frequencies. This is not a physical solution. This small problem only appears if no ohmic losses or losses in the loads are present, i.e. for the open circuit and the short circuit cases. A general solution for this problem is up to this point not known. However, to reduce the problem the second order iteration can be found for the open circuit case. After a lengthy but straight forward derivation it holds

$$\begin{aligned}
\Gamma_{\pm}^{(2)} = {} & \frac{1}{2}\Gamma_{\pm}^{(1)}(3-\Gamma_{\pm}^{(1)}) - \frac{1}{\left[2\ln\left(\frac{2h}{a}\right) \pm \ln\left(1+\frac{4h^2}{d^2}\right)\right]^2} \int_0^{\infty} g_{0,\pm}(l') \Bigg\{ \\
& \left[E_1\left(\mathrm{j}k\left(\sqrt{l'^2+4h^2}+l'\right)\right) - E_1\left(\mathrm{j}k\left(\sqrt{l'^2+a^2}+l'\right)\right) + 2\ln\left(\frac{2h}{a}\right)\right] \mathrm{e}^{\mathrm{j}kl'} \\
& + \left[E_1\left(\mathrm{j}k\left(\sqrt{l'^2+4h^2}-l'\right)\right) - E_1\left(\mathrm{j}k\left(\sqrt{l'^2+a^2}-l'\right)\right)\right] \mathrm{e}^{-\mathrm{j}kl'} \\
& \pm \Bigg\{ \left[E_1\left(\mathrm{j}k\left(\sqrt{l'^2+d^2+4h^2}+l'\right)\right) - E_1\left(\mathrm{j}k\left(\sqrt{l'^2+d^2}+l'\right)\right) + \ln\left(1+\frac{4h^2}{d^2}\right)\right] \mathrm{e}^{\mathrm{j}kl'} \\
& \qquad + \left[E_1\left(\mathrm{j}k\left(\sqrt{l'^2+d^2+4h^2}-l'\right)\right) - E_1\left(\mathrm{j}k\left(\sqrt{l'^2+d^2}-l'\right)\right)\right] \mathrm{e}^{-\mathrm{j}kl'} \Bigg\} \Bigg\}
\end{aligned} \tag{4.137}$$

where

$$\begin{aligned}
g_{0,\pm}(l) = {} & \frac{\exp(-\mathrm{j}k\sqrt{l^2+a^2})}{\sqrt{l^2+a^2}} - \frac{\exp(-\mathrm{j}k\sqrt{l^2+4h^2})}{\sqrt{l^2+4h^2}} \\
& \pm \frac{\exp(-\mathrm{j}k\sqrt{l^2+d^2})}{\sqrt{l^2+d^2}} - \frac{\exp(-\mathrm{j}k\sqrt{l^2+d^2+4h^2})}{\sqrt{l^2+d^2+4h^2}}\,.
\end{aligned} \tag{4.138}$$

The second order iteration reduces the problem but for some small frequencies the nonphysical solution persists. This effect is also seen in the last example of Ch. 5.

4.4.2 Reflection coefficient matrix for multiple wires

The iterative method is extended for many multiconductor transmission lines in [61]. The solution is restricted to parallel wires that have the same trajectory but shifted in x_1 direction as depicted in Fig. 4.11. The solution procedure is the same as for the single wire but with matrices. Details can be found in [61]. It holds for the zeroth order reflection coefficient matrix, i.e. the classical solution,

$$\underline{\underline{\boldsymbol{\Gamma}}}^{(0)} = \left(\underline{\underline{\boldsymbol{Z}}}_{\mathrm{C}} - \underline{\underline{\boldsymbol{Z}}}\right)^{-1}\left(\underline{\underline{\boldsymbol{Z}}}_{\mathrm{C}} + \underline{\underline{\boldsymbol{Z}}}\right)\mathrm{e}^{-2\mathrm{j}kl_{\mathrm{p}}} \tag{4.139}$$

with

$$\underline{\underline{\boldsymbol{Z}}}_{\mathrm{C}} = \frac{Z_0}{2\pi}\,\underline{\underline{\boldsymbol{\Lambda}}} \tag{4.140}$$

and

$$\Lambda_{mn} = \frac{1}{2}\ln\left(1 + \frac{4h^2}{d_{mn}^2}\right). \tag{4.141}$$

The distance in the x_1 direction between wire m and wire n is denoted with d_{mn} with the special case $d_{mm} = a$. The matrix $\underline{\underline{\boldsymbol{Z}}}$ is a diagonal matrix with the loads of each port on the diagonal.

The first order reflection coefficient matrix is

$$\begin{aligned}\Gamma^{(1)} = {} & \frac{1}{2}\left(\underline{\underline{\boldsymbol{\Lambda}}}^{-1}\underline{\underline{\boldsymbol{E}}} + \underline{\underline{\boldsymbol{\Gamma}}}^{(0)}\underline{\underline{\boldsymbol{\Lambda}}}^{-1}\underline{\underline{\boldsymbol{E}}}\,\underline{\underline{\boldsymbol{\Gamma}}}^{(0)}\right) \\ & - \frac{1}{4\mathrm{j}k}\int_{-l_{\mathrm{p}}}^{\infty}\int_{-l_{\mathrm{p}}}^{\infty}\Bigg\{\frac{\partial}{\partial l'}\underline{\underline{\boldsymbol{P}}}^{(0)}(l')\underline{\underline{\boldsymbol{\Lambda}}}^{-1}\Big[\underline{\underline{\boldsymbol{g}}}_{\Phi}(l', l'') - \underline{\underline{\boldsymbol{g}}}_0(l' - l'')\Big]\frac{\partial}{\partial l''}\underline{\underline{\boldsymbol{P}}}^{(0)}(l'') \\ & \qquad - k^2\underline{\underline{\boldsymbol{P}}}^{(0)}(l')\underline{\underline{\boldsymbol{\Lambda}}}^{-1}\Big[\underline{\underline{\boldsymbol{g}}}_{\mathrm{A}}(l', l'') - \underline{\underline{\boldsymbol{g}}}_0(l' - l'')\Big]\underline{\underline{\boldsymbol{P}}}^{(0)}(l'')\Bigg\}\,\mathrm{d}l''\mathrm{d}l'\end{aligned} \tag{4.142}$$

with

$$\underline{\underline{\boldsymbol{P}}}^{(0)}(l) = \underline{\underline{\mathbf{1}}}\,\mathrm{e}^{\mathrm{j}kl} + \underline{\underline{\boldsymbol{\Gamma}}}^{(0)}\mathrm{e}^{-\mathrm{j}kl} \tag{4.143}$$

$$E_{mn} = E_1\left(\mathrm{j}k\sqrt{d_{mn}^2 + 4h^2}\right) - E_1(\mathrm{j}kd_{mn}) + \Lambda_{mn} \tag{4.144}$$

$$g_{0,mn}(l) = \frac{\exp(-\mathrm{j}k\sqrt{l^2 + d_{mn}^2})}{\sqrt{l^2 + d_{mn}^2}} - \frac{\exp(-\mathrm{j}k\sqrt{l^2 + d_{mn}^2 + 4h^2})}{\sqrt{l^2 + d_{mn}^2 + 4h^2}}\,. \tag{4.145}$$

The reflection coefficient matrix is approximated as

$$\underline{\underline{\boldsymbol{\Gamma}}} \approx \underline{\underline{\boldsymbol{\Gamma}}}^{(0)} + \underline{\underline{\boldsymbol{\Gamma}}}^{(1)}\,. \tag{4.146}$$

If only one wire is present the matrix solution reduces to the scalar single wire solution.

An approximation for the scattering coefficient matrix is not yet found. However, it should be possible to use the solution procedure for the single wire case for the multiconductor case as well.

4.5 Convergence and comparison to the induced EMF method

The iterative method is an accurate extension to the classical transmission line solution as shown by the above examples. The questions that naturally arise are:

1. Does the iteration converge to the exact solution?
2. Is the iterative method a unique procedure or is it related to other known methods?

The first question is partially answered in [26]. There, the iterative method is applied for the infinite wire and indeed the iteration converges to the exact analytic solution. For the semi-infinite case there is no general study on the convergence yet. However, the higher order approximations get more and more complicated, i.e. more unsolvable integrals appear. This makes the extension of the iterative method to the second or third order not practical. Hence, at this point the examples from above shall suffice to illustrate the superior accuracy of the iterative method compared to the classical transmission line theory.

The second question is analyzed in [62] in great detail. There it is shown that the induced EMF method results in the exact same analytic approximation for the reflection coefficient as the first order iterative method. The induced EMF method is usually only applied for finite wires in free space [63]–[66]. However, as shown in the following the method can be applied to the semi-infinite wire above a ground as well.

The input impedance of a wire antenna is approximated using the induced EMF method. Let there be two EM fields $(\boldsymbol{E}_1, \boldsymbol{H}_1)$ and $(\boldsymbol{E}_2, \boldsymbol{H}_2)$ that are connected via Maxwell's equations with the current densities $\boldsymbol{J}_1$ and $\boldsymbol{J}_2$ respectively. Then the Lorentz reciprocity theorem [18] holds for any volume $\mathcal{V}$, i.e.

$$\int_{\partial\mathcal{V}} (\boldsymbol{E}_1 \times \boldsymbol{H}_2 - \boldsymbol{E}_2 \times \boldsymbol{H}_1) \cdot \hat{\boldsymbol{n}} \, \mathrm{d}\mathcal{S} = \int_{\mathcal{V}} \boldsymbol{E}_2 \cdot \boldsymbol{J}_1 - \boldsymbol{E}_1 \cdot \boldsymbol{J}_2 \, \mathrm{d}\boldsymbol{x} \tag{4.147}$$

where $\hat{\boldsymbol{n}}$ is the normal unit vector on $\partial\mathcal{V}$, the surface of $\mathcal{V}$. Equation (4.147) can be applied for the problem of the semi-infinite wire above a ground that is excited by a lumped voltage source as shown in Fig. 4.12. The volume $\mathcal{V}$ is a half sphere that is bounded by the ground plane. If the sphere is infinitely large, all radiated EM fields on the surface are plane waves. Furthermore, the guided waves near the surface of the half sphere are TEM modes since they are far away from any sources. For these fields holds

$$\boldsymbol{H}_1 = \frac{\hat{\boldsymbol{n}} \times \boldsymbol{E}_1}{Z_0} \tag{4.148}$$

$$\boldsymbol{H}_2 = \frac{\hat{\boldsymbol{n}} \times \boldsymbol{E}_2}{Z_0} \tag{4.149}$$

on $\partial\mathcal{V}$. Moreover, on the ground plane surface holds

$$\boldsymbol{n} \times \boldsymbol{E}_1 = 0 = \boldsymbol{n} \times \boldsymbol{E}_2 \,. \tag{4.150}$$

The surface integral in Eq. (4.147) vanishes with these conditions and it holds

$$\int_{\mathcal{V}} \boldsymbol{E}_2 \cdot \boldsymbol{J}_1 \, \mathrm{d}\boldsymbol{x} = \int_{\mathcal{V}} \boldsymbol{E}_1 \cdot \boldsymbol{J}_2 \, \mathrm{d}\boldsymbol{x} \,. \tag{4.151}$$

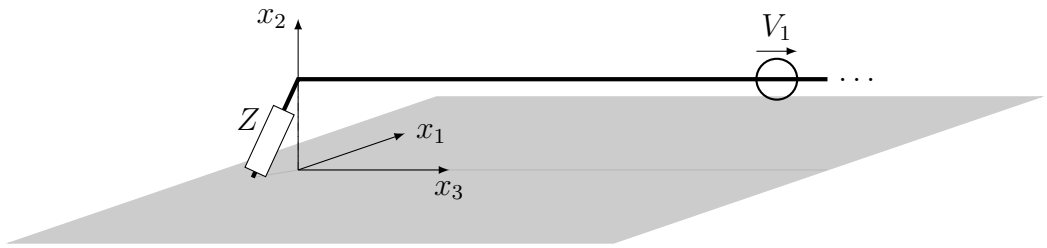

Figure 4.12: Semi-infinite wire with a lumped voltage source.

The current densities or electric fields in Eq. (4.151) can be chosen arbitrarily as long as they satisfy Maxwell's equations. For the semi-infinite wire in Fig. 4.12 with the voltage source the first electric field and the corresponding current density on the thin wire with radius a are

$$\boldsymbol{E}_1(l, a, \phi) = V_1 \delta(l - l_1) \hat{\boldsymbol{\tau}}(l_1) \tag{4.152}$$

$$\boldsymbol{J}_1(l, r, \phi) = I_1(l) \hat{\boldsymbol{\tau}}(l) \frac{\delta(r - a)}{2\pi a}\,, \tag{4.153}$$

where the voltage source is located at $l = l_1$. A second EM field is obtained by assuming a current along the wire that emits an electric field. It holds

$$\boldsymbol{J}_2(l, r, \phi) = I_2(l) \hat{\boldsymbol{\tau}}(l) \frac{\delta(r - a)}{2\pi a} \tag{4.154}$$

$$\hat{\boldsymbol{\tau}}(l) \cdot \boldsymbol{E}_2(l, a, \phi) = -E_{\tan}^{(I_2)}(l)\,. \tag{4.155}$$

Inserting the two EM fields and current densities into Eq. (4.151) results in

$$V_1 I_2(l_1) = -\int_{-l_\mathrm{p}}^{\infty} E_{\tan}^{(I_2)}(l') I_1(l')\,\mathrm{d}l' \tag{4.156}$$

The goal of the induced EMF method is to find a useful equation for the input impedance Z_in at the location of the lumped voltage source. In general it holds

$$Z_\mathrm{in} = \frac{V_1}{I_1(l_1)}\,. \tag{4.157}$$

Inserting Eq. (4.157) into the definition of the input impedance results in

$$Z_\mathrm{in} = -\frac{1}{I_1(l_1) I_2(l_1)} \int_{-l_\mathrm{p}}^{\infty} E_{\tan}^{(I_2)}(l') I_1(l')\,\mathrm{d}l'\,. \tag{4.158}$$

The current I_2 can be chosen arbitrarily. There are two convenient possibilities, i.e. $I_2 = I_1$ and $I_2 = I_1^*$ where * denotes the complex conjugate. With these currents holds

$$Z_\mathrm{in} = -\frac{1}{[I_1(l_1)]^2} \int_{-l_\mathrm{p}}^{\infty} E_{\tan}^{(I_1)}(l') I_1(l')\,\mathrm{d}l' \tag{4.159}$$

and

$$Z_{\text{in}} = -\frac{1}{|I_1(l_1)|^2} \int_{-l_\text{p}}^{\infty} E_{\tan}^{(I_1^*)}(l') I_1(l') \, \mathrm{d}l' \tag{4.160}$$

respectively.

After showing that the method of induced EMF is applicable for the semi-infinite wire the input impedance of the lumped voltage must be linked to the reflection coefficient at the port. If the voltage source in Fig. 4.12 is placed far away from the port, it 'sees' an infinite wire and a reflected TEM mode coming from the port. It holds for large l, due to the linearity of the problem,

$$I_1(l) = V_1 Y_\infty (l - l_1) + \Gamma \frac{V_1}{2Z_\text{C}} \, \mathrm{e}^{-\mathrm{j}kl_1} \mathrm{e}^{-\mathrm{j}kl} \tag{4.161}$$

With the admittance function for the infinite wire (see Eq. (3.6)). Inserting the current into Eq. (4.157) (with $l = l_1$) results in

$$Z_{\text{in}}^{-1} = Y_\infty(0) + \Gamma \frac{1}{2Z_\text{C}} \mathrm{e}^{-2\mathrm{j}kl_1} \, . \tag{4.162}$$

Rearranging the terms yields

$$\Gamma = 2Z_\text{C} [Z_{\text{in}}^{-1} - Y_\infty(0)] \, \mathrm{e}^{2\mathrm{j}kl_1} \, . \tag{4.163}$$

The classical transmission line current, i.e.

$$I_1(l) = \frac{V_1}{2Z_\text{C}} \left(\mathrm{e}^{-\mathrm{j}k|l-l_1|} + \Gamma^{(0)} \, \mathrm{e}^{-\mathrm{j}k(l+l_1)} \right) , \tag{4.164}$$

is used as a current to approximate the input impedance with Eq. (4.159). The emitted tangential electric field on the wire surface $E_{\tan}^{(I_1)}$ can be determined with an equation similar to Eq. (2.47). However, the load at the port Z has to be taken into account as well. It holds

$$\begin{aligned} E_{\tan}^{(I_1)}(l) = {} & -Z I_1(-l_\text{p}) \delta(l + l_\text{p}) \\ & + \frac{Z_0}{4\pi \mathrm{j}k} \left(\frac{\partial}{\partial l} \int_{-l_\text{p}}^{\infty} g_\Phi(l, l') \frac{\partial}{\partial l'} I_1(l') \, \mathrm{d}l' + k^2 \int_{-l_\text{p}}^{\infty} g_\text{A}(l, l') I_1(l') \, \mathrm{d}l' \right) . \end{aligned} \tag{4.165}$$

The integrals can be regularized as shown in detail in [62]. Inserting the results into Eq. (4.159) yields after some straight forward mathematical manipulations

$$Z_{\text{in}}^{-1} \approx \frac{1}{2Z_\text{C}} \frac{\left(1 + \Gamma^{(0)} \, \mathrm{e}^{-2\mathrm{j}kl_1}\right)^2}{1 + (\Gamma^{(0)} - \Gamma^{(1)}) \, \mathrm{e}^{-2\mathrm{j}kl_1}} \, . \tag{4.166}$$

The latter result only holds if l_1 tends to infinity, i.e. if the source is placed very far away from the port. Applying polynomial division on the last fraction results in

$$Z_{\text{in}}^{-1} \approx \frac{1}{2Z_\text{C}} \left(1 + \Gamma^{(0)} \, \mathrm{e}^{-2\mathrm{j}kl_1} + \Gamma^{(1)} \, \mathrm{e}^{-2\mathrm{j}kl_1} + \frac{\left(\Gamma^{(1)} \, \mathrm{e}^{-2\mathrm{j}kl_1}\right)^2}{1 + (\Gamma^{(0)} - \Gamma^{(1)}) \, \mathrm{e}^{-2\mathrm{j}kl_1}} \right) . \tag{4.167}$$

The input impedance can be inserted into Eq. (4.163) to yield

$$\Gamma \approx \Gamma^{(0)} + \Gamma^{(1)} + \left(1 - \frac{1}{2Z_\mathrm{C} Y_\infty(0)}\right) \mathrm{e}^{2\mathrm{j}kl_1} + \frac{[\Gamma^{(1)}]^2 \, \mathrm{e}^{-2\mathrm{j}kl_1}}{1 + (\Gamma^{(0)} - \Gamma^{(1)}) \, \mathrm{e}^{-2\mathrm{j}kl_1}} \,. \tag{4.168}$$

Since the classical transmission line solution is used for the current, the admittance Y_∞ should be approximated in a similar way. It holds

$$Y_\infty(0) \approx Y_\mathrm{TEM}(0) = \frac{1}{2Z_\mathrm{C}} \,. \tag{4.169}$$

and it follows

$$\Gamma \approx \Gamma^{(0)} + \Gamma^{(1)} + \frac{[\Gamma^{(1)}]^2 \, \mathrm{e}^{-2\mathrm{j}kl_1}}{1 + (\Gamma^{(0)} - \Gamma^{(1)}) \, \mathrm{e}^{-2\mathrm{j}kl_1}} \,. \tag{4.170}$$

The reflection coefficient should be independent of the location of the source l_1. Unfortunately, the solution in Eq. (4.170) depends on l_1 and the limit $l_1 \to \infty$ is not unique. In [62] small losses in form of a complex propagation constant γ are introduced to deal with the problem. The substitution $\mathrm{j}k \to \gamma$ is performed with $\Re(\gamma) > 0$. No matter how small the real part of γ is chosen the last addend in Eq. (4.170) vanishes for $l_1 \to \infty$. It results

$$\Gamma \approx \Gamma^{(0)} + \Gamma^{(1)} \,. \tag{4.171}$$

This concludes the analyses. The first order iterative method and the method of induced EMF result in the same approximation for the reflection coefficient. However, the iterative method is a more systematic approach and could be extended to higher orders. A few tricks have to be applied for the induced EMF method to work.

4.6 Summary

The iterative method to approximate the scattering and reflection coefficients is presented in this chapter. The considered ports have an arbitrary wire trajectory and can be terminated by a lumped impedance. The iterative approximation is initialized by the classical transmission line solution. The derivation of the governing equations for each iteration is based on the general MPIE for thin wires. The examples show that the first iteration is sufficient to gain a significant improvement to the classical approximation. The improved approximation considers high frequency effects and is, therefore, frequency dependent and incorporates the wire trajectory.

Moreover, the single wire reflection coefficient approximation is extended to multiple wires above a ground plane. The solution is restricted to wires with a similar trajectory, i.e. the wires are parallel and have the same port shape. However, if there are no ohmic losses present, the iterative solution for multiple wires yields nonphysical results. The absolute value of the reflection coefficient becomes slightly larger than one. But the error is marginal and vanishes as soon as a lumped load is present at the port. This inaccuracy needs to be investigated further.

Lastly, it is shown that the well known induced EMF method can be used to yield the exact same approximation for the reflection coefficient as the iterative method. This is an interesting result since it shows that the iterative method is not completely unique. However, some assumptions and tricks need to be applied to the induced EMF method to get a reasonable result. The iterative method is more systematic in its derivation.

The convergence of the iterative method for the single wire reflection coefficient cannot be proven up to this point. This should be part of future research.

Chapter 5

Experimental validation of the analytic and numerical approximations

The natural frequencies are used here as a parameter to validate the analytic and numerical models that are described in the above sections by measurements. The measurement setup is described and a complex radar cross section is introduced. The calibration procedure of the measurement setup and the data processing are described in detail. Lastly, the natural frequencies for finite wires above a ground plane are extracted from the measured complex radar cross section and are compared to the analytic and numerical approximations.

5.1 A complex radar cross section

It is difficult to measure the current along a thin wire without influencing the measurement result. Therefore, a different physical quantity needs to be measured to validate the theoretical models. The current radiates an EM field. This EM field is composed of the same natural frequencies as the current in the asymptotic region (see Sec. 2.6 and [37]). Hence, the natural frequencies that are contained in the far field of the wire are determined and compared to the theoretical results to validate the theory. This is achieved by measuring a complex mono-static radar cross section as explained in the following.

Let there be a reflective object that is excited by a plane wave. The classical radar cross section σ_0 (see [65], [66]) is then defined as

$$\sigma_0 = \lim_{R\to\infty} 4\pi R^2 \, \frac{\boldsymbol{E}_{\mathrm{rad}}(R) \cdot \boldsymbol{E}^*_{\mathrm{rad}}(R)}{\boldsymbol{E}_{\mathrm{inc}} \cdot \boldsymbol{E}^*_{\mathrm{inc}}} \,, \tag{5.1}$$

where $\boldsymbol{E}_{\mathrm{rad}}$ is the radiated electric field at a distance R from the object and $\boldsymbol{E}_{\mathrm{inc}}$ denotes the electric field of the incident plane wave. The limit ensures that only far fields are considered. The star * denotes the complex conjugate. Hence, σ_0 is a real and positive number.

The concept of the classical radar cross section is generalized in [67], [68] to a complex radar cross section σ. It holds

$$\sigma = \lim_{R\to\infty} 4\pi R^2 \, \mathrm{e}^{2\mathrm{j}kR} \, \frac{\boldsymbol{E}_{\mathrm{rad}}(R) \cdot \boldsymbol{E}_{\mathrm{rad}}(R)}{\boldsymbol{E}_{\mathrm{inc}} \cdot \boldsymbol{E}^*_{\mathrm{inc}}} \,. \tag{5.2}$$

The scalar product in the numerator does not involve the complex conjugate field anymore. Hence, a complex radar cross section arises that characterizes the object. Additionally,

the phase has to be normalized as well to get rid of the R-dependence of the radiated field. The classical radar cross section can be obtained from the complex one as

$$\sigma_0 = |\sigma| \,. \tag{5.3}$$

In general the radar cross section depends on the direction of the incident plane wave and the direction in which the radiated field is measured. Furthermore, the polarization of the excitation and response need to be taken into account. However, the natural frequencies are constant properties of the object that are independent of the excitation and polarization [37]. Hence, in the following only a single polarization and a mono-static setup are considered. Mono-static setup means that the radiated field is evaluated in the direction of the incident wave. The polarization and angle of incidents are chosen in such way that as many natural frequencies as possible are excited. A more general treatment can be found in [69], [70].

Since the radiated field is squared to obtain σ, the natural frequencies appear in the second order. Hence, the square root has to be taken to get the original first order natural frequencies, i.e.

$$\sqrt{\sigma} = \lim_{R\to\infty} \sqrt{4\pi} R \, \mathrm{e}^{\mathrm{j}kR} \, \frac{\sqrt{\boldsymbol{E}_{\mathrm{rad}}(R) \cdot \boldsymbol{E}_{\mathrm{rad}}(R)}}{\sqrt{\boldsymbol{E}_{\mathrm{inc}} \cdot \boldsymbol{E}^*_{\mathrm{inc}}}} \tag{5.4}$$

is considered from now on.

The vector fitting algorithm from Sec. 2.6 can be used to extract the natural frequencies from $\sqrt{\sigma}$. Next the measurement setup and calibration procedure are described.

5.2 Measurement setup and calibration procedure

The following measurement setup and calibration procedure was developed in collaboration with Max Rosenthal (see [68]).

A vector network analyzer (VNA) is used to measure the complex radar cross section. Figure 5.1 shows the complete setup. The VNA is connected via a coaxial cable with a horn antenna. The antenna points in the direction of the target. The measurement is conducted in an absorber-lined semi-anechoic chamber to reduce reflections from the walls or the floor. The s_{11}-parameter is measured. A photo of the setup is shown in Fig. 5.2. The target is placed on a Rohacell table. The material has similar EM properties as air and should not significantly interact with the target. The distance between the antenna and the target is approximately 2 m.

The system needs to be calibrated to minimize systematic errors. A schematic error model is shown in Fig. 5.3. The cable and VNA circuitry form one unit in the error model, the antenna an additional one. The VNA measures the outgoing and incoming power waves $a'_{1,\mathrm{m}}$ and $b'_{1,\mathrm{m}}$ and determines the input reflection coefficient

$$s'_{11,\mathrm{m}} = \frac{b'_{1,\mathrm{m}}}{a'_{1,\mathrm{m}}} \,. \tag{5.5}$$

However, the desired result is the input reflection coefficient at the target, i.e. s_{11} with

$$s_{11} = \frac{b_1}{a_1} = \frac{\sqrt{\boldsymbol{E}_{\mathrm{rad}}(R) \cdot \boldsymbol{E}_{\mathrm{rad}}(R)}}{\sqrt{\boldsymbol{E}_{\mathrm{inc}} \cdot \boldsymbol{E}^*_{\mathrm{inc}}}} \,. \tag{5.6}$$

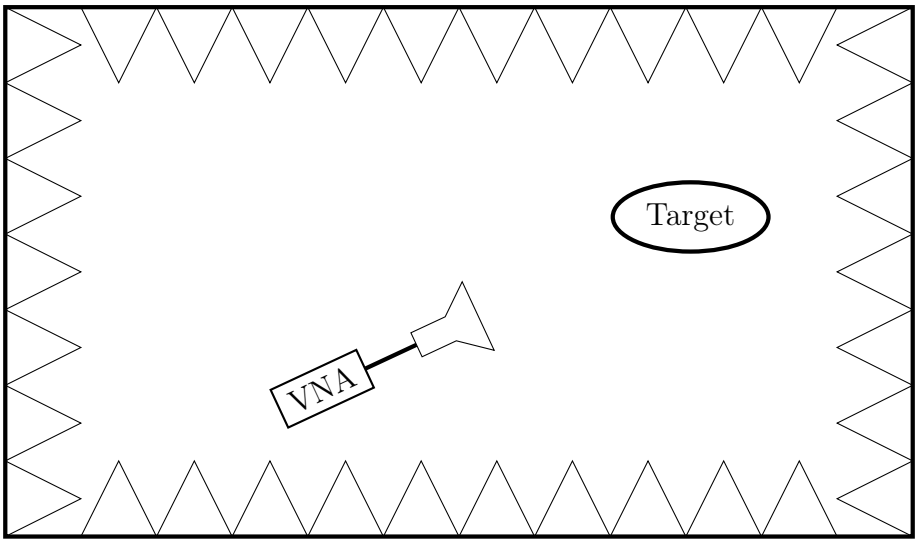

Figure 5.1: Mono-static setup to measure the complex radar cross section inside an absorber-lined semi-anechoic chamber (top view).

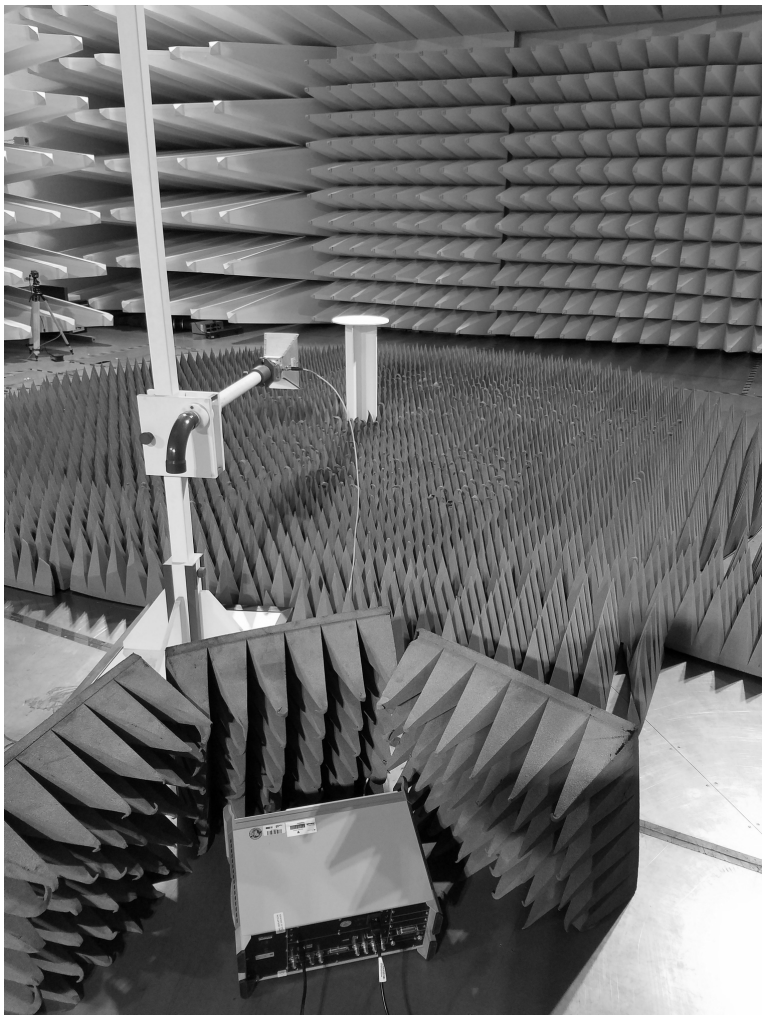

Figure 5.2: Photo of the measurement setup with a Rohacell table for the target.

The cable and VNA can be calibrated using the standard procedure with an open,

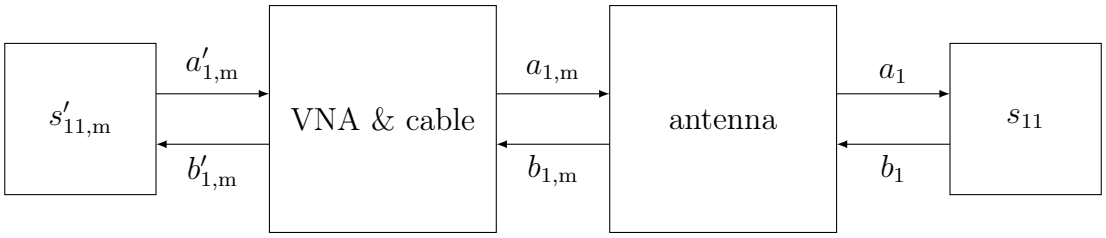

Figure 5.3: Error model for the mono-static setup.

matched, and short circuited port. The VNA comes with a corresponding calibration kit and automatically determines the error coefficients for the VNA and cable. As a result the VNA automatically converts $s'_{11,\mathrm{m}}$ to the input reflection coefficient at the antenna port, i.e.

$$s_{11,\mathrm{m}} = \frac{b_{1,\mathrm{m}}}{a_{1,\mathrm{m}}} \,. \tag{5.7}$$

Next, the antenna needs to be calibrated to convert $s_{11,\mathrm{m}}$ to the desired s_{11} at the target. The antenna can be treated as a two port that transforms the input voltage to a far field and vice versa. Hence, it can be described with a scattering matrix $\underline{\underline{\boldsymbol{S}}}_{\mathrm{antenna}}$ with

$$\underline{\underline{\boldsymbol{S}}}_{\mathrm{antenna}} = \begin{pmatrix} e_{11} & e_{12} \\ e_{21} & e_{22} \end{pmatrix} \,. \tag{5.8}$$

The error terms e_{mn} have the following physical interpretation:

1. e_{11} describes the input reflection coefficient of the antenna. It depends on the measurement environment and the mismatch between the cable and the antenna.

2. e_{12} characterizes the transformation of an electric field at the location of the antenna opening to a voltage at the antenna connector, i.e. b_1 is transformed to $b_{1,\mathrm{m}}$ if the antenna was matched with the cable . It includes all antenna characteristics, e.g. the directivity.

3. e_{21} is some kind of inverse of e_{12}. It transforms the voltage at the antenna port to a far field at the location of the target. Hence, it depends on the distance R between the target and the antenna, i.e.

   $$e_{21} = e_{21}(R) \propto R^{-1} \exp(-\mathrm{j}kR) \,. \tag{5.9}$$

   Furthermore, it includes all antenna characteristics as well.

4. e_{22} is the output reflection coefficient. It is assumed that the antenna does not reflect a significant EM field in the direction of the target. Hence, it holds

   $$e_{22} = 0 \,. \tag{5.10}$$

In summary it follows

$$\begin{pmatrix} b_{1,\mathrm{m}} \\ a_1 \end{pmatrix} = \begin{pmatrix} e_{11} & e_{12} \\ e_{21}(R) & 0 \end{pmatrix} \begin{pmatrix} a_{1,\mathrm{m}} \\ b_1 \end{pmatrix} \,, \tag{5.11}$$

where R is the shortest distance from the antenna opening to the target. Expanding the first row from Eq. (5.11) results in

$$b_{1,\mathrm{m}} = e_{11}a_{1,\mathrm{m}} + e_{12}b_1 \tag{5.12}$$
$$= e_{11}a_{1,\mathrm{m}} + e_{12}s_{11}a_1\,. \tag{5.13}$$

Inserting the second row from Eq. (5.11) into the latter equation finally yields

$$s_{11,\mathrm{m}} = e_{11} + s_{11}e_{12}e_{21}(R) \tag{5.14}$$

and

$$s_{11} = \frac{s_{11,\mathrm{m}} - e_{11}}{e_{12}e_{21}(R)}\,. \tag{5.15}$$

Two calibration measurements are needed to determine e_{11} and the R-dependent product $e_{12}e_{21}(R)$. After that Eq. (5.15) is used to determine the sought s_{11}-parameter from the measured $s_{11,\mathrm{m}}$. To determine e_{11} no target is placed in front of the antenna. Then the expected s_{11}^{empty} is zero. It follows from Eq. (5.14)

$$s_{11,\mathrm{m}}^{\mathrm{empty}} = e_{11}\,. \tag{5.16}$$

This measurement has to be done before or right after the measurement with a target to account for any small changes in the environment.

To determine the product $e_{12}e_{21}(R)$ two identical antennas are placed in front of each other as shown in Fig. 5.4. Both antennas are connected with the VNA and the s_{21}-parameter is measured. The distance between the two antenna openings is denoted with R_{cal}. The corresponding error model is shown in Fig. 5.5. The two coaxial cables and the VNA-ports are again calibrated using the standard method (open, match, short, and thru) such that the VNA automatically converts $s'_{21,\mathrm{m}}$ to

$$s_{21,\mathrm{m}} = \frac{b_{2,\mathrm{m}}}{a_{1,\mathrm{m}}}\,. \tag{5.17}$$

The two antennas have the same two port scattering matrix $\underline{\underline{\boldsymbol{S}}}_{\mathrm{antenna}}$ as in Eqs. (5.8) and (5.11) since they are identical. With this it holds

$$a_1 = a_{1,\mathrm{m}}e_{21}(R_{\mathrm{cal}}) \tag{5.18}$$
$$b_{2,\mathrm{m}} = a_1 e_{12} \tag{5.19}$$

and finally

$$s_{21,\mathrm{m}}(R_{\mathrm{cal}}) = e_{12}e_{21}(R_{\mathrm{cal}})\,. \tag{5.20}$$

Hence, the two antenna calibration method is used to determine the product $e_{12}e_{21}(R_{\mathrm{cal}})$. However, the product depends on the distance R_{cal}. A range independent parameter $s_{21,\mathrm{m}}^{\mathrm{cal}}$ is obtained by normalizing the parameter with R_{cal} (see Eq. (5.9)). It holds

$$s_{21,\mathrm{m}}^{\mathrm{cal}} = s_{21,\mathrm{m}}(R_{\mathrm{cal}})\sqrt{4\pi}R_{\mathrm{cal}}\,\mathrm{e}^{\mathrm{j}kR_{\mathrm{cal}}} \tag{5.21}$$
$$= e_{12}e_{21}(R_{\mathrm{cal}})\sqrt{4\pi}R_{\mathrm{cal}}\,\mathrm{e}^{\mathrm{j}kR_{\mathrm{cal}}}\,. \tag{5.22}$$

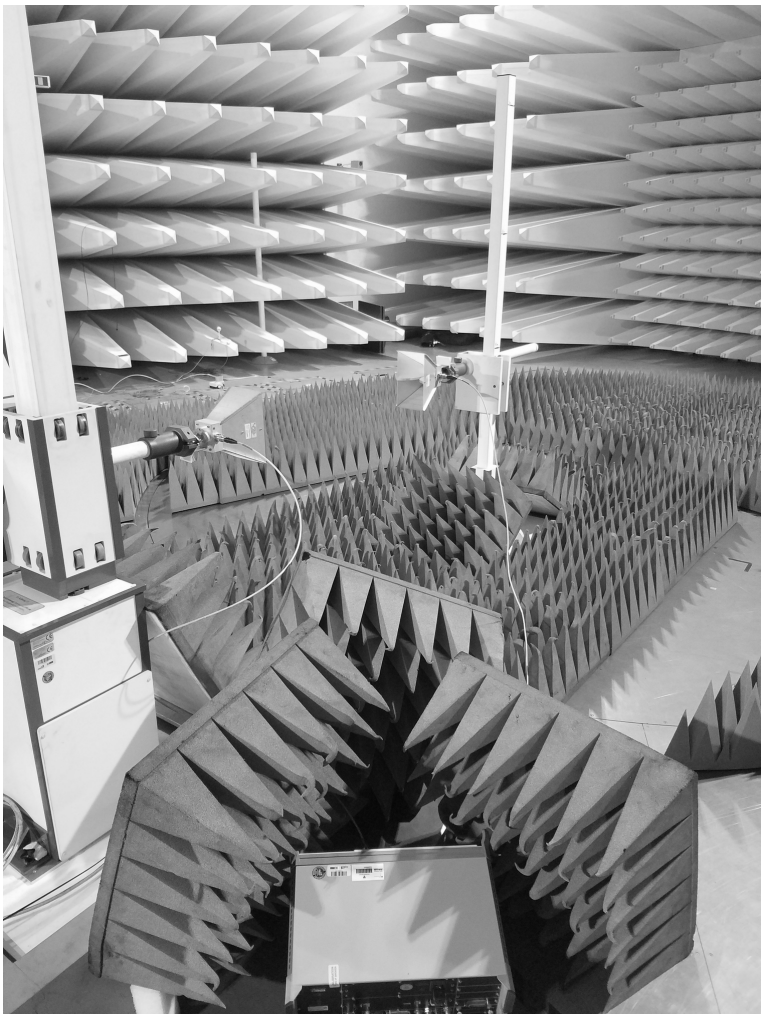

Figure 5.4: Photo of the two antenna calibration setup.

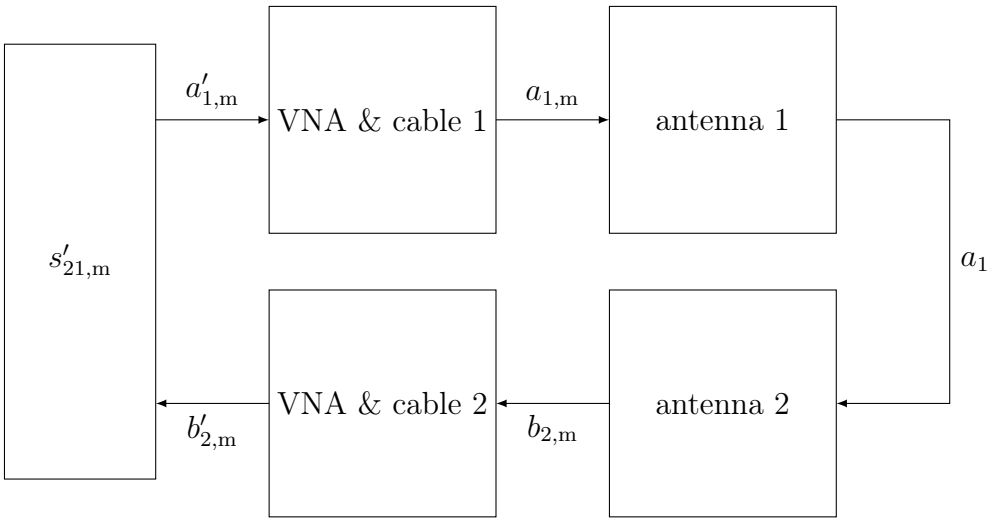

Figure 5.5: Error model for the two antenna calibration setup.

This calibration step has to be done only once since it can be assumed that the antenna properties do not change over time.

The calibration measurements Eqs. (5.16) and (5.22) are inserted into Eq. (5.15). It

holds

$$s_{11} = \frac{s_{11,\mathrm{m}} - s_{11,\mathrm{m}}^{\mathrm{empty}}}{s_{21,\mathrm{m}}^{\mathrm{cal}}} \sqrt{4\pi} R \, \mathrm{e}^{\mathrm{j}kR} \,, \tag{5.23}$$

where the product $e_{12}e_{21}(R)$ is normalized in the same manner as in Eq. (5.22) to eliminate the R-dependency.

Inserting Eqs. (5.6) and (5.23) into Eq. (5.4) finally results in

$$\sqrt{\sigma} \approx \frac{s_{11,\mathrm{m}} - s_{11,\mathrm{m}}^{\mathrm{empty}}}{s_{21,\mathrm{m}}^{\mathrm{cal}}} \, 4\pi R^2 \, \mathrm{e}^{2\mathrm{j}kR} \,. \tag{5.24}$$

The latter equation is only an approximation since a finite R is chosen.

Summary of the measurement procedure

The square root of the complex mono-static radar cross section can be measured as follows:

1. Two antenna measurement to determine $s_{21,\mathrm{m}}^{\mathrm{cal}}$ (normalized)
   - 1.1. Two port calibration of the cables and VNA (open, match, short, thru)
   - 1.2. Measure $s_{21,\mathrm{m}}$ and normalize with R_{cal}
2. Single antenna measurement to determine $s_{11,\mathrm{m}}^{\mathrm{empty}}$ and $s_{11,\mathrm{m}}$
   - 2.1. One port calibration of the cable and VNA (open, match, short)
   - 2.2. Measure $s_{11,\mathrm{m}}^{\mathrm{empty}}$ without the target
   - 2.3. Place the target on the table at a distance R without changing the environment to measure $s_{11,\mathrm{m}}$
3. Insert the three measurement results into Eq. (5.24) to obtain $\sqrt{\sigma}$

5.3 Validation of the measurement procedure and time gating

In the following the described measurement procedure is tested with a metallic sphere as a target. The measured complex radar cross section is compared to the exact analytic solution. Time gating, a method to remove targets in the background, is described and applied to eliminate additional random errors. But first an antenna calibration example is presented.

5.3.1 Antenna calibration example

Two Rhode & Schwartz HF906 horn antennas are placed in front of each other as shown in Fig. 5.4 . The distance between the two antennas is about 2 m or 3 m. The two measurements are normalized and compared in Fig. 5.6 to show that the resulting $s_{21,\mathrm{m}}^{\mathrm{cal}}$ is independent of R_{cal}. The antenna does not radiate at lower frequencies. Hence, the frequency range is 700 MHz to 8 GHz. The step size is 10 MHz and the used bandwidth is 100 Hz.

The normalized results are very similar and the R-dependence of e_{21} (see Eq. (5.9)) can be confirmed. There is a difference between the two measurements in the interval 1 GHz to 2 GHz. This is most likely, due to a slightly different antenna alignment between the two setups. In the following the 2 m calibration is used since the antenna placement is the easiest at this distance.

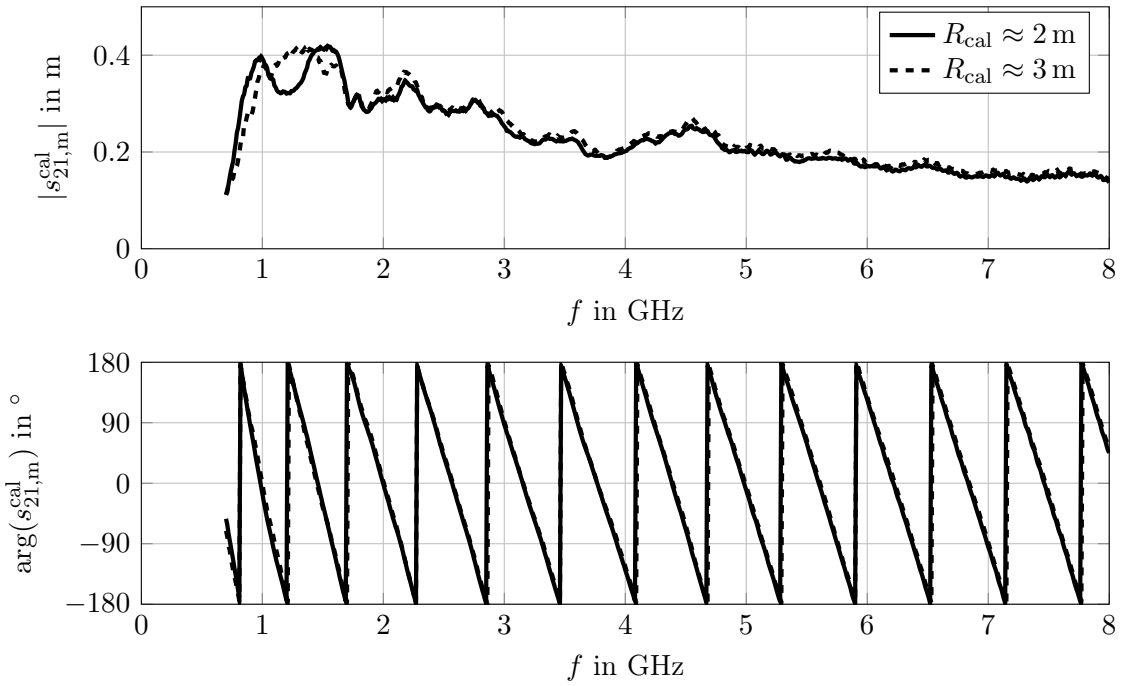

Figure 5.6: Normalized two antenna calibration measurement results for two different distances.

Two alternative calibration methods are discussed in [68]. A ground plane or a metallic sphere can be used to determine $e_{12}e_{21}(R)$. The ground plane acts as a mirror but is difficult to position since the antenna has to point exactly perpendicularly onto the plane. For the sphere there is an exact analytic reference that can be used for the calibration procedure. Details are found in [68].

5.3.2 Complex radar cross section of a metallic sphere

There is an exact analytic solution for the complex radar cross section of the metallic sphere in free space [41], [71]. Hence, a metallic sphere is used to validate the measurement procedure.

A steel sphere is placed on the table in Fig. 5.2 at about 2 m distance from the antenna. The sphere diameter is 0.2 m. Its conductivity is assumed to be perfect (infinite). The calibrated measurement result and the analytic reference are depicted in Fig. 5.7. The measured data is in the same order of magnitude as the analytic reference. The approximate shape is similar as well. However, there seems to be a random disturbance.

One way to deal with the additional noise is to use the time gating technique. The measured frequency signal, i.e.

$$\hat{s}_{11,\text{m}} = s_{11,\text{m}} - s^{\text{empty}}_{11,\text{m}}\,, \tag{5.25}$$

is transformed in the time domain using the inverse fast Fourier transform (iFFT) algorithm. The reflected signal is clearly visible in Fig. 5.8 between 13 ns and 20 ns. This corresponds

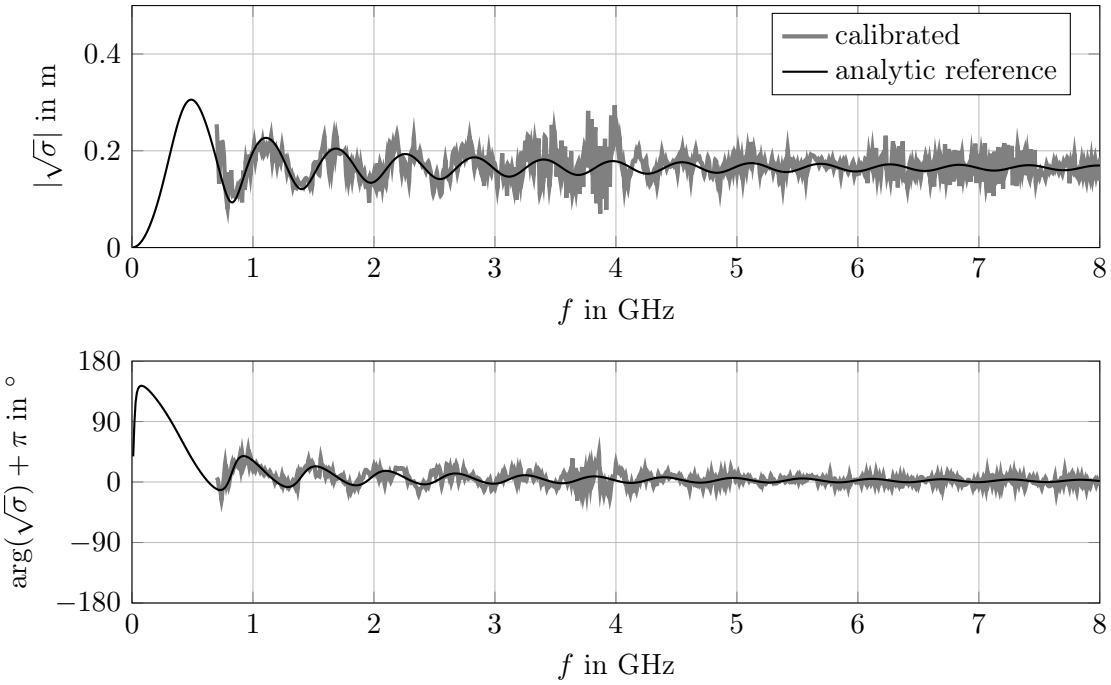

Figure 5.7: Calibrated measurement results of the metallic sphere compared to an analytic reference.

to the time that the light needs to travel from the antenna to the object and back to the antenna (13 ns correspond to about 4 m). Furthermore, there are disturbances that should not be there. They are so called ghost objects that should be eliminated. This is done by applying a window function. For simplicity a rectangular window is used here. But other windows are possible.

The time gated signal is shown in Fig. 5.8 as well. The adjusted time signal is then transformed to the frequency domain using the FFT. The result is shown in Fig. 5.9. The calibrated and time gated measurement is much smoother and coincides very well with the analytic response. The described time gating technique is used for all following measurements.

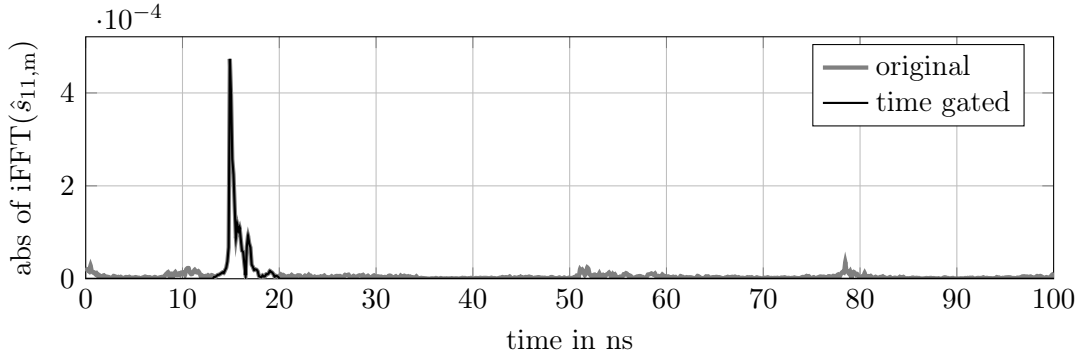

Figure 5.8: Inverse Fourier transform (absolute value) of the measured response of the metallic sphere.

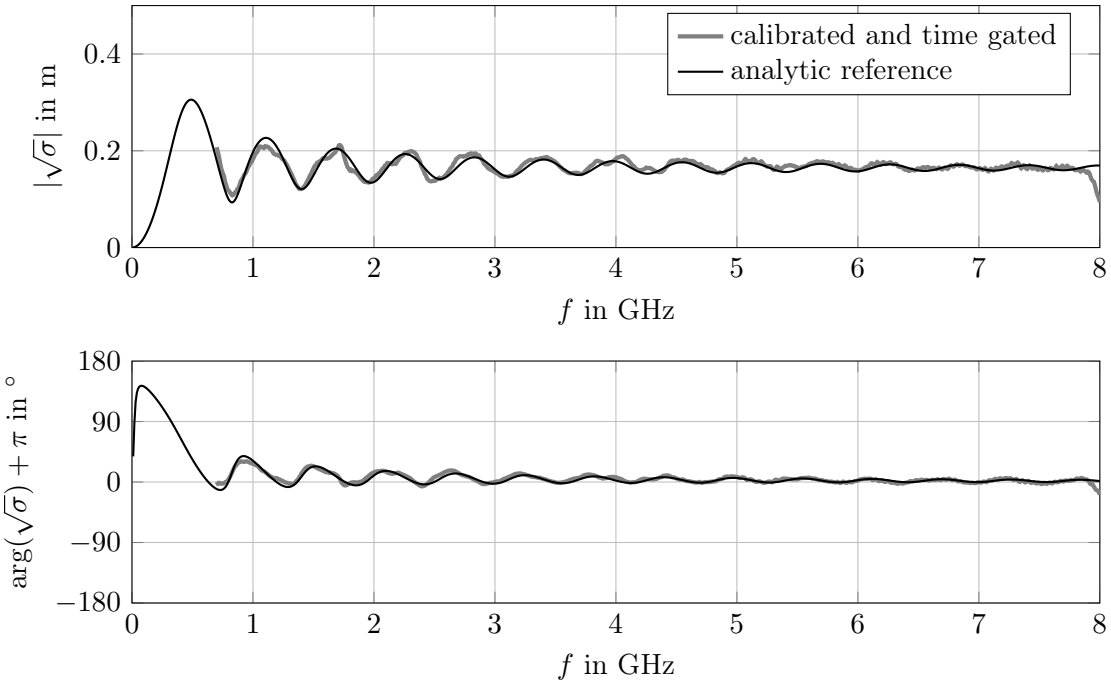

Figure 5.9: Measurement results of the metallic sphere after calibration and time gating compared to an analytic reference.

5.4 Natural frequencies

Finally, the natural frequencies s_n of wires above a ground are extracted from the measured complex radar cross section using the vector fitting algorithm from Sec. 2.6. The results are used to verify the analytic and numerical methods. The numerical solution is obtained with the contour integration method that is described in Sec. 2.6.

For the analytic solution a fixed point iteration is used to solve Eq. (3.36) with the iterative solution for the reflection coefficient (see Eqs. (4.48) and (4.65)). The fixed point iteration is initialized with the zeros iteration reflection coefficient, i.e.

$$\frac{s_n^{(0)}}{c} = \frac{\ln\big(\big|\Gamma_1^{(0)}\big(s_n^{(0)}\big)\Gamma_2^{(0)}\big(s_n^{(0)}\big)\big|\big)}{2\mathcal{L}} + \mathrm{j}\frac{\arg\big(\Gamma_1^{(0)}\big(s_n^{(0)}\big)\Gamma_2^{(0)}\big(s_n^{(0)}\big)\big)}{2\mathcal{L}} + \mathrm{j}\frac{\pi n}{\mathcal{L}}\,. \tag{5.26}$$

Inserting the zeroth iteration reflection coefficient Eq. (4.48) with $\mathrm{j}k \to s_n^{(0)}/c$ into the latter equation and rearranging the terms results in

$$\frac{s_n^{(0)}}{c} = \frac{\ln\big(\big|\frac{Z_\mathrm{C}-Z_1}{Z_\mathrm{C}+Z_1}\frac{Z_\mathrm{C}-Z_2}{Z_\mathrm{C}+Z_2}\big|\big)}{2(\mathcal{L}+l_{\mathrm{p}1}+l_{\mathrm{p}2})} + \mathrm{j}\frac{\arg\big(\frac{Z_\mathrm{C}-Z_1}{Z_\mathrm{C}+Z_1}\frac{Z_\mathrm{C}-Z_2}{Z_\mathrm{C}+Z_2}\big)}{2(\mathcal{L}+l_{\mathrm{p}1}+l_{\mathrm{p}2})} + \mathrm{j}\frac{\pi n}{\mathcal{L}+l_{\mathrm{p}1}+l_{\mathrm{p}2}}\,, \tag{5.27}$$

where $\mathcal{L}$ is the length of the horizontal part of the wire and $l_{\mathrm{p}1}$ and $l_{\mathrm{p}2}$ denote the arc length of each port respectively. Hence, the total wire length is

$$\mathcal{L}_\mathrm{tot} = \mathcal{L} + l_{\mathrm{p}1} + l_{\mathrm{p}2}\,. \tag{5.28}$$

Each following iteration $m > 0$ is obtained by using the previous natural frequency as the frequency for the reflection coefficient, i.e.

$$\frac{s_n^{(m)}}{c} = \frac{\ln\big(\big|\Gamma_1\big(s_n^{(m-1)}\big)\Gamma_2\big(s_n^{(m-1)}\big)\big|\big)}{2\mathcal{L}} + \mathrm{j}\frac{\arg\big(\Gamma_1\big(s_n^{(m-1)}\big)\Gamma_2\big(s_n^{(m-1)}\big)\big)}{2\mathcal{L}} + \mathrm{j}\frac{\pi n}{\mathcal{L}}\,. \tag{5.29}$$

where Γ is approximated with Eq. (4.66). Usually three iterations are sufficient. Hence, in the following the analytic approximation is

$$s_n \approx s_n^{(3)} \,. \tag{5.30}$$

Examples

Four examples are presented in the following. Thin wires are placed above a ground plane that is sufficiently large and the square root of the complex radar cross section is measured as described above. An example wire with an open and short circuit is shown in Fig. 5.10. The wire is supported by a small piece of Rhoacell to ensure a constant height above the ground. The width of the square copper ground plane amounts to 260 mm.

First, $s_{11,\mathrm{m}}$ is measured with the wire above the ground. Next the wire is disconnected from the ground plane without moving the ground plane. Then the reference measurement $s_{11,\mathrm{m}}^{\mathrm{empty}}$ is conducted without the wire but with the ground plane. It is important that the ground plane is located at the exact same location as before.

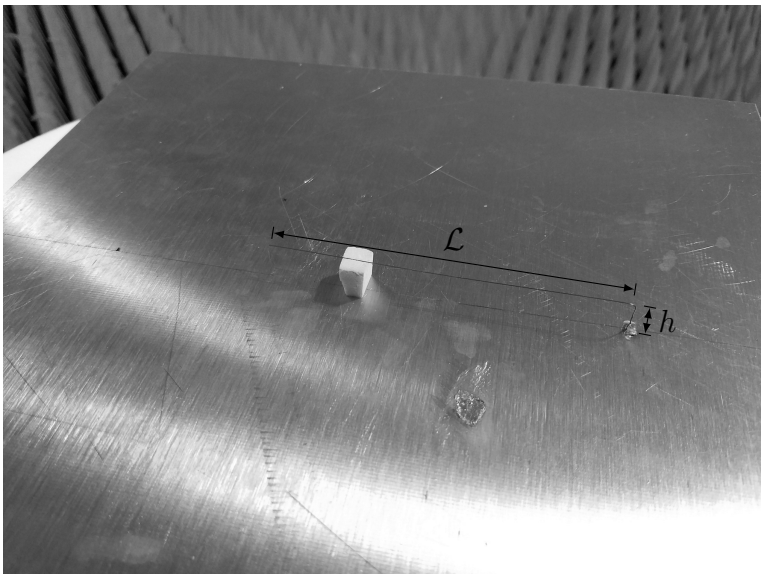

Figure 5.10: Photo of a wire with an open and a short-circuited port above a finite ground.

The **first example** is a horizontal wire that is open at both terminals. A schematic of the wire is shown in Fig. 5.11. The wire dimensions are $a = 0.125\,\mathrm{mm}$, $h = 10\,\mathrm{mm}$ and $\mathcal{L} = 151.5\,\mathrm{mm}$. The calibrated and time gated frequency response is depicted in Fig. 5.12. Furthermore, the fit, that is obtained by using the vector fitting algorithm, is plotted as well. The fit agrees very well with the measured response. The vector fitting algorithm only works if the correct R is used for Eq. (5.24). One way to deal with this is a trial and error method as described in [72].

Finally, the extracted natural frequencies are shown in Fig. 5.13. The measured, numerical and analytic natural frequencies are close to each other. The analytic results (asymptotic approach combined with the iterative method) agree very well with the measured natural frequencies and the numerical results. Additionally, the classical natural frequencies are plotted to illustrate the improvement of the analytic method. They are obtained by combining the asymptotic approach with the classical transmission line theory

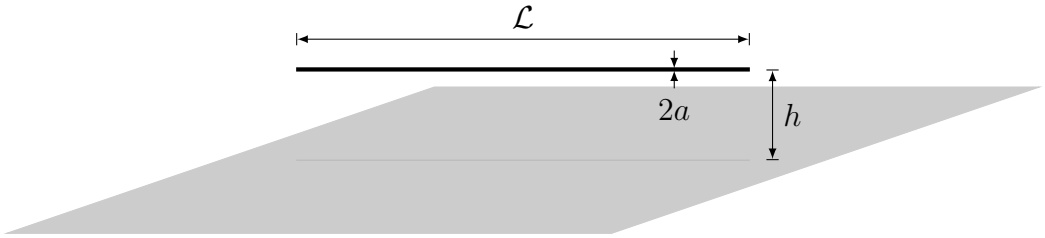

Figure 5.11: Horizontal wire with two open ports above a finite ground.

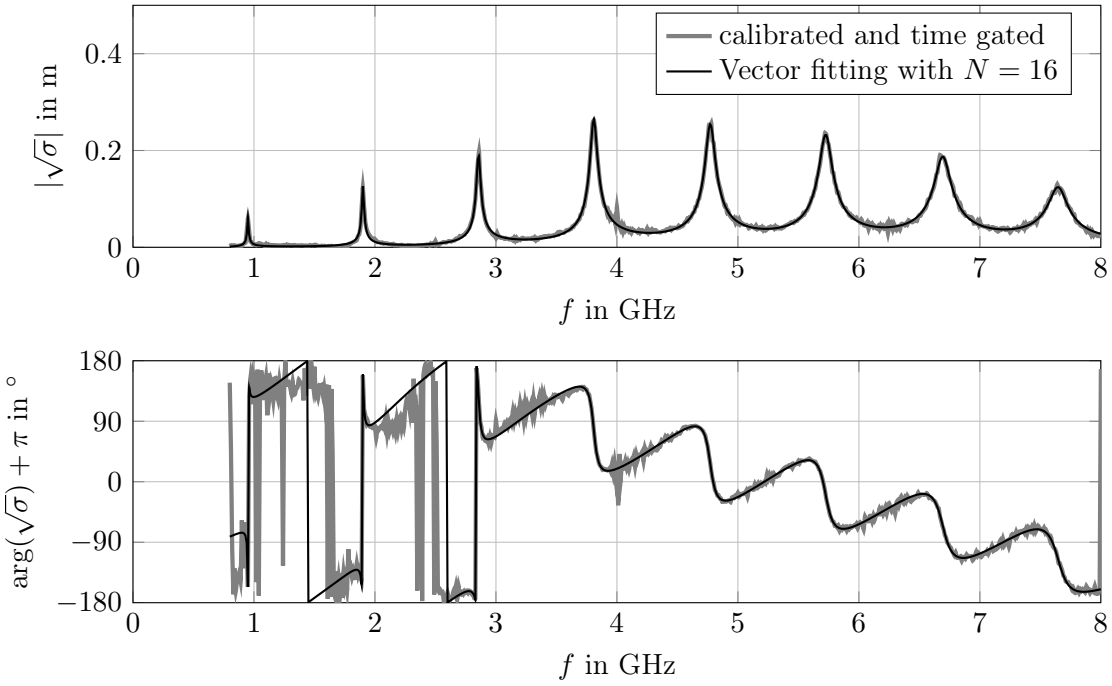

Figure 5.12: Calibrated and time gated measurement results of the wire with two open ports with the corresponding vector fitting fit.

for the reflection coefficient, i.e. they are determined with Eq. (5.27). For the considered example it holds

$$\Gamma_1^{(0)} = \Gamma_2^{(0)} = -1\,. \tag{5.31}$$

Hence, it follows for the classical natural frequencies

$$\frac{s_n^{(0)}\mathcal{L}}{\pi c} = \mathrm{j}n\,. \tag{5.32}$$

The classical natural frequencies are purely imaginary. This is due to the lack of losses in the classical transmission line theory. This is yet another example to illustrate the advantage of the iterative method compared to the classical transmission line theory (see also Sec. 4.1).

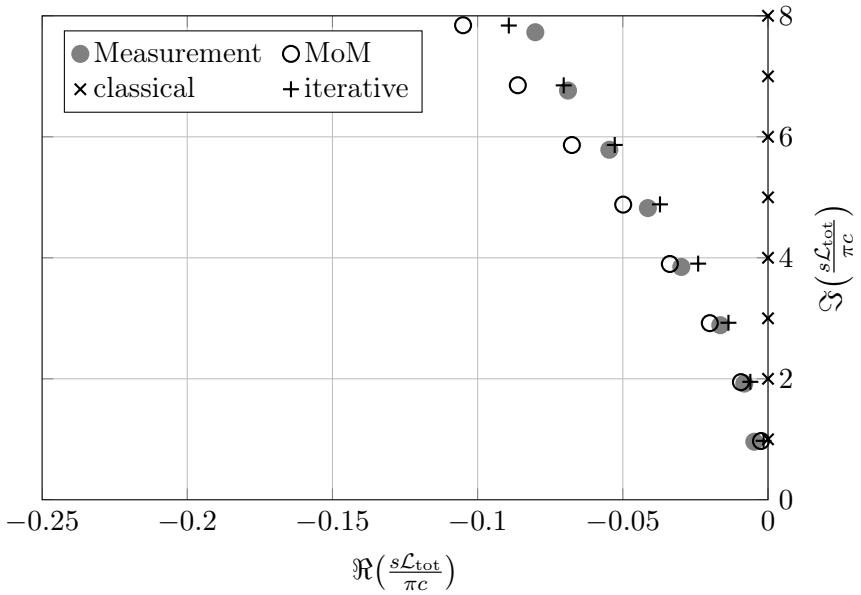

Figure 5.13: Natural frequencies of the wire with two open ports.

The **second example** is a horizontal wire which is open at one end and short circuited with a vertical riser at the other end. The wire is depicted in Fig. 5.10 and has the dimensions $a = 0.125\,\mathrm{mm}$, $h = 10\,\mathrm{mm}$ and $\mathcal{L} = 101\,\mathrm{mm}$. Figure 5.14 shows the measured

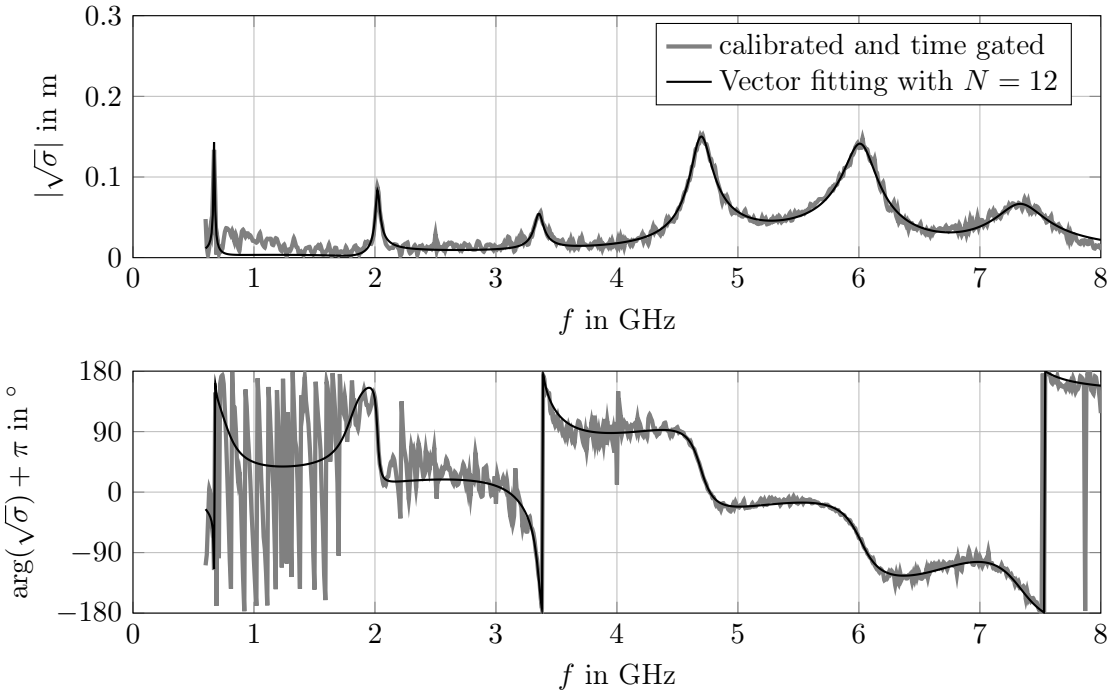

Figure 5.14: Calibrated and time gated measurement results of the wire with an open and a short-circuited port with the corresponding vector fitting fit.

frequency response and the corresponding fit. The natural frequencies are illustrated in Fig. 5.15. The same observations as for the first example can be made here as well. The

classical solution is obtained with

$$\Gamma_1^{(0)} = -1 \tag{5.33}$$

$$\Gamma_2^{(0)} = 1\,. \tag{5.34}$$

It follows

$$\frac{s_n^{(0)}(\mathcal{L}+h)}{\pi c} = \mathrm{j}\left(n - \frac{1}{2}\right). \tag{5.35}$$

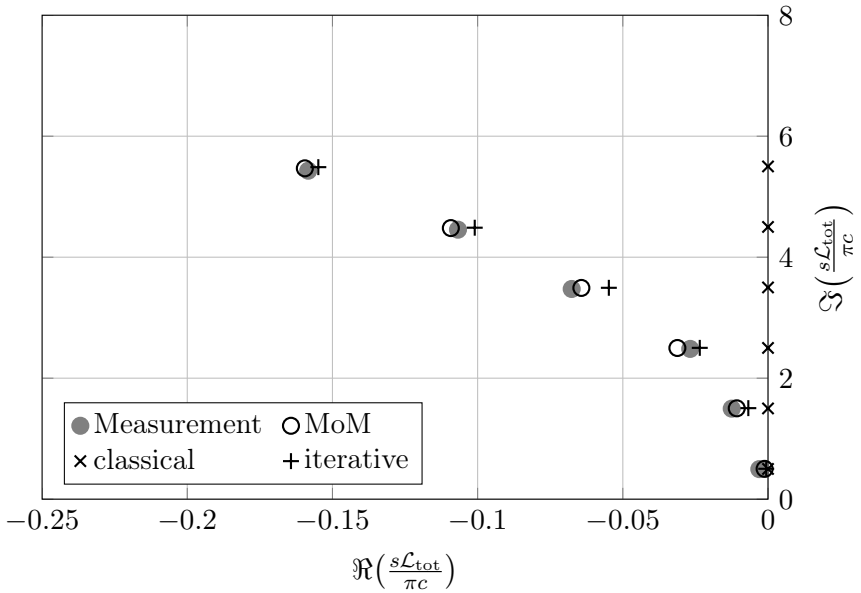

Figure 5.15: Natural frequencies of the wire with an open and a short-circuited port.

For the **third example** the wire is short circuited with vertical risers at both ends. The wire dimensions are $a = 0.125\,\mathrm{mm}$, $h = 10\,\mathrm{mm}$ and $\mathcal{L} = 152\,\mathrm{mm}$. The frequency response and natural frequencies are shown in Figs. 5.16 and 5.17 respectively. The theoretical and measured results coincide very well. However, the natural frequency at $\Im\left(\frac{s\mathcal{L}_{\mathrm{tot}}}{\pi c}\right) \approx 7$ is not detected by the measurement. This is due to the fact that not all natural frequencies are excited by the specific plane wave and not all modes radiate in the direction of the antenna. This is also visible in Fig. 5.16. The resonance at about 6 GHz is too small to be relevant for the vector fitting algorithm.

The **last example** is a multiconductor transmission line. Two parallel wires are placed above the ground as depicted in Fig. 5.18. The two wires have the same radius $a = 0.125\,\mathrm{mm}$, height above the ground $h = 10\,\mathrm{mm}$ and wire length $\mathcal{L} = 150\,\mathrm{mm}$. The constant distance between the two wires is $d = 10\,\mathrm{mm}$. Both wires are left open at the ends. The measured complex radar cross section is shown in Fig. 5.19 alongside the fit. The natural frequencies are plotted in Fig. 5.20. The agreement between the measurement, numerical simulation and analytic results is again very good. However, there is an additional measured natural frequency with $\Im\left(\frac{s\mathcal{L}_{\mathrm{tot}}}{\pi c}\right) \approx 1$ that does not seem to be right. This is most likely due to the noise at low frequencies. The vector fitting algorithm finds an additional resonance to compensate for the rapid changes of the amplitude.

The analytic natural frequencies are obtained using the second order iterative method as described in Sec. 4.4.1. The analytic results for the two wire line are compared to the

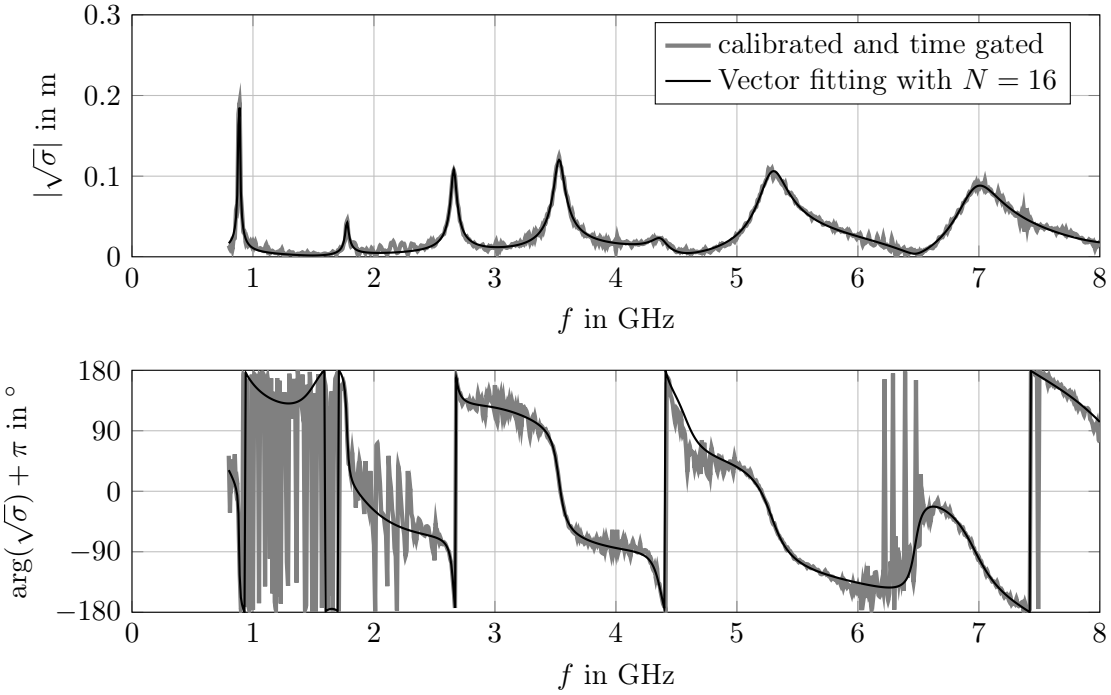

Figure 5.16: Calibrated and time gated measurement results of the wire with two short-circuited ports with the corresponding vector fitting fit.

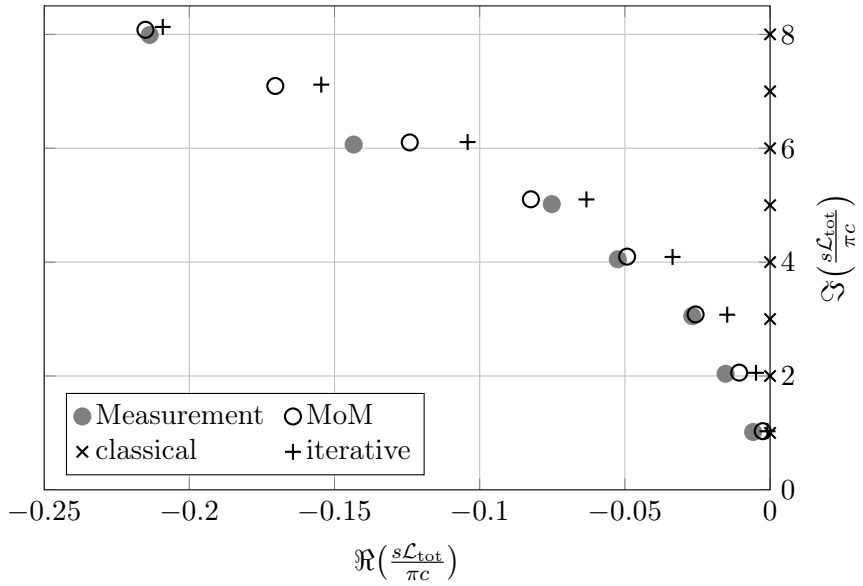

Figure 5.17: Natural frequencies of the wire with two short-circuited ports.

analytic results of a single wire line with the same dimensions in Fig. 5.21. Each single natural frequency of the single wire is split into two natural frequencies with a similar imaginary part. This splitting is characteristic for coupled resonant systems as further explained in [61], [73]. The behavior is also visible in the frequency response in Fig. 5.19. For the higher order resonances there is a sharp peak right next to a relatively wide one.

The two branches correspond to the differential and common mode current respectively. For the common mode the currents on both wires are equal and have the same sign. Hence, from a far distance the two wire line acts as a thick single wire line above a ground and

can radiate very well. Hence, the damping of the current over time is relatively large. On the other hand, the differential mode current is equal on both wires but with an opposite sign. The result is that the two radiated fields cancel each other out in many directions. Consequently not much power is radiated from the differential mode current. Hence, the damping of the current over time is not as large as for the common mode. This explains the different real parts of the differential and common mode natural frequencies [61].

The iterative solution for two wires fails to produce valid differential mode natural frequencies with a small imaginary part (see Fig. 5.21). This is due to the nonphysical behavior of the differential mode reflection coefficient as described in Sec. 4.4.1. This problem remains unsolved.

In conclusion, the measurement results validate the analytic and numerical models.

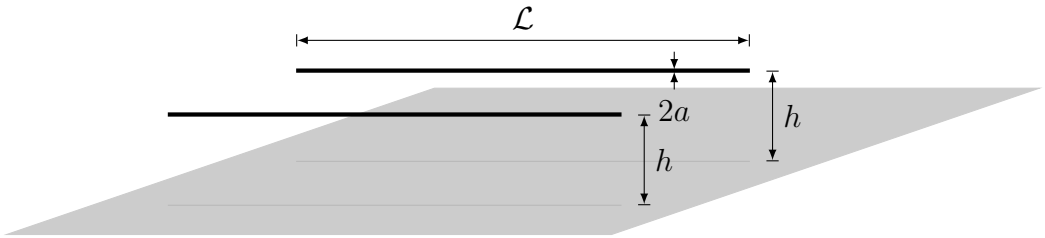

Figure 5.18: Two horizontal wires with two open ports above a finite ground.

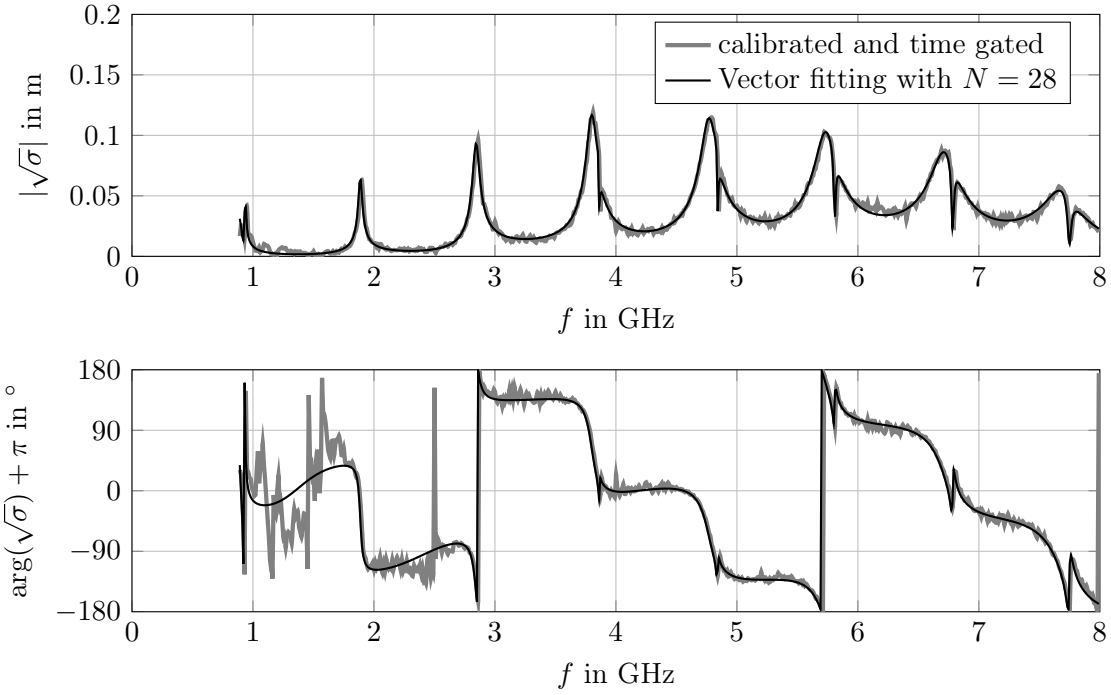

Figure 5.19: Calibrated and time gated measurement results of the two wires with two open ports with the corresponding vector fitting fit.

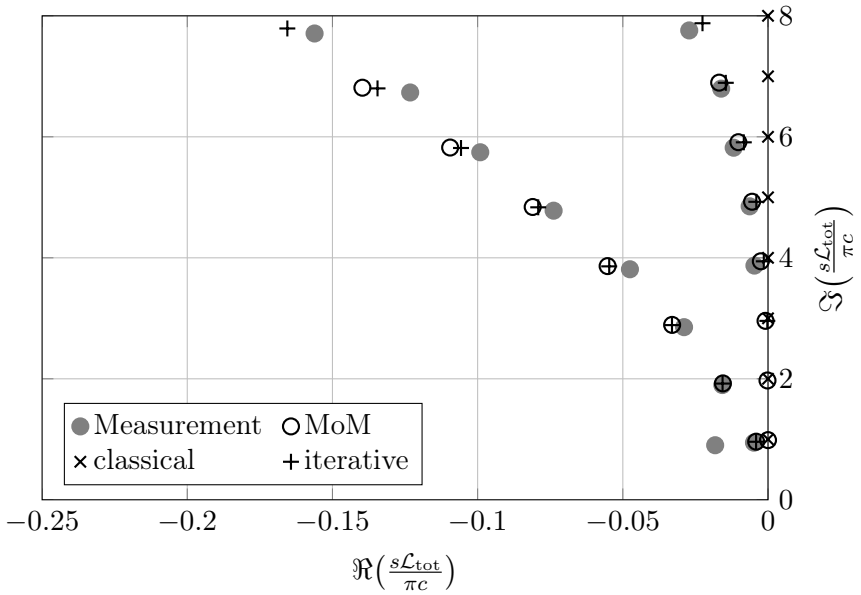

Figure 5.20: Natural frequencies of the two wires with two open ports.

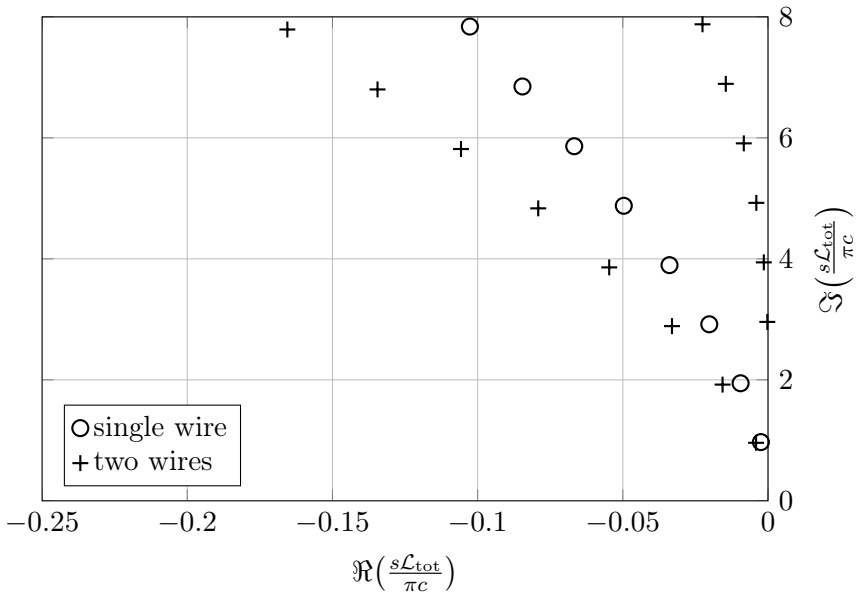

Figure 5.21: Comparison of the analytic natural frequencies for two wires and a single wire with the same dimensions.

5.5 Summary

The analytic and numerical models are compared to measurement results. A method to measure the natural frequencies of passive targets in frequency domain is described. This includes the measurement setup and a calibration procedure. A VNA and a horn antenna are used to measure the reflected field of a target that is excited by an EM field of the antenna. Time gating is applied to increase the accuracy of the measurement. The calibrated and time gated frequency response is fitted using the vector fitting algorithm to extract the natural frequencies. The analytic and numerical results coincide very well with the measurements.

Chapter 6

Summary and outlook

In the following the results and methods are summarized. Furthermore, an outlook and possible extensions are described.

6.1 Summary

Transmission lines play an important part for many applications. A widely used class of transmission lines are thin wires. The aim of this work is to increase the understanding of the propagation of waves on thin wires above a perfect electric ground plane. Hence, analytic and semi-analytic methods are used to describe the field coupling to thin wires. The asymptotic approach and the iterative method are extended for arbitrary port geometries and lumped loads.

First, the asymptotic approach for thin wires is derived to analytically describe the current on a wire that arises due to a plane wave excitation. The infinite wire above a ground plane acts as a starting point for the derivation. An exact analytic solution is available and the TEM mode, which appears due to the scattering at discontinuities, is identified as the dominant mode in a large distance from any discontinuity. Using general scattering and reflection coefficients for each port, a TEM mode approximation for the current in the middle of a finite wire is generalized. To get the analytic expression, the method of infinite reflections is applied. This derivation is an alternative to the one presented in [12], [13], where the asymptotic approach is introduced for thin wires. The solution is only valid far away from the ports and other discontinuities, i.e. on a straight part of the wire. The general scattering and reflection coefficients may include high frequency effects, e.g. radiation effects at the ports. This is a big advantage compared to the classical transmission line theory.

A novel method to extract the scattering and reflection coefficients from a MoM solution is derived. The validity of the asymptotic approach is confirmed with numerical examples. Furthermore, the examples show that the scattering and especially the reflection coefficients are in general complex. This shows again the advantage of this general approach to the classical transmission line theory.

The iterative method is an analytic alternative to determine the scattering and reflection coefficients. The idea is to separately look at each isolated port. The other port is substituted by a uniform semi-infinite wire. This removes the effect of multiple reflections due to the other port. The scattering and reflection coefficients can be determined by solving the mixed potential integral equations for the current on the semi-infinite wire and by then comparing its solution to the proposed asymptotic behavior of the current. The

iterative method is an approximate analytic method to solve the mixed potential integral equations. The iteration is initialized by the classical transmission line solution. Each next iteration uses the previous one as an excitation. The iterative method is introduced in [13], [15]. However, in this thesis it is generalized to arbitrary wire trajectories at the port and lumped loads. In [13], [15] only the simplest special case of the straight, open-circuited wire is considered. Furthermore, the solution in this thesis is regularized to allow for a fast numerical evaluation of the remaining integrals. The iteration is terminated after the first iteration. Higher order iterations become quite complicated and cannot be quickly evaluated. Numerical examples show that the analytic approximation and a numerical reference coincide very well. Moreover, the examples show the improvement compared to the classical transmission line theory. For small frequencies, i.e. large wavelengths compared to the wire height above the ground, the iterative solution and the classical one coincide. But with increasing frequency the advantage of the iterative method becomes clearly visible. The difference between the classical solution and numerical reference becomes large.

Furthermore, the iterative method is extended to multiconductor transmission lines. For two wires parallel above a ground the kernel matrices can be diagonalized. As a result two decoupled currents, i.e. the common and differential mode current, appear. The problem is reduced to the single wire solution for each current mode with modified kernels. Applying the diagonalization procedure for more than two wires above a ground proves to be challenging or even impossible. However, the iterative method can also be extended to matrices. The solution is presented in this thesis as well.

The solution of the iterative method is, moreover, compared to the induced EMF method. First, it is shown that the induced EMF method is applicable for the semi-infinite wire. Then the reflection coefficient is approximated by using the induced EMF method. The classical transmission line current is assumed for the approximation. It is shown that the result coincides with the first order iterative approximation.

Lastly, the analytic and numerical results are compared to experimental data. Since a direct current measurement would distort the result, the complex radar cross section of wires above a ground is measured. The measured complex radar cross section is then used to determine the natural frequencies by fitting the data with the well known vector fitting algorithm. The natural frequencies play an important part in the context of the singularity expansion method (SEM). They characterize each system and they are independent of the excitation, i.e. they only depend on the geometry and material properties of each object. The asymptotic approach yields a fixed point equation for the natural frequencies of the wires. The natural frequencies depend only on the wire dimensions and the reflection coefficients. There is a very good agreement between the measured, analytic and numerical natural frequencies. The analytic and numerical models are validated by the measurements.

6.2 Outlook

A problem arises for the reflection coefficient matrix for two wires if there are no ohmic losses present as shown by the examples. Then the reflection coefficient for the differential mode becomes slightly larger than 1 for small frequencies. This is a nonphysical result for the passive port. It is not clear why the iterative method yields a nonphysical solution. This problem remains open and needs to be investigated in more detail.

Furthermore, the iterative method is extended for the reflection coefficient matrix. It could be used for the scattering coefficient matrix as well to complete the analysis of the

plane wave coupling to multiconductor transmission lines in the future.

The iterative method converges to the exact solution if the infinite wire is considered. Unfortunately, a complete analysis of the convergence for the semi-infinite problem is not yet give and is part of future work.

The measurement setup might be improved. Some information of the signal is lost due to the time gating procedure. This problem could be reduced by using a bi-static setup, i.e. by separating the sending and receiving antenna instead of using one single antenna and VNA port. First experiments suggest that the noise that is seen in Fig. 5.7 becomes much smaller by decoupling the sending and receiving port and antenna. Then the time gating procedure could be omitted and the original measured signal could be used for the fit to extract the natural frequencies.

The natural frequencies play an important role in validating the analytic and numerical models. However, only the first layer of the natural frequencies is considered. The example in Fig. 2.11 shows that there are multiple layers of natural frequencies. Similarly, the perfect electric sphere has multiple layers of natural frequencies as well [37]. The layers are almost parallel to each other. But the asymptotic approach does not give any information about the higher order layers. It is not clear why this is the case. How can one find an analytic approximation of the natural frequencies that make up the higher order layers? The numerous analytic approximations in [46] approximate only the first layer as well.

There is an exact analytic solution for the current on the straight infinite wire that is excited by a plane wave or a lumped voltage source. This solution gives a formal derivation of the dominant mode that is used for the asymptotic approach for partially straight wires above a ground plane. The integral kernels for the straight infinite wire above the ground depend on the difference $l - l'$ where l and l' denote the arc length of the wire and its mirror. Hence, a convolution is present and the spacial Fourier transform can be applied on the mixed potential integral equations to find an algebraic equation. The current is then found with the inverse Fourier transform after simple mathematical manipulations. This exact approach can be generalized to other infinite or periodic wire structures. The only requirement is that the corresponding integral kernels depend on the difference $l - l'$ as well. Two novel theorems that make sure which wire structures fulfill the requirement are presented in App. A.2, e.g. the twisted pair, a helix with a straight wire on its axis. As a next step the corresponding Fourier transform of the kernels needs to be found and the current can be obtained as for the straight infinite wire. Hopefully, a dominant mode can be extracted and the asymptotic approach could be extended for more complex wire structures as well.

Appendix A

Wires

A.1 Local coordinate system along smooth wires

The local coordinate system that is introduced at the beginning of Sec. 2.2 is analyzed in more detail in this appendix. The differential operators and the infinitesimal volume element are derived for the new coordinate system using the general method described in [20]. The starting point are Eq. (2.28) and the Frenet formula (see [21] for a derivation), namely

$$\frac{\partial}{\partial l}\begin{pmatrix}\hat{\boldsymbol{\tau}}(l)\\ \hat{\boldsymbol{\eta}}(l)\\ \hat{\boldsymbol{\beta}}(l)\end{pmatrix} = \xi(l)\begin{pmatrix}0 & \kappa(l) & 0\\ -\kappa(l) & 0 & \tau(l)\\ 0 & -\tau(l) & 0\end{pmatrix}\begin{pmatrix}\hat{\boldsymbol{\tau}}(l)\\ \hat{\boldsymbol{\eta}}(l)\\ \hat{\boldsymbol{\beta}}(l)\end{pmatrix}, \tag{A.1}$$

where κ is the curvature of the trajectory and τ is the so called torsion.

First, the covariant basis vectors $\boldsymbol{u}_1, \boldsymbol{u}_2, \boldsymbol{u}_3$ are derived for the new coordinate system. It holds

$$\boldsymbol{u}_1(l,r,\phi) = \frac{\partial}{\partial l}\boldsymbol{x}(l,r,\phi) = \xi[1 - r\kappa\cos(\phi)]\hat{\boldsymbol{\tau}} + \xi r\tau\hat{\boldsymbol{\phi}} \tag{A.2}$$

$$\boldsymbol{u}_2(l,r,\phi) = \frac{\partial}{\partial r}\boldsymbol{x}(l,r,\phi) = \hat{\boldsymbol{r}} \tag{A.3}$$

$$\boldsymbol{u}_3(l,r,\phi) = \frac{\partial}{\partial \phi}\boldsymbol{x}(l,r,\phi) = r\hat{\boldsymbol{\phi}} \tag{A.4}$$

where the auxiliary unit vectors are defined as

$$\hat{\boldsymbol{r}} = \cos(\phi)\hat{\boldsymbol{\eta}} + \sin(\phi)\hat{\boldsymbol{\beta}} \tag{A.5}$$

$$\hat{\boldsymbol{\phi}} = -\sin(\phi)\hat{\boldsymbol{\eta}} + \cos(\phi)\hat{\boldsymbol{\beta}}\,. \tag{A.6}$$

The vectors $\hat{\boldsymbol{\tau}}, \hat{\boldsymbol{\eta}}$ and $\hat{\boldsymbol{\beta}}$ are orthonormal.

Now the components of the symmetric covariant metric tensor can be determined, i.e.

$$u_{11} = \boldsymbol{u}_1 \cdot \boldsymbol{u}_1 = \xi^2[(1 - r\kappa\cos(\phi))^2 + r^2\tau^2] \tag{A.7}$$

$$u_{12} = \boldsymbol{u}_1 \cdot \boldsymbol{u}_2 = 0 \tag{A.8}$$

$$u_{13} = \boldsymbol{u}_1 \cdot \boldsymbol{u}_3 = \xi r^2\tau \tag{A.9}$$

$$u_{22} = \boldsymbol{u}_2 \cdot \boldsymbol{u}_2 = 1 \tag{A.10}$$

$$u_{23} = \boldsymbol{u}_2 \cdot \boldsymbol{u}_3 = 0 \tag{A.11}$$

$$u_{33} = \boldsymbol{u}_3 \cdot \boldsymbol{u}_3 = r^3\,. \tag{A.12}$$

The resulting covariant metric tensor in matrix notation is

$$\underline{\underline{\boldsymbol{U}}}_{jk} = \begin{pmatrix} \xi^2[(1-r\kappa\cos(\phi))^2 + r^2\tau^2] & 0 & \xi r^2\tau \\ 0 & 1 & 0 \\ \xi r^2\tau & 0 & r^2 \end{pmatrix} . \tag{A.13}$$

The contravariant metric tensor $\underline{\underline{\boldsymbol{U}}}^{jk}$ is the inverse of the covariant metric tensor. It holds

$$\underline{\underline{\boldsymbol{G}}}^{jk} = \frac{1}{u}\begin{pmatrix} r^2 & 0 & -\xi r^2\tau \\ 0 & 1 & 0 \\ -\xi r^2\tau & 0 & \xi^2[(1-r\kappa\cos(\phi))^2 + r^2\tau^2] \end{pmatrix} , \tag{A.14}$$

where u is the determinant of $\underline{\underline{\boldsymbol{U}}}_{jk}$, i.e.

$$u = \xi^2 r^2[1 - r\kappa\cos(\phi)]^2 . \tag{A.15}$$

The contravariant metric tensor can be used to determine the contravariant basis vectors $\boldsymbol{u}^1, \boldsymbol{u}^2, \boldsymbol{u}^3$. It holds

$$\boldsymbol{u}^1 = u^{11}\boldsymbol{u}_1 + u^{12}\boldsymbol{u}_2 + u^{13}\boldsymbol{u}_3 = \frac{\hat{\boldsymbol{\tau}}}{\xi[1 - r\kappa\cos(\phi)]} \tag{A.16}$$

$$\boldsymbol{u}^2 = u^{21}\boldsymbol{u}_1 + u^{22}\boldsymbol{u}_2 + u^{23}\boldsymbol{u}_3 = \hat{\boldsymbol{r}} \tag{A.17}$$

$$\boldsymbol{u}^3 = u^{31}\boldsymbol{u}_1 + u^{32}\boldsymbol{u}_2 + u^{33}\boldsymbol{u}_3 = -\frac{\tau\hat{\boldsymbol{\tau}}}{1 - r\kappa\cos(\phi)} + \frac{\hat{\boldsymbol{\phi}}}{r} , \tag{A.18}$$

where u^{jk} are the components of the contravariant metric tensor respectively.

The differential operators grad and div and the infinitesimal volume element $\mathrm{d}\boldsymbol{x}$ can be determined using the just derived basis vectors and metric tensors. It holds (see [20] for more details on the general derivations)

$$\mathrm{d}\boldsymbol{x} = \sqrt{u} = \xi(l) r[1 - r\kappa(l)\cos(\phi)]\,\mathrm{d}l\,\mathrm{d}r\,\mathrm{d}\phi . \tag{A.19}$$

Let Φ be a scalar field. Then it holds

$$\operatorname{grad}\Phi(l, r, \phi) = \frac{\partial\Phi}{\partial l}\boldsymbol{g}^1 + \frac{\partial\Phi}{\partial r}\boldsymbol{g}^2 + \frac{\partial\Phi}{\partial\phi}\boldsymbol{g}^3 \tag{A.20}$$

$$= \frac{\hat{\boldsymbol{\tau}}(l)}{\xi(l)[1 - r\kappa(l)\cos(\phi)]}\frac{\partial\Phi}{\partial l} + \hat{\boldsymbol{r}}(l,\phi)\frac{\partial\Phi}{\partial r} + \Big[\frac{\hat{\boldsymbol{\phi}}(l,\phi)}{r} - \frac{\tau(l)\hat{\boldsymbol{\tau}}(l)}{1 - r\kappa(l)\cos(\phi)}\Big]\frac{\partial\Phi}{\partial\phi} . \tag{A.21}$$

Let $\boldsymbol{J}$ be a general vector field. Then it holds

$$\operatorname{div}\boldsymbol{J} = \frac{1}{\sqrt{u}}\frac{\partial}{\partial l}\big[\sqrt{u}\boldsymbol{J}\cdot\boldsymbol{u}^1\big] + \frac{1}{\sqrt{u}}\frac{\partial}{\partial r}\big[\sqrt{u}\boldsymbol{J}\cdot\boldsymbol{u}^2\big] + \frac{1}{\sqrt{u}}\frac{\partial}{\partial\phi}\big[\sqrt{u}\boldsymbol{J}\cdot\boldsymbol{u}^3\big] . \tag{A.22}$$

Inserting the specific current density from Eq. (2.30) into Eq. (A.22) results in

$$\operatorname{div} J_{\mathrm{S}}(l)\delta(r-a)\hat{\boldsymbol{\tau}}(l) = \frac{1}{\xi(l)[1 - r\kappa(l)\cos(\phi)]}\frac{\partial}{\partial l}J_{\mathrm{S}}(l) r\delta(r-a) . \tag{A.23}$$

A.2 The symmetry theorems

The general kernels for the mixed potential integral equations are given as

$$g_\Phi(l,l') = \frac{\exp\bigl(-\mathrm{j}k\sqrt{\|\boldsymbol{x}_\mathrm{c}(l)-\boldsymbol{x}_\mathrm{c}(l')\|^2+a^2}}{\sqrt{\|\boldsymbol{x}_\mathrm{c}(l)-\boldsymbol{x}_\mathrm{c}(l')\|^2+a^2}} \tag{A.24}$$

$$g_\mathrm{A}(l,l') = \frac{\exp\bigl(-\mathrm{j}k\sqrt{\|\boldsymbol{x}_\mathrm{c}(l)-\boldsymbol{x}_\mathrm{c}(l')\|^2+a^2}}{\sqrt{\|\boldsymbol{x}_\mathrm{c}(l)-\boldsymbol{x}_\mathrm{c}(l')\|^2+a^2}}\hat{\boldsymbol{\tau}}(l)\cdot\hat{\boldsymbol{\tau}}(l') \tag{A.25}$$

for a single wire in free space and

$$g_{\Phi,mn}(l,l') = \frac{\exp\bigl(-\mathrm{j}k\sqrt{\|\boldsymbol{x}_{cm}(l)-\boldsymbol{x}_{cn}(l')\|^2+a^2}}{\sqrt{\|\boldsymbol{x}_{cm}(l)-\boldsymbol{x}_{cn}(l')\|^2+a^2}} \tag{A.26}$$

$$g_{\mathrm{A},mn}(l,l') = \frac{\exp\bigl(-\mathrm{j}k\sqrt{\|\boldsymbol{x}_{cm}(l)-\boldsymbol{x}_{cn}(l')\|^2+a^2}}{\sqrt{\|\boldsymbol{x}_{cm}(l)-\boldsymbol{x}_{cn}(l')\|^2+a^2}}\hat{\boldsymbol{\tau}}_m(l)\cdot\hat{\boldsymbol{\tau}}_n(l') \tag{A.27}$$

for two wires in free space. When solving the mixed potential integral equations it is advantageous when the kernels depend on the difference $l-l'$. In the following two theorems, that give requirements for the wire trajectories to fulfill this condition, are presented and proofed. The Theorem 1 holds for a single wire and Theorem 2 for two or more wires.

Let the trajectory of the single wire be denoted by $\boldsymbol{x}_\mathrm{c}(l)$ with the natural parameter l. Then the following Theorem holds.

Theorem 1. *The following assertions are equivalent for a sufficiently smooth trajectory*

(i) $\|\boldsymbol{x}_\mathrm{c}(l)-\boldsymbol{x}_\mathrm{c}(l')\|^2 = f_1(l-l')$ *and* $\hat{\boldsymbol{\tau}}(l)\cdot\hat{\boldsymbol{\tau}}(l') = f_2(l-l')$*, where* f_1 *and* f_2 *are some arbitrary functions, i.e. the norm and the scalar product are functions of* $l-l'$*.*

(ii) The curvature κ *and torsion* τ *of* $\boldsymbol{x}_\mathrm{c}$ *are constant along the curve.*

Proof. The proof is split into two parts

"$(i)\Rightarrow(ii)$" Assuming (i) holds. The wire is characterized by its Frenet basis $\hat{\boldsymbol{\tau}}$, $\hat{\boldsymbol{\eta}}$ and $\hat{\boldsymbol{\beta}}$. A Taylor series can be developed at an arbitrary location l' (since the trajectory is sufficiently smooth)

$$\boldsymbol{x}_\mathrm{c}(l) = \boldsymbol{x}_\mathrm{c}(l') + \sum_{n=1}^{\infty}\frac{1}{n!}\frac{\mathrm{d}^n}{\mathrm{d}l^n}\boldsymbol{x}_\mathrm{c}(l)\bigg|_{l=l'}(l-l')^n\,. \tag{A.28}$$

Using (A.1) yields

$$\frac{\mathrm{d}}{\mathrm{d}l}\boldsymbol{x}_\mathrm{c}(l) = \hat{\boldsymbol{\tau}}(l) \tag{A.29}$$

$$\frac{\mathrm{d}^2}{\mathrm{d}l^2}\boldsymbol{x}_\mathrm{c}(l) = \kappa(l)\hat{\boldsymbol{\eta}}(l) \tag{A.30}$$

$$\frac{\mathrm{d}^3}{\mathrm{d}l^3}\boldsymbol{x}_\mathrm{c}(l) = -\kappa^2(l)\hat{\boldsymbol{\tau}}(l) + \frac{\mathrm{d}}{\mathrm{d}l}\kappa(l)\hat{\boldsymbol{\eta}}(l) + \kappa(l)\tau(l)\hat{\boldsymbol{\beta}}(l) \tag{A.31}$$

$$\begin{aligned}\frac{\mathrm{d}^4}{\mathrm{d}l^4}\boldsymbol{x}_\mathrm{c}(l) &= -3\kappa(l)\frac{\mathrm{d}}{\mathrm{d}l}\kappa(l)\hat{\boldsymbol{\tau}}(l)\\ &\quad + [\frac{\mathrm{d}^2}{\mathrm{d}l^2}\kappa(l) - \kappa^3(l) - \kappa(l)\tau^2(l)]\hat{\boldsymbol{\eta}}(l) + [2\tau(l)\frac{\mathrm{d}}{\mathrm{d}l}\kappa(l) + \kappa(l)\frac{\mathrm{d}}{\mathrm{d}l}\tau(l)]\hat{\boldsymbol{\beta}}(l)\end{aligned} \tag{A.32}$$

$$\frac{\mathrm{d}^5}{\mathrm{d}l^5}\boldsymbol{x}_\mathrm{c}(l) = F_2(l)\hat{\boldsymbol{\tau}}(l) + \ldots \tag{A.33}$$

with

$$F_2(l) = -3\kappa(l)\frac{\mathrm{d}^2}{\mathrm{d}l^2}\kappa(l) - 3\kappa'(l)\frac{\mathrm{d}}{\mathrm{d}l}\kappa(l) - \kappa(l)\frac{\mathrm{d}^2}{\mathrm{d}l^2}\kappa(l) + \kappa^4(l) + \kappa^2(l)\tau^2(l)\,. \tag{A.34}$$

From this follows

$$\begin{aligned}\boldsymbol{x}_\mathrm{c}(l) - \boldsymbol{x}_\mathrm{c}(l') = &\left[(l-l') - \frac{\kappa^2(l')}{6}(l-l')^3 - \frac{\kappa(l')}{8}\frac{\mathrm{d}}{\mathrm{d}l'}\kappa(l')(l-l')^4\right.\\ &\qquad\left. + \frac{F_2(l')}{120}(l-l')^5 + \ldots\right]\hat{\boldsymbol{\tau}}(l')\\ &+\left[\frac{\kappa(l')}{2}(l-l')^2 + \frac{1}{6}\frac{\mathrm{d}}{\mathrm{d}l'}\kappa(l')(l-l')^3\right.\\ &\qquad\left. + \frac{1}{24}\frac{\mathrm{d}^2}{\mathrm{d}l'^2}\kappa(l') - \frac{\kappa^3(l') + \kappa(l')\tau^2(l')}{24}(l-l')^4 + \ldots\right]\hat{\boldsymbol{\eta}}(l')\\ &+\left[\frac{\kappa(l')\tau(l')}{6}(l-l')^3\right.\\ &\qquad\left. + \left(\frac{1}{12}\tau(l')\frac{\mathrm{d}}{\mathrm{d}l'}\kappa(l') + \frac{1}{24}\kappa(l')\frac{\mathrm{d}}{\mathrm{d}l'}\tau(l')\right)(l-l')^4 + \ldots\right]\hat{\boldsymbol{\beta}}(l')\,.\end{aligned} \tag{A.35}$$

The higher order terms are left out since they are not needed for the rest of the proof.

After finding an expression for the difference of the two vectors it is straight forward to get an expression for the norm of this difference. It holds

$$\begin{aligned}\|\boldsymbol{x}_\mathrm{c}(l) - \boldsymbol{x}_\mathrm{c}(l')\|^2 = &(l-l')^2 + \frac{\kappa^2(l')}{12}(l-l')^4 - \frac{1}{24}\kappa(l')\frac{\mathrm{d}}{\mathrm{d}l'}\kappa(l')(l-l')^5\\ &+\left[\frac{F_2(l')}{120} + \frac{1}{36}\left(\frac{\mathrm{d}}{\mathrm{d}l'}\kappa(l')\right)^2\right.\\ &\qquad\left. + \frac{\kappa(l')}{48}\frac{\mathrm{d}^2}{\mathrm{d}l'^2}\kappa(l') - \frac{\kappa^4(l') + \kappa^2(l')\tau^2(l')}{48} + \frac{\kappa^2(l')\tau^2(l')}{36}\right](l-l')^6\\ &+\ldots\end{aligned} \tag{A.36}$$

since $\hat{\boldsymbol{\tau}}$, $\hat{\boldsymbol{\eta}}$ and $\hat{\boldsymbol{\beta}}$ form an orthonormal basis. Again, the higher order terms are left out.

Furthermore, it follows from the assumption (i)

$$\|\boldsymbol{x}_\mathrm{c}(l) - \boldsymbol{x}_\mathrm{c}(l')\|^2 = f_1(l-l') \tag{A.37}$$

$$= f_1(l + l_0 - l' - l_0) \tag{A.38}$$

$$= \|\boldsymbol{x}_\mathrm{c}(l + l_0) - \boldsymbol{x}_\mathrm{c}(l' + l_0)\|^2 \tag{A.39}$$

for an arbitrary l_0. By comparing the coefficients of the polynomial series it follows for $(l-l')^4$

$$\frac{\kappa^2(l')}{12} = \frac{\kappa^2(l' + l_0)}{12} \tag{A.40}$$

and, hence,

$$\kappa = \text{const.} \tag{A.41}$$

since (A.40) holds for any l_0.

Comparing the coefficients for $(l-l')^6$ and using $\kappa = \text{const.}$ results in (after some straight forward mathematical manipulations)

$$\tau^2(l') = \tau^2(l'+l_0)\,. \tag{A.42}$$

Using the argument from above yields

$$\tau = \text{const.} \tag{A.43}$$

This concludes the first part of the proof.

"$(ii) \Rightarrow (i)$" Assuming that (ii) holds. The only curve with constant curvature and torsion is the helix [74]. The cirle and straight wire can be seen as special cases of the helix with $\tau = 0$ or $\kappa = 0$ and $\tau = 0$ respectively.

The natural parameterization of the helix and its special cases is

$$\boldsymbol{x}_\mathrm{c}(l) = R_\mathrm{h}\left[\cos\left(\frac{l}{\sqrt{R_\mathrm{h}^2+S_\mathrm{h}^2}}\right)\hat{\boldsymbol{x}}_1 + \sin\left(\frac{l}{\sqrt{R_\mathrm{h}^2+S_\mathrm{h}^2}}\right)\hat{\boldsymbol{x}}_2\right] + \frac{S_\mathrm{h}\,l}{\sqrt{R_\mathrm{h}^2+S_\mathrm{h}^2}}\hat{\boldsymbol{x}}_3\,. \tag{A.44}$$

The radius R_h and lay length S_h characterize the helix. For the circle holds $S = 0$ and for the straight wire holds $R_\mathrm{h} = 0$ or $S_\mathrm{h} \to \infty$.

The distance between two points on the wire is

$$\begin{aligned}
\|\boldsymbol{x}_\mathrm{c}(l) - \boldsymbol{x}_\mathrm{c}(l')\|^2 &= R_\mathrm{h}^2\left[\cos\left(\frac{l}{\sqrt{R_\mathrm{h}^2+S_\mathrm{h}^2}}\right) - \cos\left(\frac{l'}{\sqrt{R_\mathrm{h}^2+S_\mathrm{h}^2}}\right)\right]^2 \\
&\quad + R_\mathrm{h}^2\left[\sin\left(\frac{l}{\sqrt{R_\mathrm{h}^2+S_\mathrm{h}^2}}\right) - \sin\left(\frac{l'}{\sqrt{R_\mathrm{h}^2+S_\mathrm{h}^2}}\right)\right]^2 + \frac{S_\mathrm{h}^2(l-l')^2}{R_\mathrm{h}^2+S_\mathrm{h}^2} && \text{(A.45)} \\
&= R_\mathrm{h}^2\left[2 - \cos\left(\frac{l}{\sqrt{R_\mathrm{h}^2+S_\mathrm{h}^2}}\right)\cos\left(\frac{l'}{\sqrt{R_\mathrm{h}^2+S_\mathrm{h}^2}}\right)\right. \\
&\quad \left. - \sin\left(\frac{l}{\sqrt{R_\mathrm{h}^2+S_\mathrm{h}^2}}\right)\sin\left(\frac{l'}{\sqrt{R_\mathrm{h}^2+S_\mathrm{h}^2}}\right)\right] + \frac{S_\mathrm{h}^2(l-l')^2}{R_\mathrm{h}^2+S_\mathrm{h}^2} && \text{(A.46)} \\
&= R_\mathrm{h}^2\left[2 - \cos\left(\frac{l-l'}{\sqrt{R_\mathrm{h}^2+S_\mathrm{h}^2}}\right)\right] + \frac{S_\mathrm{h}^2(l-l')^2}{R_\mathrm{h}^2+S_\mathrm{h}^2} && \text{(A.47)} \\
&= f_1(l-l') && \text{(A.48)}
\end{aligned}$$

with

$$f_1(l) = R_\mathrm{h}^2\left[2 - \cos\left(\frac{l}{\sqrt{R_\mathrm{h}^2+S_\mathrm{h}^2}}\right)\right] + \frac{S_\mathrm{h}^2 l^2}{R_\mathrm{h}^2+S_\mathrm{h}^2}\,. \tag{A.49}$$

Furthermore, the tangential unit vector can be determined using (2.25). It follows

$$\hat{\boldsymbol{\tau}}(l) = \frac{R_\mathrm{h}}{\sqrt{R_\mathrm{h}^2+S_\mathrm{h}^2}}\left[-\sin\left(\frac{l}{\sqrt{R_\mathrm{h}^2+S_\mathrm{h}^2}}\right)\boldsymbol{e}_x + \cos\left(\frac{l}{\sqrt{R_\mathrm{h}^2+S_\mathrm{h}^2}}\right)\boldsymbol{e}_y\right] + \frac{S_\mathrm{h}}{\sqrt{R_\mathrm{h}^2+S_\mathrm{h}^2}}\boldsymbol{e}_z \tag{A.50}$$

and, therefore,

$$\begin{aligned}
\hat{\boldsymbol{\tau}}(l)\cdot\hat{\boldsymbol{\tau}}(l') &= \frac{R_\mathrm{h}^2}{R_\mathrm{h}^2+S_\mathrm{h}^2}\left[\sin\left(\frac{l}{\sqrt{R_\mathrm{h}^2+S_\mathrm{h}^2}}\right)\sin\left(\frac{l'}{\sqrt{R_\mathrm{h}^2+S_\mathrm{h}^2}}\right)\right. \\
&\quad \left. + \cos\left(\frac{l}{\sqrt{R_\mathrm{h}^2+S_\mathrm{h}^2}}\right)\cos\left(\frac{l'}{\sqrt{R_\mathrm{h}^2+S_\mathrm{h}^2}}\right)\right] + \frac{S_\mathrm{h}^2}{R_\mathrm{h}^2+S_\mathrm{h}^2} && \text{(A.51)} \\
&= \frac{R_\mathrm{h}^2}{R_\mathrm{h}^2+S_\mathrm{h}^2}\cos\left(\frac{l-l'}{\sqrt{R_\mathrm{h}^2+S_\mathrm{h}^2}}\right) + \frac{S_\mathrm{h}^2}{R_\mathrm{h}^2+S_\mathrm{h}^2} && \text{(A.52)} \\
&= f_2(l-l') && \text{(A.53)}
\end{aligned}$$

with

$$f_2(l) = \frac{R_\mathrm{h}^2}{R_\mathrm{h}^2 + S_\mathrm{h}^2} \cos\left(\frac{l}{\sqrt{R_\mathrm{h}^2 + S_\mathrm{h}^2}}\right) + \frac{S_\mathrm{h}^2}{R_\mathrm{h}^2 + S_\mathrm{h}^2}\,. \tag{A.54}$$

This concludes the proof. □

Now a similar result shall be proofed for multiconductor transmission lines, specifically the two wire line. The results can be generalized for N wires inductively. The question is under what conditions two different trajectories $\boldsymbol{x}_{\mathrm{c}1}$ and $\boldsymbol{x}_{\mathrm{c}2}$ fulfill the symmetry condition.

Theorem 2. *Let $\boldsymbol{x}_{\mathrm{c}1}(l)$ and $\boldsymbol{x}_{\mathrm{c}2}(l)$ be two curves. Then the following assertions are equivalent*

(i) $\|\boldsymbol{x}_{cm}(l) - \boldsymbol{x}_{cn}(l')\|^2 = f_{mn}(l - l')$ *for* $m, n \in \{1, 2\}$*, where* f_{mn} *are some arbitrary functions, i.e. the norm is a function of* $l - l'$ *for all* m, n*.*

(ii) $\boldsymbol{x}_{\mathrm{c}1}$ *and* $\boldsymbol{x}_{\mathrm{c}2}$ *are helices (including its special cases) and one curve is just a transformation of the other, i.e.* $\boldsymbol{x}_{\mathrm{c}2}(l) = \Theta\boldsymbol{x}_{\mathrm{c}1}(l)$ *with*

$$\Theta\boldsymbol{x}_{\mathrm{c}1}(l) = \begin{pmatrix} C_1\cos(C_2) & -C_1\sin(C_2) & 0 \\ C_1\sin(C_2) & C_1\cos(C_2) & 0 \\ 0 & 0 & 1 \end{pmatrix} \boldsymbol{x}_{\mathrm{c}1}(l) + \begin{pmatrix} 0 \\ 0 \\ C_3 \end{pmatrix} \tag{A.55}$$

with the constant real parameters C_1, C_2, C_3*.*

Proof. "$(i) \Rightarrow (ii)$" Assuming that (i) holds. It follows from Theorem 1 that $\boldsymbol{x}_{\mathrm{c}1}$ and $\boldsymbol{x}_{\mathrm{c}2}$ are helices. A helix can be transformed via rotation, scaling and translation to yield an arbitrary different helix. Let such a transformation be denoted by Θ. Then $\boldsymbol{x}_{\mathrm{c}2}(l) = \Theta\boldsymbol{x}_{\mathrm{c}1}(l)$. The transformation acts on each coordinate yielding

$$\|\boldsymbol{x}_{\mathrm{c}1}(l) - \boldsymbol{x}_{\mathrm{c}2}(l')\|^2 = \|\boldsymbol{x}_{\mathrm{c}1}(l) - \Theta\boldsymbol{x}_{\mathrm{c}1}(l')\|^2 \tag{A.56}$$

$$\begin{aligned} &= [(\boldsymbol{x}_{\mathrm{c}1})_1(l) - (\Theta\boldsymbol{x}_{\mathrm{c}1})_1(l')]^2 + [(\boldsymbol{x}_{\mathrm{c}1})_2(l) - (\Theta\boldsymbol{x}_{\mathrm{c}1})_2(l')]^2 \\ &\quad + [(\boldsymbol{x}_{\mathrm{c}1})_3(l) - (\Theta\boldsymbol{x}_{\mathrm{c}1})_3(l')]^2 \end{aligned} \tag{A.57}$$

$$\begin{aligned} &= \left[R_\mathrm{h}\,\cos\left(\frac{l}{\sqrt{R_\mathrm{h}^2 + S_\mathrm{h}^2}}\right) - (\Theta\boldsymbol{x}_{\mathrm{c}1})_1(l')\right]^2 \\ &\quad + \left[R_\mathrm{h}\,\sin\left(\frac{l}{\sqrt{R_\mathrm{h}^2 + S_\mathrm{h}^2}}\right) - (\Theta\boldsymbol{x}_{\mathrm{c}1})_2(l')\right]^2 \\ &\quad + \left[\frac{S_\mathrm{h}\,l}{\sqrt{R_\mathrm{h}^2 + S_\mathrm{h}^2}} - (\Theta\boldsymbol{x}_{\mathrm{c}1})_3(l')\right]^2 \end{aligned} \tag{A.58}$$

$$\begin{aligned} &= R_\mathrm{h}^2 + (\Theta\boldsymbol{x}_{\mathrm{c}1})_1^2(l') + (\Theta\boldsymbol{x}_{\mathrm{c}1})_2^2(l') \\ &\quad - 2R_\mathrm{h}\left[(\Theta\boldsymbol{x}_{\mathrm{c}1})_1(l')\cos\left(\frac{l}{\sqrt{R_\mathrm{h}^2 + S_\mathrm{h}^2}}\right) + (\Theta\boldsymbol{x}_{\mathrm{c}1})_2(l')\sin\left(\frac{l}{\sqrt{R_\mathrm{h}^2 + S_\mathrm{h}^2}}\right)\right] \\ &\quad + \left[\frac{S_\mathrm{h}\,l}{\sqrt{R_\mathrm{h}^2 + S_\mathrm{h}^2}} - (\Theta\boldsymbol{x}_{\mathrm{c}1})_3(l')\right]^2. \end{aligned} \tag{A.59}$$

Since (i) holds, three conditions on Θ follow

$$(\Theta \boldsymbol{x}_{\mathrm{c1}})_1^2(l') + (\Theta \boldsymbol{x}_{\mathrm{c1}})_2^2(l') = \text{const.} \tag{A.60}$$

$$(\Theta \boldsymbol{x}_{\mathrm{c1}})_1(l') \cos\left(\frac{l}{\sqrt{R_{\mathrm{h}}^2 + S_{\mathrm{h}}^2}}\right) + (\Theta \boldsymbol{x}_{\mathrm{c1}})_2(l') \sin\left(\frac{l}{\sqrt{R_{\mathrm{h}}^2 + S_{\mathrm{h}}^2}}\right) = g_1(l - l') \tag{A.61}$$

$$\frac{S_{\mathrm{h}}\, l}{\sqrt{R_{\mathrm{h}}^2 + S_{\mathrm{h}}^2}} - (\Theta \boldsymbol{x}_{\mathrm{c1}})_3(l') = g_2(l - l') \tag{A.62}$$

for all l', where g_1 and g_2 are arbitrary functions.

The first condition (A.60) is fulfilled if and only if

$$(\Theta \boldsymbol{x}_{\mathrm{c1}})_1(l') = C_1 \cos(\alpha(l')) \tag{A.63}$$

$$(\Theta \boldsymbol{x}_{\mathrm{c1}})_2(l') = C_1 \sin(\alpha(l')) \tag{A.64}$$

where α is a yet unknown function. Inserting the latter results into (A.61) yields

$$g_1(l - l') = C_1 \cos\left(\frac{l}{\sqrt{R_{\mathrm{h}}^2 + S_{\mathrm{h}}^2}} - \alpha(l')\right) \tag{A.65}$$

after some simple mathematical manipulations. It follows

$$\alpha(l') = \frac{l'}{\sqrt{R_{\mathrm{h}}^2 + S_{\mathrm{h}}^2}} + C_2\,. \tag{A.66}$$

Similarly, from (A.62) follows immediately

$$(\Theta \boldsymbol{x}_1)_3(l') = \frac{S_{\mathrm{h}}\, l'}{\sqrt{R_{\mathrm{h}}^2 + S_{\mathrm{h}}^2}} + C_3\,. \tag{A.67}$$

In summary, the transformation depends on three parameters C_1, C_2 and C_3 with

$$(\Theta \boldsymbol{x}_{\mathrm{c1}})_1(l') = C_1 \cos\left(\frac{l'}{\sqrt{R_{\mathrm{h}}^2 + S_{\mathrm{h}}^2}} + C_2\right) \tag{A.68}$$

$$(\Theta \boldsymbol{x}_{\mathrm{c1}})_2(l') = C_1 \sin\left(\frac{l'}{\sqrt{R_{\mathrm{h}}^2 + S_{\mathrm{h}}^2}} + C_2\right) \tag{A.69}$$

$$(\Theta \boldsymbol{x}_{\mathrm{c1}})_3(l') = \frac{S_{\mathrm{h}}\, l'}{\sqrt{R_{\mathrm{h}}^2 + S_{\mathrm{h}}^2}} + C_3\,. \tag{A.70}$$

The latter results describe a scaling in the x_1-x_2-plane with C_1, a rotation in the x_1-x_2-plane by C_2 and a translation in x_3-direction by C_3. This coincides with the transformation given in (ii).

The proof of the implication $(ii) \Rightarrow (i)$ is straight forward by inserting the helix equation for $\boldsymbol{x}_{\mathrm{c1}}$ into (A.55) and seeing that $\boldsymbol{x}_{\mathrm{c2}}$ is a helix as well and that (i) is fulfilled. □

Appendix B

Mathematical identities and simplifications

B.1 Integral identities

Important integral identities are presented in this appendix. It holds with the definition of E_1 in Eq. (4.63))

$$\int_0^\infty \left(\frac{\exp(-\mathrm{j}k\sqrt{(l-l')^2+a^2})}{\sqrt{(l-l')^2+a^2}} - \frac{\exp(-\mathrm{j}k\sqrt{(l-l')^2+b^2})}{\sqrt{(l-l')^2+b^2}} \right) \mathrm{e}^{-\mathrm{j}kl'} \,\mathrm{d}l' = \left[E_1(\mathrm{j}k(\sqrt{l^2+a^2}-l)) - E_1(\mathrm{j}k(\sqrt{l^2+b^2}-l)) \right] \mathrm{e}^{-\mathrm{j}kl} \quad \text{(B.1)}$$

$$\int_0^\infty \left(\frac{\exp(-\mathrm{j}k\sqrt{(l-l')^2+a^2})}{\sqrt{(l-l')^2+a^2}} - \frac{\exp(-\mathrm{j}k\sqrt{(l-l')^2+b^2})}{\sqrt{(l-l')^2+b^2}} \right) \mathrm{e}^{\mathrm{j}kl'} \,\mathrm{d}l' = \left[E_1(\mathrm{j}k(\sqrt{l^2+b^2}+l)) - E_1(\mathrm{j}k(\sqrt{l^2+a^2}+l)) + 2\ln\left(\frac{b}{a}\right) \right] \mathrm{e}^{\mathrm{j}kl} \quad \text{(B.2)}$$

$$\begin{aligned} \int_0^\zeta \left(\frac{\exp(-\mathrm{j}k\sqrt{(l-l')^2+a^2})}{\sqrt{(l-l')^2+a^2}} - \frac{\exp(-\mathrm{j}k\sqrt{(l-l')^2+b^2})}{\sqrt{(l-l')^2+b^2}} \right) \mathrm{e}^{\pm\mathrm{j}kl'} \,\mathrm{d}l' \\ = \pm \Big[E_1(\mathrm{j}k(\sqrt{l^2+b^2} \pm l)) + E_1(\mathrm{j}k(\sqrt{(l-\zeta)^2+b^2} \pm (l-\zeta))) \\ - E_1(\mathrm{j}k(\sqrt{l^2+a^2} \pm l)) - E_1(\mathrm{j}k(\sqrt{(l-\zeta)^2+a^2} \pm (l-\zeta))) \Big] \mathrm{e}^{\pm\mathrm{j}kl} \end{aligned} \quad \text{(B.3)}$$

B.2 Simplification of the first iteration reflection coefficient

In the following the Eq. (4.61) is simplified. The integrals are analyzed separately. The first integral can be solved with the identities from App. B.1. It holds

$$\frac{\hat{\boldsymbol{\mathcal{D}}} P^{(0)}(-l_\mathrm{p})}{4\mathrm{j}k\ln\left(\frac{2h}{a}\right)} \int_{-l_\mathrm{p}}^\infty P^{(0)}(l') g_0(l'+l_\mathrm{p}) \,\mathrm{d}l' \quad \text{(B.4)}$$

$$= \frac{\hat{\boldsymbol{\mathcal{D}}} P^{(0)}(-l_\mathrm{p})}{4\mathrm{j}k \ln\left(\frac{2h}{a}\right)} \int_{-l_\mathrm{p}}^{\infty} \left(\mathrm{e}^{\mathrm{j}kl'} + \Gamma^{(0)} \mathrm{e}^{-\mathrm{j}kl'}\right) g_0(l' + l_\mathrm{p}) \,\mathrm{d}l' \tag{B.5}$$

$$= \frac{Z}{Z_\mathrm{C} + Z} \frac{\mathrm{e}^{-\mathrm{j}kl_\mathrm{p}}}{2 \ln\left(\frac{2h}{a}\right)} \int_{-l_\mathrm{p}}^{\infty} \left(\mathrm{e}^{\mathrm{j}kl'} + \Gamma^{(0)} \mathrm{e}^{-\mathrm{j}kl'}\right) g_0(l' + l_\mathrm{p}) \,\mathrm{d}l' \tag{B.6}$$

$$= \frac{Z}{Z_\mathrm{C} + Z} \frac{\mathrm{e}^{-2\mathrm{j}kl_\mathrm{p}}}{2 \ln\left(\frac{2h}{a}\right)} \int_{0}^{\infty} \left(\mathrm{e}^{\mathrm{j}k\xi} + \frac{Z_\mathrm{C} - Z}{Z_\mathrm{C} + Z} \mathrm{e}^{-\mathrm{j}k\xi}\right) g_0(\xi) \,\mathrm{d}\xi \tag{B.7}$$

$$= \frac{Z}{Z_\mathrm{C} + Z} \frac{\mathrm{e}^{-2\mathrm{j}kl_\mathrm{p}}}{2 \ln\left(\frac{2h}{a}\right)} \left[[E_1(2\mathrm{j}kh) - E_1(\mathrm{j}ka)] \frac{2Z}{Z_\mathrm{C} + Z} + 2 \ln\left(\frac{2h}{a}\right) \right]. \tag{B.8}$$

The next integral is simplified using integration by parts, i.e.

$$\frac{1}{4\mathrm{j}k \ln\left(\frac{2h}{a}\right)} \int_{-l_\mathrm{p}}^{\infty} P^{(0)}(l') \hat{\boldsymbol{\mathcal{D}}} [\hat{\boldsymbol{\mathcal{G}}}_\Phi - \hat{\boldsymbol{\mathcal{G}}}_0] \hat{\boldsymbol{\mathcal{D}}} P^{(0)}(l') \,\mathrm{d}l' \tag{B.9}$$

$$= \frac{1}{4\mathrm{j}k \ln\left(\frac{2h}{a}\right)} \int_{-l_\mathrm{p}}^{\infty} P^{(0)}(l') \frac{\partial}{\partial l'} [\hat{\boldsymbol{\mathcal{G}}}_\Phi - \hat{\boldsymbol{\mathcal{G}}}_0] \hat{\boldsymbol{\mathcal{D}}} P^{(0)}(l') \,\mathrm{d}l' \tag{B.10}$$

$$= \frac{1}{4\mathrm{j}k \ln\left(\frac{2h}{a}\right)} \left[P^{(0)}(l') [\hat{\boldsymbol{\mathcal{G}}}_\Phi - \hat{\boldsymbol{\mathcal{G}}}_0] \hat{\boldsymbol{\mathcal{D}}} P^{(0)}(l') \right]_{l'=-l_\mathrm{p}}^{\infty}$$
$$- \frac{1}{4\mathrm{j}k \ln\left(\frac{2h}{a}\right)} \int_{-l_\mathrm{p}}^{\infty} \frac{\partial}{\partial l'} P^{(0)}(l') [\hat{\boldsymbol{\mathcal{G}}}_\Phi - \hat{\boldsymbol{\mathcal{G}}}_0] \hat{\boldsymbol{\mathcal{D}}} P^{(0)}(l') \,\mathrm{d}l' \tag{B.11}$$

$$= -\frac{P^{(0)}(-l_\mathrm{p})}{4\mathrm{j}k \ln\left(\frac{2h}{a}\right)} \int_{-l_\mathrm{p}}^{\infty} [g_\Phi(-l_\mathrm{p}, l'') - g_0(l_\mathrm{p} + l'')] \frac{\partial}{\partial l''} P^{(0)}(l'') \,\mathrm{d}l''$$
$$- \frac{1}{4\mathrm{j}k \ln\left(\frac{2h}{a}\right)} \int_{-l_\mathrm{p}}^{\infty} \int_{-l_\mathrm{p}}^{\infty} \frac{\partial}{\partial l'} P^{(0)}(l') [g_\Phi(l', l'') - g_0(l' - l'')] \frac{\partial}{\partial l''} P^{(0)}(l'') \,\mathrm{d}l'' \mathrm{d}l'. \tag{B.12}$$

If the wire is connected to the ground, the function $g_\Phi(-l_\mathrm{p}, l'')$ is 0 for all l''. If the wire is not connected to the ground the function $P^{(0)}(-l_\mathrm{p})$ becomes 0. Hence, the term including $P^{(0)}(-l_\mathrm{p}) g_\Phi(-l_\mathrm{p}, l'')$ always vanishes. It holds

$$\frac{1}{4\mathrm{j}k \ln\left(\frac{2h}{a}\right)} \int_{-l_\mathrm{p}}^{\infty} P^{(0)}(l') \hat{\boldsymbol{\mathcal{D}}} [\hat{\boldsymbol{\mathcal{G}}}_\Phi - \hat{\boldsymbol{\mathcal{G}}}_0] \hat{\boldsymbol{\mathcal{D}}} P^{(0)}(l') \,\mathrm{d}l'$$

$$= \frac{P^{(0)}(-l_\mathrm{p})}{4\mathrm{j}k \ln\left(\frac{2h}{a}\right)} \int_{-l_\mathrm{p}}^{\infty} g_0(l_\mathrm{p} + l'') \frac{\partial}{\partial l''} P^{(0)}(l'') \,\mathrm{d}l''$$
$$- \frac{1}{4\mathrm{j}k \ln\left(\frac{2h}{a}\right)} \int_{-l_\mathrm{p}}^{\infty} \int_{-l_\mathrm{p}}^{\infty} \frac{\partial}{\partial l'} P^{(0)}(l') [g_\Phi(l', l'') - g_0(l' - l'')] \frac{\partial}{\partial l''} P^{(0)}(l'') \,\mathrm{d}l'' \mathrm{d}l'. \tag{B.13}$$

The single integral is solved using the results from App. B.1 to yield

$$\frac{1}{4\mathrm{j}k\ln\left(\frac{2h}{a}\right)}\int_{-l_\mathrm{p}}^{\infty} P^{(0)}(l')\hat{\boldsymbol{\mathcal{D}}}[\hat{\boldsymbol{\mathcal{G}}}_\Phi-\hat{\boldsymbol{\mathcal{G}}}_0]\hat{\boldsymbol{\mathcal{D}}}P^{(0)}(l')\,\mathrm{d}l'$$

$$=\frac{1}{4\ln\left(\frac{2h}{a}\right)}\left(\mathrm{e}^{-\mathrm{j}kl_\mathrm{p}}+\Gamma^{(0)}\mathrm{e}^{\mathrm{j}kl_\mathrm{p}}\right)\int_{-l_\mathrm{p}}^{\infty} g_0(l_\mathrm{p}+l'')\left(\mathrm{e}^{\mathrm{j}kl''}-\Gamma^{(0)}\mathrm{e}^{-\mathrm{j}kl''}\right)\mathrm{d}l''$$

$$-\frac{1}{4\mathrm{j}k\ln\left(\frac{2h}{a}\right)}\int_{-l_\mathrm{p}}^{\infty}\int_{-l_\mathrm{p}}^{\infty}\frac{\partial}{\partial l'}P^{(0)}(l')[g_\Phi(l',l'')-g_0(l'-l'')]\frac{\partial}{\partial l''}P^{(0)}(l'')\,\mathrm{d}l''\mathrm{d}l' \quad \text{(B.14)}$$

$$=\frac{\mathrm{e}^{-2\mathrm{j}kl_\mathrm{p}}}{4\ln\left(\frac{2h}{a}\right)}\left(1+\frac{Z_\mathrm{C}-Z}{Z_\mathrm{C}+Z}\right)\int_{0}^{\infty} g_0(\xi)\left(\mathrm{e}^{\mathrm{j}k\xi}-\frac{Z_\mathrm{C}-Z}{Z_\mathrm{C}+Z}\mathrm{e}^{-\mathrm{j}k\xi}\right)\mathrm{d}\xi$$

$$-\frac{1}{4\mathrm{j}k\ln\left(\frac{2h}{a}\right)}\int_{-l_\mathrm{p}}^{\infty}\int_{-l_\mathrm{p}}^{\infty}\frac{\partial}{\partial l'}P^{(0)}(l')[g_\Phi(l',l'')-g_0(l'-l'')]\frac{\partial}{\partial l''}P^{(0)}(l'')\,\mathrm{d}l''\mathrm{d}l' \quad \text{(B.15)}$$

$$=\frac{\mathrm{e}^{-2\mathrm{j}kl_\mathrm{p}}}{4\ln\left(\frac{2h}{a}\right)}\frac{2Z_\mathrm{C}}{Z_\mathrm{C}+Z}\left[[E_1(2\mathrm{j}kh)-E_1(\mathrm{j}ka)]\frac{2Z_\mathrm{C}}{Z_\mathrm{C}+Z}+2\ln\left(\frac{2h}{a}\right)\right]$$

$$-\frac{1}{4\mathrm{j}k\ln\left(\frac{2h}{a}\right)}\int_{-l_\mathrm{p}}^{\infty}\int_{-l_\mathrm{p}}^{\infty}\frac{\partial}{\partial l'}P^{(0)}(l')[g_\Phi(l',l'')-g_0(l'-l'')]\frac{\partial}{\partial l''}P^{(0)}(l'')\,\mathrm{d}l''\mathrm{d}l'. \quad \text{(B.16)}$$

Inserting Eqs. (B.8) and (B.16) into Eq. (4.61) and expanding the operators results in

$$\Gamma^{(1)}=-\frac{2ZZ_\mathrm{C}}{(Z_\mathrm{C}+Z)^2}\,\mathrm{e}^{-2\mathrm{j}kl_\mathrm{p}}+\frac{Z_\mathrm{C}^2+Z^2}{(Z_\mathrm{C}+Z)^2}\frac{E_1(2\mathrm{j}kh)-E_1(\mathrm{j}ka)}{\ln\left(\frac{2h}{a}\right)}\,\mathrm{e}^{-2\mathrm{j}kl_\mathrm{p}}+\mathrm{e}^{-2\mathrm{j}kl_\mathrm{p}}$$

$$+\frac{1}{4\mathrm{j}k\ln\left(\frac{2h}{a}\right)}\int_{-l_\mathrm{p}}^{\infty}\int_{-l_\mathrm{p}}^{\infty}\Big\{k^2P^{(0)}(l')[g_\mathrm{A}(l',l'')-g_0(l'-l'')]P^{(0)}(l'')$$

$$-\frac{\partial}{\partial l'}P^{(0)}(l')[g_\Phi(l',l'')-g_0(l'-l'')]\frac{\partial}{\partial l''}P^{(0)}(l'')\Big\}\,\mathrm{d}l''\mathrm{d}l'. \quad \text{(B.17)}$$

Simplifying the result and rearranging the terms yields Eq. (4.62).

B.3 Simplification of the double integral for the first iteration reflection and scattering coefficient

Equation (4.65), the reflection coefficient for the first iteration, is modified in this appendix. The integration with the infinite interval is solved analytically, leaving only the finite

integration intervals. Thus, the double integral

$$\mathcal{I} = \int_{-l_\mathrm{p}}^{0} \int_{0}^{\infty} \Big\{ \frac{\partial}{\partial l'} P^{(0)}(l') [g_\Phi(l', l'') - g_0(l' - l'')] \frac{\partial}{\partial l''} P^{(0)}(l'') \\ - k^2 P^{(0)}(l') [g_\mathrm{A}(l', l'') - g_0(l' - l'')] P^{(0)}(l'') \Big\} \,\mathrm{d}l'' \mathrm{d}l' \quad \text{(B.18)}$$

is analyzed in this section.

The wire is parametrized as

$$\boldsymbol{x}_\mathrm{c}(l) = \begin{cases} \chi_1(l)\hat{\boldsymbol{x}}_1 + \chi_2(l)\hat{\boldsymbol{x}}_2 + \chi_3(l)\hat{\boldsymbol{x}}_3 & \text{for } -l_\mathrm{p} \leq l < 0 \\ h\,\hat{\boldsymbol{x}}_2 + l\,\hat{\boldsymbol{x}}_3 & \text{for } 0 \leq l < \infty\,. \end{cases} \quad \text{(B.19)}$$

The functions $\chi_1(l), \chi_2(l), \chi_3(l)$ characterize the specific port and are arbitrary continuous functions at this point. The tangential unit vector is

$$\hat{\boldsymbol{\tau}}(l) = \begin{cases} \hat{\boldsymbol{\tau}}_\mathrm{p}(l) & \text{for } -l_\mathrm{p} \leq l < 0 \\ \hat{\boldsymbol{x}}_3 & \text{for } 0 \leq l < \infty\,, \end{cases} \quad \text{(B.20)}$$

where $\hat{\boldsymbol{\tau}}_\mathrm{p}$ depends on the trajectory of the port. With this parametrization it holds for $-l_\mathrm{p} \leq l' < 0$ and $0 \leq l'' < \infty$

$$\|\boldsymbol{x}_\mathrm{c}(l') - \boldsymbol{x}_\mathrm{c}(l'')\|^2 = \chi_1^2(l') + [\chi_2(l') - h]^2 + [\chi_3(l') - l'']^2 \quad \text{(B.21)}$$

$$\|\boldsymbol{x}_\mathrm{c}(l') - \underset{\sim}{\boldsymbol{x}}_\mathrm{c}(l'')\|^2 = \chi_1^2(l') + [\chi_2(l') + h]^2 + [\chi_3(l') - l'']^2 \quad \text{(B.22)}$$

$$\hat{\boldsymbol{\tau}}(l') \cdot \hat{\boldsymbol{\tau}}(l'') = \hat{\boldsymbol{\tau}}(l') \cdot \hat{\boldsymbol{x}}_3 \quad \text{(B.23)}$$

$$\hat{\boldsymbol{\tau}}(l') \cdot \underset{\sim}{\hat{\boldsymbol{\tau}}}(l'') = \hat{\boldsymbol{\tau}}(l') \cdot \hat{\boldsymbol{x}}_3\,. \quad \text{(B.24)}$$

With this it follows from Eqs. (2.36) and (2.41)

$$g_\mathrm{A}(l', l'') = g_\Phi(l', l'')\, \hat{\boldsymbol{\tau}}(l') \cdot \hat{\boldsymbol{x}}_3 \quad \text{(B.25)}$$

and

$$g_\Phi(l', l'') = \frac{\exp\big(-\mathrm{j}k\sqrt{\chi_1^2(l') + [\chi_2(l') - h]^2 + [\chi_3(l') - l'']^2 + a^2}\big)}{\sqrt{\chi_1^2(l') + [\chi_2(l') - h]^2 + [\chi_3(l') - l'']^2 + a^2}} \\ - \frac{\exp\big(-\mathrm{j}k\sqrt{\chi_1^2(l') + [\chi_2(l') + h]^2 + [\chi_3(l') - l'']^2 + a^2}\big)}{\sqrt{\chi_1^2(l') + [\chi_2(l') + h]^2 + [\chi_3(l') - l'']^2 + a^2}} \quad \text{(B.26)}$$

for $-l_\mathrm{p} \leq l' < 0$ and $0 \leq l'' < \infty$. Inserting the latter equation into Eq. (B.18) and inserting $P^{(0)}(l'')$ results in

$$\mathcal{I} = \int_{-l_\mathrm{p}}^{0} \int_{0}^{\infty} \Big\{ g_\Phi(l', l'') \Big(\mathrm{j}k \frac{\partial}{\partial l'} P^{(0)}(l') - k^2 P^{(0)}(l') \hat{\boldsymbol{\tau}}(l') \cdot \hat{\boldsymbol{x}}_3 \Big) \mathrm{e}^{\mathrm{j}kl''} \\ - g_\Phi(l', l'') \Big(\mathrm{j}k \frac{\partial}{\partial l'} P^{(0)}(l') + k^2 P^{(0)}(l') \hat{\boldsymbol{\tau}}(l') \cdot \hat{\boldsymbol{x}}_3 \Big) \Gamma^{(0)}\, \mathrm{e}^{-\mathrm{j}kl''} \\ - g_0(l' - l'') \Big(\mathrm{j}k \frac{\partial}{\partial l'} P^{(0)}(l') - k^2 P^{(0)}(l') \Big) \mathrm{e}^{\mathrm{j}kl''} \\ + g_0(l' - l'') \Big(\mathrm{j}k \frac{\partial}{\partial l'} P^{(0)}(l') + k^2 P^{(0)}(l') \Big) \Gamma^{(0)}\, \mathrm{e}^{-\mathrm{j}kl''} \Big\} \,\mathrm{d}l'' \mathrm{d}l'\,. \quad \text{(B.27)}$$

Using the integral identities from App. B.1 yields

$$\begin{aligned}
\mathcal{I} = \int_{-l_\mathrm{p}}^{0} \Bigg\{ & \left(\mathrm{j}k \frac{\partial}{\partial l'} P^{(0)}(l') - k^2 P^{(0)}(l') \hat{\boldsymbol{\tau}}(l') \cdot \hat{\boldsymbol{x}}_3 \right) \Bigg[\ln\left(\frac{\chi_1^2(l') + [\chi_2(l') + h]^2 + a^2}{\chi_1^2(l') + [\chi_2(l') - h]^2 + a^2} \right) \\
& + E_1\Big(\mathrm{j}k \Big(\sqrt{\chi_1^2(l') + [\chi_2(l') + h]^2 + \chi_3^2(l') + a^2} + \chi_3(l') \Big) \Big) \\
& - E_1\Big(\mathrm{j}k \Big(\sqrt{\chi_1^2(l') + [\chi_2(l') - h]^2 + \chi_3^2(l') + a^2} + \chi_3(l') \Big) \Big) \Bigg] \mathrm{e}^{\mathrm{j}k\chi_3(l')} \\
& + \left(\mathrm{j}k \frac{\partial}{\partial l'} P^{(0)}(l') + k^2 P^{(0)}(l') \hat{\boldsymbol{\tau}}(l') \cdot \hat{\boldsymbol{x}}_3 \right) \Gamma^{(0)} \Big[\\
& \qquad E_1\Big(\mathrm{j}k \Big(\sqrt{\chi_1^2(l') + [\chi_2(l') + h]^2 + \chi_3^2(l') + a^2} - \chi_3(l') \Big) \Big) \\
& \qquad - E_1\Big(\mathrm{j}k \Big(\sqrt{\chi_1^2(l') + [\chi_2(l') - h]^2 + \chi_3^2(l') + a^2} - \chi_3(l') \Big) \Big) \Big] \mathrm{e}^{-\mathrm{j}k\chi_3(l')} \\
& - \left(\mathrm{j}k \frac{\partial}{\partial l'} P^{(0)}(l') - k^2 P^{(0)}(l') \right) \Bigg[2 \ln\left(\frac{2h}{a} \right) + E_1\Big(\mathrm{j}k \Big(\sqrt{l'^2 + 4h^2} + l' \Big) \Big) \\
& \qquad - E_1\Big(\mathrm{j}k \Big(\sqrt{l'^2 + a^2} + l' \Big) \Big) \Bigg] \mathrm{e}^{\mathrm{j}kl'} \\
& - \left(\mathrm{j}k \frac{\partial}{\partial l'} P^{(0)}(l') + k^2 P^{(0)}(l') \right) \Gamma^{(0)} \Big[E_1\Big(\mathrm{j}k \Big(\sqrt{l'^2 + 4h^2} - l' \Big) \Big) \\
& \qquad - E_1\Big(\mathrm{j}k \Big(\sqrt{l'^2 + a^2} - l' \Big) \Big) \Big] \mathrm{e}^{-\mathrm{j}kl'} \Bigg\} \, \mathrm{d}l' \qquad \text{(B.28)}
\end{aligned}$$

This concludes the derivation. The numerical integration of the single integral with finite limits is much faster than the double integration in Eq. (B.18).

B.4 Asymptotic approximation of the first iteration scattered current

In the following Eq. (4.104) is approximated asymptotically. First, the second addend in Eq. (4.104) is analyzed. It holds

$$\begin{aligned}
\left[\hat{\mathbf{Id}} - \frac{1}{2\ln\left(\frac{2h}{a}\right)} \hat{\boldsymbol{\mathcal{G}}}_0 \right] I^{(0)}(l) &= I^{(0)}(l) - \frac{1}{2\ln\left(\frac{2h}{a}\right)} \int_{-l_\mathrm{p}}^{\infty} g_0(l - l') I^{(0)}(l') \, \mathrm{d}l' \qquad \text{(B.29)} \\
&= I^{(0)}(l) - \frac{1}{2\ln\left(\frac{2h}{a}\right)} \int_{-l_\mathrm{p}}^{0} g_0(l - l') I_\mathrm{p}^{(0)}(l') \, \mathrm{d}l' \\
&\quad - \frac{1}{2\ln\left(\frac{2h}{a}\right)} \int_{0}^{\infty} g_0(l - l') \left(I_\infty^{(0)} \, \mathrm{e}^{-\mathrm{j}k_\theta l'} + \Psi^{(0)} \, \mathrm{e}^{-\mathrm{j}kl'} \right) \mathrm{d}l' \qquad \text{(B.30)} \\
&= I^{(0)}(l) - \frac{1}{2\ln\left(\frac{2h}{a}\right)} \int_{-l_\mathrm{p}}^{0} g_0(l - l') I_\mathrm{p}^{(0)}(l') \, \mathrm{d}l'
\end{aligned}$$

$$- \frac{1}{2\ln\left(\frac{2h}{a}\right)} \int_{-l}^{\infty} g_0(\xi)\left(I_\infty^{(0)}\,\mathrm{e}^{-\mathrm{j}k_\theta(\xi+l)} + \Psi^{(0)}\,\mathrm{e}^{-\mathrm{j}k(\xi+l)}\right)\mathrm{d}\xi\,. \quad \text{(B.31)}$$

When l becomes greater the function $g_0(l-l')$ tends to 0 when l' is bounded. Hence, it holds asymptotically for large l

$$\left[\hat{\mathbf{Id}} - \frac{1}{2\ln\left(\frac{2h}{a}\right)}\hat{\boldsymbol{\mathcal{G}}}_0\right] I^{(0)}(l) \sim I_\infty^{(0)}\left(1 - \frac{1}{2\ln\left(\frac{2h}{a}\right)} \int_{-\infty}^{\infty} g_0(\xi)\,\mathrm{e}^{-\mathrm{j}k_\theta\xi}\,\mathrm{d}\xi\right)\mathrm{e}^{-\mathrm{j}k_\theta l}$$
$$+ \Psi^{(0)}\left(1 - \frac{1}{2\ln\left(\frac{2h}{a}\right)} \int_{-\infty}^{\infty} g_0(\xi)\,\mathrm{e}^{-\mathrm{j}k\xi}\,\mathrm{d}\xi\right)\mathrm{e}^{-\mathrm{j}kl}\,. \quad \text{(B.32)}$$

The remaining integrals are the Fourier transform of g_0 (see Eq. (2.59)). It follows

$$\left[\hat{\mathbf{Id}} - \frac{1}{2\ln\left(\frac{2h}{a}\right)}\hat{\boldsymbol{\mathcal{G}}}_0\right] I^{(0)}(l) \sim I_\infty^{(0)}\left(1 - \frac{\tilde{g}_0(k_\theta)}{2\ln\left(\frac{2h}{a}\right)}\right)\mathrm{e}^{-\mathrm{j}k_\theta l}\,. \quad \text{(B.33)}$$

Next, the integral involving $\hat{\boldsymbol{\mathcal{G}}}_\Phi$ in Eq. (4.104) is analyzed for large l using Eqs. (4.52) and (4.57). Using integration by parts results, similarly as in Eq. (B.13), in

$$- \frac{1}{2\ln\left(\frac{2h}{a}\right)} \int_{-l_\mathrm{p}}^{\infty} K(l,l')\hat{\boldsymbol{\mathcal{D}}}[\hat{\boldsymbol{\mathcal{G}}}_\Phi - \hat{\boldsymbol{\mathcal{G}}}_0]\hat{\boldsymbol{\mathcal{D}}} I^{(0)}(l')\,\mathrm{d}l'$$
$$\sim \frac{P^{(0)}(-l_\mathrm{p})}{4\mathrm{j}k\ln\left(\frac{2h}{a}\right)} \int_{-l_\mathrm{p}}^{\infty} g_0(l_\mathrm{p}+l'')\frac{\partial}{\partial l''} I^{(0)}(l'')\,\mathrm{d}l''\mathrm{e}^{-\mathrm{j}kl}$$
$$- \frac{\mathrm{e}^{-\mathrm{j}kl}}{4\mathrm{j}k\ln\left(\frac{2h}{a}\right)} \int_{-l_\mathrm{p}}^{\infty}\int_{-l_\mathrm{p}}^{\infty} \frac{\partial}{\partial l'} P^{(0)}(l')[g_\Phi(l',l'') - g_0(l'-l'')]\frac{\partial}{\partial l''} I^{(0)}(l'')\,\mathrm{d}l''\mathrm{d}l'. \quad \text{(B.34)}$$

Evaluating $P^{(0)}(-l_\mathrm{p})$ and rewriting the first integral in operator form yields

$$- \frac{1}{2\ln\left(\frac{2h}{a}\right)} \int_{-l_\mathrm{p}}^{\infty} K(l,l')\hat{\boldsymbol{\mathcal{D}}}[\hat{\boldsymbol{\mathcal{G}}}_\Phi - \hat{\boldsymbol{\mathcal{G}}}_0]\hat{\boldsymbol{\mathcal{D}}} I^{(0)}(l')\,\mathrm{d}l'$$
$$\sim \frac{1}{\mathrm{j}k}\frac{Z_\mathrm{C}}{Z_\mathrm{C}+Z}\frac{\mathrm{e}^{-\mathrm{j}kl_\mathrm{p}}}{2\ln\left(\frac{2h}{a}\right)}\hat{\boldsymbol{\mathcal{G}}}_0\hat{\boldsymbol{\mathcal{D}}} I^{(0)}(-l_\mathrm{p})\,\mathrm{e}^{-\mathrm{j}kl}$$
$$- \frac{\mathrm{e}^{-\mathrm{j}kl}}{4\mathrm{j}k\ln\left(\frac{2h}{a}\right)} \int_{-l_\mathrm{p}}^{\infty}\int_{-l_\mathrm{p}}^{\infty} \frac{\partial}{\partial l'} P^{(0)}(l')[g_\Phi(l',l'') - g_0(l'-l'')]\frac{\partial}{\partial l''} I^{(0)}(l'')\,\mathrm{d}l''\mathrm{d}l'. \quad \text{(B.35)}$$

Moreover, the integral involving $\hat{\boldsymbol{\mathcal{G}}}_\mathrm{A}$ in Eq. (4.104) is asymptotically evaluated with

$$- \frac{1}{2\ln\left(\frac{2h}{a}\right)} \int_{-l_\mathrm{p}}^{\infty} K(l,l')k^2[\hat{\boldsymbol{\mathcal{G}}}_\mathrm{A} - \hat{\boldsymbol{\mathcal{G}}}_0] I^{(0)}(l')\,\mathrm{d}l'$$
$$\sim \frac{\mathrm{e}^{-\mathrm{j}kl}}{4\mathrm{j}k\ln\left(\frac{2h}{a}\right)} \int_{-l_\mathrm{p}}^{\infty}\int_{-l_\mathrm{p}}^{\infty} k^2 P^{(0)}(l')[g_\mathrm{A}(l',l'') - g_0(l'-l'')] I^{(0)}(l'')\,\mathrm{d}l''\mathrm{d}l'. \quad \text{(B.36)}$$

The last integral in Eq. (4.104) can be asymptotically evaluated using integration by parts as well. It holds

$$\frac{I^{(0)}(-l_\mathrm{p})}{2\ln\left(\frac{2h}{a}\right)} \int\limits_{-l_\mathrm{p}}^{\infty} K(l,l')\hat{\boldsymbol{\mathcal{D}}} g_0(l'+l_\mathrm{p})\,\mathrm{d}l' \tag{B.37}$$

$$\sim -\frac{I^{(0)}(-l_\mathrm{p})}{4\mathrm{j}k\ln\left(\frac{2h}{a}\right)} \int\limits_{-l_\mathrm{p}}^{\infty} P^{(0)}(l')\hat{\boldsymbol{\mathcal{D}}} g_0(l'+l_\mathrm{p})\,\mathrm{d}l'\,\mathrm{e}^{-\mathrm{j}kl} \tag{B.38}$$

$$= -\frac{I^{(0)}(-l_\mathrm{p})}{4\mathrm{j}k\ln\left(\frac{2h}{a}\right)} \left[\left[P^{(0)}(l')g_0(l'+l_\mathrm{p})\right]_{l'=-l_\mathrm{p}}^{\infty} - \int\limits_{-l_\mathrm{p}}^{\infty} \hat{\boldsymbol{\mathcal{D}}} P^{(0)}(l')g_0(l'+l_\mathrm{p})\,\mathrm{d}l'\right] \mathrm{e}^{-\mathrm{j}kl} \tag{B.39}$$

$$= \frac{I^{(0)}(-l_\mathrm{p})}{4\mathrm{j}k\ln\left(\frac{2h}{a}\right)} \left[P^{(0)}(-l_\mathrm{p})g_0(0) + \int\limits_{-l_\mathrm{p}}^{\infty} \hat{\boldsymbol{\mathcal{D}}} P^{(0)}(l')g_0(l'+l_\mathrm{p})\,\mathrm{d}l'\right] \mathrm{e}^{-\mathrm{j}kl} \tag{B.40}$$

Evaluating $P^{(0)}(-l_\mathrm{p})$ yields

$$\begin{aligned}\frac{I^{(0)}(-l_\mathrm{p})}{2\ln\left(\frac{2h}{a}\right)} \int\limits_{-l_\mathrm{p}}^{\infty} K(l,l')\hat{\boldsymbol{\mathcal{D}}} g_0(l'+l_\mathrm{p})\,\mathrm{d}l' \sim \frac{1}{\mathrm{j}k}\frac{Z_\mathrm{C}}{Z_\mathrm{C}+Z}\frac{\mathrm{e}^{-\mathrm{j}kl_\mathrm{p}}}{2\ln\left(\frac{2h}{a}\right)} g_0(0) I^{(0)}(-l_\mathrm{p})\,\mathrm{e}^{-\mathrm{j}kl} \\ + \frac{I^{(0)}(-l_\mathrm{p})}{4\mathrm{j}k\ln\left(\frac{2h}{a}\right)} \int\limits_{-l_\mathrm{p}}^{\infty} \hat{\boldsymbol{\mathcal{D}}} P^{(0)}(l')g_0(l'+l_\mathrm{p})\,\mathrm{d}l'\Bigg] \mathrm{e}^{-\mathrm{j}kl}\,.\end{aligned} \tag{B.41}$$

Inserting Eqs. (4.109), (B.33), (B.35), (B.36) and (B.41) into Eq. (4.104) results in the asymptotic approximation for the first iteration current, i.e. Eq. (4.110).

Bibliography

[1] R. F. Harrington, *Field Computation by Moment Methods*, English. Piscataway, NJ: IEEE Press, 1993, ISBN: 0780310144.

[2] P. Silvester and R. Ferrari, *Finite Elements for Electrical Engineers*. Cambridge University Press, 1996.

[3] A. Kost, *Numerische Methoden in der Berechnung elektromagnetischer Felder*. Springer, 2013, in German.

[4] A. Taflove and S. Hagness, Eds., *Computational Electrodynamics - The Finite-Difference Time-Domain Method*. Artech House, 2005.

[5] T. Weiland, *Eine Methode zur Lösung der Maxwellschen Gleichungen für sechskomponentige Felder auf diskreter Basis*. Hirzel, 1977, in German.

[6] C. R. Paul, *Analysis of Multiconductor Transmission Lines*, English, 2nd ed. Hoboken, N.J.: Wiley-Interscience, 2008.

[7] H.-G. Unger, *Elektromagnetische Wellen auf Leitungen*, German, 4th ed. Heidelberg, Germany: Hüthig, 1996, ISBN: 3778523902.

[8] H. Haase, *Full-wave field interactions of nonuniform transmission lines*, ser. Res electricae Magdeburgenses 9. Magdeburg: Univ., 2005, Dissertation.

[9] J. Guo, M. Rubinstein, V. Cooray, and F. Rachidi, "On the modeling of non-vertical risers in the interaction of electromagnetic fields with overhead lines," *IEEE Transactions on Electromagnetic Compatibility*, vol. 61, no. 3, pp. 631–636, 2019. DOI: 10.1109/TEMC.2019.2903335.

[10] S. V. Tkachenko, F. Middelstaedt, and R. Vick, "Method of modal parameters for the straight wire and singularity expansion method," *IEEE Letters on Electromagnetic Compatibility Practice and Applications*, vol. 2, no. 4, pp. 152–155, 2020. DOI: 10.1109/LEMCPA.2020.3020751.

[11] ——, "The method of modal parameters for the wire segments with symmetrical geometry and singularity expansion method," *IEEE Letters on Electromagnetic Compatibility Practice and Applications*, vol. 4, no. 1, pp. 2–6, 2022. DOI: 10.1109/LEMCPA.2021.3132254.

[12] S. Tkatchenko, F. Rachidi, and M. Ianoz, "High-frequency electromagnetic field coupling to long terminated lines," *IEEE Transactions on Electromagnetic Compatibility*, vol. 43, no. 2, pp. 117–129, 2001. DOI: 10.1109/15.925531.

[13] F. Rachidi and S. V. Tkachenko, *Electromagnetic Field Interaction with Transmission Lines*. WIT Press, 2008.

[14] S. V. Tkachenko, J. Nitsch, R. Vick, F. Rachidi, and D. Poljak, "Singularity expansion method (sem) for long terminated transmission lines," in *2013 International Conference on Electromagnetics in Advanced Applications (ICEAA)*, 2013, pp. 1091–1094. DOI: 10.1109/ICEAA.2013.6632411.

[15] S. Tkatchenko, F. Rachidi, and M. Ianoz, "Electromagnetic field coupling to a line of finite length: Theory and fast iterative solutions in frequency and time domains," *IEEE Transactions on Electromagnetic Compatibility*, vol. 37, no. 4, pp. 509–518, 1995. DOI: 10.1109/15.477335.

[16] K. Simonyi, *Theoretische Elektrotechnik*, German, 9th ed. Berlin, Germany: Dt. Verl. der Wiss., 1989, ISBN: 3326000456.

[17] J. D. Jackson, *Classical Electrodynamics*, English, 3rd ed. New York, NY: Wiley, 1999, ISBN: 047130932X.

[18] R. E. Collin, *Field Theory of Guided Waves*, English, 2nd ed. New York, NY: IEEE, 1991, ISBN: 0879422378.

[19] A. Sommerfeld, "Die Greensche Funktion der Schwingungslgleichung," *Jahresbericht der Deutschen Mathematiker-Vereinigung*, vol. 21, pp. 309–352, 1912. [Online]. Available: http://eudml.org/doc/145344.

[20] H. Klingbeil, *Elektromagnetische Feldtheorie: ein Lehr- und Übungsbuch*, German, 2nd ed. Wiesbaden, Germany: Vieweg + Teubner, 2011, ISBN: 3834814032.

[21] B. A. Dubrovin, A. T. Fomenko, and S. P. Novikov, *Modern Geometry. Pt. 1: Geometry of Surfaces, Transformation Groups, and Fields*, English, 2nd ed. New York, NY: Springer, 1992, ISBN: 0387976639.

[22] W. C. Gibson, *The Method of Moments in Electromagnetics*, 1st ed. Boca Raton, FL: Chapman & Hall/CRC, 2008.

[23] S. A. Schelkunoff, *Electromagnetic Waves*, English, 8th ed. Princeton/N.J.: van Nostrand, 1956.

[24] L. Marin, "Transient electromagnetic properties of two, infinite, parallel wires," *Appl. Phys.*, vol. 5, pp. 335–345, 1975. DOI: 10.1007/BF00928022.

[25] Y. Leviatan and A. Adams, "The response of a two-wire transmission line to incident field and voltage excitation, including the effects of higher order modes," *IEEE Transactions on Antennas and Propagation*, vol. 30, no. 5, pp. 998–1003, 1982. DOI: 10.1109/TAP.1982.1142893.

[26] F. Middelstaedt, S. V. Tkachenko, and R. Vick, "Analysis of an iterative approach to determine the current on the straight infinite wire above ground," *Advances in Radio Science*, vol. 17, pp. 169–176, 2019. DOI: 10.5194/ars-17-169-2019. [Online]. Available: https://ars.copernicus.org/articles/17/169/2019/.

[27] F. M. Tesche, M. V. Ianoz, and T. Karlsson, *EMC Analysis Methods and Computational Models*, English. New York: Wiley, 1997, ISBN: 047115573X.

[28] J. Nitsch and S. Tkachenko, "Source dependent transmission line parameters - plane wave vs. TEM excitation," Air Force Weapons Laboratory, Kirtland Air Force Base, Albuquerque, NM, USA, Interaction Note 577, 2002. [Online]. Available: http://ece-research.unm.edu/summa/notes/In/0577.pdf.

[29] C. Taylor, R. Satterwhite, and C. Harrison, "The response of a terminated two-wire transmission line excited by a nonuniform electromagnetic field," *IEEE Transactions on Antennas and Propagation*, vol. 13, no. 6, pp. 987–989, 1965. DOI: 10.1109/TAP.1965.1138574.

[30] A. K. Agrawal, H. J. Price, and S. H. Gurbaxani, "Transient response of multiconductor transmission lines excited by a nonuniform electromagnetic field," *IEEE Transactions on Electromagnetic Compatibility*, vol. EMC-22, no. 2, pp. 119–129, 1980. DOI: 10.1109/TEMC.1980.303824.

[31] F. Rachidi, "Formulation of the field-to-transmission line coupling equations in terms of magnetic excitation field," *IEEE Transactions on Electromagnetic Compatibility*, vol. 35, no. 3, pp. 404–407, 1993. DOI: 10.1109/15.277316.

[32] M. Leone and A. Mantzke, "A foster-type field-to-transmission line coupling model for broadband simulation," *IEEE Transactions on Electromagnetic Compatibility*, vol. 56, no. 6, pp. 1630–1637, 2014. DOI: 10.1109/TEMC.2014.2336792.

[33] A. Mantzke, S. Südekum, and M. Leone, "Broadband equivalent-circuit model for uniform multiconductor transmission lines," *IEEE Transactions on Electromagnetic Compatibility*, vol. 59, no. 4, pp. 1252–1259, 2017. DOI: 10.1109/TEMC.2016.2636565.

[34] G. J. Burke and A. J. Poggio, "Numerical Electromagnetics Code (NEC) - Method of Moments - Part I: Program Description - Theory," Lawrence Livermore Laboratory, Tech. Rep., 1981.

[35] T. Sarkar, "A note on the choice weighting functions in the method of moments," *IEEE Transactions on Antennas and Propagation*, vol. 33, no. 4, pp. 436–441, 1985. DOI: 10.1109/TAP.1985.1143590.

[36] T. Sarkar, A. Djordjevic, and E. Arvas, "On the choice of expansion and weighting functions in the numerical solution of operator equations," *IEEE Transactions on Antennas and Propagation*, vol. 33, no. 9, pp. 988–996, 1985. DOI: 10.1109/TAP.1985.1143707.

[37] C. E. Baum, "On the singularity expansion method for the solution of electromagnetic interaction problems," Air Force Weapons Laboratory, Kirtland Air Force Base, Albuquerque, NM, USA, Interaction Note 88, Dec. 1971. [Online]. Available: http://ece-research.unm.edu/summa/notes/In/0088.pdf.

[38] F. Tesche, "On the analysis of scattering and antenna problems using the singularity expansion technique," *IEEE Transactions on Antennas and Propagation*, vol. 21, no. 1, pp. 53–62, 1973. DOI: 10.1109/TAP.1973.1140398.

[39] ——, "The far-field response of a step-excited linear antenna using SEM [singularity expansion method]," *IEEE Transactions on Antennas and Propagation*, vol. 23, no. 6, pp. 834–838, 1975. DOI: 10.1109/TAP.1975.1141183.

[40] C. E. Baum, "Transient electromagnetic fields," in *Transient Electromagnetic Fields*, L. B. Felsen, Ed. Berlin, Heidelberg: Springer Berlin Heidelberg, 1976, ch. The singularity expansion method, pp. 129–179, ISBN: 978-3-540-38095-5. DOI: 10.1007/3540075534_8.

[41] J. A. Stratton, *Electromagnetic Theory*, English. Piscataway, NJ: IEEE Press [u.a.], 2007, ISBN: 0470131535.

[42] T. Sarkar and O. Pereira, "Using the matrix pencil method to estimate the parameters of a sum of complex exponentials," *IEEE Antennas and Propagation Magazine*, vol. 37, no. 1, pp. 48–55, 1995. DOI: 10.1109/74.370583.

[43] L. Marin, "Natural-mode representation of transient scattered fields," *IEEE Transactions on Antennas and Propagation*, vol. 21, no. 6, pp. 809–818, 1973. DOI: 10.1109/TAP.1973.1140603.

[44] B. K. Singaraju, D. V. Giri, and C. E. Baum, "Further developments in the application of contour integration to the evaluation of the zeros of analytic functions and relevant computer programs," Air Force Weapons Laboratory, Kirtland Air Force Base, Albuquerque, NM, USA, Mathematics Note 42, Mar. 1976. [Online]. Available: http://ece-research.unm.edu/summa/notes/Mathematics/0042.pdf.

[45] L. V. Ahlfors, *Complex Analysis: An Introduction to the Theory of Analytic Functions of one Complex Variable*, English. New York: McGraw-Hill, 1953.

[46] D. V. Giri and F. M. Tesche, "An overview of the natural frequencies of a straight wire by various methods," *IEEE Transactions on Antennas and Propagation*, vol. 60, no. 12, pp. 5859–5866, 2012. DOI: 10.1109/TAP.2012.2211317.

[47] B. Gustavsen and A. Semlyen, "Rational approximation of frequency domain responses by vector fitting," *IEEE Transactions on Power Delivery*, vol. 14, no. 3, pp. 1052–1061, 1999. DOI: 10.1109/61.772353.

[48] B. Gustavsen, "Improving the pole relocating properties of vector fitting," *IEEE Transactions on Power Delivery*, vol. 21, no. 3, pp. 1587–1592, 2006. DOI: 10.1109/TPWRD.2005.860281.

[49] D. Deschrijver, M. Mrozowski, T. Dhaene, and D. De Zutter, "Macromodeling of multiport systems using a fast implementation of the vector fitting method," *IEEE Microwave and Wireless Components Letters*, vol. 18, no. 6, pp. 383–385, 2008. DOI: 10.1109/LMWC.2008.922585.

[50] S. Tkatchenko, F. Rachidi, M. Ianoz, and L. M. Martynov, "Exact field to transmission line coupling equations for lines of finite length," in *Proceedings of EMC '96 ROMA. International Symposium on Electromagnetic Compatibility*, 1996.

[51] S. Tkatchenko, F. Rachidi, M. Ianoz, and L. Martynov, "An asymptotic approach for the calculation of electromagnetic field coupling to long terminated lines," in *Proceedings of EMC '98 ROMA. International Symposium on Electromagnetic Compatibility*, 1998.

[52] F. Middelstaedt, S. Tkachenko, R. Vick, and R. Rambousky, "Analytic approximation of natural frequencies of bent wire structures above ground," in *2015 IEEE International Symposium on Electromagnetic Compatibility (EMC)*, 2015, pp. 812–817. DOI: 10.1109/ISEMC.2015.7256268.

[53] G. Lugrin, S. V. Tkachenko, F. Rachidi, M. Rubinstein, and R. Cherkaoui, "High-frequency electromagnetic coupling to multiconductor transmission lines of finite length," *IEEE Transactions on Electromagnetic Compatibility*, vol. 57, no. 6, pp. 1714–1723, 2015. DOI: 10.1109/TEMC.2015.2475156.

[54] A. G. Akritas, E. K. Akritas, and G. I. Malaschonok, "Various proofs of sylvester's (determinant) identity," *Mathematics and Computers in Simulation*, vol. 42, no. 4, pp. 585–593, 1996, ISSN: 0378-4754. DOI: https://doi.org/10.1016/S0378-4754(96)00035-3.

[55] F. Middelstaedt, S. V. Tkachenko, R. Rambousky, and R. Vick, "High-frequency electromagnetic field coupling to a long, finite wire with vertical risers above ground," *IEEE Transactions on Electromagnetic Compatibility*, vol. 58, no. 4, pp. 1169–1175, 2016. DOI: 10.1109/TEMC.2016.2544110.

[56] F. Middelstaedt, S. V. Tkachenko, and R. Vick, "Transmission line reflection coefficient including high-frequency effects," *IEEE Transactions on Antennas and Propagation*, vol. 66, no. 8, pp. 4115–4122, 2018. DOI: 10.1109/TAP.2018.2839914.

[57] L. A. Weinstein, *The theory of diffraction and the factorization method*. Golem Press, 1969.

[58] C. M. Bender and S. A. Orzsag, *Advanced Mathematical Methods for Scientists and Engineers I: Asymptotic Methods and Perturbation Theory*. New York, NY: Springer, 1999, ISBN: 9781475730692. DOI: 10.1007/978-1-4757-3069-2.

[59] M. Abramowitz and I. A. Stegun, *Handbook of Mathematical Functions with Formulas, Graphs, and Mathematical Tables*. New York: Dover, 1964.

[60] J. Nitsch and S. Tkachenko, "High-frequency multiconductor transmission-line theory," *Foundations of Physics*, vol. 40, no. 9, pp. 1231–1252, Oct. 2010. DOI: 10.1007/s10701-010-9443-1.

[61] F. Middelstaedt, S. V. Tkachenko, and R. Vick, "Natural frequencies of long symmetric multiconductor transmission lines," *IEEE Transactions on Antennas and Propagation*, vol. 67, no. 6, pp. 3881–3888, 2019. DOI: 10.1109/TAP.2019.2902748.

[62] ——, "The induced emf method as an alternative to the iterative method for the approximation of the reflection coefficient on thin wires," *IEEE Transactions on Antennas and Propagation*, vol. 69, no. 8, pp. 4781–4788, 2021. DOI: 10.1109/TAP.2021.3060091.

[63] P. S. Carter, "Circuit relations in radiating systems and applications to antenna problems," *Proceedings of the Institute of Radio Engineers*, vol. 20, no. 6, pp. 1004–1041, Jun. 1932, ISSN: 2162-6626. DOI: 10.1109/JRPROC.1932.227723.

[64] D. Otto, "A note on the induced emf method for antenna impedance," *IEEE Transactions on Antennas and Propagation*, vol. 17, no. 1, pp. 101–102, Jan. 1969, ISSN: 0018-926X. DOI: 10.1109/TAP.1969.1139347.

[65] J. D. Kraus, *Antennas*, 2nd ed. New York, NY: McGraw-Hill, 1988.

[66] C. A. Balanis, *Antenna theory: analysis and design*, 3rd ed. Hoboken, N.J.: Wiley-Interscience, 2005.

[67] S. Riegger and W. Wiesbeck, "Wide-band polarimetry and complex radar cross section signatures," *Proceedings of the IEEE*, vol. 77, no. 5, pp. 649–658, 1989. DOI: 10.1109/5.32055.

[68] M. Rosenthal, F. Middelstaedt, and R. Vick, "Mono-static radar cross-section measurement and calibration for complex natural resonance extraction," in *2022 International Symposium on Electromagnetic Compatibility – EMC Europe*, 2022, pp. 221–226. DOI: 10.1109/EMCEurope51680.2022.9901128.

[69] W. Wiesbeck and S. Riegger, "A complete error model for free space polarimetric measurements," *IEEE Transactions on Antennas and Propagation*, vol. 39, no. 8, pp. 1105–1111, 1991. DOI: 10.1109/8.97343.

[70] W. Wiesbeck and D. Kahny, "Single reference, three target calibration and error correction for monostatic, polarimetric free space measurements," *Proceedings of the IEEE*, vol. 79, no. 10, pp. 1551–1558, 1991. DOI: 10.1109/5.104229.

[71] G. Mie, "Beiträge zur optik trüber medien, speziell kolloidaler metallösungen," *Annalen der Physik*, vol. 330, no. 3, pp. 377–445, 1908. DOI: https://doi.org/10.1002/andp.19083300302. eprint: https://onlinelibrary.wiley.com/doi/pdf/10.1002/andp.19083300302.

[72] B. Gustavsen, "Time delay identification for transmission line modeling," in *Proceedings. 8th IEEE Workshop on Signal Propagation on Interconnects*, 2004, pp. 103–106. DOI: 10.1109/SPI.2004.1409018.

[73] C. Aiken, "Two-mesh tuned coupled circuit filters," *Proceedings of the Institute of Radio Engineers*, vol. 25, no. 2, pp. 230–272, 1937. DOI: 10.1109/JRPROC.1937.228928.

[74] B. O'Neill, *Elementary Differential Geometry*, 1st ed. Academic Press Inc., 1966.

List of Figures

Declaration of Honor

I hereby declare that I produced this thesis without prohibited external assistance and that none other than the listed references and tools have been used.

In the case of co-authorship, especially in the context of a cumulative dissertation, the own contribution is correctly and completely stated. I did not make use of any commercial consultant concerning graduation. A third party did not receive any nonmonetary perquisites neither directly nor indirectly for activities which are connected with the contents of the presented thesis. All sources of information are clearly marked, including my own publications.

In particular I have not consciously:

- Fabricated data or rejected undesired results
- Misused statistical methods with the aim of drawing other conclusions than those warranted by the available data
- Plagiarized data or publications
- Presented the results of other researchers in a distorted way

I do know that violations of copyright may lead to injunction and damage claims of the author and also to prosecution by the law enforcement authorities.

I hereby agree that the thesis may need to be reviewed with an electronic data processing for plagiarism.

This work has not yet been submitted as a doctoral thesis in the same or a similar form in Germany or in any other country. It has not yet been published as a whole.

Magdeburg, April 2024

Res Electricae Magdeburgenses

MAgdeburger FOrum zur Elektrotechnik

MAFO-01 Orths, A.: *Multikriterielle, optimale Planung von Verteilungsnetzen im liberalisierten Energiemarkt unter Verwendung von spieltheoretischen Verfahren*, 2003. ISBN 3-929757-57-5.

MAFO-02 Purmann, M.: *Optimierung des Betriebsverhaltens von PEM-Brennstoffzellen unter Berücksichtigung von elektrischem und Gesamtwirkungsgrad bei unterschiedlichen Lastanforderungen und Betriebsparametern*, 2004. ISBN 3-929757-63-X.

MAFO-03 Al-Hamid, M.: *Extraktion von höheren Moden in TEM-Wellenleitern*, 2004. ISBN 3-929757-64-8.

MAFO-04 Haase, H., J. Nitsch, and T. Steinmetz: *Transmission-Line Super Theory – A new Approach to an Effective Calculation of Electromagnetic Interference*, 2004. ISBN 3-929757-67-2.

MAFO-05 Bachry, A.: *Power Quality Studies in Distribution Systems Involving Spectral Decomposition*, 2004. ISBN 3-929757-68-0.

MAFO-06 Styczynski, Z. A.: *Power Network and Renewables – A Scientific Report*, 2004. ISBN 3-929757-69-9.

MAFO-07 Blume, E.: *Numerische Analyse der Kopplung linearer Antennen innerhalb eines Resonators*, 2004. ISBN 3-929757-71-0.

MAFO-08 Handschin, E. and Z. A. Styczynski: *Power System Application of the Modern Battery Storage*, 2004. ISBN 3-929757-75-3.

MAFO-09 Haase, H.: *Full-Wave Field Interactions of Nonuniform Transmission Lines*, 2005. ISBN 3-929757-78-8.

MAFO-10 Nitsch, D.: *Die Wirkung eingekoppelter ultrabreitbandiger elektromagnetischer Impulse auf komplexe elektronische Systeme*, 2005. ISBN 3-929757-79-6.

MAFO-11 Hadzi-Kostova, B.: *Protection Concepts in Distribution Networks with Decentralized Energy Resources*, 2005. ISBN 3-929757-84-2.

MAFO-12 Steinmetz, T.: *Ungleichförmige und zufällig geführte Mehrfachleitungen in komplexen technischen Systemen*, 2006. Nummerierung geändert, ISBN 3-929757-98-2.

MAFO-13 Styczynski, Z. and J. Haubrock: *Influence of Distributed and Renewable Generation on Power System Security – Proceedings of the CRIS Workshop 2006*, 2006. ISBN 3-929757-99-0.

MAFO-14 Heideck, G.: *Ein autonomes Brennstoffzellensystem: Optimierungsansätze*, 2006. ISBN 3-929757-94-X.

MAFO-15 Styczynski, Z. und H.-D. Musikowski: *Dresdener Kreis Elektroenergieversorgung 7*, 2006. ISBN 3-929757-85-0.

MAFO-16 Gronwald, F.: *Antenna Theory in Resonating Systems derived from Fundamental Electromagnetism*, 2007. ISBN 3-929757-93-1.

MAFO-17 Krauthäuser, H.G.: *Grundlagen und Anwendungen von Modenverwirbelungskammern*, 2007. ISBN 978-3-929757-43-9.

MAFO-18 Dzienis, C.: *Ersatzmodelle nichtlinearer Lasten in elektrischen Verteilungsnetzen*, 2007. ISBN 978-3-929757-07-1.

MAFO-19 Styczynski, Z. and J. Haubrock: *Renewable and Dispersed Power Generation in Power Systems*, 2007. ISBN 978-3-929757-44-6.

MAFO-20 Haubrock, J.: *Parametrierung elektrischer Äquivalentschaltbilder von PEM-Brennstoffzellen*, 2008. ISBN 978-3-940961-02-0.

MAFO-21 Angelov, A. N.: *Rechnergestütztes Lernen im Bereich der Regenerativen Energien (Ausgewählte Aspekte)*, 2008. ISBN 978-3-940961-03-7.

MAFO-22 Komarnicki, P.: *Anwendung hochgenauer, synchroner Messungen zur Verbesserung des Betriebs von Verteilungsnetzen*, 2008. ISBN 978-3-940961-04-4.

MAFO-23 Roggatz, C.: *Trainingssimulator für die Führung von elektrischen Systemen mit dezentralen Energieeinspeisungen – Trainingsszenarien und Umsetzung*, 2008. ISBN 978-3-940961-05-1.

MAFO-24 Rudion, K.: *Aggregated Modelling of Wind Farms*, 2008. ISBN 978-3-940961-14-3.

MAFO-25 Ganjavi, M. R.: *Protection System Coordination Using Expert System*, 2008. ISBN 978-3-940961-15-0.

MAFO-26 Bofinger, S.: *Energieversorgungsnetze mit einem hohen Anteil an photovoltaischer Solarenergie: Standortbestimmung, Solarstromprognose, Netzintegration*, 2008. ISBN 978-3-940961-25-9.

MAFO-27 Styczynski, Z. and P. Komarnicki: *Distributed and Renewable Power Generation*, 2008. ISBN 978-3-940961-26-6.

MAFO-28 Kochetov, S. V.: *Time- and Frequency-Domain Modeling of Passive Interconnection Structures in Field and Circuit Analysis*, 2008. ISBN 978-3-940961-27-3.

MAFO-29 Magdowski, M.: *Entwicklung und Validierung eines Werkzeugs zur Berechnung der elektromagnetischen Einkopplung von stochastischen Feldern in Leitungsstrukturen*, 2008. ISBN 978-3-940961-28-0.

MAFO-30 Sonnemann, F.: *Elektromagnetische Effekte an elektrischen Zündmitteln (EED) mit angeschlossener Zündkreiselektronik (ZKE) bei impulsförmiger, breitbandiger Bestrahlung*, 2009. ISBN 978-3-940961-32-7.

MAFO-31 Smieja, T.: *Multikriterielle Planung interregionaler Elektrizitätsnetze im liberalisierten Energiemarkt*, 2009. ISBN 978-3-940961-35-8.

MAFO-32 Heyde, C. O.: *Dynamic Voltage Security Assessment for On-Line Control Room Application*, 2010. ISBN 978-3-940961-40-2.

MAFO-33 Styczynski, Z. A. and N. I. Voropai (Editors): *Renewable Energy Systems Fundamentals, Technologies, Techniques and Economics*, 2010. ISBN 978-3-940961-42-6.

MAFO-34 Styczynski, Z. A. и N. I. Voropai (Editors): Renewable Energy Systems Fundamentals, Technologies, Techniques and Economics (Russian Version), 2010. ISBN 978-3-940961-44-0.

MAFO-35 Styczynski, Z. A. and A. Lindemann (Editors): *Integration of Renewable Energies into the Grid / Proceedings of the Power & Energy Student Summit 2010*, 2010. ISBN 978-3-940961-47-1.

MAFO-36 Styczynski, Z. A. und H.-D. Musikowski (Editors): *Dresdener Kreis Elektroenergieversorgung 11*, 2010. ISBN 978-3-940961-51-8.

MAFO-37 Gurbiel, M. A.: *Definition and Testing of a Digital Interface of a Power Substation*, 2011. ISBN 978-3-940961-54-9.

MAFO-38 Lombardi, P.: *Multi Criteria Optimization of an Autonomous Virtual Power Plant*, 2011. ISBN 978-3-940961-55-6.

MAFO-39 Powalko, M.: *Beobachtbarkeit eines elektrischen Verteilungsnetzes – Ein Beitrag zum Smart Grid*, 2011. ISBN 978-3-940961-62-4.

MAFO-40 Styczynski, Z. A., K. Rudion, and C. Nguyen-Mau (Editorial Board): *Power System Dynamic Security Assessment*, 2011. ISBN 978-3-940961-61-7.

MAFO-41 Käbisch, M: *Optimale Dimensionierung und Betriebsführung einer brennstoffzellenbasierten Auxiliary Power Unit im Fahrzeug*, 2011. ISBN 978-3-940961-67-9.

MAFO-42 Styczynski, Z. A. und N. I. Voropai (Editors): *Special Issue Grant 220 Russian Federation SSmart Grid for Efficient Energy Power System for the Future", Proceedings Volume I*, 2012. ISBN 978-3-940961-74-7.

MAFO-43 Styczynski, Z. A., P. Komarnicki und A. Naumann (Editors): *Abschlussbericht Harz.ErneuerbareEnergien-mobility*, 2012. ISBN 978-3-940961-71-6.

MAFO-44 Heuer, M.: *Diagnosetool für stationär betriebene PEM-Brennstoffzellensysteme*, 2012. ISBN 978-3-940961-77-8.

MAFO-45 Stötzer, M.: *Demand Side Integration in elektrischen Verteilnetzen – Potenzialanalyse und Bewertung*, 2012. ISBN 978-3-940961-78-5.

MAFO-46 Magdowski, M.: *Vergleich der Einkopplung deterministischer und statistischer elektromagnetischer Felder in Leitungen*, 2012. ISBN 978-3-940961-75-4.

MAFO-47 Naumann, A.: *Leitwarte im Smart Grid*, 2012. ISBN 978-3-940961-81-5.

MAFO-48 Rudion, K.: *Offshore Power System Planning – Selected Aspects*, 2012. ISBN 978-3-940961-82-2.

MAFO-49 Nguyen-Mau, C.: *Electric Power System Stability Enhancement by Voltage Source Converter based High Voltage Direct Current Technology*, 2012. ISBN 978-3-940961-84-6.

MAFO-50 Guo, H.: *Measurement-Based Load Modeling for Smart Grid Planning*, 2012. ISBN 978-3-940961-86-0.

MAFO-51 Styczynski, Z. A.: *Proceedings No. 2 in the Scope of Mega Grant Baikal*, 2013. ISBN 978-3-940961-95-2.

MAFO-52 Styczynski, Z. A.: *Proceedings No. 3 in the Scope of Mega Grant Baikal*, 2013. ISBN 978-3-940961-98-3.

MAFO-53 Wenge, C.: *Optimaler Betrieb von mobilen Speichern im Smart Grid. -Mobilitätsleitwarte-*, 2013. ISBN 978-3-944722-01-6.

MAFO-54 Röhrig, C.: *Smart Distribution Planung unter Berücksichtigung von residualen Lasten*, 2014. ISBN 978-3-944722-06-1.

MAFO-55 Middelstädt, F.: *Research of SEM Poles of Complex Wire Structures*, 2014. ISBN 978-3-944722-07-8.

MAFO-56 Styczynski, Z. A. (Editor): *Power Network and Renewables – A Scientific Report – 15 Years Research*, 2014. ISBN 978-3-944722-08-5.

MAFO-57 Solonina, N. N., V. S. Stepanov, and K. V. Suslov: *Information technology in intelligent power networks*, 2014. ISBN 978-3-944722-13-9.

MAFO-58 Krebs, R.: *Fundamentals of Power System Protection*, 2014. ISBN 978-3-944722-15-3.

MAFO-59 Moskalenko, N.: *Optimal Dynamic Energy Management System in Smart Homes*, 2014. ISBN 978-3-944722-16-0.

MAFO-60 Hauer, I.: *Optimale Last- und Erzeugungsanpassung bei kritischen Netzzuständen – Algorithmen und deren Bewertung*, 2014. ISBN 978-3-944722-18-4.

MAFO-61 Richter, M.: *Dresdner Kreis Elektroenergieversorgung 15, Begleitband zum Workshop 2014*, 2014. ISBN 978-3-944722-21-4.

MAFO-62 Styczynski, Z. A., A. Richter und P. Kühne: *Second ELECON Workshop – Begleitband zum Workshop 2014*, 2014. ISBN 978-3-944722-23-8.

MAFO-63 Bernstein, P.: *Modellgestützte optimale Betriebsführung von PEM-Brennstoffzellen für autonome Anlagen*, 2015. ISBN 978-3-944722-24-5.

MAFO-64 Rabe, S.: *Betrieb einer Zweipunkt-Offshore-HGÜ-Verbindung – Modelluntersuchungen*, 2015. ISBN 978-3-944722-31-3.

MAFO-65 Arendarski, B.: *Reliability Assessment of Smart Grids*, 2015. ISBN 978-3-944722-32-0.

MAFO-66 Pan, X.: *Numerisches EMV-Simulationsverfahren zur Berechnung der Störaussendung elektrischer Antriebssysteme in Hybridfahrzeugen*, 2016. ISBN 978-3-944722-34-4.

MAFO-67 Richter, M.: *PMU-basierte Zustandsabschätzung in Smart Distribution*, 2016. ISBN 978-3-944722-43-6.

MAFO-68 Bielchev, I.: *Adaptiver Distanzschutz im Standard IEC 61850*, 2016. ISBN 978-3-944722-45-0.

MAFO-69 Hassan, A.: *Modeling of Single and Double-Shielded Cables for EMC Applications*, 2016. ISBN 978-3-944722-41-2.

MAFO-70 Liu, X.: *Control of Voltage Source Converter Based High Voltage Direct Current Transmission Systems for Grid Code Compliance*, 2016. ISBN 978-3-944722-46-7.

MAFO-71 Kaiser, M.: *Fusion of Interventional Ultrasound & X-ray*, 2016. ISBN 978-3-944722-51-1.

MAFO-72 Grieger, F.: *Ein Beitrag zur Bestimmung der Zuverlässigkeit von Leistungshalbleiterbauelementen unter Berücksichtigung der Anwendung*, 2016. ISBN 978-3-944722-52-8.

MAFO-73 Li, M.: *Towards a Robust Electromagnetic Tracking System for Use in Medical Applications*, 2018. ISBN 978-3-944722-66-5.

MAFO-74 Klabunde, C., J. Dancker, N. Gast, T. Schröter, F. Schulz, J. Rossberg und A. Richter: *Statusbericht der Otto-von-Guericke-Universität Magdeburg zum Verbundprojekt: Intelligentes Multi-Energie-System (SmartMES)*, 2018. ISBN 978-3-944722-69-6.

MAFO-75 Schröter, T.: *19. Dresdner Kreis Elektroenergieversorgung, Begleitband zum Workshop 2018 in Magdeburg*, 2018. ISBN 978-3-944722-79-5.

MAFO-76 Klabunde, C., J. Dancker, N. Gast, T. Schröter, F. Schulz und J. Rossberg: *Intelligentes Multi-Energie-System (SmartMES) – Statusbericht der Otto-von-Guericke-Universität Magdeburg zum Verbundprojekt, 2. Statusseminar 04. April 2019 in Magdeburg*, 2019. ISBN 987-3-944722-80-1.

MAFO-77 Helm, S., J. Dancker, M. Fritsch und T. Schröter: *Power and Energy Student Summit 2019, 09.–11. Juli*, 2019. ISBN 978-3-944722-84-9.

MAFO-78 Chychykina, I.: *Comparison of Different Redispatch Optimization Strategies*, 2019. ISBN 978-3-944722-89-4.

MAFO-79 Balischewski, S.: *Multifunktionaler Einsatz von Batteriespeichern in elektrischen Verteilnetzen*, 2020. ISBN 978-3-944722-92-4.

MAFO-80 Petzold, J.: *Analytische Beschreibung der Kopplung elektromagnetischer Felder durch Aperturen in Resonatoren*, 2020. ISBN 978-3-944722-91-7.

MAFO-81 Middelstädt, L.: *Transiente Effekte in leistungselektronischen Schaltungen mit schnellschaltenden Leistungshalbleitern unter besonderer Berücksichtigung der elektromagnetischen Verträglichkeit*, 2020. ISBN 978-3-944722-95-5.

MAFO-82 Liu, Y.: *Contribution to Improve the EMI Performance of Electrical Drive Systems in Vehicles With Special Consideration of Power Semiconductor Modules*, 2021. ISBN 978-3-948749-01-9.

MAFO-83 Gerlach, A.: *Regelung von direktangetriebenen elektrischen Maschinen für Verbrennungsmotoren*, 2021. ISBN 978-3-948749-03-3.

MAFO-84 Zhang, Y.: *Analysis and Control of Resonances in HVDC Connected DFIG-Based Offshore Wind Farms*, 2021. ISBN 978-3-948749-05-7.

MAFO-85 Pannicke, E.: *Empfangsspulen für bildgeführte Eingriffe mittels Magnetresonanztomographie*, 2021. ISBN 978-3-948749-12-5.

MAFO-86 Kasper, J.: *Analysis of the Stochastic Electromagnetic Field Coupling to Single and Multiconductor Transmission Line Structures*, 2021. ISBN 978-3-948749-13-2.

MAFO-87 Hauer, I.: *Abschlussbericht zum Projekt InKola: Infrastrukturkopplung – Platzierung und Betrieb von Ladestationen aus Verkehrs- und Energienetzsicht*, 2022. ISBN 978-3-948749-15-6.

MAFO-88 Raya, M.: *Circuit Models of Shielded Single and Multiconductor Cables for EMC Analyses*, 2022. ISBN 978-3-948749-16-3.

MAFO-89 Pribahsnik, F.: *GaN-Specific Mechanical Phenomena and Their Influence on Reliability in Power HEMT Operation*, 2022. ISBN 978-3-948749-17-0.

MAFO-90 Willmann, B.: *Elektromagnetische Umweltverträglichkeit eines Elektrofahrzeugs mit kontaktlosem Ladesystem*, 2022. ISBN 978-3-948749-19-4.

MAFO-91 Dancker, J.: *Sensitivity Factors for Integrated Energy Systems: A Joined Quasi-Steady-State Approach*, 2022. ISBN 978-3-948749-24-8.

MAFO-92 Tayyab, M.: *Holistic Approach for Microgrid Planning and Operation for E-Mobility Infrastructure Under Consideration of Multi-Type Uncertainties*, 2022. ISBN 978-3-948749-25-5.

MAFO-93 Richter, A.: *Virtuelle Kraftwerke im Verteilnetz – Systemstützender Betrieb im wirtschaftlichen Kontext – Eine gesamtheitliche Betrachtung virtueller Kraftwerke*, 2022. ISBN 978-3-948749-28-6.

MAFO-94 Woldu, T.: *Modeling and Simulation of Power System Dynamics for Studying the Impacts of Increasing Wind Power in a Weak Grid System*, 2022. ISBN 978-3-948749-31-6.

MAFO-95 Könneke, N.: *Entwurf eines Testbetts für Assistenzsysteme in der Netz- und Systemführung*, 2023. ISBN 978-3-948749-32-3.

MAFO-96 Glende, E. und M. Gebhardt: *23. Dresdner Kreis Elektroenergieversorgung, Begleitband zum Workshop 2022 in Magdeburg*, 2022. ISBN 978-3-948749-33-0.

MAFO-97 Kempiak, C.: *Lastwechselmethoden für Siliziumkarbid-MOSFETs unter Berücksichtigung von deren Schwellspannungsinstabilität*, 2023. ISBN 978-3-948749-38-5.

MAFO-98 Fritsch, M.: *Measurement of Partial Discharges on Power Cables: A Step Towards Successful Online Monitoring*, 2024. ISBN 978-3-948749-43-9.